Calibration of the PICO-0.1 bubble chamber
and
Development of coated inner vessels for dark matter search

by

Frédéric Girard

A thesis submitted in partial fulfillment
of the requirements for the degree of
Master of Science (MSc) in Physics

The Faculty of Graduate Studies
Laurentian University
Sudbury, Ontario, Canada

THESIS DEFENCE COMMITTEE/COMITÉ DE SOUTENANCE DE THÈSE
Laurentian Université/Université Laurentienne
Faculty of Graduate Studies/Faculté des études supérieures

Title of Thesis Titre de la thèse	Calibration of the PICO-0.1 bubble chamber and Development of coated inner vessels for dark matter search
Name of Candidate Nom du candidat	Girard, Frédéric
Degree Diplôme	Master of Science
Department/Program Département/Programme	Physics
Date of Defence Date de la soutenance	June 5, 2017

APPROVED/APPROUVÉ

Thesis Examiners/Examinateurs de thèse:

Dr. Ubi Wichoski
(Co-Supervisor/Co-directeur(trice) de thèse)

Dr. Viktor Zacek
(Co-Supervisor/Co-directeur(trice) de thèse)

Dr. Mohamed Azzouz
(Committee member/Membre du comité)

Dr. Rizwan Haq
(Committee member/Membre du comité)

Dr. Wolfgang Rau
(External Examiner/Examinateur externe)

Approved for the Faculty of Graduate Studies
Approuvé pour la Faculté des études supérieures
Dr. David Lesbarrères
Monsieur David Lesbarrères
Dean, Faculty of Graduate Studies
Doyen, Faculté des études supérieures

ACCESSIBILITY CLAUSE AND PERMISSION TO USE

ABSTRACT

The detection of dark matter is one of the biggest challenges in modern physics. The PICO experiment aims for the direct detection of Weakly Interacting Massive Particles (WIMPs) with bubble chambers.

In this thesis, results from calibrations of the PICO-0.1 test chamber is presented. Calibrations were performed at the Tandem Van de Graaff facility of the Université de Montréal. Monoenergetic neutrons were produced from the ^{51}V(p,n)^{51}Cr reaction with a 1.6 MeV proton beam.

Two ^{3}He neutron counters used during calibrations for neutron flux normalization were also calibrated. This result is contributing in improving Monte Carlo simulations of PICO-0.1.

Finally, preliminary work was done toward the use of new inner vessel materials with coated surfaces for bubble chambers. A Condensation Bubble Chambers (CBCs) was used as a test-bench. Progress has been made toward the usability of Poly-methyl-methacrylate vessels, but more work is needed to solve spontaneous wall nucleation problems.

Keywords: Dark Matter, WIMP, Cosmology, PICO experiment, SNOLAB, Bubble Chamber, ^{51}V, ^{51}Cr, Geyser, Condensation Bubble Chamber

ACKNOWLEDGMENTS

First of all, I want to thank my research directors. Viktor, you gave me my first chance to prove myself as a scientist. Thank you for the time and efforts invested in me. Ubi, thank you for the trust you've put in me. You offered me your support during the last two years and I am deeply grateful for this.

I'd like to thank the PICO collaboration as a whole. You gave me endless learning opportunities, and the desire to pursue the scientific dream. Thank you all.

Mathieu, j'ai énormément appris de toi, et j'en serai toujours reconnaissant. Tu m'as appris virtuellement tout ce que je connais de l'expérience PICO, des chambres à bulles, et de la matière sombre. Merci pour tout.

Mirjam, tu as été le pilier de ma santé mentale durant les longues journées au bunker, loin de la lumière du jour. Merci.

À mes collègues; Arthur, Olivia, Andréa, Alessandro, Frédéric, merci. À tout le monde qui m'ont assisté un jour ou l'autre au laboratoire, merci. Nick, Louis, Jean, Tom, François, Martin, vous m'avez tous "sauvé la vie" à un moment ou à un autre.

J'aimerais remercier mes amis qui m'ont aidé tout au long de mes années au baccalauréat. Vous ne m'avez jamais abandonné, et m'avez redonné espoir dans les moments les plus durs. Shannon, Andréanne, Patricia, Daniel, Olivier et Alexandre, merci.

Merci à mes amis: Luc-Olivier, Shayne, Ben, Bob, Frank. Thursday Night Blackout forever!

À mes parents, qui ont su stimuler ma curiosité, qui m'ont offert toutes les chances de m'épanouir lors de mon enfance, qui m'ont encouragé à poursuivre mes études post-secondaires, qui m'ont donné la chance de poursuivre mes études graduées, qui m'ont tout donné, merci.

Finalement, merci Jennifer, d'avoir été là pour me motiver, m'appuyer, et me pousser à continuer mes études. Sans toi, la chose aurait été beaucoup moins facile. Je t'aime!

À la mémoire de Roland Poudrier. (1942-2015)

TABLE OF CONTENTS

LIST OF TABLES

LIST OF FIGURES

LIST OF APPENDICES

CONTRIBUTION OF THE AUTHOR

My personal contribution to the PICO experiment regarding the work of this thesis is mainly related to the operation of the PICO-0.1 test chamber. I worked alongside Mathieu Laurin, who was responsible for most of the experimental work with PICO at the Université de Montréal at the time I started my graduate studies.

I operated the Tandem Van de Graaff accelerator and the PICO-0.1 test chamber during the neutron calibration. I helped in the primary analysis of the data to ensure data quality and to maintain the operational status of the chamber. I completed the data acquisition for the γ calibration started by Mathieu and slowly took over as the main operator of PICO-0.1 for subsequent calibrations.

I supervised the acquisition of antimony source for the SbBe calibration and performed the experiment. Finally I led the decommissioning (C_3F_8) and recommissioning (C_2ClF_5) of PICO-0.1, after which Arthur Plante took over as the main operator of the chamber.

In parallel to the calibration of PICO-0.1, I performed the ^{51}V absolute neutron flux measurement. I also performed the full data analysis with the help of a summer student, Alessandro Ambler. The analysis led to the determination of the efficiency of the two ^{3}He neutron counters deployed with PICO-0.1.

Finally, I performed R&D work on a *Condensation Bubble Chamber* we used to test surface coating on the inside surface of inner vessels. I commissioned and operated the chamber multiple times and developed an analysis algorithm, producing the first results from this detector.

CHAPTER 1

INTRODUCTION

The direct observation of dark matter is probably one of the biggest challenge in modern physics. Up until now, the only evidence of its existence has been observations of its gravitational effects, as there is yet no indication it could interact with normal matter by the other fundamental forces: the electromagnetic, strong and weak nuclear forces.

The race is on for direct detection experiments that look for elastic scattering of dark matter with normal nuclei. Over the last few decades, several large-scale experiments have been deployed over the world in deep underground laboratories to shield them from cosmic radiation. Different types of experiments include HPGe detectors, liquid Argon or liquid Xenon detectors, droplet detectors, bubble chambers and scintillating crystal detectors.

The PICO experiment, a joint effort from the previous dark matter experiments PICASSO and COUPP, operates two bubble chambers (PICO-2L, PICO-60) at SNOLAB in Sudbury, Ontario. The collaboration includes universities and research centers from Canada, the United States of America, as well as from Mexico, India and the Czech Republic. PICO bubble chambers are highly sensitive detectors containing liquids in a metastable superheated state. The experiment aims for the direct detection of Weakly Interacting Massive Particles (WIMPs) by nuclear recoils of WIMPs with fluorine atoms from the active liquid, which can produce macroscopic bubbles.

WIMPs direct detection assumes that we can exclude any signal produced by background radiation (alpha, neutron, gamma, etc.). Therefore, the collaboration built several small sized calibration chambers used to study the response of a bubble chamber when subjected to diverse types of radiation. The PICO-0.1 bubble chamber was calibrated at the Université de Montréal. The main neutron calibration was done by the production of mono-energetic neutrons from the nuclear reaction $^{51}\mathrm{V}(p,n)^{51}\mathrm{Cr}$ produced with the University's Tandem Van de Graaff electrostatic accelerator's proton beam. In addition, gamma calibrations were done with several gamma radiation sources,

such as ^{22}Na, ^{60}Co, ^{124}Sb, ^{133}Ba, ^{241}Am. The complete understanding of background radiation helps us reject background signal in dark matter physics runs of the PICO-2L and PICO-60 bubble chambers.

The PICO collaboration is planning the build a ton-scale bubble chamber, PICO-500. To lower the cost of the detector, a proposition was made by the collaboration to replace the current fused silica vessel by an acrylic, or Poly-methyl-methacrylate (PMMA), vessel. Fused silica is currently used due to its great radio purity and high stability. PMMA can also be a low radioactivity material, but on the other hand, the roughness of the surface of the material currently renders it unusable in a bubble chamber setup, causing surface boiling of the active fluid. It was proposed to investigate on the applications of surface coated vessels in bubble chambers. The concept was tested on a novel type of bubble chamber, nicknamed "Geyser". Given its simplified operation, it allowed to be tested at low cost, only needing a few electronic and acoustic sensors to record data. The use of giant acrylic vessels in experiments such as SNO has already established the possibility of using this material for large scale experiments, with high radio purity and lower cost of fabrication.

The theory of dark matter and its direct detection is discussed in chapter 2. The theory of bubble chambers is exposed in chapter 3, where the PICO experiment is also globally presented. The original work for this thesis is presented in the three following chapters:

1) The PICO-0.1 bubble chamber calibrations are described and different results are presented in chapter 4.

2) Results from an absolute flux measurement for the ^{51}V(p,n)^{51}Cr reaction and ^{3}He neutron counters efficiency determination are presented in chapter 5.

3) Preliminary work on the development of coated PMMA inner vessels for bubble chambers is presented in chapter 6. The *"Geyser"*, or *Condensation Bubble Chamber* (CBC) is described, and preliminary results are analyzed.

CHAPTER 2

DARK MATTER

Dark matter is mysterious, elusive, yet believed to be everywhere. In our day to day lives, no trace of its presence is observed. It cannot be seen, cannot be touched, cannot be produced... yet. However, some astrophysical phenomena seem to be unexplainable without it. Questioned for over forty years, the existence of dark matter is today generally accepted by the scientific community.

This chapter begins with the description of the Cosmological Standard model in section 2.1.2. The main evidence of the existence of dark matter are presented in section 2.2. An overview of the different candidate particles for dark matter is given in section 2.3. Finally, the principle of direct detection is presented in section 2.4.3.

2.1 Cosmology

There are multiple evidences of the existence of dark matter. These observations should be supported by a common cosmological model. The model that currently best describes the evolution of the Universe is the "*Lambda Cold Dark Matter*" (ΛCDM) model.

This model is based on the cosmological principle which state that no reference frame is preferred in the Universe. This, in turn, implies that the Universe is homogeneous and isotropic. It is identical everywhere at large scale and identical in every direction.

2.1.1 The Big Bang

In 1929, Edwin Hubble observed that the light of distant galaxies shows a red-shift increasing with distance [1].

This was the first observational evidence that the Universe is expanding. Reverting back in time, the Universe can be shrunk down to a singularity that, at the beginning of time, started swelling up, an event known as the Big Bang. Since then, the Universe has been expanding and

cooling down.

— $t < 10^{-43}$ s: Plank epoch

At the Plank time, the Universe had a temperature of 10^{32} K. According to the ΛCDM model, the gravitational force decoupled from the two electroweak and strong nuclear forces, known as the unified electronuclear force. Without a unified theory of quantum mechanics and gravity, the Universe before the Planck time (time light takes to travel a Planck length ($1.616 \cdot 10^{-15}$ m) in vacuum) cannot be described.

— $t = 10^{-43}$ s: Grand unification epoch

During the Grand unification epoch, physical properties such as mass, charge, color and flavor were meaningless. All matter was condensed in a hot "soup" in thermal equilibrium. Near the end of the Grand unification era, the temperature had dropped down to 10^{27} K.

— $t = 10^{-36}$ s: Electroweak era and inflation

During this epoch, the electroweak force and the strong nuclear force decoupled from each other. Soon after, the Universe inflation period started. It expanded exponentially, its size swelling up rapidly by $\sim 10^{26}$ orders of magnitude. This rapid expansion would explain the observed homogeneity of the Universe.

During this period, dark matter evolved independently from matter. Quantum fluctuations rendered the distribution of dark matter inhomogeneous and would eventually lead to the formation of gravitational wells, forming the large scale structures of the Universe (Figure 2.1).

— $t = 10^{-12}$ s: Baryogenesis

After the inflation, which lasted 10^{-32} s, the Universe was constituted of a quark-gluon plasma [4]. The fall in temperature (T = 10^{16} K) due to the inflation lead to the epoch call "baryogenesis", where primordial particles first acquired their masses. The electromagnetic and weak nuclear

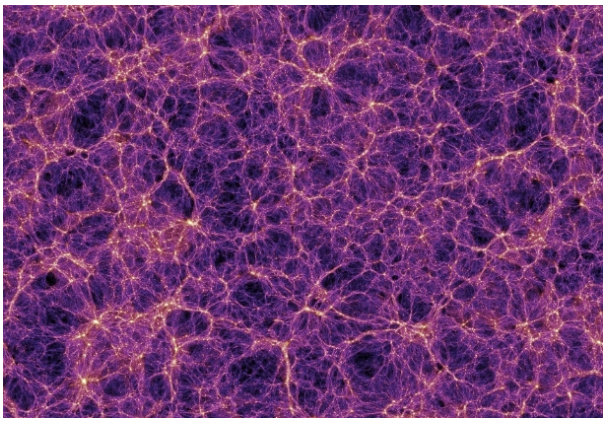

Figure 2.1: Large scale structures of the Universe [2].

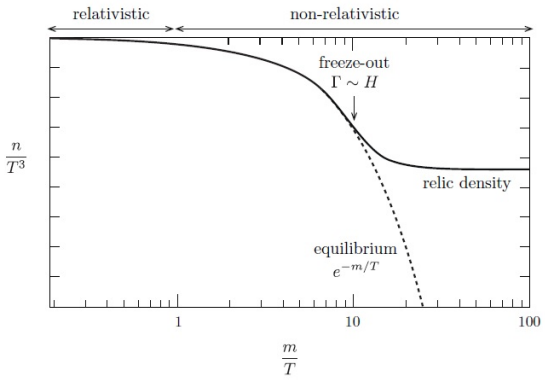

Figure 2.2: Dark matter freeze-out [3]. If dark matter stayed in thermal equilibrium, its density would follow the Boltzmann-suppressed equilibrium abundance (exponential). Because of its weakly interacting nature, dark matter fell out of equilibrium as the Universe cooled down. The dark matter number density froze out (i.e. stayed constant) as dark matter particles could not annihilate anymore.

forces finally decoupled from each other. Formerly in thermal equilibrium with the primordial "soup", the reduced temperature made it impossible for baryons to produce new dark matter particles, while at the same time, the dark matter density became too low to allow for dark matter annihilation. The dark matter density "froze-out". The freeze-out mechanism is presented graphically in Figure 2.2.

— t = 2 minutes: Nucleosynthesis

At $t = 10^{-4}$ s, quarks condensed to form hadrons. The high density of ionized hadrons didn't allow for the free propagation of light. At $t \approx 2$ minutes began the nucleosynthesis. At that moment, the temperature of the Universe fell under the nuclear binding energy, leading to the formation of the first light nuclei (^{3}He, ^{4}He, Li, Be). This process lasted only 17 minutes. In the end, there was about four times more hydrogen nuclei than helium nuclei and some other light nuclei.

— t = 380000 years: Recombination

As the Universe kept cooling down, electrons became bounded to protons to form atoms. Photons, previously strongly coupled to electrons, could then propagate without interacting with ionized particles. These photons are what we observe today as the Cosmic Microwave Background (CMB) at $T = 2.73$ K.

Due to the quantum fluctuations before the inflation period, the distribution of dark matter was inhomogeneous. This implies that dark matter overdensities acted as gravitational wells which formed the baryonic structures of the early Universe during the period called the "dark ages". These structures evolved to form what is seen today in the Universe as a web of baryonic matter (Figure 2.1). The accumulation of baryonic matter in gravitational wells led to the production of stars in the knots of the dark matter web structure between 300 and 500 million years after the Big Bang, during a period called the re-ionization. Finally, complex galactic systems formed a billion years after the big bang.

2.1.2 Cosmological standard model

The ΛCDM model describes the evolution of the Universe from Einstein's field equation [5]:

$$G_{\mu\nu} + \Lambda g_{\mu\nu} = \frac{8\pi G}{c^4} T_{\mu\nu} \tag{2.1}$$

where $G_{\mu\nu}$ is the Einstein tensor, Λ is the cosmological constant, $g_{\mu\nu}$ is the metric tensor, G is Newton's gravitational constant, c is the speed of light and $T_{\mu\nu}$ is the momentum-energy tensor. In natural units, we can pose $c = h = 1$, so that:

$$G_{\mu\nu} + \Lambda g_{\mu\nu} = 8\pi G T_{\mu\nu} \tag{2.2}$$

For a homogeneous and isotropic expanding Universe described by the Friedmann-Lemaître-Robertson-Walker (FLRW) metric, an exact solution of Einstein's field equation can be found [6]:

$$ds^2 = -dt^2 + a^2(t)\left[\frac{dr^2}{1-\kappa r^2} + r^2 d\Omega^2\right] \tag{2.3}$$

where ds is a differential space-time interval and dt is a differential time interval and $a(t)$ is a scale factor. The factor κ is the Universe curvature factor, and can take the values -1 for a hyperbolic geometry, 0 for a Euclidean geometry or +1 for a spherical geometry. Inserting the metric from equation 2.3 in equation 2.2, we can get the Friedmann equation:

$$H^2 = \left(\frac{\dot{a}}{a}\right)^2 = \frac{8\pi G}{3}\rho - \frac{\kappa}{a^2} \tag{2.4}$$

that governs the time evolution and dynamics of the Universe. In this equation, $H(t)$ is the Hubble parameter, which represents the expansion rate of the Universe. It presently has value of:

$$H_0 = 100\,h\,km\,s^{-1}\,Mpc^{-1} \tag{2.5}$$

with $h = 0.679 \pm 0.006$ [7]. We can define the critical density of the Universe:

$$\rho_c = \frac{3H^2}{8\pi G} \tag{2.6}$$

A Universe with a density of ρ_c is said to be of a flat geometry. From ρ_c, we can define the total density parameter:

$$\Omega_i = \frac{\rho_i}{\rho_c} = \frac{8\pi G\rho_i}{3H^2} \tag{2.7}$$

where the subscript i stands for the different matter species: *baryons (b), photons (γ), neutrinos (ν)* and *Cold Dark Matter (c).* Another component Ω_Λ accounts for the dark energy density, responsible for the accelerated expansion of the Universe. From these density parameters, the Friedmann equation can be re-written as:

$$\Omega = \sum_i \Omega_i + \Omega_\Lambda = \frac{k}{R^2H^2} + 1 \tag{2.8}$$

For a flat Universe, $\Omega = 1$.

The various density parameters have been measured indirectly and are tabulated in Table 2.I

Parameter	Measured value
$\Omega_b h^2$	0.02227 ± 0.00020
$\Omega_c h^2$	0.1184 ± 0.0012
Ω_m	0.306 ± 0.007
Ω_Λ	0.694 ± 0.007

Table 2.I: Table of measured cosmological parameters [7]. Ω_b is the baryonic matter density, Ω_c is the cold dark matter density, Ω_m is the sum of matter densities: $\Omega_m = \Omega_b + \Omega_c$. Ω_Λ is the cosmological constant.

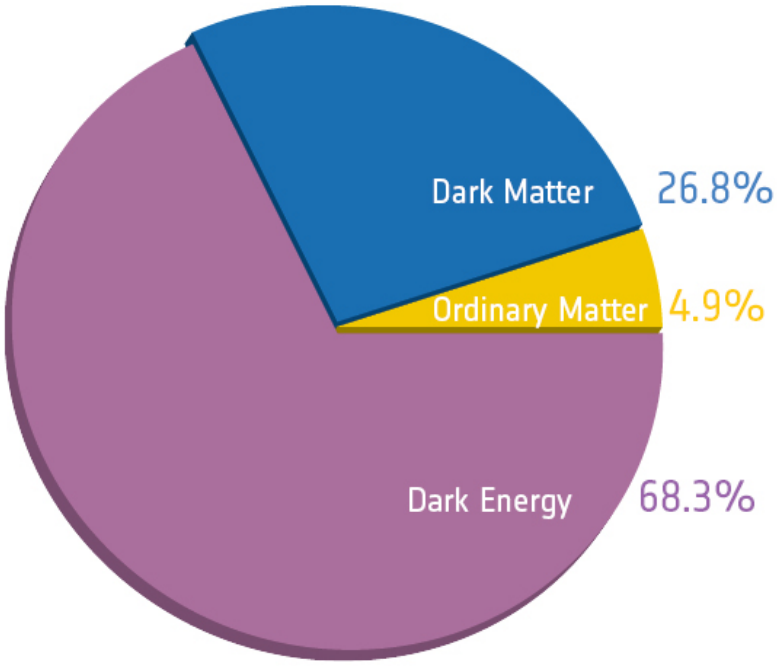

Figure 2.3: Relative energy density of the Universe [8].

[7]. The measurement of these parameters reveals information about the matter/energy constituents of the Universe. As presented in Figure 2.3, from the PLANCK CMB measurements, the Universe is constituted of 4.9% of normal matter and 26.8% of dark matter. The rest, about 68.3%, is dark energy, responsible for the accelerated expansion of the Universe. Furthermore, the sum of the measured densities gives $\Omega_{tot} \approx 1$, supporting flat Universe cosmological models.

Overall, the ΛCMD cosmological model forms a solid theoretical basis for the existence of dark matter, supported by cosmological observations.

2.2 Evidence of the existence of dark matter

In 1932, Jan Oort was the first astronomer to observe a truly abnormal behavior in our Milky Way when he measured that stars in our direct neighborhood were moving too fast. This observation led him to believe that a surplus of matter was either hidden by brighter stars, especially near the galactic center, or simply too dim on its own to be observed [9].

A year later, Fritz Zwicky was taking Doppler effect measurements in the Coma cluster, measuring the average speed of galaxies. From the amount of light emitted from the system, he was able to estimate its mass. Using the virial theorem, he calculated the gravitational mass in the cluster and showed it differed by two orders of magnitudes from the expected mass [10]. To Zwicky, the only explanation had to be the presence of a non-luminous type of matter that held the system together gravitationally. He named this excess matter "Dunkle Materie", German for "Dark Matter".

2.2.1 Rotation curves

In 1970, almost forty years after the observations of Fritz Zwicky, astronomer Vera Rubin observed a new evidence of the existence of dark matter. Working with instrument maker Kent Ford, they measured the rotation curve, the average angular velocity as a function of the distance from the galactic center, of the Andromeda galaxy [12].

From Newtonian mechanics, the expected angular velocity $v(r)$ of a galactic object is:

$$v(r) = \sqrt{\frac{GM(r)}{r}} \tag{2.9}$$

where $M(r)$ is the galactic mass contained in the inner shells. However, what they found was that the measured angular velocity away from the galactic center was much greater than that expected from calculations based on the mass observed in the outer regions. An example of the measured and calculated rotation curves is shown in Figure 2.4 [11]. In fact, according to Newtonian mechanics, the rotation is such that the galaxy could not be held together by only the gravity of observable

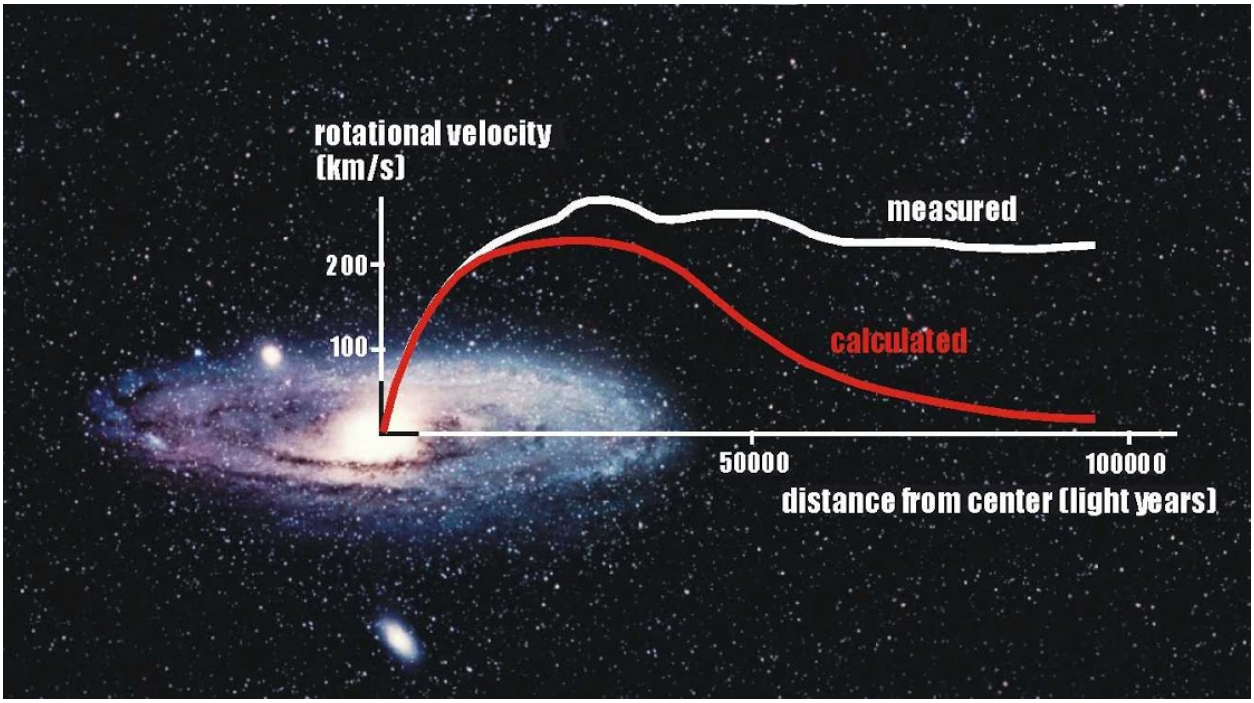

Figure 2.4: Rotation curves in galaxies [11]. The red curve is calculated from Newtonian and Keplerian mechanics. The measured curve in white shows a velocity excess in the outer regions of galaxies. An outer halo of dark matter in those regions would explain this difference.

matter.

During the following decades, Rubin observed the same behavior in over two hundred galaxies, showing evidence of the existence of a non-luminous, non-interacting halo of unobserved matter in most galaxies that would account for over 90% of the total galactic mass.

2.2.2 Gravitational lensing

Another evidence of the existence of dark matter is gravitational lensing. As stated in Einstein's theory of general relativity, light follows the curvature of space-time, described by the global metric in equation 2.1. Massive objects warp space-time locally, modifying the metric $g_{\mu\nu} \rightarrow g^*_{\mu\nu}$. This results in an apparent deflection of light, as observed by Arthur Eddington during a full solar eclipse in 1919. He observed the deflection of the light of distant stars passing near the sun in accordance with predictions from Einstein's theory. In 1937, Fritz Zwicky predicted that galaxies could provoke gravitational effects such as gravitational lensing [14].

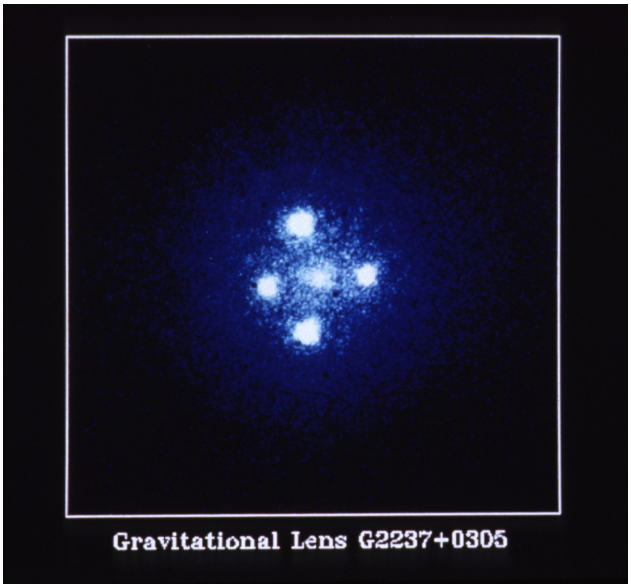

Figure 2.5: Einstein's cross [13]. A strong mass density in the foreground made four other images of the same quasar appear.

A large concentration of invisible mass located between an observer and a distant object can distort and redirect light coming from it. This effect is clearly seen in Figure 2.5. This object, named Einstein's cross, is a quasar whose light was bent by a galaxy containing a super-massive black hole, so that four duplicates of the same object are observed.

Dark matter would create the same effect. Figure 2.6 shows the resulting cluster from the collision of two galaxy clusters, named the Bullet cluster [17]. While merging, the interstellar gases of the galaxies heated up to 10^6 K due to electromagnetic interactions, emitting a large amount of X-rays that were measured by the Chandra X-ray Observatory in 2006 [18]. The observed X-ray emission is highlighted in pink on the image. The gases were slowed down significantly due to their interaction. However, weak gravitational lensing is observed along the projected trajectory of the galaxy clusters and suggests the presence of invisible masses that didn't interact during the merger, continuing their way with no significant loss of velocity. A map of the masses, considered as dark matter, was reconstructed from the weak lensing data and highlighted in blue in the image.

This effect was observed in multiple systems since, as in Figure 2.7 in a cluster called "El Gordo" (spanish for "*The Fat One*"). This cluster is located 8 billion light years away from our galaxy, and is the largest object of this type observed. Much like the much closer Bullet cluster,

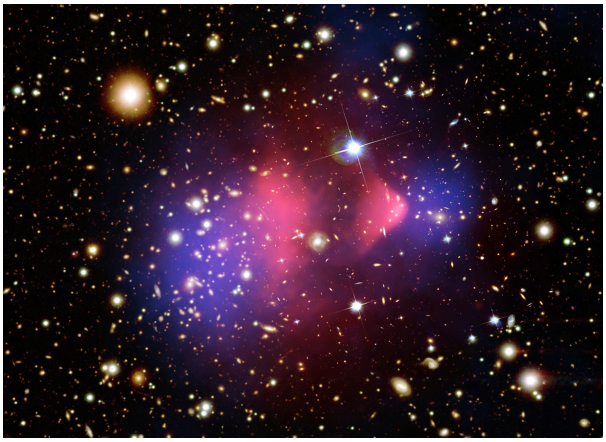

Figure 2.6: Bullet cluster [15]. The X-ray emission is highlighted in pink. The blue regions are the reconstructed dark matter masses obtained from weak gravitational lensing.

Figure 2.7: "El Gordo" cluster [16]. The largest object of this type, the cluster was probably formed in the same manner as the Bullet cluster. The color chart is the same as Figure 2.6

which is located only 4 billion light years away, "El Gordo" shows a heated region in its center and gravitational lensing allowed for the reconstruction of dark matter regions that passed through without interacting.

This is currently considered the most important evidence of the existence of dark matter as it is a model-independent observation.

2.2.3 Cosmic Microwave Background

In 1964, the two Bell Laboratories engineers Arno Penzias and Robert Woodrow Wilson detected an unexplained radio noise while working on a Holmdel radiometer, a horn radio-antenna intended for radio astronomical observations. After removing all possible noise sources, the isotropic signal of some dozen GHz was still present, night and day, even with the antenna chilled at Liquid Helium temperature. Robert Dicke, inventor of the radiometer Penzia and Wilson built, suggested that this GHz black body signal could be the Cosmic Microwave Background physicist were looking for, predicted in 1948 by Ralph Alpher and Robert Herman. The results were published in 1965 [21] and Penzia and Wilson were awarded the Nobel Prize in Physics in 1978 for their discovery.

This signal was first determined to have a temperature of $T = 3.5 \pm 1.0$ K and is now measured by the *FIRAS* instrument on the *Cosmic Background Explorer* (COBE) to have a mean temperature

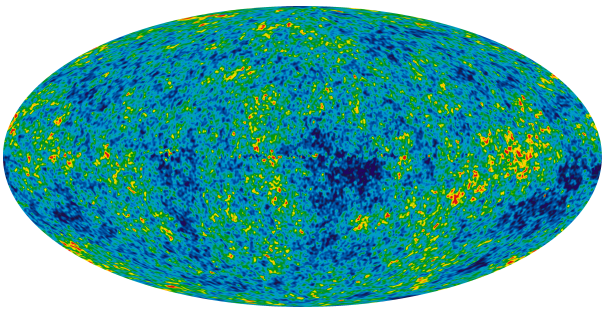

Figure 2.8: WMAP - CMB [19]. The measurements of the anisotropy and polarization of the CMB by WMAP set the first strong constraints of parameter values of the Cosmological Standard Model.

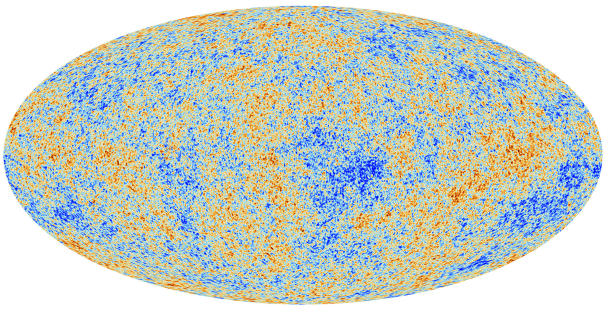

Figure 2.9: Planck - CMB [20]. Measurements of the Planck telescope in both the microwave and infrared spectra improved significantly over the observations of WMAP, setting greater constrains in the dark matter and dark energy density parameters.

of $T = 2.7255 \pm 0.0006$ K [7]. The signal is a relic from the recombination epoch of the Universe as discussed in section 2.1.1, when protons and electrons formed atoms, later allowing the interaction-free propagation of photons.

The first ground based measurement showed the CMB to have a uniform temperature distribution [21]. However, COBE first measured anisotropies in the CMB while measuring the first full sky map [22]. Furthermore, in recent measurements, the Wilkinson Microwave Anisotropy Probe - WMAP [23] (Figure 2.8) and the Planck space observatory [24] (Figure 2.9) have mapped the anisotropies to much higher precision, in the order of 10^{-5}, and have also observed polarization anisotropies in the order of 10^{-6}, in accordance with predictions of the Cosmological Standard Model [7]. Ground-based observatories such as the Atacama Cosmology Telescope (ACT) and the South Pole Telescope (SPT) allow the measurement of the CMB at smaller angular scales [7]. These anisotropies can be expressed by using spherical harmonic expansion [25]:

$$T(\theta,\phi) = \sum_{lm} a_{lm} Y_{lm}(\theta,\phi) \tag{2.10}$$

where a_{lm} is the amplitude of each mode and Y_{lm} are the spherical harmonics:

$$Y_{lm} = \sqrt{\frac{2l+1}{4\pi}\frac{(l-m)!}{(l+m)!}} P_l^m(cos\theta) e^{im\phi} \tag{2.11}$$

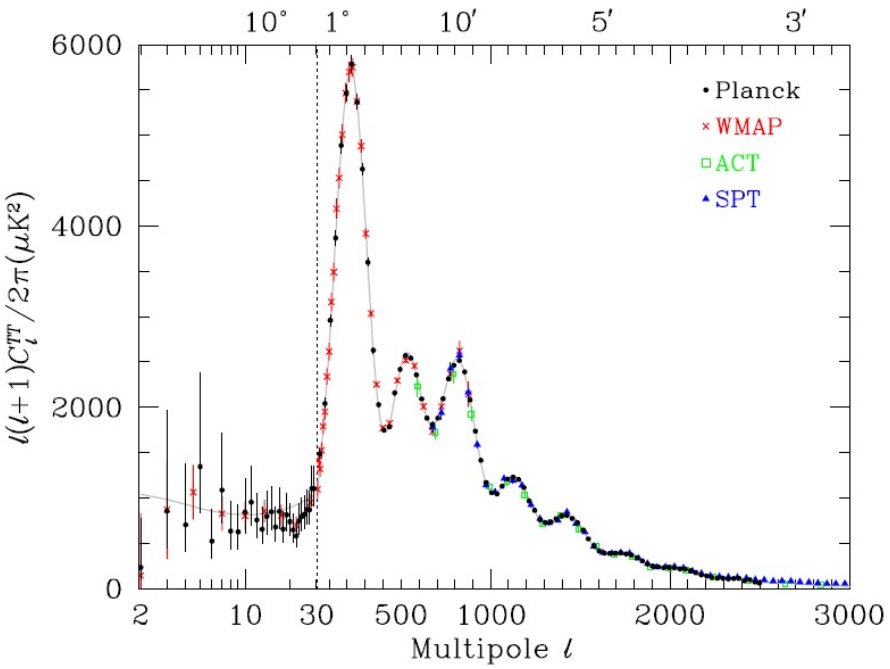

Figure 2.10: CMB anisotropy power spectrum. The x axis represents the angular scale of the temperature measurement.

The angular power terms are:

$$C_l \equiv \left\langle |a_{lm}|^2 \right\rangle \tag{2.12}$$

The power spectrum is finally given by:

$$\Delta T^2 = \frac{l(l+1)C_l T}{2\pi} \tag{2.13}$$

In this formulation, the m index is treated as the azimuthal order of the parameters, and l as the angular order. Therefore, small "l"s represent larger angular scales, while larger "l"s represent smaller angular scales. The measurements of Planck, WMAP, as well as the ground-based experiments ACT and SPT, are shown in Figure 2.10.

Information about the different matter densities presented in table 2.I is obtained with the help of these measurements [7]. Three peaks can easily be identified in the range $100 < l < 1000$. The position of the first peak depends on the geometry of the Universe. In a hyperbolic geometry, the first peak would be shifted toward higher angular orders while preserving its shape. The

measurements are, therefore, demonstrating the flat geometry of the Universe. The first peak also informs on the baryonic density by its height relative to the other peaks. The other peaks allow the calculation of the dark matter density Ω_c. The temperature fluctuation on this scale is believed to have been produced before the recombination epoch, when the proton-electron plasma was tightly coupled to photons, behaving much like a "photon-baryon" fluid. Dark matter was the dominating perturbation source in the gravitational potential, and generated oscillations in the hot matter "soup". Small in scale, the temporal phases of the oscillations were frozen-in at the recombination epoch and are now identified as this harmonic series of peaks.

2.2.4 Modified Newtonian Dynamics

In an attempt to explain the observed rotation curves of galaxies, a Modified Newtonian Dynamics (MOND) theory was considered. Proposed by Mordehai Milgrom in 1983, this theory is proposed as an alternative to the existence of dark matter. It assumes that Newton's second law of motion doesn't hold at small acceleration scales (such as in galaxies and galaxy clusters) and needs to be modified. This is done by introducing a new fundamental constant, a_0, changing Newton's law to [26]:

$$\vec{F}_N = m_g \mu\left(\frac{a}{a_0}\right)\vec{a} \tag{2.14}$$

where $\mu\left(\frac{a}{a_0}\right)$ is known as the interpolating function to be determined. In the limit $\mu\left(\frac{a}{a_0}\right) \to 1$, Newton's second law is again obtained. Taking:

$$\mu\left(\frac{a}{a_0}\right) = \left(1+\frac{a_0}{a}\right)^{-1} \tag{2.15}$$

or

$$\mu\left(\frac{a}{a_0}\right) = \left(1+\left(\frac{a_0}{a}\right)^2\right)^{-1/2} \tag{2.16}$$

we find that in the *deep-MOND* regime ($a \ll a_0$):

$$\vec{F}_N = m_g \frac{a^2}{a_0} \tag{2.17}$$

From this, we can determine the expected velocity of a galactic object in circular motion around the center of the galaxy according to the MOND theory:

$$\frac{GMm}{r^2} = m\frac{\left(\frac{v^2}{r}\right)^2}{a_0} \Rightarrow v = (GMa_0)^{1/4} \tag{2.18}$$

The MOND theory has had some success in describing the rotation curves of multiple galaxies. However, not all galaxies show abnormal rotation curves. Furthermore, the theory doesn't explain the unexpected results of galactic collisions as in the Bullet cluster, nor does it explain results from CMB measurements. In light of the apparent limitation of the theory, dark matter is still considered a more plausible explanation of the various observation.

2.3 Dark matter candidate particles

Even with the multiple evidence of the existence of dark matter, its nature is still unknown. Many beyond the standard model theories propose the existence of new particles that could constitute dark matter. Figure 2.11 gives a global idea of the quantity of dark matter particles proposed by different models.

2.3.1 Axions

Charge-parity (CP) violation was observed in 1964 in kaon decays, proving that CP in the weak nuclear force isn't conserved. In quantum chromodynamics (QCD), CP violation is allowed, but has never been observed. In 1977, Roberto Peccei and Helen Quinn proposed a new symmetry that could explain the lack of CP violation in QCD [28]. This symmetry also introduces a new particle, named *axion*. The axion would be a charge-less, spin-less boson, with a mass between 10^{-6} and 1

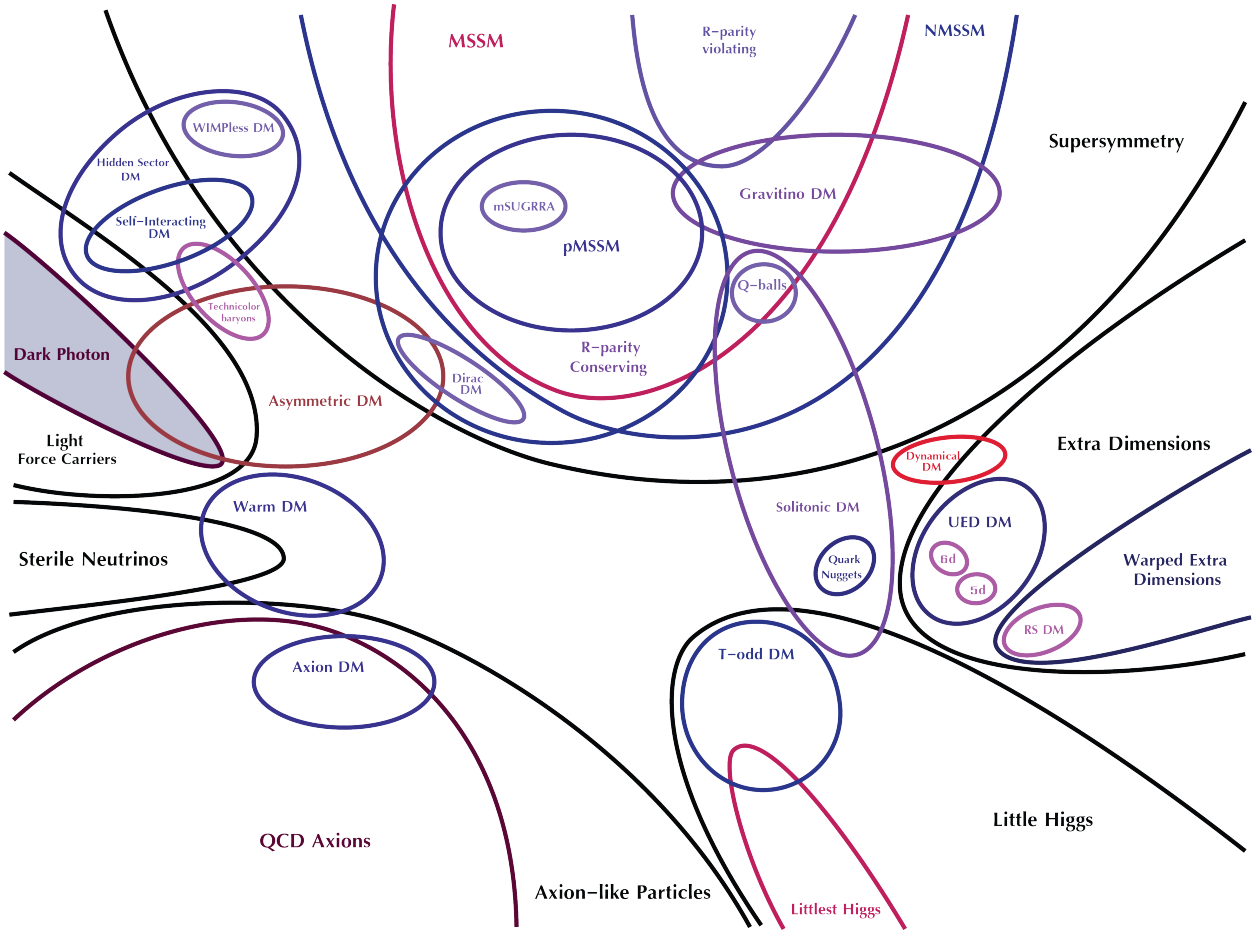

Figure 2.11: Dark Matter candidates [27]. Beyond the standard model theories are delimited by black curves, dark matter types are delimited by the red-purple curves and candidates by the blue-purple curves.

eV.

Stable and interacting only gravitationally and electromagnetically, the axion could be the particle constituting CDM. If they were, a mass range of 10^{-6} to 10^{-4} eV would be expected.

Axions could be observed via the Primakoff effect, where axions in a strong magnetic field could transform into photons. Experiments, such as PVLAS, CAST and ADMX use resonating cavities of adjustable resonance frequency to search axions in sections of mass range. Also, multiple dark matter search experiments, such as CDMS, EDELWEISS, CoGeNT, DAMA are sensitive to axions [29], but are not as sensitive for axion detection as the previously mentioned axion detection experiments. No detection has been claimed yet, though axions are still a credible candidate particle for dark matter.

2.3.2 MACHOs

A second potential source for dark matter are *MAssive Compact Halo Objects* (MACHOs). MACHOs include objects such as black holes, neutron stars, and even white, red and brown dwarf stars. These objects emit very little to no electromagnetic radiation and can only be detected by gravitational micro-lensing [7].

By measuring the deuterium-to-hydrogen ratio (D/H), and knowing reaction rates from nuclear physics, abundances of light elements can be calculated [30]. The measure of D/H lets us determine the total baryon density, Ω_b, which only accounts for 20% of the total matter density. Futhermore, Big Bang Nucleosynthesis and acoustic peak analysis from the CMB impose upper limits on the baryonic matter/ total matter ratio. Therefore, MACHOs could not account for all the expected mass of dark matter.

The MACHO collaboration however claimed to have found MACHOs counting for up to 20% of the expected dark matter, in the Milky-Way halo, by micro-lensing observations. They included in their results white and red dwarfs. These results could not be replicated by the EROS-2 collaboration. Both collaborations have combined their upper limits constraint MACHOs to account for at most 25% of halo dark matter and at most 10% of dark matter in the spherical halo model [31].

2.3.3 WIMPs

Weakly interacting Massive particles, or WIMPs, are the best candidates for dark matter to this day. This type of particle would have a large rest mass, between 1 GeV and 100 TeV [29]. It would have to be a neutral particle that interacts weakly with other particles (standard or dark) and gravitationally. This type of particle would have been in thermal equilibrium in the early Universe. With the inflation, their density would have been exponentially suppressed and the annihilation rate of WIMPs would have dropped to zero This would have caused them to fall out of equilibrium to form thermalized, Cold Dark Matter [32]. They could are also used to successfully predict the large structures of the Universe [29].

Multiple *beyond the standard model* theories predict WIMPs. The Minimal Supersymmetric

Standard Model (MSSM), a subset of Supersymmetry, predicts the existence of neutralinos, stable hypothetical particles under R-parity conservation. The lightest neutralino would be a linear combination of the photino, the zino, and two higgsinos, respectively the superpartners of the photon, the Z boson and the Higgs boson. The composition of WIMPs has however not yet been confirmed. The prediction of a dark matter particle with a mass around the weak scale and coupling to standard model particles with a strength in the order of the electroweak scale that fits the observed relic abundance is sometimes called "The WIMP miracle" [33]. For this reason, most dark matter detection experiments are searching for WIMP-like particles.

2.4 Detection of WIMPs

Even though the existence of dark matter is now well established due to all the different evidence discussed in the past sections, its detection has yet to be made. Now, only astronomical observations, such as gravitational lensing and rotation curves of galaxies, were used to infer the existence of WIMPs. Their interaction through the gravitational force can allow us to determine some of their properties. However, if dark matter particles can interact with matter, there exist three other types of detection methods, as demonstrated by the diagram in Figure 2.12. Assuming dark matter is a particle, and in particular WIMPs, it could be produced in collider experiments from standard model particles, could be indirectly detected from the detection of its annihilation products or could be directly detected from elastic scattering with normal matter. All three detection method are complementary to one another, as not one detection method can determine WIMPs properties by itself.

2.4.1 Production in colliders

The first detection method is the production of WIMPs in particle colliders. Colliders have proved to be valuable tools in the search of new, exotic particles in the last 70 years. More recently, the ATLAS and CMS experiments announced the discovery of the Higgs boson at the Large Hadron Collider (LHC), effectively completing the detection of all the particles of the Standard Model [34].

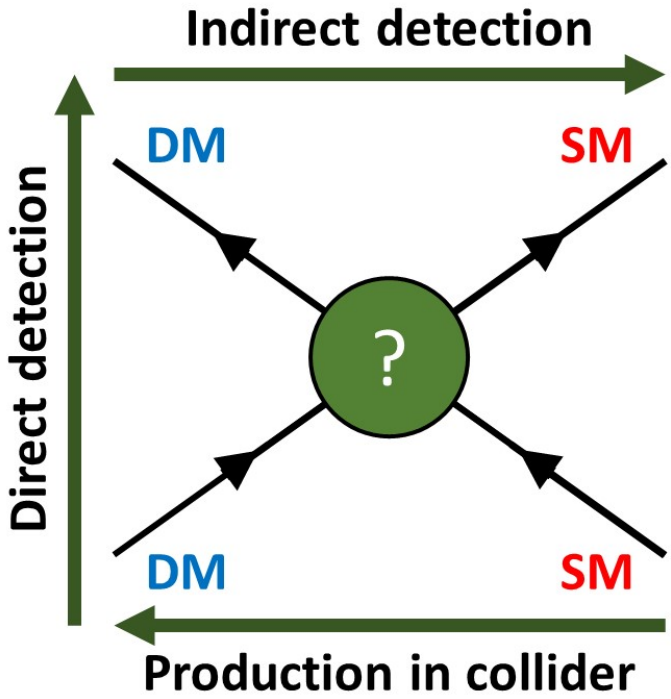

Figure 2.12: Dark matter detection methods. The dark green arrows show which way to read the Feynman diagram.

Evidence of WIMPs production in such experiments would come in the form of missing transverse momentum. When reconstructing collision events in a detector from coinciding vertices, the energy of all products is measured either with calorimeters or from curved tracks in ionization chambers for charged particles. Missing energy is then a sign of the production of non-interacting particles.

The major problem for the search of dark matter in collider experiment is that a new particle doesn't automatically mean a dark matter particle. Even though WIMPs are expected to be produced at higher center-of-mass energies, new heavy particles constituted of SM particles could also be produced, such as pentaquarks detected in 2015 at the LHC [35], with a mass of 1.5 GeV. Thankfully, such particles are electrically charged and short-lived, thus easily ruled-out for dark matter.

Finally, from the cosmological standard model, it is expected that WIMPs are stable. Therefore, no decay products are going to be detected in colliders and a WIMP signal would be identified as

missing energy. Even though a lot of parameters wouldn't be measured by the production of WIMPs in colliders, the detection of a beyond the SM particle, and the study of its properties, could help orient indirect and direct detection searches in the WIMP parameter-space.

2.4.2 Indirect detection

The second detection method is the indirect detection of dark matter. This mainly consist in the detection of decay (or annihilation) products of WIMPs. As mentioned in section 2.1.1, dark matter fell out of thermal equilibrium after the inflation of the Universe since the interaction cross-section of dark matter is of the scale of the weak force. If WIMPs are Majorana particles (i.e. their own antiparticle), annihilation could still happen in regions of high dark matter density, such as in galactic centers or in celestial bodies like our Sun. WIMPs could decay to quark-antiquark pairs, as well as W and Z boson pairs. These would further decay to SM particles. Decay products could include γ-rays, neutrinos, electrons, positrons, protons, antiprotons, and possibly antideuterons [36]. One advantage indirect detection has over direct detection is the possibility (depending on the decay scheme) to provide stronger constrains on the mass of the particle deduced from the nature and energy of the detected decay products.

Several experiments are looking for such decay products. For example, the VERITAS experiment is looking for γ-rays emission in strong dark matter density regions with a land-based Cherenkov telescope. This experiment poses the strongest constraints on CDM models to date. The experiment is also looking for e^+e^- emission.

Current and future neutrino experiments would be sensitive to highly energetic neutrinos produced by WIMPs annihilation. Experiments like SuperK, IceCube and ANTARES could therefore identify surplus signal coming from the sun or distant cosmic objects. These experiments detect Cherenkov radiation, emitted by secondary products of neutrino interaction with, respetively, purified water, ice from the Antarctic ice cap and sea water in the Mediterranean sea. Other notable experiments are the space-based Alpha Magnetic Spectrometer (AMS-02) detector and FERMI Gamma-ray Space Telescope. AMS-002 is currently mounted on the International Space Station

(ISS) and detecting cosmic rays in order to identify, amongst others, WIMP decay products (e^+e^-). FERMI searches the 10 keV - 300 GeV energy range of the gamma spectrum.

2.4.3 Direct detection

The last detection method in the search for dark matter is direct detection. WIMPs can interact with normal matter by elastic scattering with nuclei, or in the case of axions, through their interaction with virtual photons in a magnetic field [37]. This section is focused on the former case.

WIMPs transfer energy to nuclei when scattering with ordinary matter. The recoil energy acquired by the nucleus can be calculated by:

$$E_R = 2E_\chi \frac{m_A m_\chi}{\left(m_A + m_\chi\right)^2} \left(1 - cos(\theta)\right) \tag{2.19}$$

where E_χ is the kinetic energy of the WIMP, m_A and m_χ are the masses of a nucleus and WIMP respectively, and θ is the scattering angle of the WIMP. For the theoretical mass range of WIMPs (1 GeV to 100 TeV), nuclear recoils are expected to range between 1 and 100 keV [29]. Detecting such low energy recoils imply that experiments should have a strong background radiation discrimination. The recoil energy spectrum is given by:

$$\frac{dR}{dE_R} = \frac{R_0}{\langle E_R \rangle} e^{-E_R/\langle E_R \rangle} F(q^2) \tag{2.20}$$

where R_0 is the total WIMPs interaction count rate, $F(q^2)$ is the form factor squared and $\langle E_R \rangle$ is the average recoil energy:

$$\langle E_R \rangle = 2\frac{m_A m_\chi^2}{(m_A + m_\chi)^2} \left\langle v_\chi^2 \right\rangle \tag{2.21}$$

where $\left\langle v_\chi \right\rangle$ is the average WIMP velocity. In the solar system reference frame, $\left\langle v_\chi \right\rangle \approx \langle v_0 \rangle \approx 220$ km/s where $\langle v_0 \rangle$ is the orbital velocity of the sun. The WIMP velocity in the reference frame of the Earth can be written as $\vec{v}_\chi + \vec{v}_{Earth}$. With Earth revolving around the Sun, an annual modulation is

expected, with a peak in June and a minimum in December in the northern hemisphere.

Direct detection experiments are designed to measure the WIMP interaction count rate R_0 from equation 2.20. Assuming a detection efficiency of 100%, this rate can be expressed as:

$$R_0 = \frac{2}{\sqrt{\pi}} \frac{N_A}{A} \frac{\rho_\chi}{m_\chi} \left\langle v_\chi \right\rangle \sigma_A \tag{2.22}$$

where N_A is the Avogadro constant, ρ_χ is the WIMP density and $\left\langle v_\chi \right\rangle$ is the average velocity of WIMPs.

The local dark matter density in our solar system is [7]:

$$\rho_{DM}^{local} = (0.39 \pm 0.03) \cdot (1.2 \pm 0.2) \cdot (1 \pm 0.2) \frac{GeV}{cm^3} \tag{2.23}$$

where the first factor is the average dark matter density at one solar distance from the center of the galaxy, the second factor is a correction factor that accounts for the increase in dark matter density in the galactic disk due to the presence of baryonic matter and the third factor accounts for corrections due to deviations from the perfectly spherical halo model [7].

From equation 2.22, we can get an expression for the WIMP interaction cross section as a function of the count rate:

$$\sigma_A = R_0 \left(\frac{2}{\sqrt{\pi}} \frac{N_A}{A} \frac{\rho_\chi}{m_\chi} \left\langle v_\chi \right\rangle \right)^{-1} \tag{2.24}$$

The cross-section can also be re-written using the reduced mass as [38]:

$$\sigma_A = 4 G_F^2 \left(\frac{m_\chi m_A}{m_\chi + m_A} \right)^2 C_A \tag{2.25}$$

where G_F is the Fermi coupling constant. This coupling factor typically gives an interaction cross section of the order of the weak interaction cross section. C_A is the enhancement factor which depends on whether the interaction is spin dependent (SD) or spin independent (SI).

Nucleus	Z	Odd Nucleon	J	$\langle S_p \rangle$	$\langle S_n \rangle$	C_A^p/C_p	C_A^n/C_n
^{1}H	1	p	1/2	0.5	0	1	0
^{19}F	9	p	1/2	0.441	-0.109	$7.78 \cdot 10^{-1}$	$4.75 \cdot 10^{-2}$
^{23}Na	11	p	3/2	0.248	0.020	$1.37 \cdot 10^{-1}$	$8.89 \cdot 10^{-4}$
^{27}Al	13	p	5/2	-0.343	0.030	$2.20 \cdot 10^{-1}$	$1.68 \cdot 10^{-3}$
^{29}Si	14	n	1/2	-0.002	0.130	$1.60 \cdot 10^{-5}$	$6.76 \cdot 10^{-2}$
^{35}Cl	17	p	3/2	-0.083	0.004	$1.53 \cdot 10^{-2}$	$3.56 \cdot 10^{-5}$
^{39}K	19	p	3/2	-0.180	0.050	$7.20 \cdot 10^{-2}$	$5.56 \cdot 10^{-3}$
^{73}Ge	32	n	9/2	0.030	0.378	$1.47 \cdot 10^{-3}$	$2.33 \cdot 10^{-1}$
^{93}Nb	41	p	9/2	0.460	0.080	$3.45 \cdot 10^{-1}$	$1.04 \cdot 10^{-2}$
^{125}Te	52	n	1/2	0.001	0.287	$4.00 \cdot 10^{-6}$	$3.29 \cdot 10^{-1}$
^{127}I	53	p	5/2	0.309	0.075	$1.78 \cdot 10^{-1}$	$1.05 \cdot 10^{-2}$
^{129}Xe	54	n	1/2	0.028	0.359	$3.14 \cdot 10^{-3}$	$5.16 \cdot 10^{-1}$
^{129}Xe	54	n	3/2	-0.009	-0.227	$1.80 \cdot 10^{-4}$	$1.15 \cdot 10^{-1}$

Table 2.II: Table of nuclear properties [38]. $\langle S_p \rangle$ and $\langle S_n \rangle$ are the proton and neutron spin values, C_A^p/C_p and C_A^n/C_n are proton and neutron enhancement factors.

For SI interactions, the enhancement factor is given by [38]:

$$C_A^{SI} = \frac{1}{4\pi} \left(Z f_p + (A-Z) f_n\right)^2 \tag{2.26}$$

where f_p and f_n are the coupling factors of WIMPs to, respectively, the proton and the neutron. Assuming the invariance of the isospin, $f_p = f_n$. In that case, the SI enhancement factor is proportional to the square of the atomic mass number of the nucleus A^2 [29].

For SD interactions, the enhancement factor is given by [38]:

$$C_A^{SD} = \frac{8}{\pi} \left[a_p \langle S_p \rangle + a_n \langle S_n \rangle\right]^2 \frac{(J+1)}{J} \tag{2.27}$$

where a_p and a_n are the proton and neutron coupling forces and $\langle S_p \rangle$ and $\langle S_n \rangle$ are the expected proton and neutron spin values. J is the total nuclear spin.

Table 2.II presents nuclei properties used in calculating limits in SD interaction. From the enhancement factor equations 2.26 and 2.27, it is clear the target nuclei composition will influence the sensitivity to SD and SI interactions. Protons and neutrons tend to occupy shells in pairs in the nucleus. Nuclei with an unpaired nucleon will be sensitive to SD interactions. The sensitivity

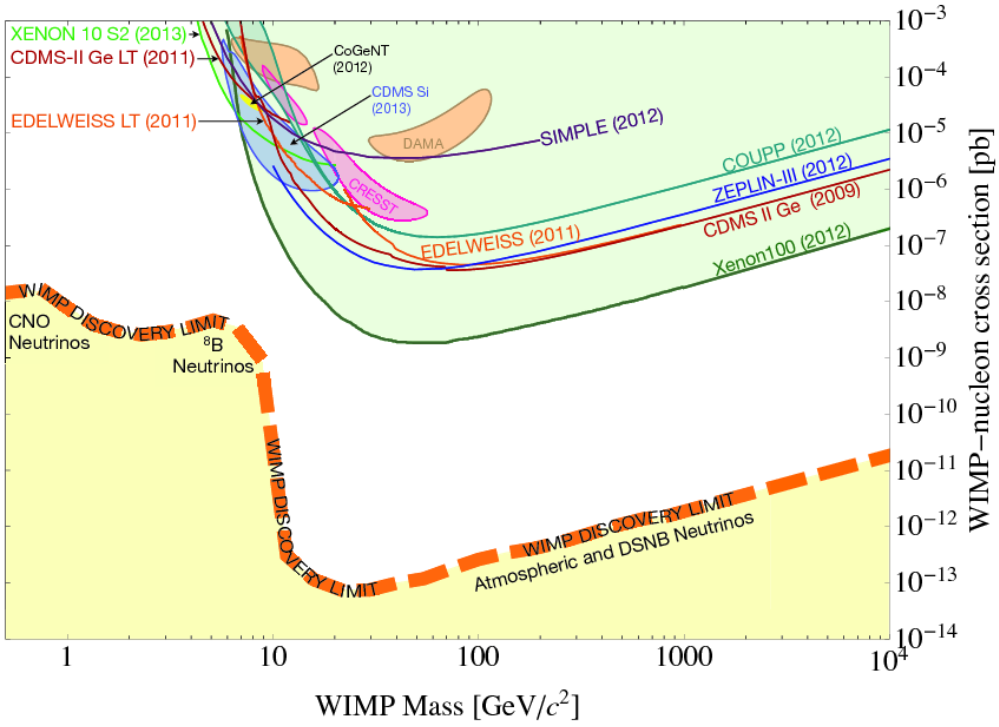

Figure 2.13: Dark matter cross-section to WIMP mass exclusion plot and neutrino floor [39]. Curves delimit exclusion zones (above) for WIMP-nucleon cross-section as a function of WIMP mass. Contour lines show regions of interest for possible WIMP signal.

depends on whether the uncoupled nucleon is a proton or a neutron. Due to the A^2 dependence of the SI cross-section, it is therefore wiser to pick heavier nuclei when searching for SI interactions.

Equations 2.24 and 2.25 give the cross section as function of the WIMP mass. Direct detection experiments using different target elements are compared to one another with limit plots, seen in Figure 2.13, that define exclusion zones (above the curves) for WIMP-nucleon interaction cross-sections at different WIMP masses. The shape of limit curves is influenced by the WIMP momentum dependence of the form factor in equation 2.20. As experiments get more sensitive, curves can exclude lower cross-sections in the absence of a WIMP signal.

Figure 2.13 also shows the coherent neutrino background (orange dashed line). Experiments may get sensitive enough to detect neutrino interactions. Neutrinos are produced abundantly in the sun from P-P and CNO processes with a maximum energy of 18.8 MeV (from the P-P IV branch) [40]. Higher energy neutrinos are produced in the Earth's atmosphere from cosmic rays inter-

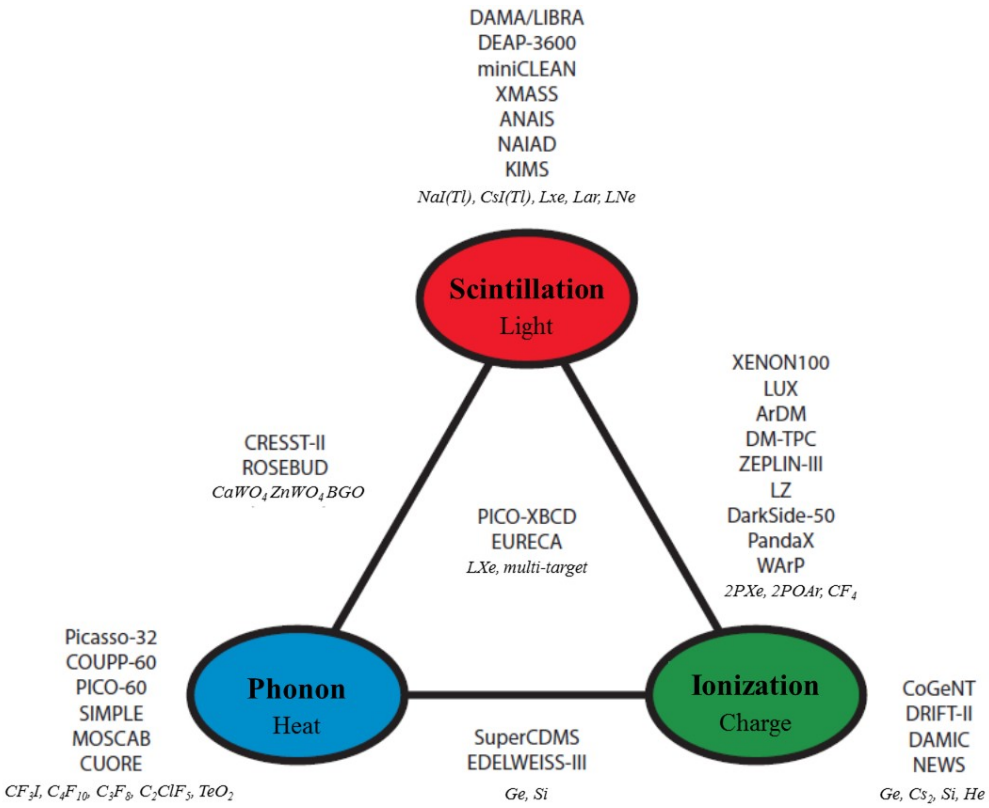

Figure 2.14: Active direct detection dark matter experiments.

actions. The coherent neutrino background is currently considered the discovery limit for direct detection experiments, as detectors would be quickly saturated in neutrino events indistinguishable from WIMP events. A better understanding of neutrino scattering, annual modulation or the deployment of directional detectors could help in the search of dark matter beyond this limit.

2.4.4 Direct detection experiments

All direct detection experiments aim to detect very weak nuclear recoils. In an effort to significantly reduce the exposure of detectors to radiation from cosmic rays, direct detection dark matter searches are typically performed in deep-underground laboratories. Direct detection experiments don't measure the energy of a WIMP, but ratter the energy transferred to the medium of the detector. A detection can be obtained by one experiment, but the determination of properties of WIMPs will require at least two detections with different active media.

There exist several direct detection techniques. Figure 2.14 shows a diagram of the classi-

fication of direct detection experiments by detection technique(s). They can be divided in three categories: scintillation experiments, ionization experiments and phonon experiments.

Scintillation is the process of transforming kinetic energy in electromagnetic radiation. When a particle recoils in a detector, energy is transferred to the active material of the detector and photons are emitted because of the recombination of ionized electrons with nuclei. Scintillation can be achieved either in solid crystals such a NaI or CsI, or in liquids such as organic liquids and liquid noble gases (LXe, LAr, LNe).

The most notable pure scintillation experiment to date is probably the DAMA/LIBRA experiment (Figure 2.15). Using highly radiopure NaI(Tl) crystal, the collaboration claims to have observed a seasonal signal modulation compatible with the expected dark matter halo flux variation with a significance of 8.9σ for recoils energies from 2 to 6 keV [41]. This result is, however, not replicated by more sensitive experiments. More sensitive crystal scintillator experiments, such as ANAiS, KIMS, CINDMS, PICO-LON and COSINUS should either confirm or refute the DAMA/LIBRA claim [29, 43, 44]. Furthermore, experiments in the southern hemisphere, such as DM-ICE (Figure 2.16) located at the bottom of the IceCube detector array in the Antarctic, could determine if the modulation signal is seasonal, and thus out of phase in different hemispheres, or due to the motion of the solar system in the galaxy, thus always in phase.

LXe experiments are also well suited for the direct detection of WIMPs. The heavy nucleus gives a very good sensitivity to SI interaction and provides self-shielding against γ-rays due to their short interaction length. Neutrons can be discriminated by their tendency to multiple scatter. LXe is highly scintillating in the VUV (Vacuum Ultra-Violet) range. Scintillation light can be collected by photo-multiplier tubes (PMT), generally placed on the outside of a spherical or cylindrical detector for maximum light collection. In addition, LXe experiments can combine scintillation with ionization. If an electric field is applied in a detector, ionized electrons can drift towards an anode at the surface of the liquid in a Time Projection Chamber (TPC) configuration. This allows for a 3D representation of events at the cost of a lower scintillation sensitivity, as fewer ionized electrons recombine with xenon atoms.

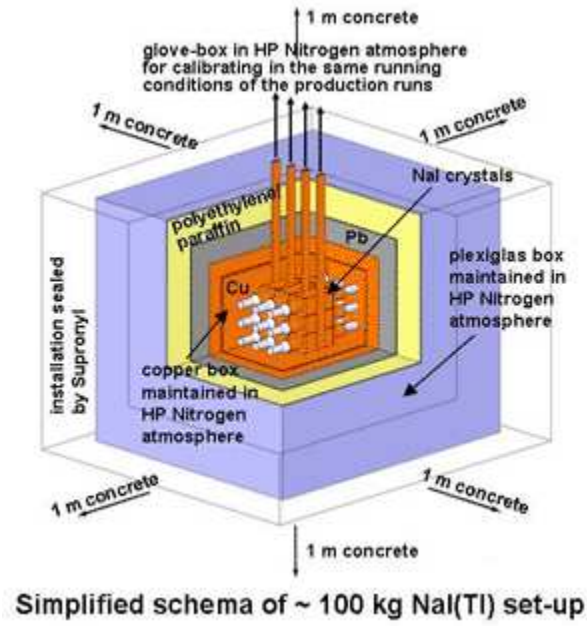

Figure 2.15: DAMA/LIBRA experiment [41]. The experiment saw a seasonal fluctuation in the rate of interaction, thought to be associated with WIMP interactions. The result has not been replicated in any other experiment.

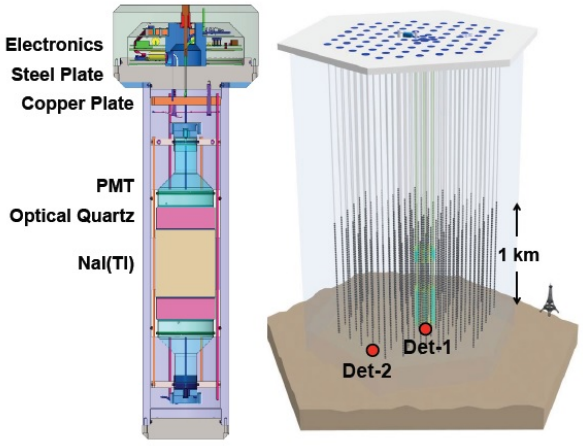

Figure 2.16: DM-ICE experiment [42]. Other solid-state crystal experiments could confirm or refute the DAMA/LIBRA seasonal fluctuation result.

The XMASS experiment, shown in Figure 2.17 ran a 835 kg scintillating LXe detector and plans to build a 20-ton multipurpose LXe detector for dark matter search [47]. Notable current experiments using the TPC configuration include XENON1T [46] (Figure 2.18), LUX [48] and PandaX-II [49].

LAr experiments are very similar to LXe experiments. Scintillation is emitted in the hard UV range, adding the need of a wavelength shifter in the PMT assembly. Furthermore, ^{39}Ar is a radioactive isotope naturally present in atmospheric argon that adds an intrinsic background. Fortunately, pulse shape analysis can be performed to discriminate these background events. Argon has the advantage of being much cheaper than Xe due to its larger abundance in the air. ^{39}Ar is a source of background that is efficiently discriminated by a sensitive pulse shape analysis. The two LAr experiments MiniCLEAN [50] and DEAP-3600 [51] are under way at *SNOLAB*. The two-phase TPCs, ArDM [52] and DarkSide-50 [53], are operated in Europe at the *Laboratorio Subterráneo de Canfranc* (LSC) and in *Laboratori Nazionali del Gran Sasso* (LNGS) respectively.

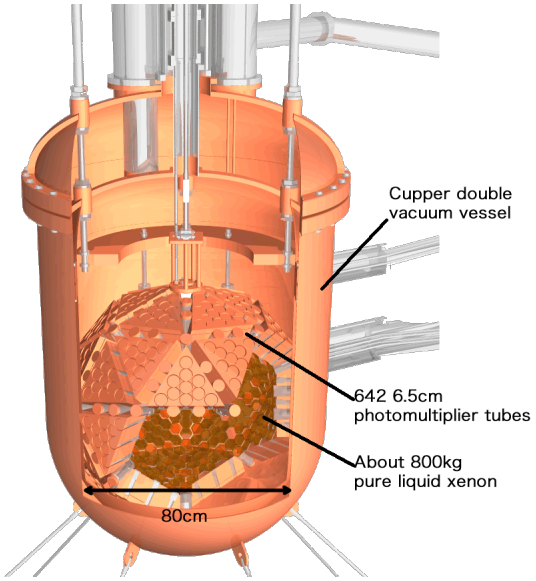

Figure 2.17: XMASS LXe experiment [45].

Figure 2.18: XENON1T experiment [46].

Cryogenic solid-state detectors were the first to set limits on the WIMP interaction cross-section of halo dark matter of the Milky-Way. They can detect ionization exclusively or combine it with another readout technique in detectors known as bolometers. These solid-state detectors consist usually of highly purified crystals such as High Purity Germanium (HPGe) or silicon, which have a very good energy resolution. As all ionization experiments, these are highly sensitive to γ radiation (especially radiation coming from the constituents of the detector) which constitute one of the main sources of background. For that matter, detector housings are often composed of low radiation copper and other radiopure materials. The relatively compact size of these experiments allows for low radiation lead shielding. Notable cryogenic solid-state experiments include CDMS, EDELWEISS and CRESST, the latter using calcium tungstate. The SuperCDMS and EDELWEISS-III bolometric experiments (and their predecessors) use a combination of ionization and phonon readouts to improve on the rejection of electron-recoil events produced from β decays.

Finally, some experiments detect nuclear recoils in the form of heat, or deposited kinetic energy. The most common type of detector that exploits this detection method is the bubble chamber.

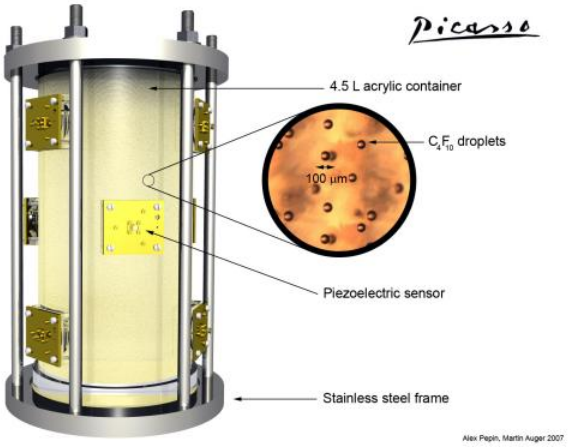

Figure 2.19: The PICASSO experiment [54]. A gel matrix isolates micro-droplets of Freon, acting as individual bubble chambers that can be run continuously over long periods of time.

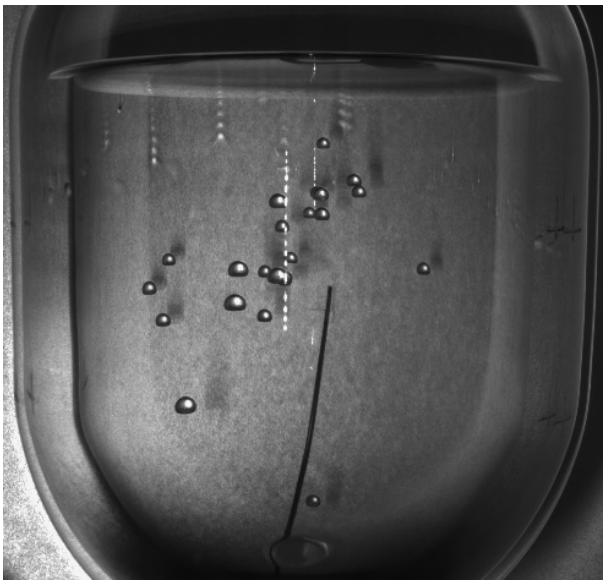

Figure 2.20: The PICO experiment [55]. The traditional bubble chamber format yields a larger fiducial mass over droplet detectors, but needs to be recompressed after every event.

Superheated liquids are kept in a metastable liquid state in clean containers and undergo explosive phase transitions when enough energy is deposited by foreign particles. The droplet detector, a variation of the traditional bubble chamber, was used by the PICASSO (Figure 2.19) and SIMPLE experiments. Micro-droplets of the active liquid were suspended in a gel matrix, each droplet acting as an individual bubble chamber.

Bubble chamber experiments searching for dark matter usually have Freon as their active fluid. Freon is constituted of fluorocarbon molecules, rich in fluorine nuclei. This gives them a higher sensitivity to SD interactions on odd protons, as seen in table 2.II. Furthermore, iodine loaded Freon such as CF_3I can be chosen to get a better sensitivity to SI interactions. However, the low density in heavy nuclei usually makes bubble chambers less sensitive to SI interactions than LXe or solid-state experiments.

The PICO experiment (Figure 2.20), a joint effort by the former PICASSO and COUPP collaborations, operates low background bubble chambers to search for WIMPs. The bubble chamber concept and the PICO experiment are explored in more details in chapter 3.

CHAPTER 3

THE PICO EXPERIMENT

The PICO experiment is a dark matter search experiment with bubble chambers, threshold detectors that employ superheated liquids to detect nuclear recoils from energetic particles. PICO is the result of the merger in 2013 of the PICASSO experiment (Project in Canada to Search for Supersymmetric Objects) and the COUPP experiment (Chicagoland Observatory for Underground Particle Physics). These experiments brought their technologies together to form a competitive experiment in the search for WIMPs.

In this chapter, the concept of bubble chambers is explained in section 3.1. A summary of Seitz's theory of nucleation is presented in section 3.2, followed by a general presentation of the current PICO bubble chambers at SNOLAB in section 3.3.

3.1 Bubble chambers

The bubble chamber was invented by Donald A. Glaser in 1952, for which he won the Noble prize in Physics in 1960. At the time, it was an upgrade from the cloud chamber, a devise used to observe tracks of particles produced by rare nuclear decays [56]. Compared to gaseous mediums, fluids have a greater density, improving the chance of interaction with energetic particles. The original design consisted of a spherical chamber filled with liquid hydrogen installed in a constant magnetic field. Charged particles entering the chamber would deposit their energy in the medium, leaving arced tracks of small bubbles that could then be photographed. The momentum of the particles could be determined from the radius of their track.

Liquids in bubble chambers are kept in a metastable, superheated state. Figure 3.1 shows the phase diagram of a typical material. Superheat is easier to achieve by quickly lowering the pressure of the liquid at a constant temperature as pressure can be modified with a small variation of volume, whereas temperature changes at constant pressure happen gradually. In normal conditions, when

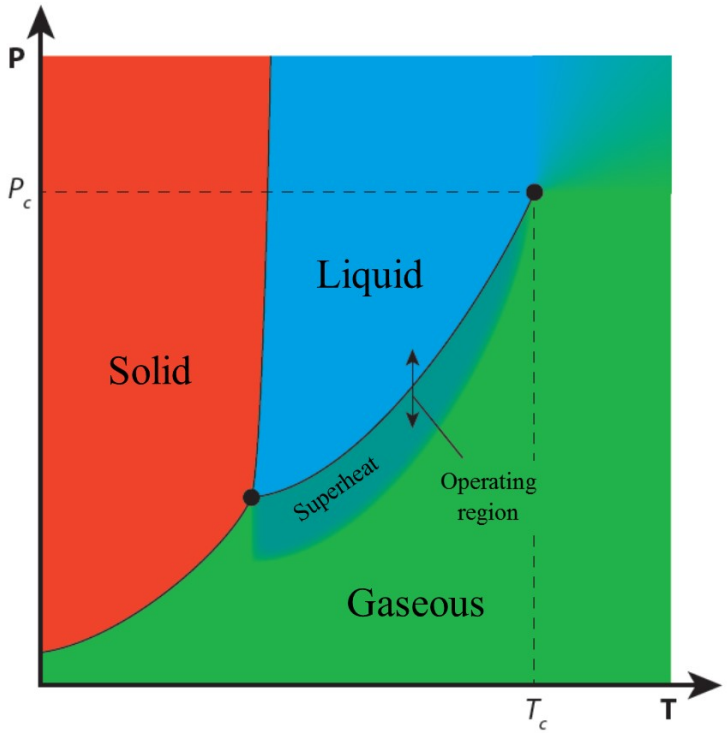

Figure 3.1: Phases of matter diagram. The superheated region spans from the critical point (after which the phase of matter is more or less defined) down to the triple point (the point where the three phases of matter coexist). Lowering the pressure of a liquid past the liquid-gaseous curve has the effect of increasing its superheat.

the pressure falls under the vapor pressure (black curve in Figure 3.1), a fluid goes through a phase transition. Liquid expanding to gas increases the overall pressure of the system. However, if the chamber is fully filled with no gaseous region, no phase transition occurs as the chamber is slowly expanded and the fluid becomes superheated.

Energetic particles can interact with the superheated liquid. The energy deposited can trigger an explosive phase transition, as explained in section 3.2. Charged particles, especially Minimum Ionizing Particles (MIPs) such as muons, can ionize the active fluid with very little energy loss. This produces a series of bubbles in a straight line, as seen in Figure 3.2 a). The PICO detectors have been shown to be insensitive to muons at the operating thresholds. [57]. Neutrons, massive and chargeless, can deposit their energy by elastic scattering with nuclei. Neutrons can scatter multiple times, and can produce signature multiple bubble events as seen in Figure 3.2 b). Finally, single events as seen in Figure 3.2 c) can be produced by various particles. Alpha decays from

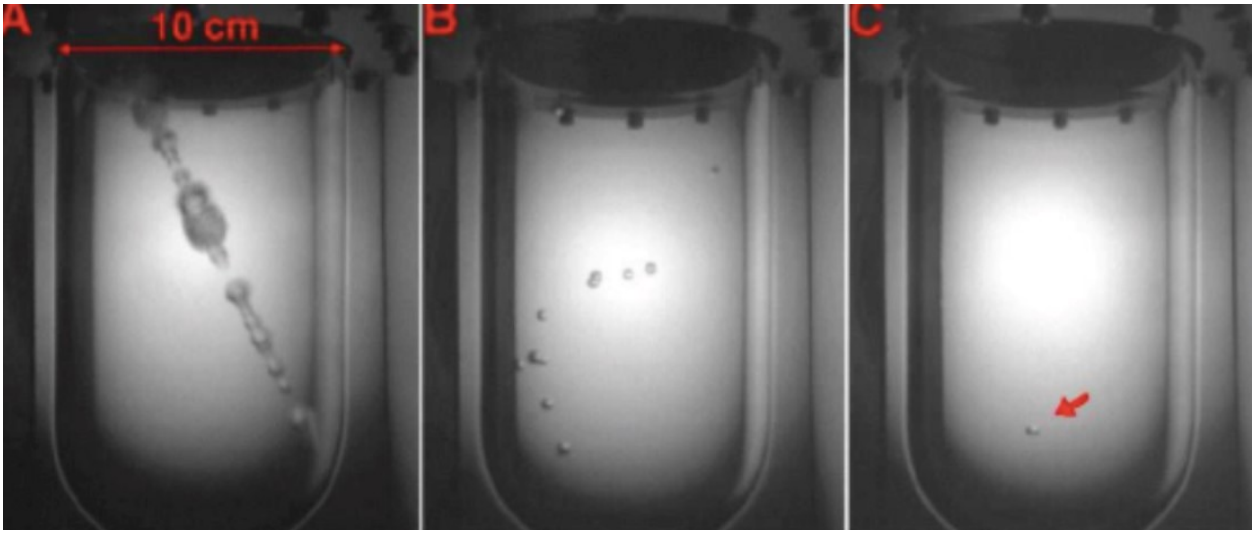

Figure 3.2: Types of bubble production. a) Muon multiple bubble event, b) Neutron multiple bubble event, c) Neutron, α or γ-ray single bubble event.

within the bubble chambers, either from the detector's materials or from contaminants such as Radon daughters that can get trapped on the surface of materials, produce single bubble events with an efficiency of 100% because of the Bragg peak [58]. γ radiation can ionize atoms from the superheated liquid. Ejected electrons, called delta-electrons, deposit their energy quickly and cannot produce a bubble. Finally, neutrons can also produce single bubble events. WIMPs, from their small cross-section, are expected to only produce single bubbles.

Superheat is easier to achieve in clean, smooth inner vessels. Dust or particulates can provide nucleation sites where the dissolved micro-pockets of vapor of the superheated fluid can produce bubbles. The same phenomenon can occur in the surface of porous inner vessels. For this reason, they are usually made of highly polished quartz or fused silica.

In low threshold energy bubble chambers, nucleation is detected by a series of sensors controlled by a Data Acquisition system (DAQ). Pressure transducers actively monitor the pressure inside the inner vessel as a pressure increase would indicate a phase transition has occurred. Piezoelectric sensors record the sound-waves produced by the rapid expansion of bubbles. The acoustic signal can help to identify the recoiling particle. Finally, stereoscopic CCD cameras can be deployed to get a real-time visual scan of the active fluid. This in turn helps in determining the spa-

tial coordinates of bubbles. Any of the three monitoring systems can trigger an event and prompt the DAQ to record a series of variables. The acoustic signal and inner pressure are recorded in a "slow DAQ" (e.g. no continuous analysis) buffer to ensure a high data sampling, while the camera feed is continuously analyzed in a fast DAQ. Events are therefore usually triggered from the CCD cameras.

3.2 Seitz theory of nucleation

In 1957, Frederick Seitz wrote a paper entitled *On the theory of bubble chambers* [59] in which he details his "Thermal Spike" theory. This model postulates that a minimum, critical energy E_c must be deposited locally in a superheated medium for a proto-bubble to be produced. If it were to reach a volume of critical radius R_c, the proto-bubble would become unstable and grow. In this model, two radial forces act against one another. Pressure from the vapor phase of the proto-bubble exerts an outward force on the interface while the surface tension pushes the interface inward. The requirement that a proto-bubble can only grow if $R_{bubble} \geqslant R_c$ accounts for the surface tension of the interface, adding a constricting force. This mechanism is illustrated by Figure 3.3

The two parameters R_c and E_c are related to the thermodynamical properties of the superheated fluid. First, the critical radius is: [60]:

$$R_c = \frac{2\sigma}{p_v - p_f} = \frac{2\sigma}{\Delta p} \tag{3.1}$$

where σ is the surface tension, p_v is the pressure of the gas and p_f is the pressure of the fluid.

The second parameter, E_c, can be described as the sum of the work done by the proto-bubble:

$$\begin{aligned} E_c(T) &= W_m + W_{ev} + W_{lv} + W_{irr} \\ &= -\frac{4\pi}{3} R_c^3 \Delta p + \frac{4\pi}{3} R_c^3 \rho_v h_{lv} + 4\pi R_c^2 \left(\sigma - T \frac{d\sigma}{dT} \right) + W_{irr} \end{aligned} \tag{3.2}$$

The first term on the right side, W_m, is the reversible mechanical work done during the expansion to a bubble of size R_c against the pressure, where R_c and Δp is the same critical radius and differential

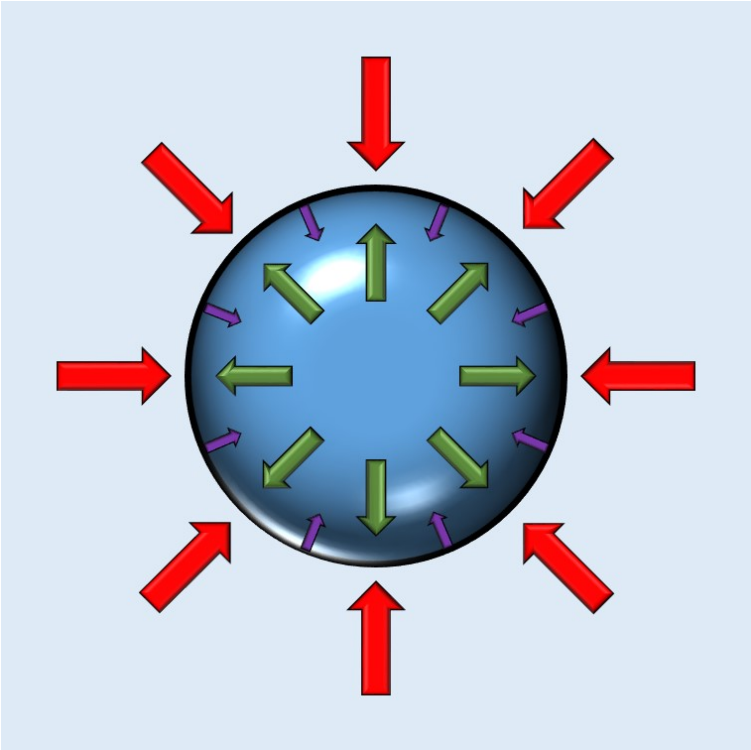

Figure 3.3: Bubble growth diagram. Out of equilibrium, bubble growth is governed by the differential pressure $\Delta P = p_v - p_f$ and the surface tension. Arrows represent the different forces in play: Red - from the pressure of the fluid; Purple - from the surface tension; Green - from the pressure of the vapor phase.

pressure as in equation 3.1. The second term, W_{ev}, is the energy needed to evaporate the liquid as the bubble grows to critical size. Here, ρ_v is the density of the gas phase and h_{lv} is the latent heat of evaporation. The third term, W_{lv}, is the work required to create the interface of a proto-bubble. Finally, W_{irr} is the irreversible work done during the nucleation process.

In Seitz's model, the efficiency of bubble nucleation for an energy deposition of $E \geqslant E_c$ is 100%. However, neutron calibrations and simulations showed that the efficiency is much lower for recoiled particles with tracks larger than the critical radius [61, 62]. With R_c and E_c, a criterion for bubble nucleation can be expressed:

$$E_{dep}(T) = \int_0^{L_c(T)} \frac{dE}{dx} dx \geqslant E_c(T) \tag{3.3}$$

where E_{dep} is the energy deposited and $\frac{dE}{dx}$ is the energy loss per distance traveled. The critical

length $L_c(T)$ is the maximum distance within which energy can be deposited for a bubble to be nucleated. This criterion simply states that, in order to grow, a proto-bubble must be produced with a deposited energy greater than the critical energy E_c, within a length L_c. The energy deposited can be considered as the sum of all energy losses due to nuclear recoils along the path of a nucleus. Also, typically, the critical length is taken to be:

$$L_c = b \cdot R_c \tag{3.4}$$

where b, the Harper parameter, must be determined experimentally [60].

In bubble chambers, the probability of nucleation, or the response of the detector, can be expressed by:

$$P(E_R, E_{th}, \alpha) = 1 - e^{\left(\alpha\left(1-\frac{E_R}{E_{th}}\right)\right)} \tag{3.5}$$

with E_R the recoil energy and E_{th} the threshold energy. Bubble chambers being threshold detectors, nucleation can only happen for $E_R > E_{th}$. In equation 3.5, the nucleation probability would be negative otherwise. α is an empirical nucleation parameter. This nucleation probability is directly related to the observed count rate:

$$R_{obs}(M_W, \sigma_A, E_t h, \alpha) = \int_0^{E_R,max} P(E_R, E_{th}, \alpha)\frac{dR}{dE_R}dE_R \tag{3.6}$$

3.3 PICO at SNOLAB

As mentioned in section 2.4.4, dark matter direct detection experiments are performed underground to be shielded from cosmic radiation that would otherwise be a dominating source of background signal. The PICO experiment is located in the VALE-Creighton nickel mine at SNOLAB, in Sudbury, Ontario at a depth of 2 km, 6010 meter water equivalent (MWE) [63]. The cavern excavation started in 1990 to house the Sudbury Neutrino Observatory (SNO). After the stunning success of the experiment, the laboratory space was expanded to become a permanent site where several low background experiments could be performed in the fields of neutrino astronomy, neu-

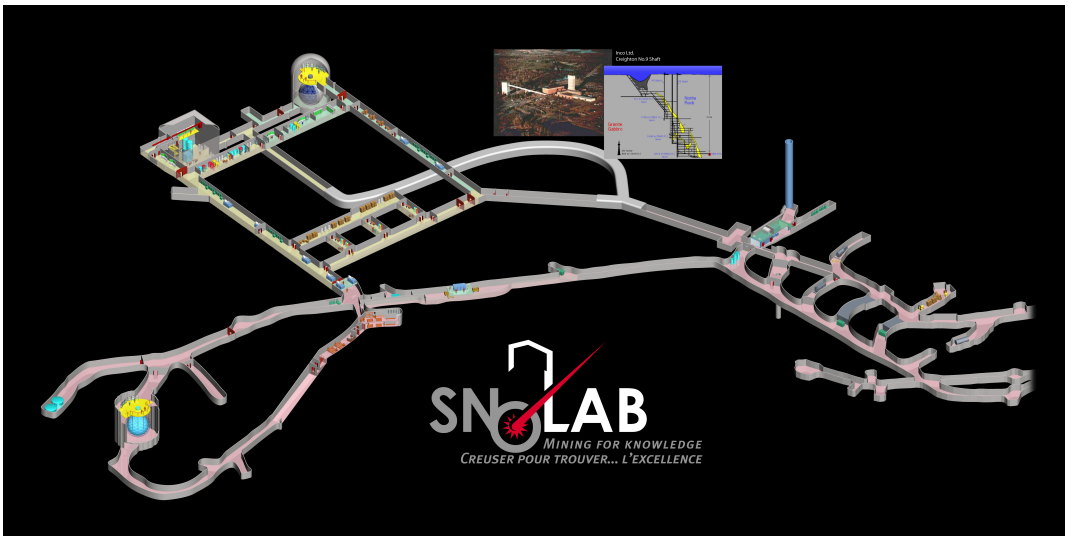

Figure 3.4: SNOLAB underground laboratory overview [63].

trinoless double-beta decay ($0\nu\beta\beta$) and dark matter search. To further limit background radiation that could originate from dust, the whole laboratory is a class 2000 cleanroom. Figure 3.4 gives an overview of the underground facility.

The PICO collaboration deployed two chambers in the facility. PICO-60 (formerly COUPP-60) shown in figure 3.5, is a 60 kg, medium scale detector. PICO-2L (formerly COUPP-2L) is a two liters, small scale experiment (Figure 3.6). Both chambers were first commissioned at SNOLAB in 2010.

Both chambers produced world leading SD limits. PICO-60 first ran with CF_3I [62], iodine making the experiment more sensitive to SI interactions. With the dominating SI limits of Xe experiments, the high sensitivity of fluorine for SD detection and the two successful runs of PICO-2L [61, 64], PICO-60 was filled with C_3F_8 for its second run, carried out in late 2016 [65].

Figures 3.7 and 3.8 show the improved SI and SD results from PICO-60 (C_3F_8), along with the results of PICO-2L and PICASSO (2014). PICO-60 set the best SD limits as of February 2017.

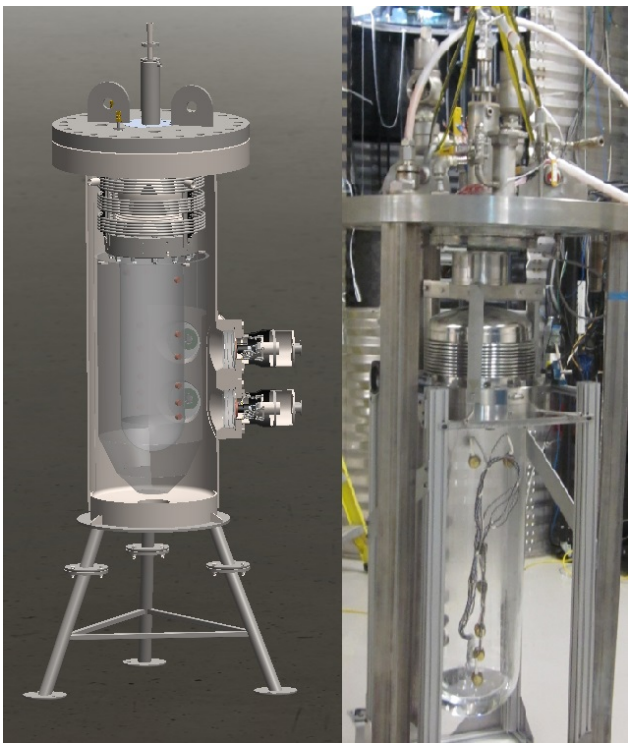

Figure 3.5: PICO-60. Left: engineering model of the chamber and the pressure vessel; Right: inner vessel and bellows assembly.

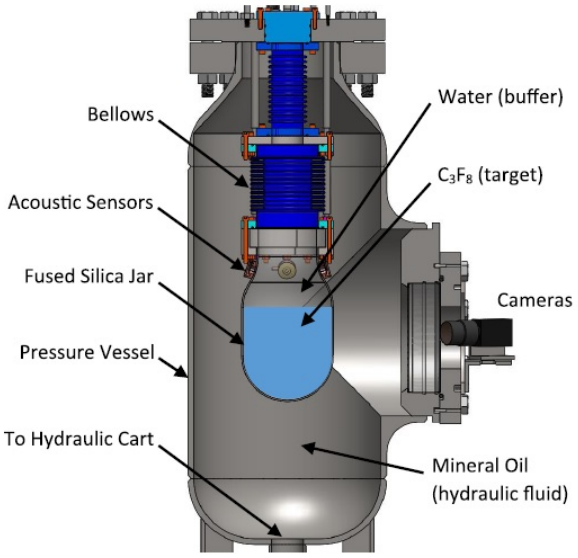

Figure 3.6: Schematic of PICO-2L.

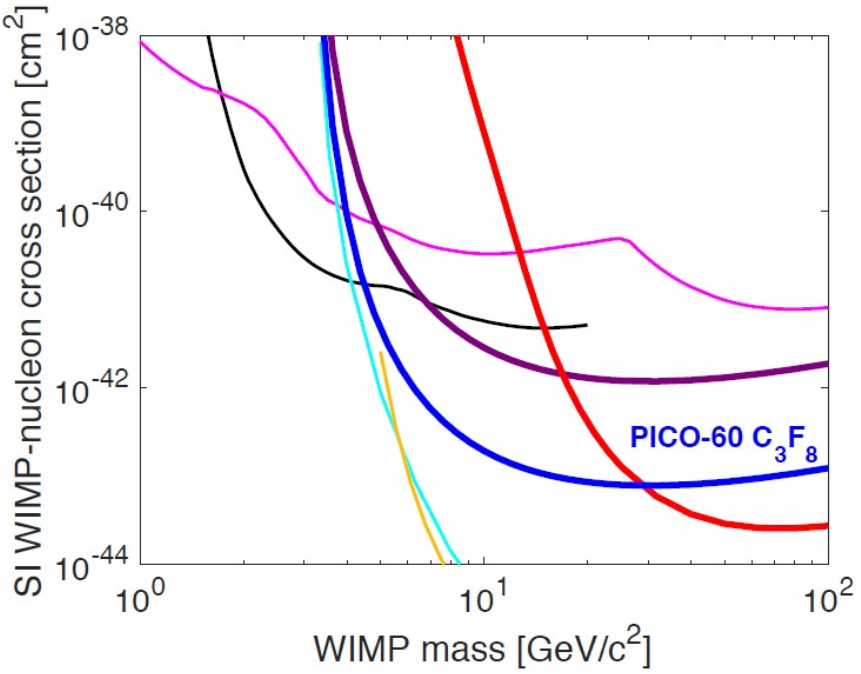

Figure 3.7: PICO spin-independent (SI) exclusion plot (2017) at 90% C.L. On the same plot are shown exclusion curves of PICO-60 CF_3I (red), PICO-2L (purple), LUX (yellow), PandaX-II (cyan), CRESST-II (magenta), CDMSlite (black).

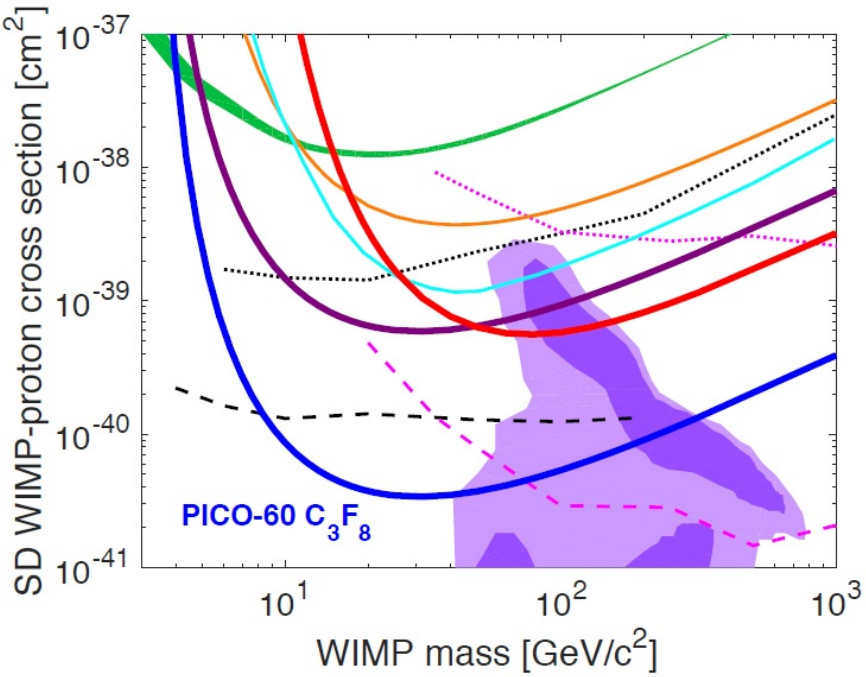

Figure 3.8: PICO spin-dependent (SD) exclusion plot (2017) at 90% C.L. Also shown: PICO-60 CF_3I (red), PICO-2L (purple), PICASSO (green), SIMPLE (orange); PandaX-II (cyan), IceCube (dashed pink) and SuperK (dashed black). The purple area represents the parameter space of the CMSSM theory.

CHAPTER 4

CALIBRATION OF THE PICO-0.1 TEST CHAMBER

The first original topic covered in this thesis is the calibrations of the PICO-0.1 test chamber. PICO-0.1 is a 0.1 kg calibration chamber meant to study the response of superheated liquids, such as C_3F_8 and C_2ClF_5, to various types of background radiation. Built by Mike Crisler at Fermilab in 2013, the chamber was sent to the Université de Montréal to perform calibrations with mono-energetic neutrons at the in-house accelerator facility. Such calibrations had been developed in the past by the Montreal team for the PICASSO experiment to calibrate droplet detectors [66, 67], and therefore, Montreal was a natural environment to perform similar calibrations. This neutron calibration was done at the Tandem Van de Graaff facility of the René J.A. Levesque laboratory. An accelerated proton beam produce mono energetic neutrons from nuclear reactions with a ^{51}V target. The calibration started in 2013, extending to the end of the summer of 2014.

Following the neutron calibrations, gamma measurements were undertaken to confirm rejection curves already obtained by other chambers. These gamma calibrations were concluded at the end of June 2015. Multiple sources were used in order to cover for low and high gamma energies.

Designed to be similar to the PICO-2L chamber, PICO-0.1 turned out to be one of the cleanest and most stable calibration chamber built by the PICO collaboration. For this reason, it was decided that this calibration chamber would serve to study external radioactive sources exclusively. The spiking of test chambers with foreign material have shown to leave everlasting backgrounds. Such tests have been performed by Daniel Baxter of Northwestern University with the *COUPP Iodine Recoil Threshold Experiment* (CIRTE) calibration chamber. The study of inner vessel contamination was performed with a dedicated detector, the Queen's University Test Chamber (QTC), built for this purpose by Guillaume Giroux.

This chapter gives an overview of the calibrations performed at Université de Montréal as part of this thesis. The PICO-0.1 chamber is described in section 4.1, and the Tandem Van de

Graaff accelerator is detailed in section 4.2. Finally, the results of the different measurements are presented in section 4.3. These include:

1) Neutron Calibration. The detector was calibrated with mono-energetic neutrons from the ^{51}V(p,n)^{51}Cr reaction

2) Gamma Calibration. Gamma emitting sources of various energies were used to determine the γ-rejection of C_3F_8.

3) SbBe Calibration. Mono-energetic neutrons produced with a SbBe source were used to complete the neutron calibration at lower neutron energy.

4) Low threshold operation. The chamber was run at a higher temperature to investigate the stability at lower operating thresholds (< 1 keV).

5) C_2ClF_5. The deployment of chlorinated freon in PICO-0.1 allows for the fine-tuning of the thermodynamic model used by the PICO collaboration for superheated liquids.

4.1 The PICO-0.1 bubble chamber

As for all PICO detectors, the energy threshold in PICO-0.1 is set by adjusting the inner pressure for a given temperature. The detector is controlled by a home-made *LabVIEW* program designed by members of the COUPP collaboration, and powered by a Data Acquisition System (DAQ) built by National Instruments.

The PICO-0.1 bubble chamber (Figure 4.1) consists of six interdependent systems: 1) inner vessel; 2) hydraulic pressure control; 3) pressure monitoring; 4) stereoscopic cameras; 5) the acoustic sensors; 6) temperature control.

4.1.1 Inner vessel

The inner vessel of PICO-0.1 in made of natural quartz. Quartz is a fairly radio pure material with a smooth surface, more robust than glass. In larger chambers, fused silica is preferred for its higher radio purity and lower cost. The inner vessel of PICO-0.1 is filled with C_3F_8 as the active fluid. The first fill was performed at Montreal in 2013 using ultra-pure water as a buffer liquid, as

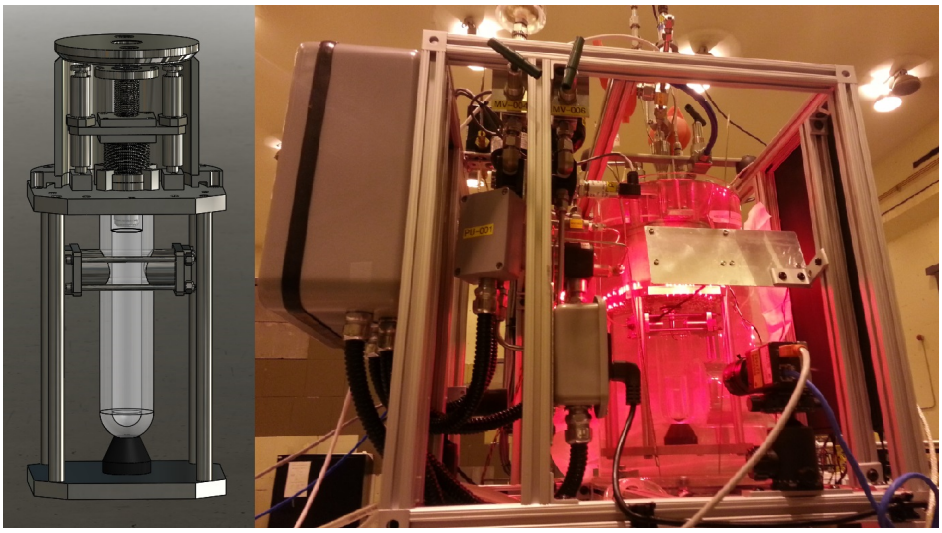

Figure 4.1: The PICO-0.1 bubble chamber. a) SOLIDWORK model of the inner vessel and bellows assembly; b) Fully assembled chamber.

in PICO-2L. The role of the buffer fluid is to isolate the active liquid from the various parts in the top hat assembly, especially the metal bellows. Although operating at a relatively stable rate, the small volume of the chamber led to foaming at the C_3F_8-water interface. This behavior was not observed in the PICO-2L chamber.

The first fill was ended rapidly to solve the foaming problem and Linear Alkylbenzene (LAB) was tested as a buffer liquid this time with excellent results. The fill was terminated by January 2014 and the C_3F_8-LAB combination proved to be much more stable than the C_3F_8-water combination, with no persistent foaming and no droplet migration between the two liquids, as shown in Figure 4.2.

4.1.2 Hydraulic pressure control system

The hydraulic pressure control system is a closed system constituted of several valves, accumulators and a pump, filled with mineral oil. Figure 4.3 shows a schematic of the system. Fluid is accumulated in the first accumulator, pressurized at around 200 PSIA (after some cycles, the system auto-adjusts the pressure at around 180 PSIA). The inner vessel of the chamber is compressed at 180-200 PSIA by opening one of the compression valves. In this state, the detector is inactive.

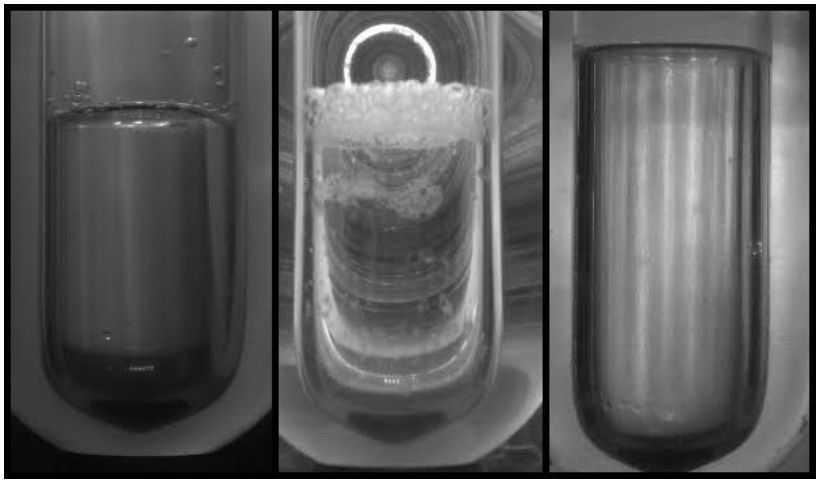

Figure 4.2: Inner vessel of PICO-0.1. From left to right: Water buffer right after the fill; Water buffer with foaming; LAB buffer.

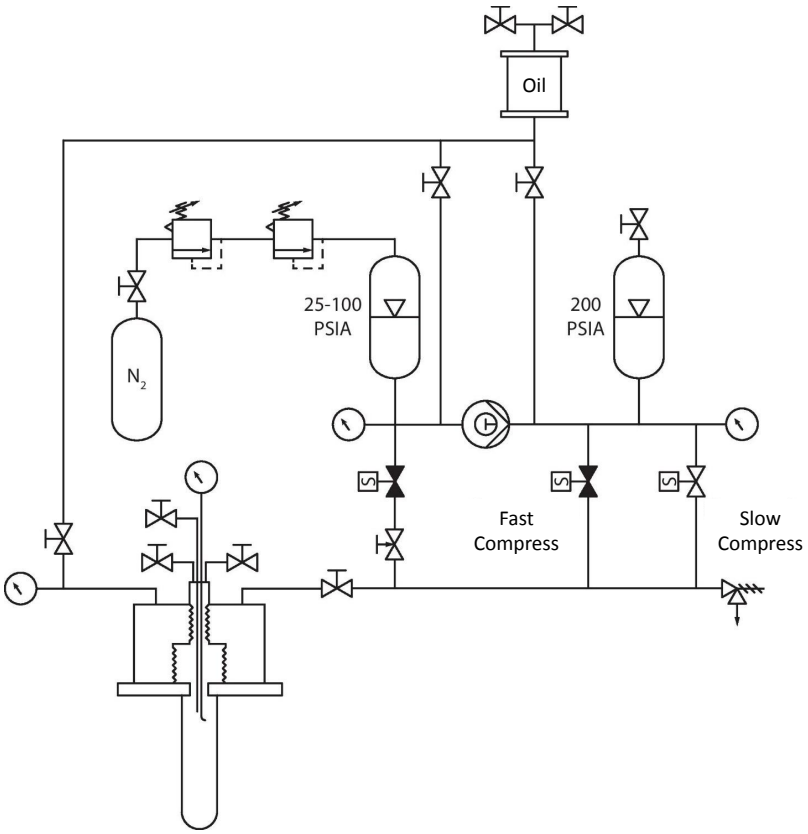

Figure 4.3: Hydraulic system schematic of PICO-0.1.

To expand the bubble chamber to its operational pressure, an air regulator, supplied by either a nitrogen bottle or hooked up to a centralized air system, sets the pressure in the second accumulator and the DAQ closes the compression valve while opening the valve to the second accumulator.

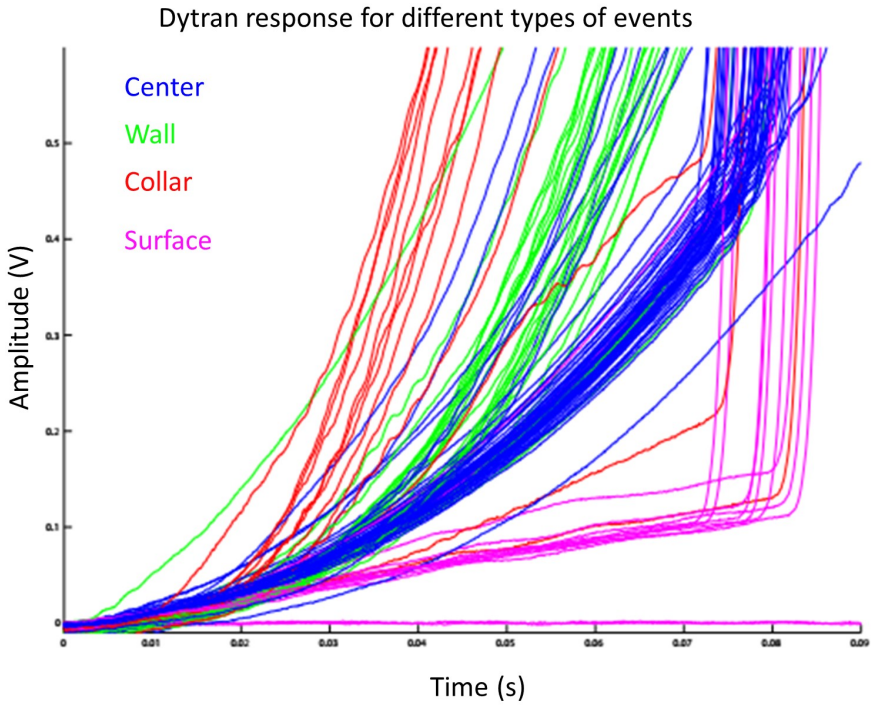

Figure 4.4: Comparison of the Dytran pressure rate of rise for different event types. Events were categorized by eye. Center events happen away from the components of the chamber. Wall events are characterized by a single bubble emerging from the quartz surface. Surface events describe events in which a bubble is formed at the interface of the active and buffer fluid. Collar events include bubbles that form at the triple contact line of both fluids with the quartz surface.

This allows the pressure in the inner vessel to drop. The detector is now in the active, expanded state. After an event trigger from the DAQ, valves are closed and the compression valve reopens, effectively re-compressing the chamber. When the accumulated fluid level in the first accumulator drops too low, the DAQ triggers the activation of a pump to transfer mineral oil from the second accumulator to the first, reverting the system to its initial state.

4.1.3 Pressure monitoring system

The inner pressure of PICO-0.1 is monitored with a pressure sensor from *Dytran instruments*. The *type 2005V* sensor has a sampling rate of up to 40 kHz. When a bubble is produced, the pressure rises due to the displacement of the liquid. It has been shown that the production site of a bubble influences the rate of rise of the pressure. As shown by the curves from Figure 4.4 obtained

from hand-scanned events, collar (red) and wall (green) bubbles tend to grow faster than bubbles in the bulk (blue), possibly because of the presence of cavities that can accelerate the nucleation process [68]. Furthermore, the presence of particulates of foreign materials (dust, quartz particles from the jar, stainless-steel, etc.) with sharp edges, stuck in the wall or collected at the collar, could cause unwanted nucleation in a similar way. Bubbles nucleating on the surface (pink) seem to produce a limited rise in pressure that can be explained by the bubble leaving the superheated bulk, not accreting as much liquid in the vapor phase as other bubbles.

The Dytran analysis can also determine the multiplicity, or number of bubbles, of events. Neutrons can undergo multiple collisions in the active fluid. They can therefore produce multiple bubbles, as long as the energy of the recoil nuclei is higher than the critical energy E_c. Intuitively, we could conceive that the rate of rise of two bubbles separated enough from each other, in order to not interfere with each other, should be faster than that of a single bubble. Although not following a linear relation, parameters extracted from a polynomial fit of the pressure curves can help to determine the multiplicity (number of bubbles) of events.

4.1.4 Stereoscopic camera system

The main trigger source of the detector is provided by the optical system. A stereoscopic camera system, composed of two *Basler A602f* cameras, is mounted on the aluminum chassis of the detector. The cameras acquire images alternately, at a combined frequency of 150 images/s. Each camera is coupled to a set of 16 red LED for illumination. In order to limit reflexion on the walls of the chamber, the LED sets are only lit when their associated camera is active. This stereoscopic system angled at nearly 90˚ allows for an easy 3D reconstruction of events.

4.1.5 Acoustic sensors system

Two piezoelectric sensors are mounted on PICO-0.1, as seen in (Figure 4.5). Both sensors are encased in a stainless-steel housing and are screwed against the quartz vessel. Vacuum grease is applied between the casing and the vessel for optimum acoustic transmission. The sensors

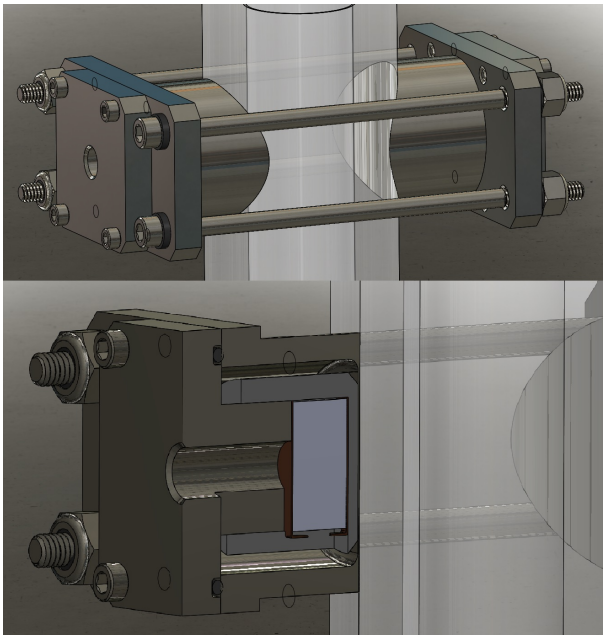

Figure 4.5: Piezoelectric sensors assembly. The sensors are encased in stainless-steel, immersed in water.

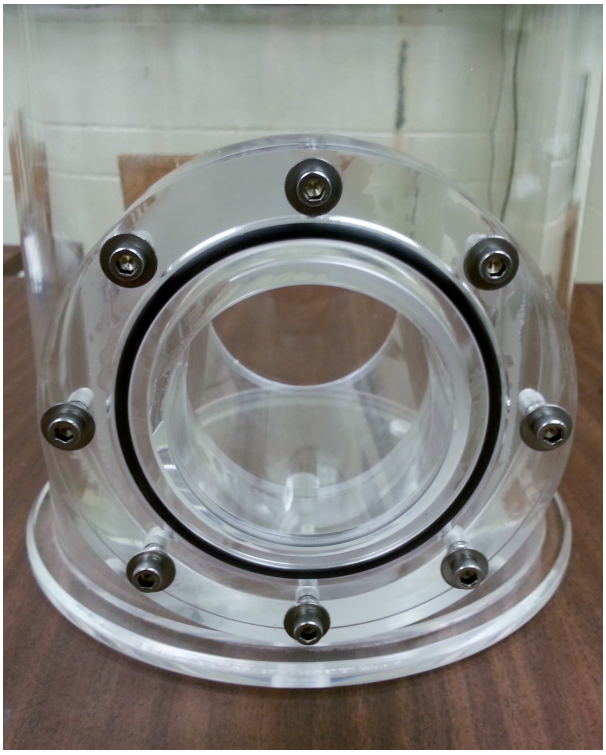

Figure 4.6: PICO-0.1 thermal bath. A hollow side channel limits the amount of water between the inner vessel and the radiation sources.

are paired with a PICASSO preamp with a gain of G = 12500, allowing for a maximum signal amplitude of $\pm$10 V. The DAQ is setup for a signal sampling of up to 1 Msample/s, for a maximum acquisition frequency of 500 kHz.

4.1.6 Temperature control system

The whole quartz inner vessel assembly sits in a water bath, kept at a predetermined constant temperature by circulating distilled water. Four temperature probes are placed inside the water bath at different heights. The temperature is recorded separately for every event. In the analysis, the average temperature of the four probes is considered as the inner fluid temperature, to account for the temperature gradient of about 0.5° C in the thermal bath. To limit the absorption of radiation in water between the sources and the inner vessel, a channel was incorporated in the thermal bath design as seen in Figure 4.6.

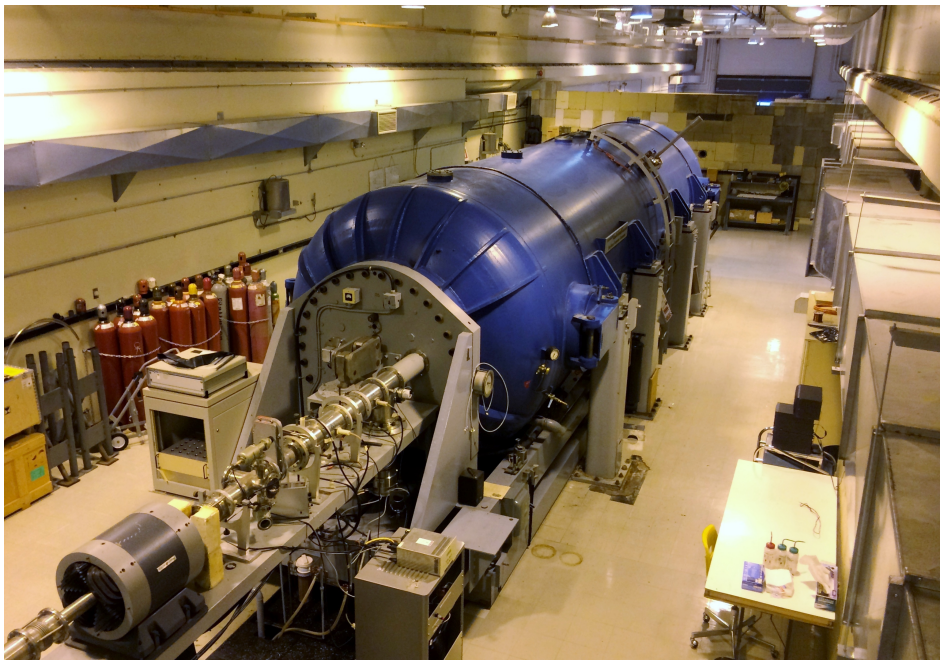

Figure 4.7: Tandem Van de Graaff accelerator at the Université de Montréal.

4.2 Tandem Van de Graaff accelerator

The Tandem Van de Graaff electrostatic accelerator at the Université de Montréal (Figure 4.7) is located at the René J.A. Levesque laboratory. It was inaugurated in 1966, acquired from *Atomic Energy of Canada's laboratories* located at Chalk River. The accelerator can achieve a maximum terminal voltage of 6 MV. The electric tension can be used twice by having the high voltage terminal located at the center of the accelerator housing and stripping charges from the accelerated nucleon, thus, the name *Tandem*. Therefore, protons for example, can be accelerated to an energy of up to 12 MeV.

The accelerator is operated by the PICO collaboration to produce mono energetic neutrons via specific nuclear reactions with a proton beam. The known energy of the neutrons allows us to calibrate detectors with high precision, as reflected by the precision in the keV range.

The accelerator itself is composed essentially by three distinct parts: the injector, the main accelerator housing and the energy selector magnet. The fourth part of the setup, the target, is located at the end of the 0° beam line for PICO (Figure 4.13).

4.2.1 Injector

The injector is the source of ions to be accelerated. The one installed at the tandem is a dual injector: a *Model 358 duoplasmatron* ion source and a *Model 860 sputtering* ion source. The first uses a gas plasma while the sputtering source uses solid elements in the form of powder pellets, usually for production of heavy ions beam. Even though protons can be produced from solid materials, the proton flux would be rather small and the pellets would be depleted rapidly. To fulfill our needs, we inject molecular hydrogen gas from a metal canister into the duoplasmatron source. The gas in the bottle is maintained in liquid form under pressure, which grants a lifetime of over 1000 hours of continuous use per canister.

The duoplasmatron source uses a two-stage gas discharge to produce ion beams [69]. As schematized in Figure 4.8, a heated, coated filament produces thermal electrons which sustain a first gas discharge after hydrogen is inserted in the chamber. Ions are produced by the second discharge, and are confined by a strong magnetic field produced in a small volume between the intermediate and main anode. This confinement produces a high plasma density. This plasma, which can be manually started by shorting out the circuit of the first anode, has positive ions in its center and negative ions in its outer perimeter. An extraction cone kept at a potential of 20 kV is placed off-center to extract negative ions.

After the extraction, the negative ions travel through two Einzel lenses, focusing lenses which produce a symmetrical electric field. This symmetry ensures that all ions passing through them exit with their energy unchanged, but ions that entered from the outer edges are deflected toward the focal point of the lens. The ions then enter a calibrated 90° analyzing magnet of mass analysis. For a chosen magnetic field, heavier atoms follow a wider arc through the magnet than lighter particles. This enables us to filter out undesirable particles before entering the acceleration tube. The last step of the pre-acceleration stage is the strong focusing of the ion beam by a system of so-called Q-snout lenses. Unlike older lensing methods which were made of metallic grids, the Q-snout produces no x-rays from atomic collisions and thus allows for a safer operation of the accelerator. When entering the Q-snout, ions encounter a large electric field gradient referenced to

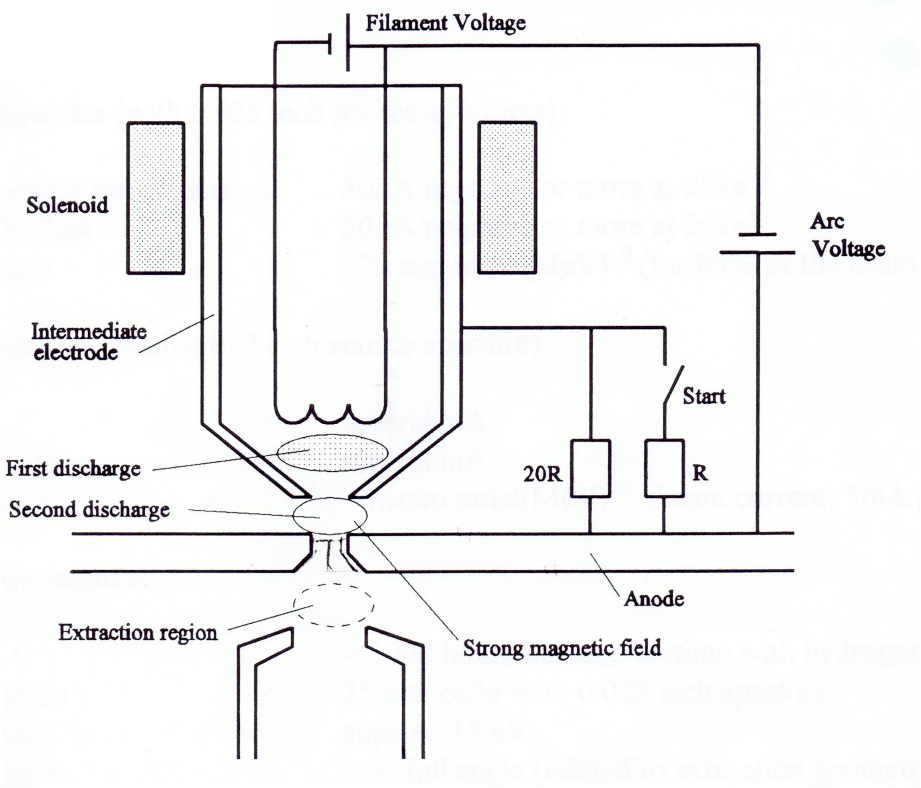

Figure 4.8: Diagram of the *Model 358 duoplasmatron* ion source. A hydrogen plasma is produced by a two-stage discharge. A heated filament produces thermo-electrons in the first discharge region. Guided by a strong magnetic field from a solenoid, electrons travel to the second discharge region where hydrogen is injected. The ionized gas stats a secondary discharge between the intermediate electrode and the anode. Ions are extracted by a 20 kV potential.

the terminal voltage of the accelerator. This feedback creates an automatic lensing that is adapted to the full range of the operating tension. It also ensures that ions are accelerated to the correct energy by automatic feedback to voltage fluctuations at the terminal.

4.2.2 Main accelerator housing

The main accelerator section is the most prominent feature of a Tandem Van de Graaff accelerator. It is a gas tank filled with SF_6, an inert gas pressurized at 58 PSI, whose purpose is to limit arcing between components under high tension. The acceleration tube in its center is made out of glass sections and is supported by a cantilever system composed of a piston located on the high-energy side, and four columns constituted of glass blocks separated by metal plates. The cantilever

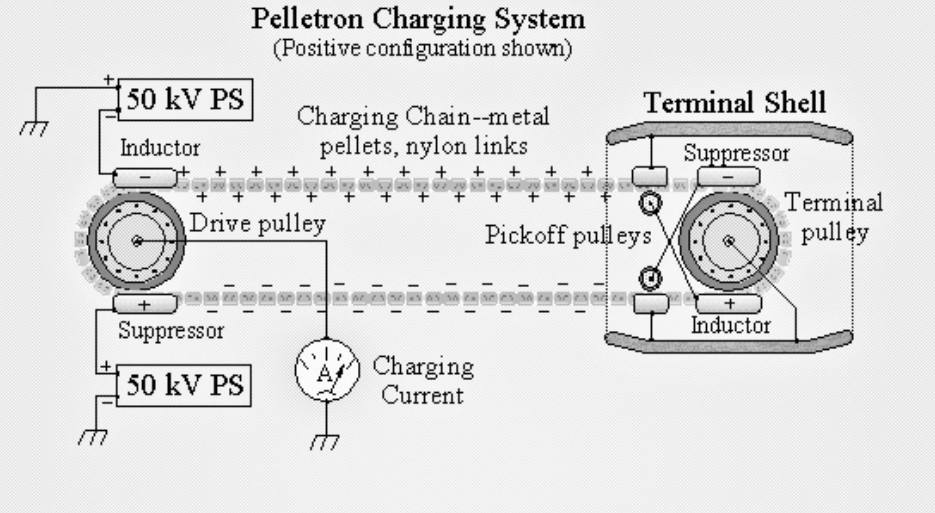

Figure 4.9: Diagram of a pelletron changing chain.

system is essential in isolating the high-voltage electrode within the tank.

The Tandem Van de Graaff accelerator has two pelletron charging chains to transport charges. The high-tension chains are made of metal pellets linked by insulating nylon joints. As shown in Figure 4.9, they revolve on a set of pulleys, the drive and terminal pulley, which also act as electrodes. Analog to the leather belts in Van de Graaff generators, pelletron charging chains build up positive charges by picking them up at one end, at the drive pulley, and accumulating them at the other end at near the terminal. Two small pickoff pulleys transfer the charges to the terminal. A negatively charged suppressor electrode at the terminal prevents arcing as the charges are deposited. The main advantage of using pelletron charging chains as opposed to leather or paper belts are a better terminal stability, cleaner operation since no dust is produced, longer lifetime and no arcing.

Along its entire length, the acceleration tube is linked to equipotential planes by metal electrodes (Figure 4.10), perpendicular to the ion beam axis. Every plane is linked to the next by a resistance, forming a series circuit which produces a constant electric field gradient in the acceleration tube. A surrounding stainless-steel ring, as shown in Figure 4.11, renders the gradient uniform throughout the plane, ensuring a uniform acceleration of ions independent of their radial position in the tube.

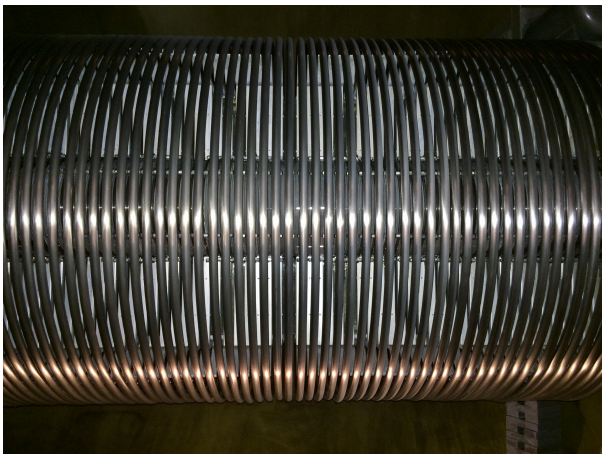

Figure 4.10: Acceleration tube inside equipotential rings.

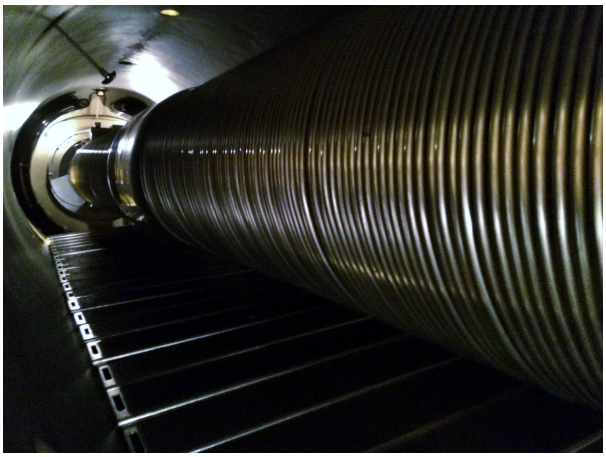

Figure 4.11: Inside view of the main accelerator housing.

As its name suggests, the Tandem uses the same terminal voltage twice. To do so, the electric field in the accelerator needs to be symmetrical. That is, the gradient passes, in the first half, from zero to the terminal voltage in the middle, and from terminal voltage to ground in the second half. In normal conditions, negative ions subjected to such a field would oscillate from one end to the other indefinitely. Instead, a stripper in the middle of the acceleration tube "strips" electrons from the ions, changing their charge from negative to positive. The first strippers were thin sheets of metal, but were replaced by a mist of oxygen gas for a better efficiency. The now positive ions will themselves acquire a kinetic energy in multiples of the terminal voltage depending on their net charge. Hydrogen is however limited to -1/+1 charge.

4.2.3 Energy analyzing magnet

When the now positively charged ions exit the acceleration tube, they have acquired an energy which depends on their charge state. For the neutron calibration, protons have typically an energy in the 1-2 MeV range. Even though they are subjected to a precisely set electric field in the acceleration tube, proton energy at the exit of the accelerator may vary slightly due to atomic collisions or small tension fluctuation. A near mono-energetic beam can be obtained with an energy analyzing magnet, shown in Figure 4.12. The method is similar to the one of the mass analyzing magnet in the ion source. The magnetic field is much stronger since the energy of the

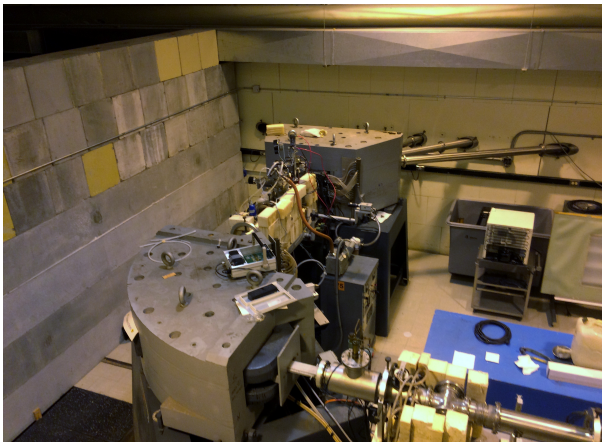

Figure 4.12: Energy analyzing magnet (bottom) and beam line selector magnet (top).

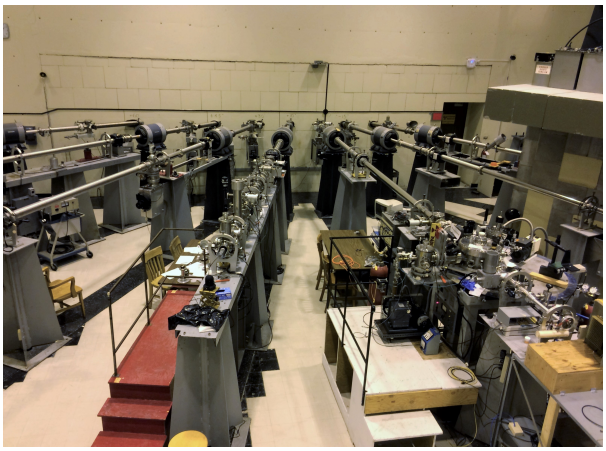

Figure 4.13: Target hall of the Tandem Van de Graaff facility. The PICO-0.1 neutron calibration was performed on the 0° beam line, third from the right.

ions is higher.

Before entering the analyzing magnet, the ions are focused by a quadrupole magnetic lens to increase the ion beam density. Ions then enter the analyzing magnetic field, which is controlled by a nuclear magnetic resonance probe for increased precision and stability. The magnetic field resolution is 0.1 gauss, which maps linearly for proton energy with a resolution of 0.2 keV. The path of the proton beam is curved on a 90° arc by the magnetic field. Ions with a higher kinetic energy follow a wider curvature radius while less energetic ions follow a smaller arced path. After the bend, a narrow slit selects ions with the correct energy and sends them towards the beam line selector magnet. The rest of the ions are stopped when they hit the slit blades.

The beam line selector magnet (Figure 4.12) produces a magnetic field that deflects the ion beam into one of the seven lines in the target hall, shown in Figure 4.13. This allows to have multiple experimental setups mounted permanently, each one ready to be used for a specific purpose. The line used by the PICASSO/PICO experiments for neutron calibration is the 0° line. Instrumentation installed on the line includes a second quadrupole magnetic lens and a set of four deflector plates, for x and y deflection of the beam (z being the axis of propagation of the protons). Finally, at the end of the beam line, a carousel holder is installed, which allows switching of different targets without breaking the vacuum.

4.2.4 Target

The final part of the setup used for calibrating PICO-0.1 is the vanadium-51 (^{51}V) target. This target substrate is highly polished platinum where a 14 nm thin layer of ^{51}V (natural abundance of 99.75%) was vapor deposited at the *École Polytechnique de Montréal*. The target is mounted in the carousel holder at the end of the beam line and constantly kept under vacuum to avoid oxidation.

Neutrons are produced by the ^{51}V(p,n)^{51}Cr nuclear reaction. This reaction shows several narrow mono energetic resonances at around 1.6 MeV of proton energy, as shown in Figure 4.14 and table 4.I [70]. Without the high resolution of the analyzing magnet, this process wouldn't be feasible since the resonances are so close to one another. The resolution of the peaks with this setup is of about 0.25 keV of neutron energy and is determined by the thickness of the vanadium target. This spectrum must be mapped out in small sections to assure the proper selection of the neutron energy at the beginning of each runs. A mapping of two or three peaks and a comparison of the relative intensities was usually sufficient to obtain certainty about the energy of the selected resonance. The cumulative experimental spectrum is shown in Figure 4.15.

Due to the small cross section of this nuclear reaction and the essentially isotropic emission of the produced neutrons, the neutron flux from the target is rather weak. Even though the flux is directly proportional to the flux of incident protons, we are limited in beam current by the rapid rise in temperature of the target when subjected to a high proton fluxes. The rapid heating of the target would effectively vaporize the thin film of vanadium from the platinum substrate. Even at low proton current, the weakening of the flux over several years revealed a slow degradation of the target. The applied proton current on the target is thus usually set at around 3.5 μA.

4.2.5 Beam line instrumentation

Some auxiliary equipment is needed for the neutron calibration measurement. A *model 1000C* current integrator from *Brookhaven Instruments Corporation* is hooked up at the end of the beam line and measures the accumulated charge of protons that reach the end of the beam line. When searching for resonances from the Vanadium target, the integrator stops the proton beam when

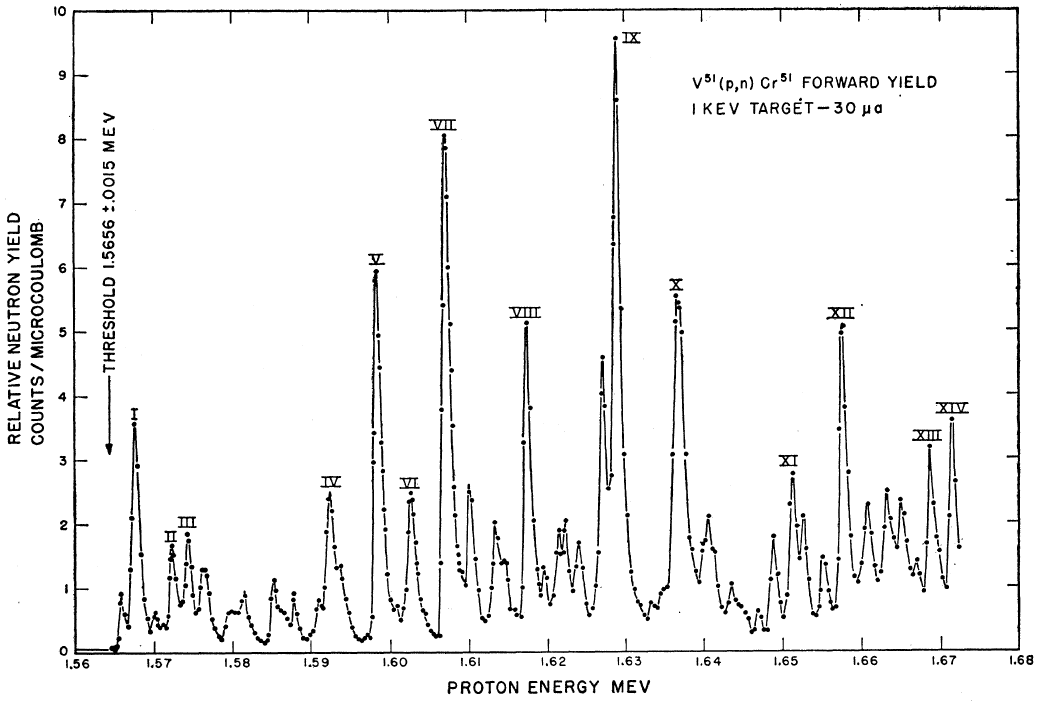

Figure 4.14: ^{51}V(p,n)^{51}Cr neutron energy spectrum from [70].

Resonance	Proton energy (MeV)	Neutron energy (keV)
I	1.568	4.8
II	1.573	11.3
III	1.575	13.6
IV	1.592	34
V	1.598	40
VI	1.603	45
VII	1.607	50
VIII	1.617	61
IX	1.629	74
X	1.637	82
XI	1.651	97
XII	1.658	104
XIII	1.669	116
XIV	1.672	119

Table 4.I: Table of proton-neutron energy of the ^{51}V(p,n)^{51}Cr reaction [70].

40μA have been collected. This instrument allows for a 0.02% error on the integrated charge [71], a level of precision largely sufficient to ensure the uniform exposure of the target to the different proton energies.

Finally, two ^{3}He neutron counters measure the relative neutron flux from the target (4.16). One

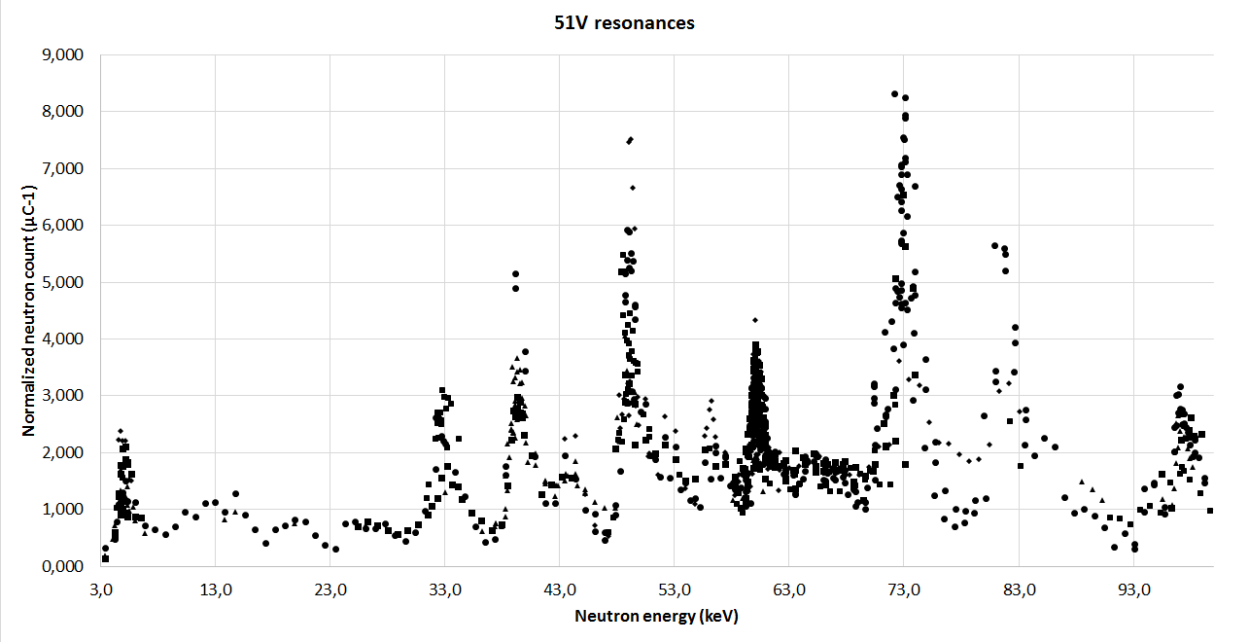

Figure 4.15: ^{51}V(p,n)^{51}Cr neutron spectrum as a function of neutron energy.

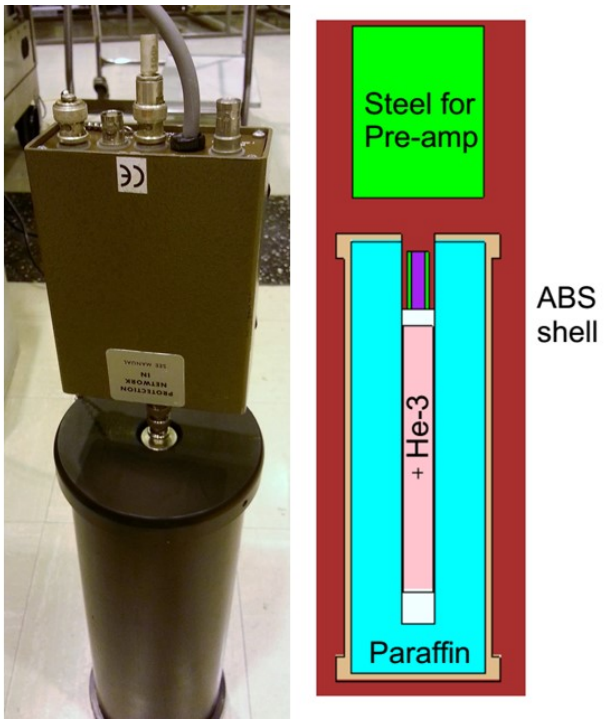

Figure 4.16: ^{3}He neutron counter. The ABS outer shell contains a paraffin moderator, hollowed out to insert the ^{3}He capsule.

counter (U-Montréal Neutron Counter) is located underneath the target holder of the beam-pipe, while the second (U-Chicago Neutron Counter, Figure 4.16) is located underneath PICO-0.1.

In these counters, fast neutrons are first thermalized by a layer of paraffin, a material rich in hydrogen. Thermal neutrons then interact with the ^{3}He by the ^{3}He(n_{th},p)^{3}H reaction with a Q-value of 760 keV. The proton and tritium recoil and ionize the surrounding ^{3}He gas in a cylindrical proportional gas counter. A thin wire placed in the middle of the ^{3}He chamber is held at a bias voltage of 2.5 kV. Electrons produce induction in the wire, multiply in an avalanche and generate a pulse signal. Pulses are finally amplified and time-stretched to allow a gate counter to easily detect pulses over electric noise. The efficiencies of the counters were determined and cross-calibrated with the method described in chapter 5.

4.3 Measurements and results

This section presents results and discussion of five measurements taken as part of the main work of this thesis with the PICO-0.1 test chamber. The measurements are:

1) Neutron Calibration

2) Gamma Calibration

3) SbBe Calibration

4) Low threshold operation

5) C_2ClF_5

4.3.1 Neutron calibration

Low energy neutron interactions in bubble chambers, approximately up to 500 keV, resemble that of WIMPs since both particles are massive, charge-less, and undergo elastic scattering with target nuclei. WIMPs interact on the scale of the electroweak nuclear force while neutrons interact via the strong nuclear force. The latter interacts therefore much more easily. Despite the fact that neutrons constitute a major background source for all dark matter searches, they can be used to calibrate detectors. The expected response curve and efficiencies with respect to WIMP interactions can be determined by calibrating the chambers with a mono-energetic neutron source.

The recoil energy of the target is described by:

$$E_R = \frac{2m_n m_A}{(m_n + m_A)^2}(1 - cos\theta)E_n \tag{4.1}$$

where m_n and m_A are the masses of the neutron and the target respectively, θ is the scattering angle and E_n is the neutron energy. We can determine the maximum recoil energy by fixing $\theta = \pi$. For carbon and fluorine, atoms constituting C_3F_8 molecules, the maximum recoil energies are:

$$E_{R,Cmax} = 0.28 \cdot E_n \tag{4.2}$$

$$E_{R,Fmax} = 0.19 \cdot E_n \tag{4.3}$$

Assuming an isotropic angular distribution of the elastic scattering, neutrons produce a box-shape recoil spectrum, shown in Figure 4.17.a. Bubble chambers being threshold detectors, only energy transfers greater than the threshold energy of the chamber can produce a bubble. The response at a given threshold is the sum of the response of recoils with energies higher than the threshold energy. Given a box-shaped recoil spectrum, the response has a linear relation to the threshold energy, as seen in Figure 4.17.b. Furthermore, the total response is the sum of the contribution of carbon and fluorine in C_3F_8. Figure 4.18 shows the effect of the α parameter of equation 3.5 on the neutron detection efficiency. As the α parameter tends towards infinity, the count-rate becomes linear with the threshold energy and corresponds to a nucleation efficiency of 100% [72].

Since the mean kinetic energy of WIMPs in the galactic halo is small ($\sim$ 200 keV), very little energy is transferred to targets. Therefore, small neutron energies are required to perform the calibration. The ^{51}V target produces mono-energetic neutrons of energies shown in table 4.I. Of those, resonances I, IV, V, VII, VIII and XI were chosen due to their higher relative strength.

Some of the ^{51}V resonances coincide with resonances in the neutron-fluorine cross-section. Both neutron-carbon and neutron-fluorine cross-sections en presented in Figure 4.19.

For every event, the chamber was expanded 10 seconds prior to the automatic activation of the

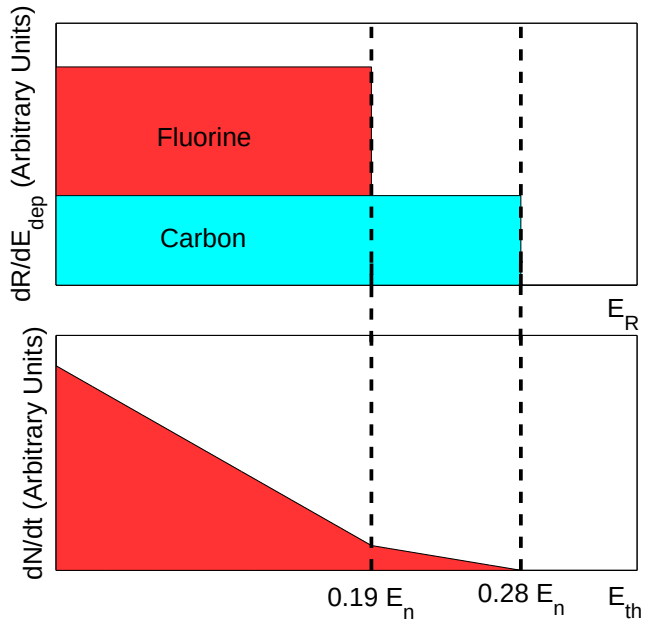

Figure 4.17: Recoil spectrum and theoretical response of mono-energetic neutrons. *Top*: Assuming elastic scattering is isotropic, the recoil spectrum is box shaped. *Bottom*: As the threshold energy is lowered, more recoils have sufficient energy to nucleate bubbles, increasing the nucleation rate. The idealistic nucleation rate is the integral of the recoil spectrum from the threshold energy to infinity. This results in a linear shape.

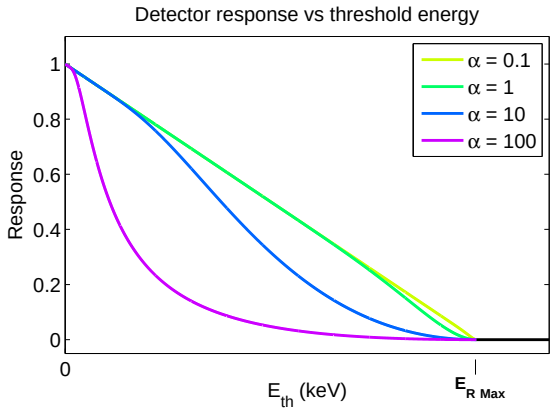

Figure 4.18: Effect of the α parameter on the neutron detection efficiency. As the α parameter tends to infinity, the response becomes linear with the threshold energy, as expected for a box-shape recoil spectrum.

proton beam to ensure stability. The neutron counters were used to normalize each event with the variable neutron flux that depends on the proton current, beam focus and target physical condition.

Figure 4.20 shows the background subtracted count rates for six neutron energies as a func-

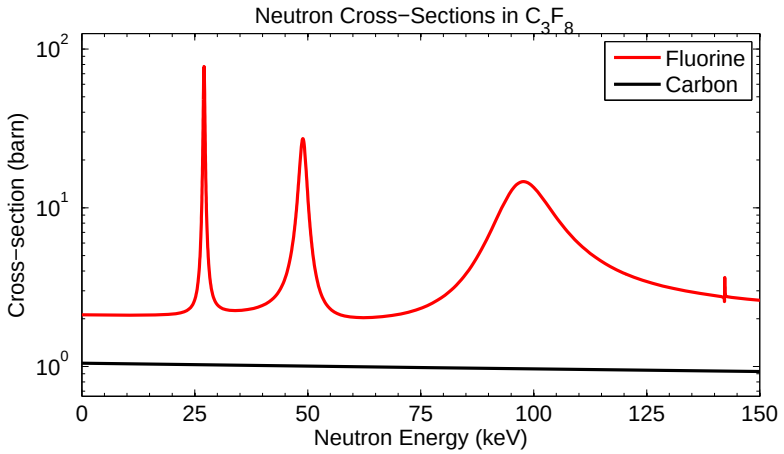

Figure 4.19: Neutron-carbon and neutron-fluorine interaction cross-sections. The cross sections were weighted with the stoichiometric ratios for C_3F_8.

Source	γ energy (keV)	Activity (μCi)	Half-life	Production date
^{60}Co	1173 & 1332	1000	1925.28 d	Mar-1975
^{124}Sb	603 & 1691	25	60.20 d	Feb-10-2015
^{137}Cs	662	10000	30.08 y	Oct-1982
^{241}Am	60	9.4	432.6 y	Nov-1982

Table 4.II: Table of γ sources.

tion of threshold energy. Vertical dashed lines mark the highest detection threshold for fluorine ($E_{R,Fmax}$) for each neutron energies.

At higher thresholds ($E_{th} > E_{R,Cmax}$) the theoretical response falls to zero. However, experimentally, backgrounds absent from background runs must be considered in simulations. For example, interactions of the proton beam with the beam-pipe could produce high-energy particles that could interact in the chamber. Also, fluctuation in the ambient background and spontaneous nucleation (wall, collar events) can result in a non-zero count-rate.

With this data and Geant4 or MCNP simulations, it is now possible to determine the nucleation probability $P(E_R, E_{th}, \alpha)$ from equation 3.6 and therefore determine the value of the α parameter for each neutron energy. However, at the time of writing this thesis, such simulations had not been carried out.

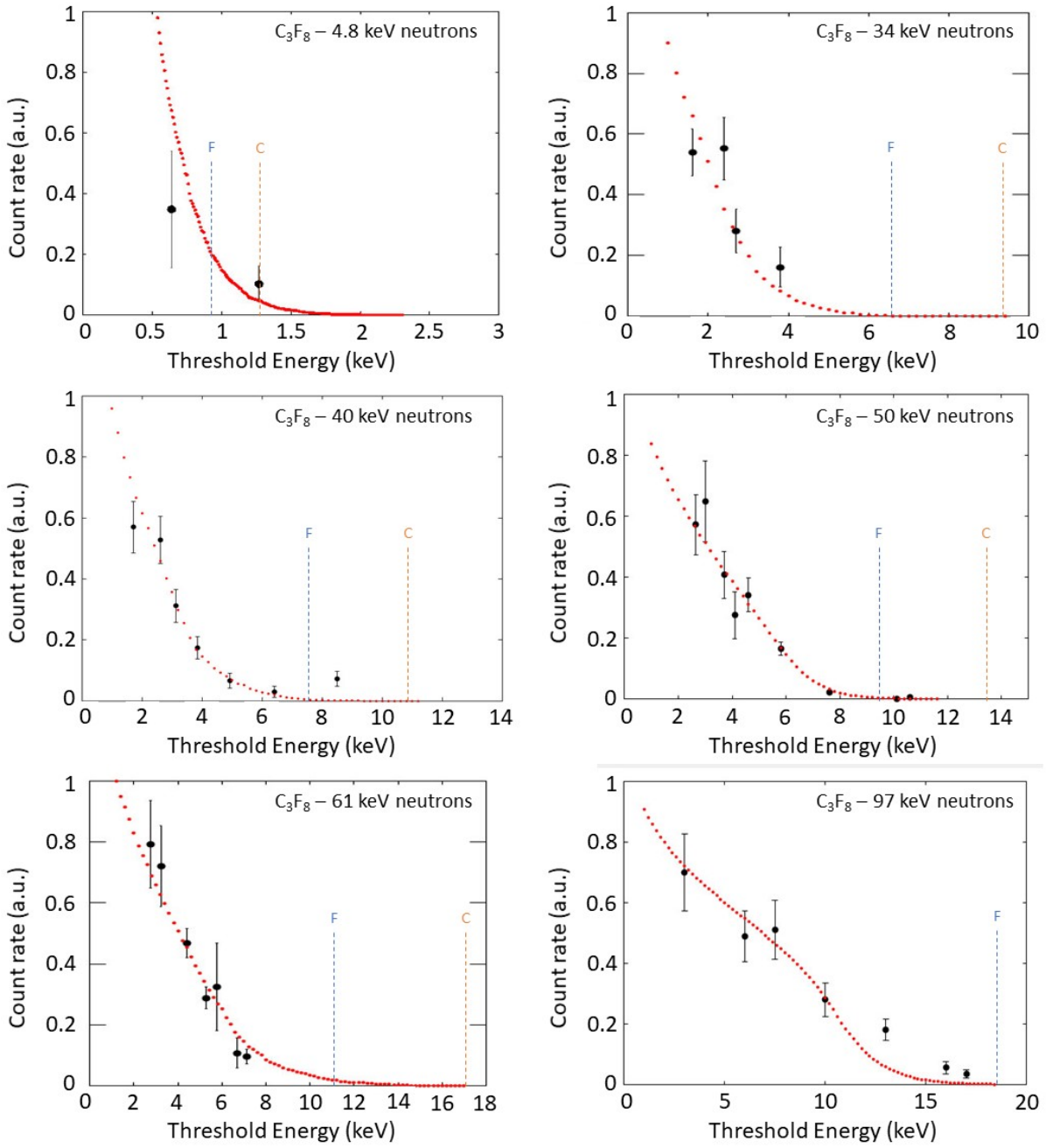

Figure 4.20: Response of the PICO-0.1 bubble chamber for different neutron energies. The analysis was performed by Guillaume Giroux [73]. Vertical dashed lines indicate the highest carbon and fluorine trigger threshold associated to each neutron energies (from eq. 4.2 and 4.3)

4.3.2 Gamma calibration

The PICO-0.1 bubble chamber was also used to measure the global γ-rejection of C_3F_8 as an active liquid. Gammas emitted from radioactive sources in the keV energy range interact mostly

by Compton scattering with electrons. Ionized electrons of small energy (keV), called Delta-rays, can produce secondary ionization that can produce bubbles if they deposit enough energy locally.

Although a less important source of background, compared to neutrons, at normal operating thresholds, γ radiation becomes rapidly the dominating background at thresholds below 1 keV by ionizing atoms in the target liquid. The understanding of this γ background is, therefore, very important for low threshold operation.

The PICO collaboration measured a nucleation probability down to below 10^{-10} at thresholds higher than 3 keV for most chambers filled with C_3F_8. However, measurements performed with the CIRTE calibration chamber deployed at Northwestern University showed worse γ rejections for the same active fluid. It was first proposed that γ rejection could be worse in small scale chamber as opposed to large detectors.

At the end of 2014 through the beginning of 2015, PICO-0.1 was calibrated with multiple γ sources to either confirm or refute the results of CIRTE. The list of γ-emitting sources used for this calibration is tabulated in table 4.II. The chamber was moved from the target hall of the accelerator facility to a spacious room to avoid back-scattering. The sources were placed on a graduated rail to allow their distance to the middle of the chamber to be measured. The distance was shortened as the threshold was increased to keep the count rate approximately constant, at a rate of about one events every 20 seconds.

Monte Carlo simulations were performed to calculate the nucleation probability of every source by normalizing by source activity and by including the geometry of the setup. The results are shown in Figure 4.21. The results of PICO-0.1 confirmed that the γ-rejection is independent of the gamma energy, but depends on the type of active fluid. The results obtained with PICO-0.1 are in contradiction to the results from CIRTE as the data was in accordance with data from large detectors.

The reason for the anomalous rejection curves obtained with CIRTE was finally found to be due to traces of tungsten in the active fluid. This residual contamination was left on parts of the chamber after voluntary particulate spiking of the active fluid in a past measurement, even

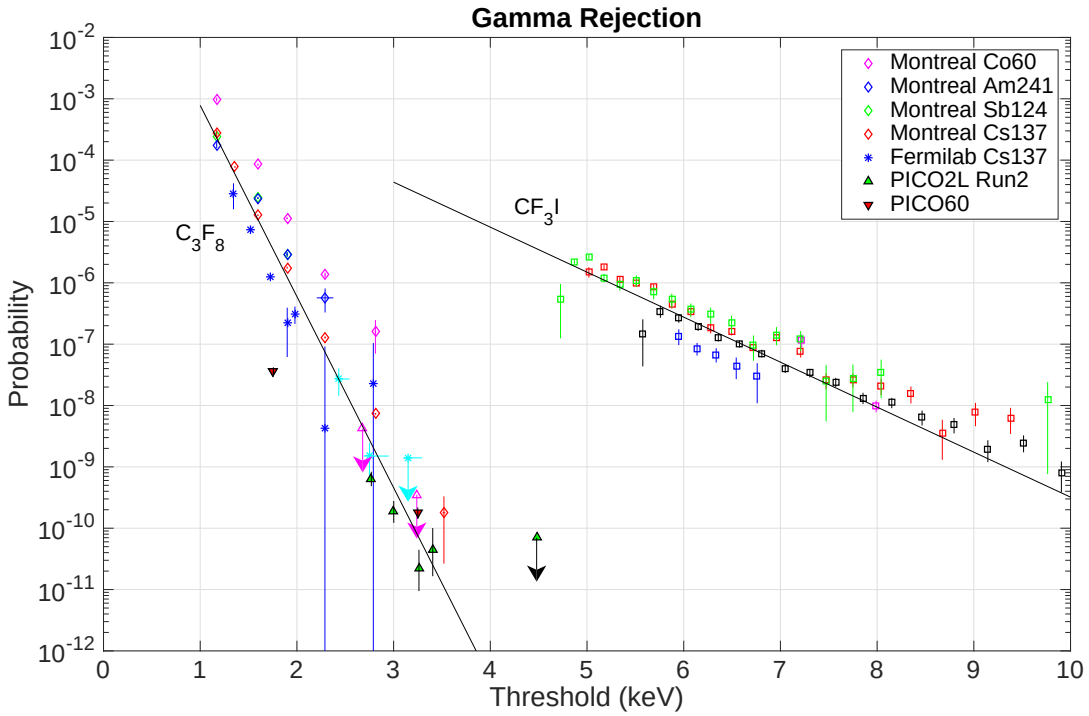

Figure 4.21: γ-rejection master plot. The rejection curve is not function of the gamma energy, but changes for different active fluids. CF_3I data taken with different COUPP bubble chambers.

after thorough cleaning of the entire detector. Gammas would then interact with the particulates, producing bubbles in a more efficient way and thus reducing the γ-rejection for this particular test chamber. Following this discovery and the commissioning of the Queen's University Test Chamber (QTC), the CIRTE test chamber was permanently decommissioned.

4.3.3 SbBe calibration

Given the lack of significant resonances in the ^{51}V(p,n)^{51}Cr reaction for energies below 34 keV, the calibration with C_3F_8 was completed with an antimony-beryllium (SbBe) source. A (γ,n) reaction with a threshold of 1.666 MeV can occur in ^{9}Be. The 1.69 keV γ-line from ^{124}Sb, with a 47.1% transition probability, can produce neutrons with a 24 keV mean energy [74].

Antimony sources were activated at the SLOWPOKE nuclear reactor of the École Polytechnique de Montréal by neutron capture from antimony-trioxyde (Sb_2O_3). The reactor contains 5 kg of uranium enriched with 20% of ^{235}U, producing a neutron flux of up to $10^{12}\, n \cdot cm^{-2} \cdot s^{-1}$. Sb_2O_3

Source	Initial activity (μCi)	Reference date	Uncertainty (%)
Sb1	25	Feb-10-2015	3
Sb2	24	Feb-10-2015	3
Sb3	5.578	Feb-10-2015	3
Sb4	107	Jul-03-2015	10
Sb4 (reactivation)	86.68	Jan-15-2016	5
Sb5	59.9	Mar-21-2016	5
Sb6	61.2	Mar-21-2016	5
Sb7	55.4	Mar-21-2016	5
Sb4 (reactivation)	834.7	Jul-27-2016	5
Sb5 (reactivation)	566	Jul-27-2016	5
Sb6 (reactivation)	525	Jul-27-2016	5

Table 4.III: Table of ^{124}Sb sources produced at the École Polytechnique de Montréal.

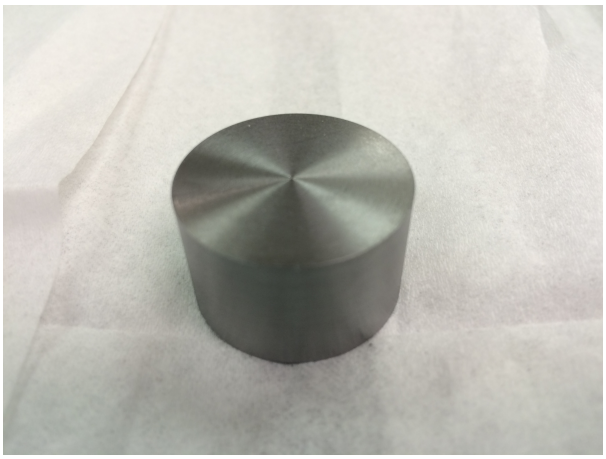

Figure 4.22: Beryllium disk. Dimensions: 1" diameter x 5/8" height.

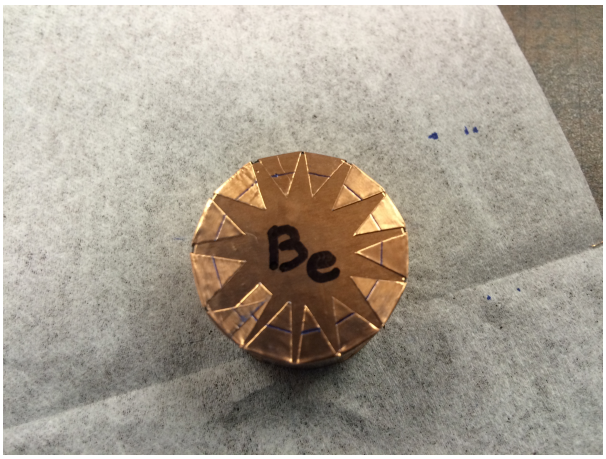

Figure 4.23: Beryllium disk with copper tape cover.

was encapsulated in plastic, thermo-sealed and inserted in the beam line near the reactor core. Natural antimony being composed of 57.21% of ^{121}Sb and 42.79% of ^{123}Sb, both ^{122}Sb and ^{124}Sb were produced, with a half-life of 2.72 and 60.20 days respectively. A three-week relaxation period was enforced to allow for the decay of ^{122}Sb to ensure a safe manipulation of the sources. Table 4.III presents the properties of all antimony sources produced at the SLOWPOKE facility for the PICO collaboration.

Following the γ calibration, PICO-0.1 was calibrated with the SbBe source. A beryllium disk of 1" diameter x 5/8" height was purchased from the *Materion* company, shown in Figure 4.22. The disk was covered with copper tape (Figure 4.23) to ensure safe manipulation of the product,

beryllium being a known carcinogenic product. To limit the exposure to γ radiation from the antimony source, two 3.5" diameter lead cylinders were inserted in the channel of the water bath for a total thickness of 4".

Figure 4.24 shows the bubble rate for three ^{124}Sb sources (Sb4 (reactivation), Sb5 (reactivation), Sb6 (reactivation)) as a function of the threshold energy. Data were also taken without the beryllium disk to measure the response of the chamber to both background and γ radiation from the antimony. The count rate shown in Figure 4.24 is background subtracted and was normalized for the decreasing activity of the ^{124}Sb source. As with 4.8 keV neutrons, low threshold operation of PICO-0.1 (below 3 keV) makes the chamber subject to nucleation from γ radiation. Proper simulations using the γ-rejection of section 4.3.2 are therefore needed to interpret the data correctly.

4.3.4 Low threshold operation

By the end of the C_3F_8-LAB fill, the extremely good behavior of the chamber prompted us to lower the threshold of the detector to an all-time low. The temperature was raised from 18 $^\circ$C to 24 $^\circ$C while the operating pressures were kept unchanged.

Figure 4.25 shows the combined background count rate as a function of threshold energy. At this temperature, stable conditions were obtained down to 0.8 keV. The background signal became quickly dominated by γ radiation, as discussed in section 4.3.2. This was expected since trial and error during the neutron calibration showed that the background started to increase rapidly below a threshold energy of 2 keV. Therefore, in the past, the chamber was never operated below this threshold.

Nevertheless, this result proved that PICO bubble chambers can be operated at low thresholds with C_3F_8 without suffering from technical problems. Appropriate gamma-shielding may allow for an even lower threshold operation, as PICO-0.1 wasn't shielded at all. This measurement is also a confirmation of the high γ rejection observed during the neutron calibration at thresholds higher than 2 keV.

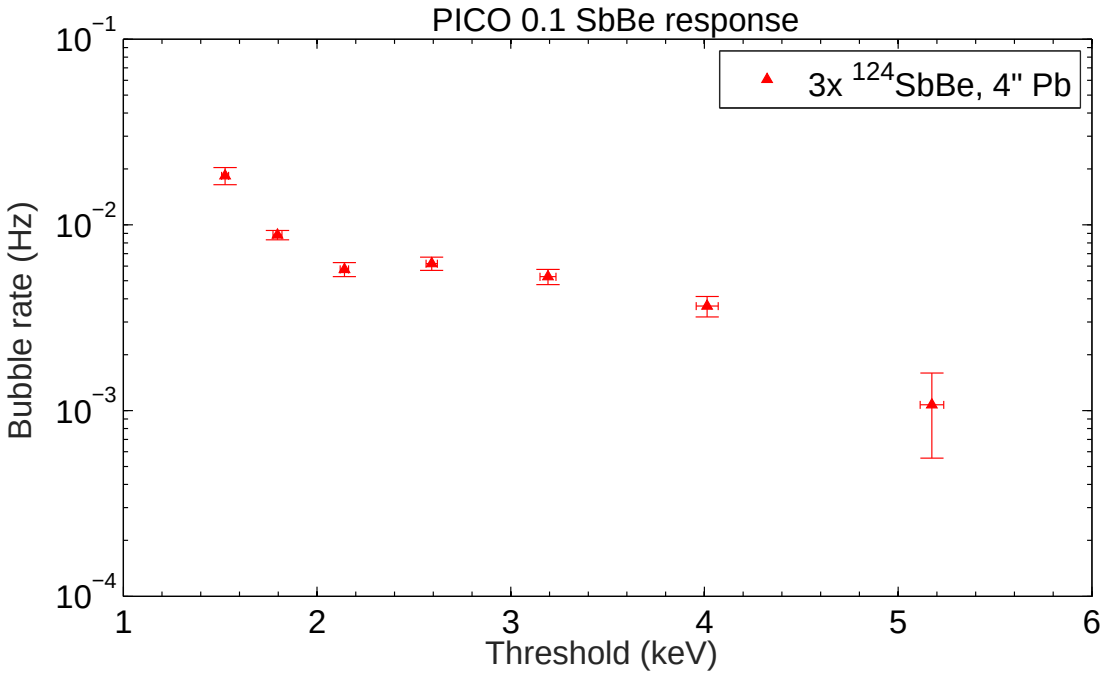

Figure 4.24: SbBe bubble rate as a function of threshold energy. Background and γ response are subtracted.

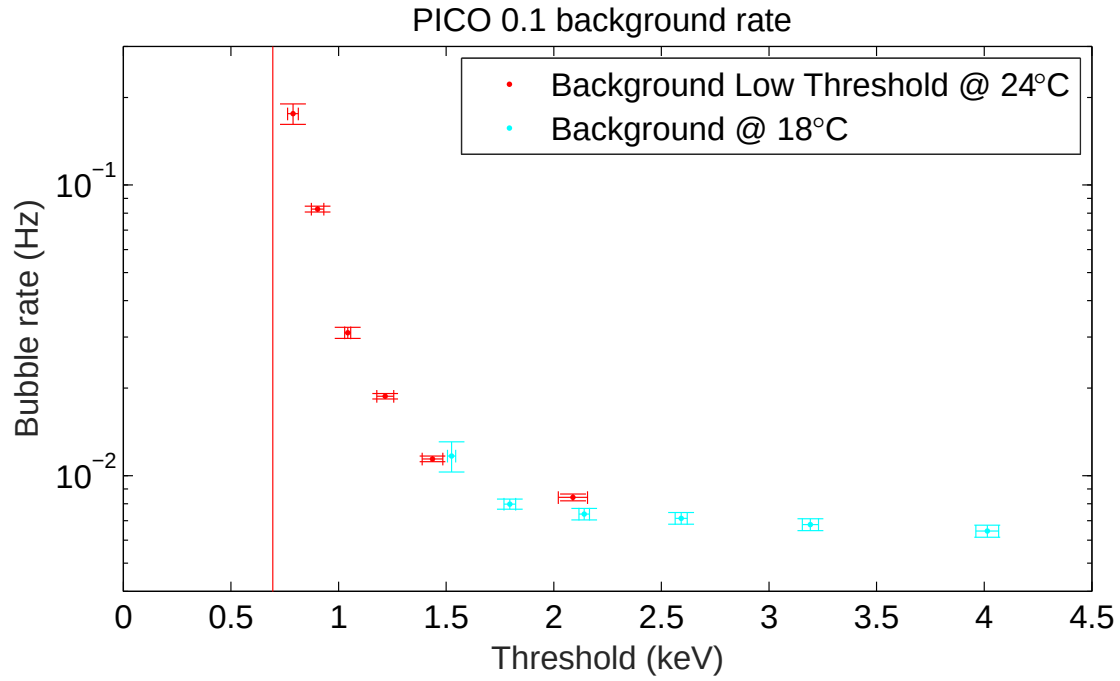

Figure 4.25: Low threshold background rate. The red vertical line is the error-bar of a low statistics data point at $E_{th} = 0.7$ keV.

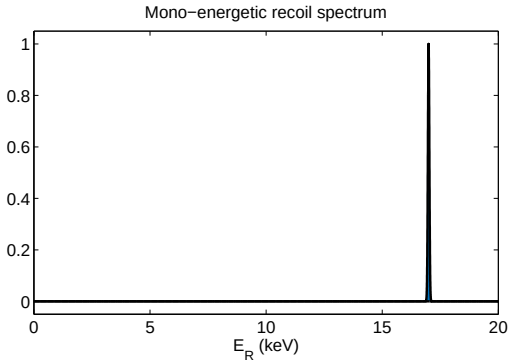

Figure 4.26: Mono-energetic recoil spectrum.

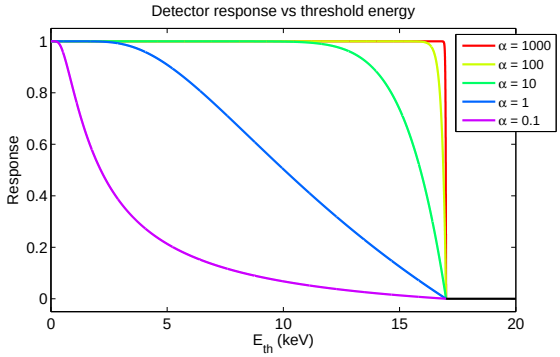

Figure 4.27: Effect of the α parameter on the mono-energetic recoil response. As α tends to infinity, the response becomes box shaped.

4.3.5 C_2ClF_5

During summer 2016, the C_3F_8 fill of PICO-0.1 was ended after more than two years of operation. The chamber was disassembled to be washed and re-filled with a different freon: C_2ClF_5.

The motivation to use this liquid was to study the nuclear reaction $^{35}Cl(n_{th},p)^{35}S$. In this reaction, a thermal neutron ($E_n \approx 0.025$ eV) interacts with the Chlorine atoms of the active fluid, producing a proton with an energy of about 600 keV and a sulfur atom with an energy of 17 keV. The proton deposits less than 1 keV in the critical radius. This reaction allows to measure the mono-energetic 17 keV recoil of sulfur atoms in the liquid and to compare with Monte Carlo simulations of the detection process.

The recoil spectrum of the $^{35}Cl(n_{th},p)^{35}S$ reaction should be mono-energetic as shown in Figure 4.26. Assuming 100% nucleation efficiency, the response of a bubble chamber to mono-energetic recoils is box shaped, as presented in Figure 4.27. In reality, the nucleation probability is described by equation 3.5 and the count rate by equation 3.6, depending on the free parameter α. Measurement of the count rate can therefore inform on the value of the α parameter. Furthermore, Monte Carlo simulations of the total nuclear damage cascades compared with the experimental data could allow for the determination of the Harper parameter of equation 3.4.

For the measurement with PICO-0.1, thermal neutrons were produced with the ^{124}SbBe neutron source as some of the 24 keV neutrons are thermalized in the thermal water bath of the bubble

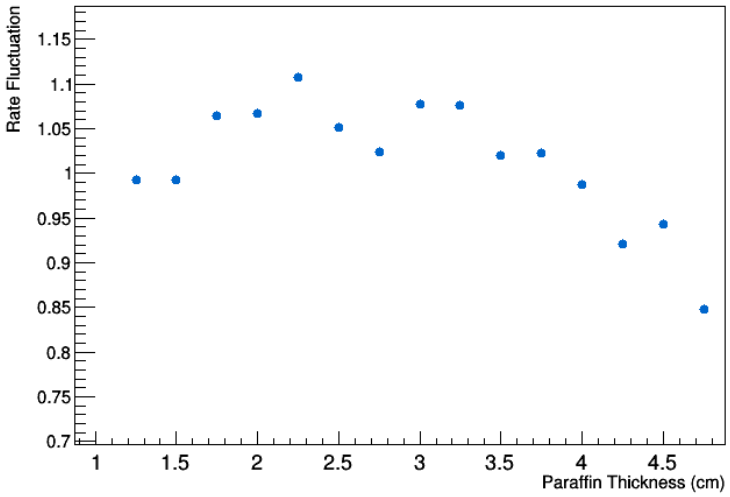

Figure 4.28: Rate fluctuation as a function of paraffin thickness. Error bars are too small to show on the plot.

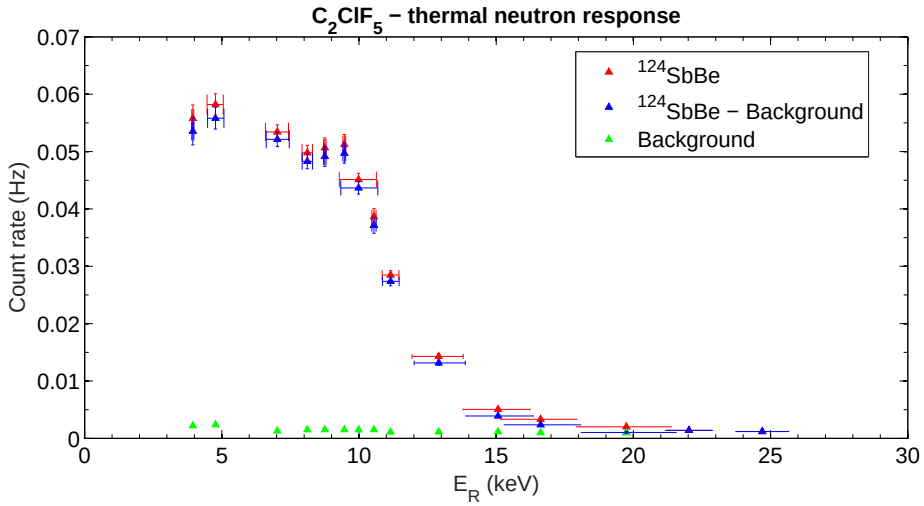

Figure 4.29: C_2ClF_5 - count rate from sulfur recoils. Thermal neutrons interact with the chlorine by the $^{35}Cl(n_{th},p)^{35}S$ nuclear reaction.

chamber. To further increase the thermal neutron flux, a paraffin disk was placed between the chamber and the source. A MCNP simulation performed by Olivia Scallon (Figure 4.28) showed that a 2.25 cm paraffin thickness maximizes the thermal neutron flux, increasing it by a factor 30. Given its relatively weak activity, the source was again placed inside the water channel of the thermal bath, as close to the chamber as possible.

Figure 4.29 shows the count rate as a function of the threshold energy. Data were taken over a

three-month period, during which both ^{124}SbBe and ^{124}Sb (background) data were taken for a total exposure of 22.35 live-days. Most of the early runs were excluded from the data-set as chambers go through an adaptation period following a new fill. No lead shielding was used to shield γ radiation as the threshold energy was set outside the γ sensitive zone ($E_{th} < 3\,keV$).

From this preliminary result, it is clear that the nucleation efficiency is not 100%, as the response of the detector is not box shaped as expected, but smoother. An in dept analysis with Monte Carlo simulations is required to interpret the data, possibly constraint the alpha parameter for this response and the Harper parameter (b) present in the determination of the critical length. An acoustical analysis can also be performed to possibly discriminated the nucleation from the emitted proton to that of the sulfur recoil.

CHAPTER 5

^{51}V TARGET - ABSOLUTE NEUTRON FLUX MEASUREMENT

The second original work part of this thesis is a measurement of the absolute neutron flux from a vanadium target and the determination of two ^{3}He neutron counter efficiencies. The measurement was performed during summer 2015. Count rates during neutron calibration are usually normalized with the neutron count rate of one or two ^{3}He neutron counters, to correct the response of PICO-0.1 for fluctuations in the neutron flux. The absolute flux measurement allowed, for the first time, to put a number on the neutron flux produced by the ^{51}V target and to measure the efficiency of the ^{3}He neutron counters precisely, making Monte Carlo simulations more precise. This measurement is important for PICO-0.1 calibrations as it determines very precisely the efficiency of both neutron counters. The results presented in this chapter are to be published in a future PICO calibration paper.

The measurement was done by activating a new ^{51}V target with the proton beam at the 50 keV resonance of the ^{51}V(p,n)^{51}Cr nuclear reaction. The activity of the metastable ^{51}Cr was then calculated from a High Purity Germanium detector (HPGe) measuring the 320 keV gammas emitted from the target. A careful reconstruction of the target activation as a function of time allowed to determine the total number of neutrons produced over the activation period, and correspondingly the absolute neutron flux and the efficiencies of the ^{3}He neutron counters.

In this chapter, the experimental method is detailed in section 5.1, followed by the description of the HPGe detector in section 5.2. Finally, the data recorded are presented in section 5.3, along with a measurement of the angular distribution of the produced neutrons in section 5.4. The final results are presented in section 5.5.

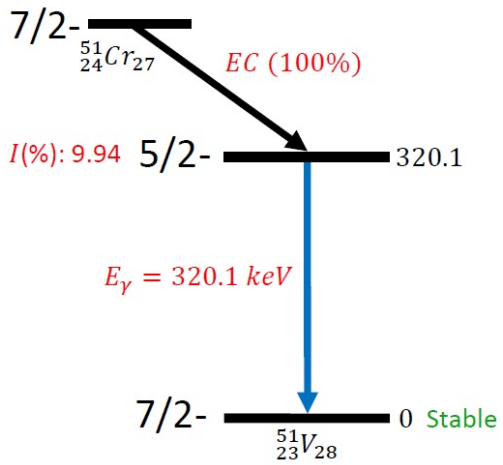

Figure 5.1: ^{51}Cr decay scheme.

5.1 Method

The integrated neutron flux is obtained by counting the number of ^{51}Cr atoms, produced with the emission of a neutron, in the ^{51}V target. ^{51}Cr disintegrates into ^{51}V via electron capture with a half-life of 27.7010±0.0011 days [75]. Figure 5.1 shows the decay scheme of ^{51}Cr. 9.910±0.010% of the nuclei are in a metastable state J^n = 5/2- and decay to the J^n = 7/2- ground state by emission of a 320 keV γ-ray. Therefore, measurement of the gamma activity allows the determination of the number of chromium atoms produced during the activation, which equals the number of emitted neutrons.

Since the vanadium target used for calibrations had been periodically irradiated over the years (especially over the last few months before the measurement) it was decided to perform the experiment on a new target, produced at the same time as the first one, in order not to start with a target containing an unknown quantity of ^{51}Cr.

The Chromium activity was then recorded with a p-type HPGe detector in a low background environment, deep in the hill-side, shielded by massif concrete. The end cap of the detector was shielded with lead bricks to further reduce environmental background radiation. A calibrated ^{133}Ba standard source was acquired to calibrate the energy response and the efficiency of the HPGe detector. Following activation, the target was put in a plastic container filled with nitrogen gas,

then placed in the lead shield at the same distance as the ^{133}Ba source was. The distance was kept fixed for all measurements. The data acquisition by the HPGe detector lasted up to 48 hours, and it was found that a 24-hour run was sufficient to get a small enough statistical error.

To analyze the data, an algorithm was developed to subtract the background and integrate the count rate of the γ-peaks. Data were then fitted by exponential decay law to calculate the activity of the target right after the activation. Using these activation data, the reconstructions of the chromium production and decay rates during the activation, which corresponds to the total number of neutrons produced, were performed. Dividing this number by the duration of the activation runs gives a measure of the absolute neutron flux.

5.2 HPGe detector

The HPGe detector employed for this measurement is shown in Figure 5.2 and Figure 5.3 with a lead shielding. It is a P-type, side-mounted detector built by *Princeton Gamma Tech* (PGT). The detector is kept at 77 K in liquid nitrogen (LN_2) since it was acquired by the lab, but hadn't been used recently. Therefore, it was necessary to perform a proper energy and efficiency calibration.

5.2.1 Detector design

A HPGe detector is typically composed of a highly-purified germanium crystal, a preamp stage and a cryostat.

Germanium crystals in HPGe detectors can be conceived in several configurations. The one used for this measurement is a coaxial, P-type (using holes as charge carriers) crystal with a lithium-diffusion N+ contact layer [76]. In addition, an ion implanted P+ contact was produced. A bias voltage applied to the crystal by an external power supply creates a depletion zone in the crystal, increasing the resistance of the p-n junction region.

The fact that the detector is somewhat old and may be fragile prevented the opening the end cap. The actual crystal size and shape could therefore not be directly determined. Even without precise knowledge of the detector geometry, the efficiency and solid angle could be determined by precise

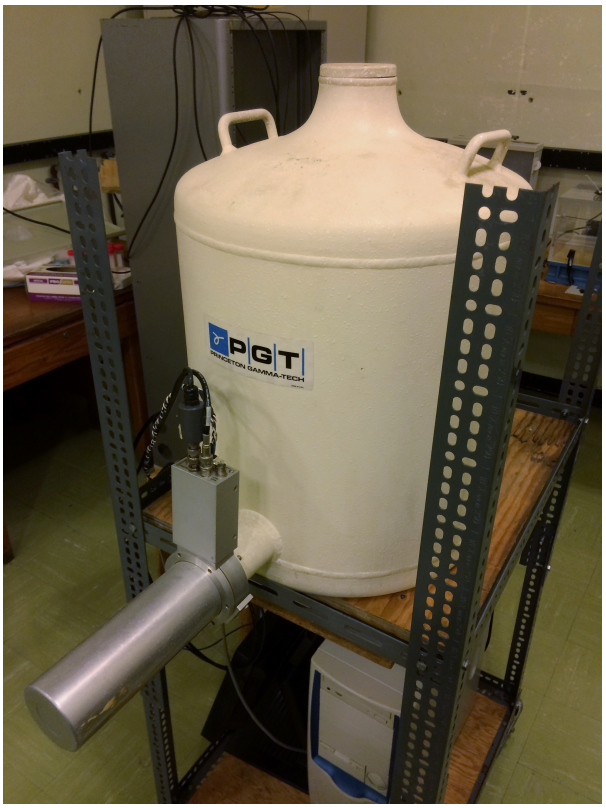

Figure 5.2: Side looking, P-type HPGe detector.

Figure 5.3: HPGe detector shielded with lead bricks.

source positioning during calibrations and measurement, and a systematic error was included in the error propagation. In this case, the detector efficiency was determined with a source placed 9.5 cm away from the detector.

When a photon interacts in the crystal, a charge displacement current is produced. When the interaction is by photoelectric effect, the charge is proportional to the energy of the incident gamma. Some other electromagnetic effects can result in partial energy deposition of the primary photon, such as Compton scattering and pair production. Compton scattering is inevitable, but can be manageable by either collimation of the source (to reduce the number of scattering photons reaching the crystal) or putting it at a greater distance from the crystal to reduce the solid angle from the source to the crystal. Pair production can only happen with a photon of energy equal or higher than the electron-positron pair rest mass of 1.022 MeV. The present measurement doesn't involve such photons, and thus this effect can only come from environmental background.

The pre-amplifier stage is part of the end cap assembly. Its function is to convert the collected charge to an analog signal with proportional amplitude. A simple pulse shape analysis confirmed that the pulses were Gaussian shaped, which could thereafter be directly analyzed by a *Canberra Model 1510* Integrated Signal Processor. This module uses an analogue-to-digital converter (ADC) to sort gamma energies in 2048 bins of a multichannel analyzer and also provides the bias voltage for the pre-amplifier of the HPGe detector. Although rated for 3.5 kV, the maximum bias voltage that could be applied to the detector was 900 V. This leads to the assumption that some of the lithium had diffused, in which case there should be a loss of efficiency, but no loss in resolution, as detailed in section 5.2.2.

Germanium is a semi-conductor which has a small bandgap energy at high (room) temperature. Therefore, the crystal needs to be cooled to LN_2 temperature to limit the high leakage current generated at higher temperatures. Furthermore, the lithium contact layer can diffuse and redistribute itself in the Ge crystal at room temperature, which could lead to a loss of efficiency. The crystal is, therefore, in contact with a metal rod called "cold finger" which allows heat transfer from the crystal to the LN_2. A Dewar, a vacuum-sealed container, holds the LN_2 and needs to be refilled periodically (e.g., weekly or biweekly depending on the size of the Dewar).

5.2.2 Calibration

The energy response and efficiency of the HPGe detector were calibrated with a 1.036 μCi ^{133}Ba calibration source (Figure 5.4). It emits five main gamma lines, tabulated in table 5.I, four of which have an energy near the 320 keV γ-line of ^{51}Cr. Due to higher background level and drop of efficiency below 100 keV, the gamma peak *I* at 80 keV was not included in the analysis, even though this peak has very good statistics. The spectrum of the source used is shown in Figure 5.5.

As mentioned in the previous section, not knowing the precise dimensions of the HPGe detector, it was decided an additional calibration would be performed instead of the standard ^{60}Co calibrated at 25 cm. Knowing that the 320 keV emission of ^{51}Cr would be rather weak, the solid angle was maximized with respect to the crystal to increase statistics. The calibration source was

Figure 5.4: ^{133}Ba source for calibration of the HPGe detector.

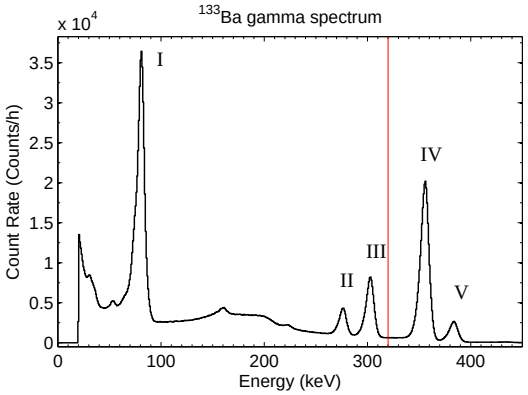

Figure 5.5: Experimental ^{133}Ba gamma spectrum. The red line indicates the 320 keV of ^{51}Cr relative to the spectrum of the calibration source.

Gamma No.	Energy (keV)	Branching ratio (%)
I	80.9979 (11)	32.9 (3)
II	276.3989 (12)	7.16 (5)
III	302.8508 (5)	18.34 (13)
IV	356.0129 (7)	62.05 (19)
V	383.8485 (12)	8.94 (6)

Table 5.I: Table of ^{133}Ba main gamma radiation energies and branching ratios. Numbers in parenthesis are the error on the last digits [75].

placed at 9.5 cm, centered, in front of the detector. All measurements were taken inside the lead shield.

The energy calibration was performed using raw data. The energy spectrum was stored in the multichannel analyzer with 2048 channels. A simple peak finding algorithm was used to identify the five main γ-lines. A linear fit with least squares minimizing function from MATLAB was then performed convert bins to energy. Figures 5.6 and 5.7 show the calibration plot and the calibrated spectrum.

The same ^{133}Ba spectrum was used to calibrate the efficiency of the detector with the source placed at 9.5 cm. To do this the line intensity was found by integrating the peak area and by subsequently subtracting the extrapolated background from a linear extrapolation from data points outside the peak region. Figure 5.8 give a visual representation of the background subtraction.

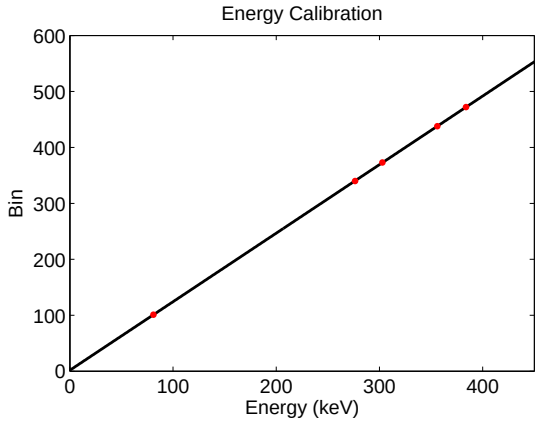

Figure 5.6: HPGe detector calibration plot. The black line is the calibration fit, red points are the measured bins of the peaks as a function of the theoretical energy.

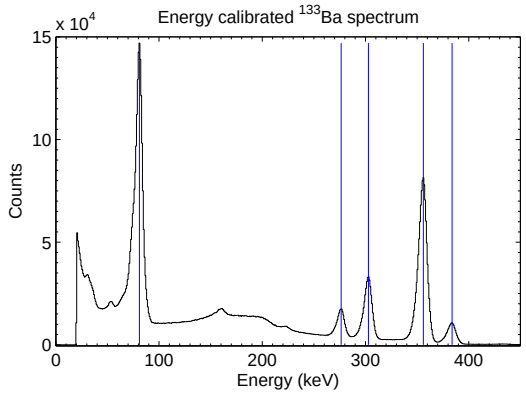

Figure 5.7: Energy calibrated ^{133}Ba spectrum. Blue lines indicate the theoretical energy of each peak.

The integrated peak count rates were then related to the source activity by correcting with the tabulated branching ratios. The final efficiency is then given by by equation 5.1:

$$\varepsilon_{\gamma i} = \int_{E_{min}}^{E_{max}} R(E_i)\mathrm{d}E \cdot (A_{Ba} \cdot BR_i \cdot 3600\,s)^{-1} \tag{5.1}$$

where $R(E_i)$ is the count rate of peak i as a function of energy, A_{Ba} is the activity of the calibration source, BR_i is the branching ratio of peak i. The four efficiencies were then fitted with a second degree polynomial function to obtain the efficiency at the 320 keV γ line of ^{51}Cr. Figure 5.9 shows the efficiency curve in the region around 320 keV.

The errors of this measurement include the error on the branching ratios (~ 0.3 %), the statistical error ($\sqrt{N}$), the error on the activity of the calibration source quoted by the manufacturer (3.1 %), an error on the calibration source position relative to the crystal (2 %). Finally, the efficiency of the HPGe detector obtained from the fit at the 320 keV γ-line is 0.248 ± 0.011 %.

5.3 Data recording

The data acquired during this measurement can be categorized in two sets: data from the ^{3}He neutron counters during the irradiation of the target and data from the counting of the activity of

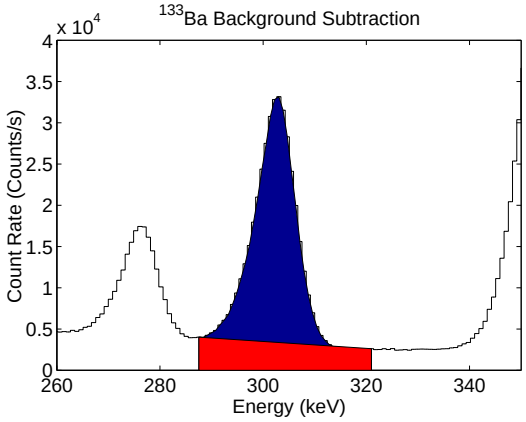

Figure 5.8: Peak integration and background subtraction. The blue surface represents the peak integration. The red surface represents the background signal, found by linear extrapolation, to be subtracted.

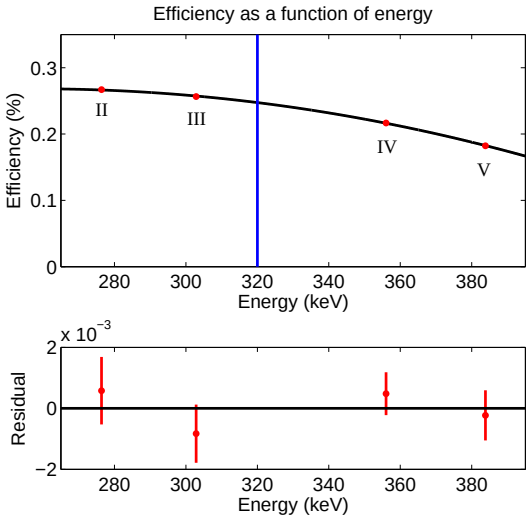

Figure 5.9: *Top*: Efficiency fit of the HPGe detector in the region of interest. Red points are the measured values of the four ^{133}Ba gamma peaks. The blue line represents the 320 keV γ-ray line of ^{51}Cr. *Bottom*: Residual plot.

the target with the HPGe counter.

5.3.1 Neutron counting during the target irradiation

The data described in this section was used to relate the neutron counts in the two ^{3}He counters to the target activation. It has also been used to correct for the disintegration of ^{51}Cr during the activation period.

The target activation was performed from May 4th to May 7th 2015. The overall activation time was 56.07 hours at a mean proton current of 3.5 μA. In order to preserve the same neutron yield, PICO 0.1 was placed in front of the beam line in the same position as during calibration runs. Also, both ^{3}He neutron counters were positioned as in the usual calibration runs with the chamber. Data were recorded automatically during each activation run with a National Instruments acquisition card controlled by a homemade LABVIEW program.

In order to find the correct resonance, as mentioned in section 4.2.4, the spectrum was scanned in small increments of the magnetic field of the energy analyzing magnet. Since the present mea-

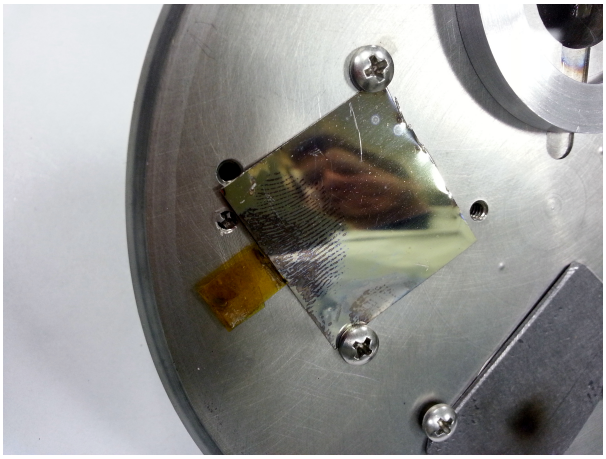

Figure 5.10: Vanadium target before activation. The thumbprint is a relic occurring after the vapor deposition of ^{51}V.

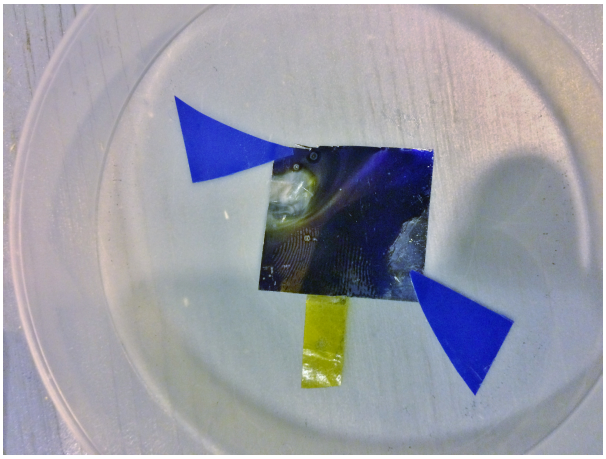

Figure 5.11: Vanadium target after activation. Notice the blackening due to the heat generated by the high proton current.

surement was performed with a new target with mono-energetic neutrons, an old target was used to locate the 50 keV resonance, leaving the new one intact until the beginning of the first activation run (Figure 5.10). Figure 5.11 shows the same vanadium target after the activation. The darkening is caused by the heat generated by the proton beam. The silver colored spot to the left is the irradiation spot.

In total, during this irradiation the U-Montréal neutron counter recorded $(21017 \pm 6) \cdot 10^2$ neutrons and $(522 \pm 3) \cdot 10^3$ neutrons were counted by the U-Chicago counter. Respectively, the total accumulated proton charge was 11818.8 ± 0.1 μC. Figure 5.12 shows the accumulated neutrons as a function of time for the whole activation period. It was known that in this geometry, due to the proximity to the beam line, the U-Montréal counter detects more neutrons than the U-Chicago counter. This was confirmed by an additional measurement with a neutron source placed at the same distance from both counters. This confirmed that the U-Chicago counter is 17x more sensitive than the U-Montréal one.

5.3.2 Determination of the ^{51}Cr activity

The data described in this section was included in the calculation of the total activity of the target after the activation. This activity, corresponding to the total number of neutrons produced,

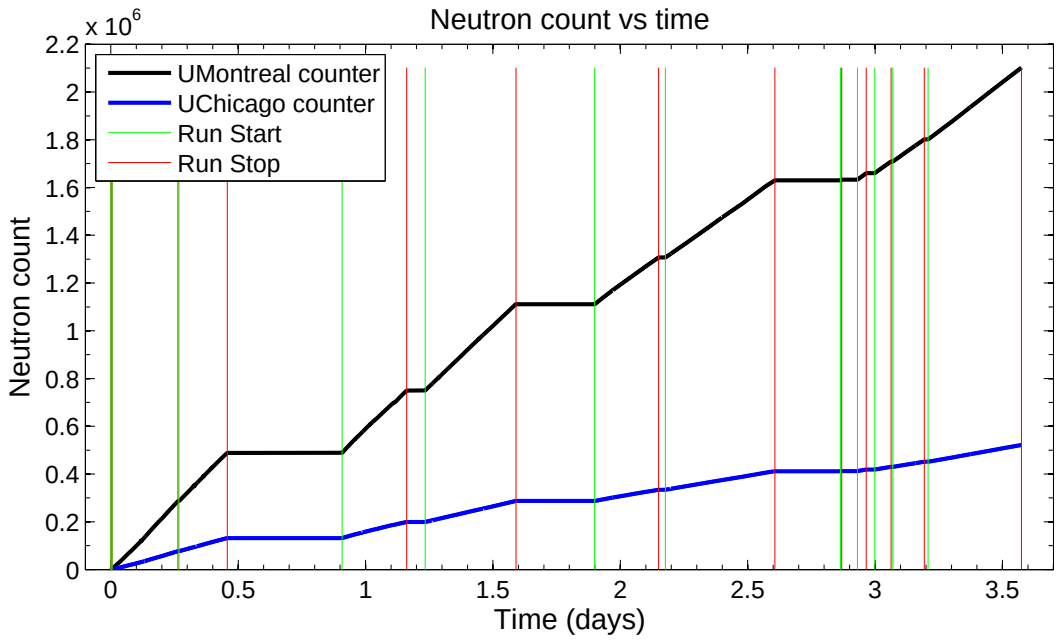

Figure 5.12: Neutron counts as a function of time. Green vertical lines mark the start of a new beam run, red vertical lines mark the end of the run. The U-Montréal counter recorded a much higher number of neutrons because of its proximity to the target.

was then compared with the ^{3}He count rates to calculate the neutron counter efficiencies.

After activation, the vanadium target was stored in a plastic container in nitrogen atmosphere and data recording in front of the HPGe counter was carried out with the target 9.5 cm away from the HPGe detector.

Measurements were taken over a period of over 60 days, shortly interrupted by ^{133}Ba calibration and background runs to ensure that the experimental conditions were stable. Due to the low activity of the source, ^{51}Cr runs were 24h long in average to acquire sufficient statistics. Overall, 15 spectra were recorded in the same geometry. Figure 5.13 shows a typical ^{51}Cr spectrum, while Figure 5.14 represents a background spectrum. Note the 320.08 keV peak from the ^{51}Cr.

5.4 Angular distribution of neutrons

While the measurements were ongoing with the HPGe, an attempt was made to replicate the results from [70] regarding the angular isotropy of the neutrons emitted in the ^{51}V(p,n)^{51}Cr reaction. To do so, the U-Chicago neutron counter was placed at a constant distance from the target

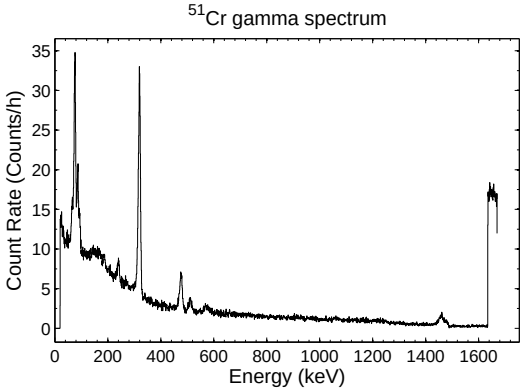

Figure 5.13: ^{51}Cr gamma spectrum. (320.08 keV)

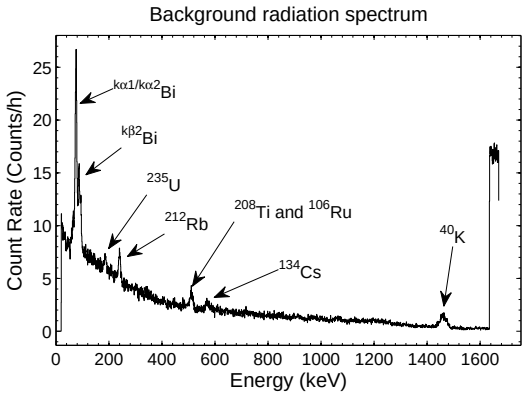

Figure 5.14: Background radiation gamma spectrum. Peak identification from [77].

holder, at various angles with respect to beam line axis. The U-Montréal neutron counter was kept at a fixed position 90° below the target holder for flux normalization.

As seen in Figure 5.15, the normalized response for the 50 keV resonance is far from being flat, as opposed to the results of [70]. For large angles (> 45°), the stainless-steel flange and the plastic ring of the source holder are in the trajectory of neutrons to the neutron counter. The neutron interactions in the flange were previously neglected, but this measurement showed that it had to be included in Monte Carlo simulations. Figure 5.16 shows the same measurement for the 40 keV resonance.

Without a Monte Carlo simulation, no direct correction for the absorption can be made as the absorption should be energy dependent. Finally, since the U-Montréal neutron counter is always located underneath the source holder, the total neutron count is always affected by the flange absorption. This means that it can't be trusted for the absolute flux measurement, as the absorption is energy dependent, but it is still reliable for normalizing beam data at given beam energies.

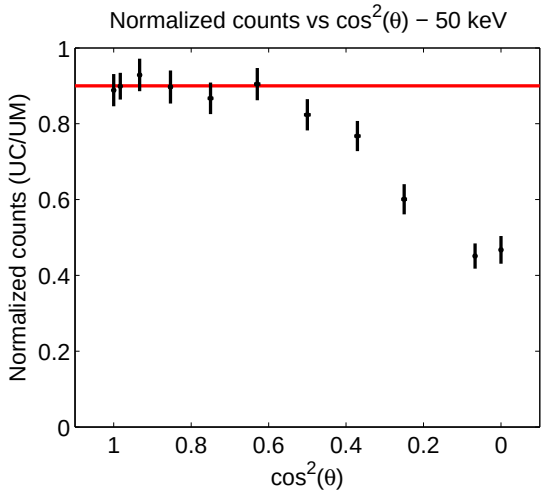

Figure 5.15: Angular response of the U-Chicago neutron counter on the ^{51}V 50 keV resonance. The red line is the expected response from [70].

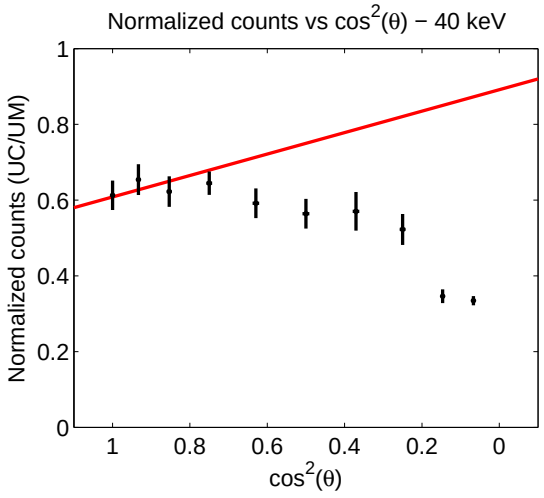

Figure 5.16: Angular response of the U-Chicago neutron counter on the ^{51}V 40 keV resonance. The red line is the expected response from [70].

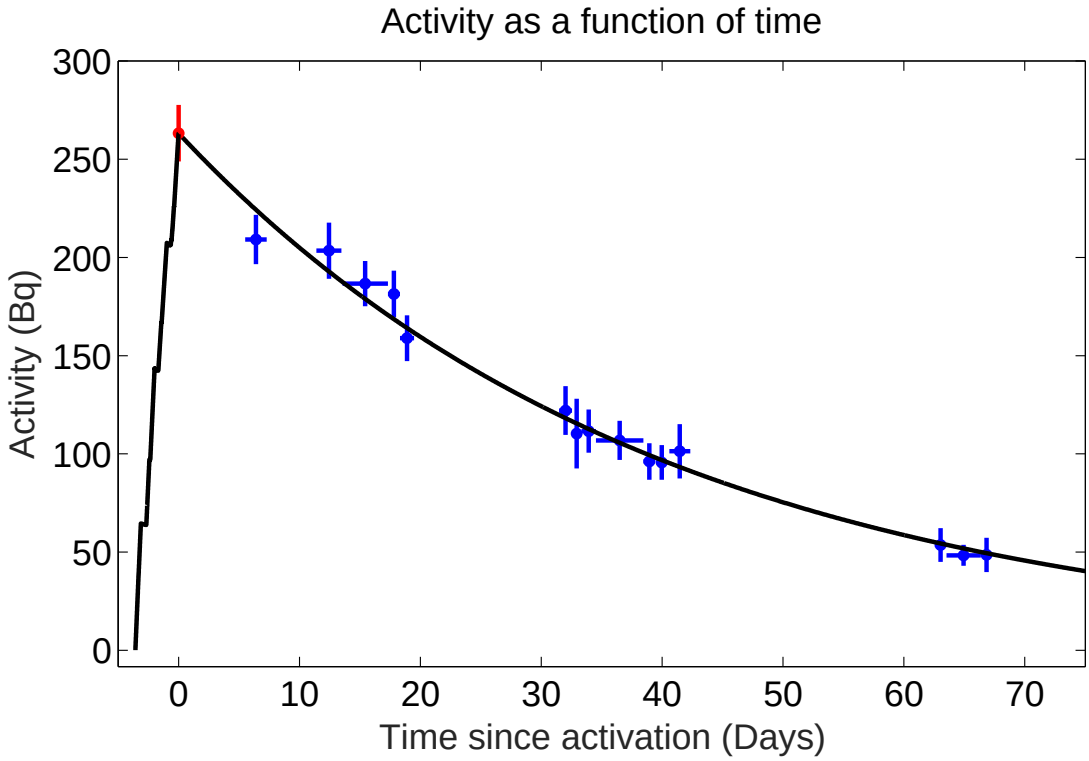

Figure 5.17: Activity of the target as a function of time. The blue points are data obtained from the HPGe counter. Vertical error-bars account for statistical and systematic errors. Horizontal error-bars are the total elapsed time of each runs. The red point is initial activity determined by the fit.

5.5 Results

The number of gammas detected per runs is obtained from the HPGe counter data. The activity of the target can be determined for each data point with the equation:

$$A_i = \frac{N_i \cdot \varepsilon_{320\,keV}}{t_i} \tag{5.2}$$

where A_i is the activity of the i^{th} data point, N_i is the number of counts of the i^{th} data point, $\varepsilon_{320\,keV}$ is the intrinsic efficiency of the HPGe detector at 320 keV (accounting for the geometry), and t_i is the duration of the i^{th} run.

Since the phenomenon observed is a nuclear decay, the data was fitted with :

$$A = A_0\, e^{-t/\tau} \tag{5.3}$$

where A is the activity of the target for every data point, A_0 is the activity at t_0 (referred to as the initial target activity), t is the time. The decay time constant is $\tau = ln(2) \cdot t_{1/2}$ and $t_{1/2}$ is the half-life. For ^{51}Cr, the half-life is 27.7010$\pm$0.0011 days [75]. The fit was performed in ROOT with the MINUIT package. The free parameter A_0 was found by a least square fit to be to be 263.3$\pm$14.4 Bq. The fit is shown in Figure 5.17.

The initial activity A_0 allows us to determine the total number of neutrons produced by simulating the activation. Using the relative neutron production rates from the ^{3}He counters, the exact neutron production rates needed to get the calculated initial activity A_0 were found, assuming the target wasn't active prior to the activation. Since the activation wasn't instantaneous, decay of ^{51}Cr during the irradiation period had to be accounted for. The result of this calculation is displayed in Figure 5.18.

From the simulation, the total number of neutrons produced during the activation is $(9.52 \pm 0.52) \cdot 10^8$ neutrons. With this number, the efficiencies of both ^{3}He counters could be determined

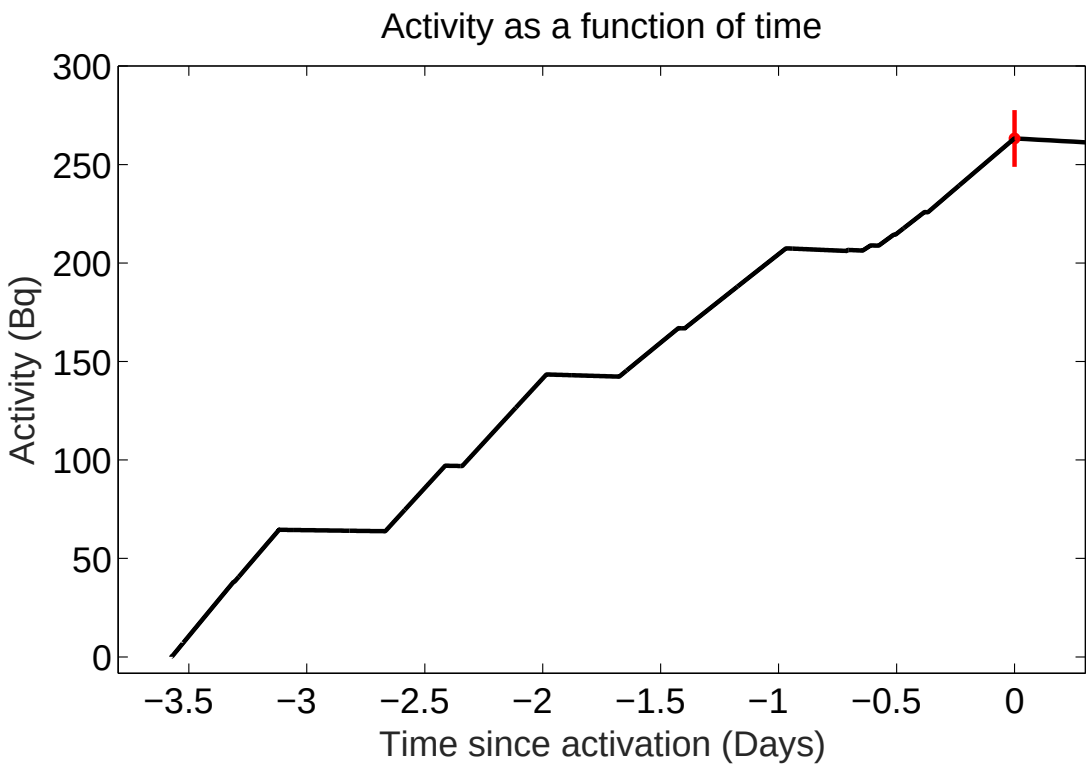

Figure 5.18: Activation curve of the Vanadium target. This simulation allowed to determined the total neutron production by adjusting the production rate of each runs according to the relative rates from the ^{3}He neutron counters. The red point is initial target activity determined by the activity fit. Prior to the activation, the activity of the target is assumed to be zero.

^{3}He counter	Neutrons counted	$\varepsilon_{^3He}$	$\frac{\varepsilon_{^3He}}{\varepsilon_{MC}}$
U-Montréal	2102712	$5.48 \cdot 10^{-4}$	0.706 ± 0.038
U-Chicago	521605	$2.21 \cdot 10^{-3}$	1.2443 ± 0.059

Table 5.II: Table of neutron counters efficiencies determined from the total neutron production.

with equation 5.4

$$\varepsilon_{^3He} = \frac{N_{^3He}}{N_{tot}} \tag{5.4}$$

where $\varepsilon_{^3He}$ is the efficiency of an ^{3}He neutron counter, $N_{^3He}$ is the number of neutrons counted by the respective ^{3}He counter (Figure 5.12) and N_{tot} is the total amount of neutrons produced. The efficiencies are tabulated in the 3^{rd} column of table 5.II. Once the efficiencies are calculated, they can be compared to the efficiencies obtained from the Monte Carlo simulations. These results are shown in the 4^{th} column of table 5.II.

As mentioned in section 5.4, the stainless-steel flange absorption make the simulation of the

U-Montréal neutron counter difficult and uncertain. Consequently, Monte Carlo simulations overestimate its efficiency. However, the U-Chicago neutron counter is unobstructed, sitting directly in front of the target holder, at almost 0° and the measurement showed that the Monte Carlo underestimated the neutron count. This must be investigated by future simulations.

CHAPTER 6

DEVELOPMENT OF COATED PMMA INNER VESSELS

The final research topic covered in this thesis is the development of coated Poly-methyl-methacrylate (PMMA) inner vessels in bubble chambers.

The bubble chamber technology is now over 60 years old. A lot of technological innovations were integrated over the years, from the first hydrogen chamber to today's state of the art, low threshold chambers. In 1973, B. Hahn and H. W. Reist proposed a new type of bubble chamber nicknamed "the Geyser" [78]. It was designed to detect the rare spontaneous fission of ^{238}U in superheated alcohol. From the figure 6.1, the chamber was a simple glass round bottom flask with an elongated condensation neck. Bubbles produced would expand, sending liquid alcohol up in the neck, much like a Geyser. Geysers are also called "condensation bubble chambers" (CBC) and are now used in a dark matter direct detection experiments by the MOSCAB collaboration, in Milano, Italy [79–81]. The PICO experiment also showed interest in the technique, with prototypes built at the University of Alberta and at the Université de Montréal.

As part of the work for this thesis, the simplistic design of the Geyser was exploited to perform low cost testing of different inner vessel materials. Acrylic (PMMA) and plain glass vessels were considered. The background being dominated by wall nucleation, a preliminary study of surface coating was undertaken to mitigate the problem.

In this chapter, the concept of the condensation chamber is presented in section 6.1. A PMMA CBC design is described in section 6.2 and preliminary results of coating trials are presented.

6.1 The Geyser

The CBC is a detector using superheated liquids that does not require the manual or automatic re-compression of the chamber. Instead of using a hydraulic pressure system (as in PICO detectors), CBCs have two thermal regions (top and bottom), operated at different temperatures (hot

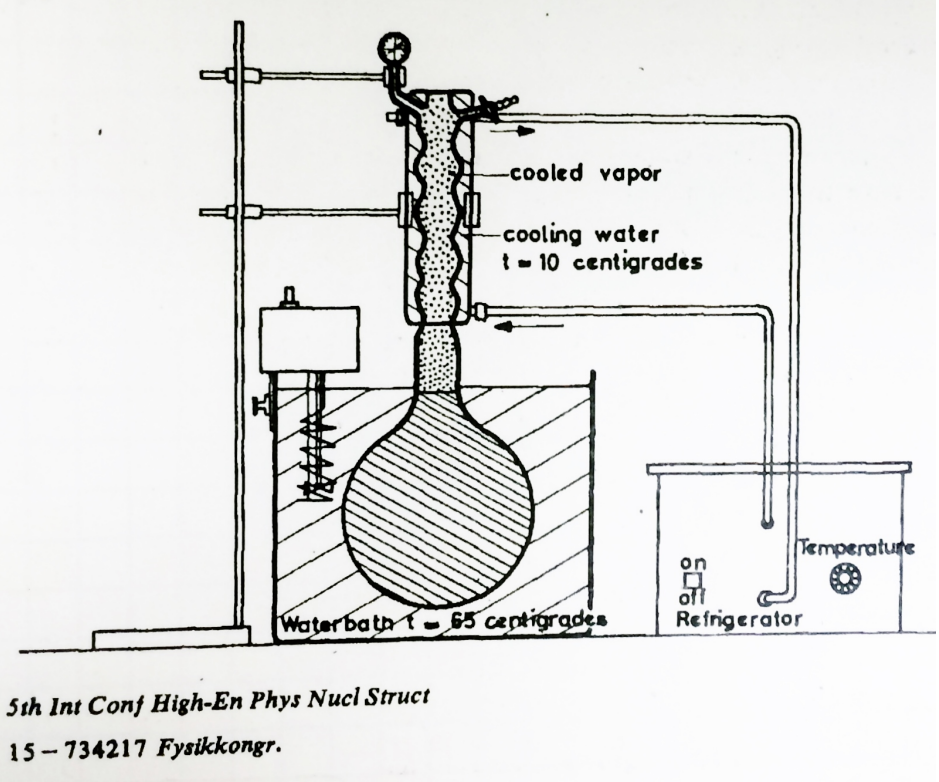

Figure 6.1: Original Geyser design [78]. The bulk is submerged in a warming bath while a refrigerant is circulated at the neck. Bubbles produced from nuclear recoils rise in the neck where vapors are condensed.

and cold). At the bottom of the chamber, a hot thermal bath keeps the active fluid (Alcohol, C_3F_8, C_5F_{12}, etc.) in a superheated state. The top part of the chamber is set below the boiling temperature (typically, as cold as possible) and only the vapor phase of the active fluid is in contact with the condenser. At equilibrium, the chamber is pressurized at the vapor pressure of the active fluid.

As seen in Figure 6.2, bubbles are allowed to expand freely in a CBC, as opposed to PICO chambers where bubbles are re-compressed as fast a possible to limit fluid displacement. When a bubble is produced in the bottom part of the chamber, the inner pressure of the chamber rises until there is equilibrium between the inner bubble pressure and the liquid pressure. Consequently, this raises the threshold of the chamber, rendering it inactive. The hot bubble then rises to the top of the chamber, fusing into the cold vapor phase zone where it condenses back to liquid.

An optional inner buffer fluid of lower density can be introduced to separate the top and bottom sections of the chamber. As in PICO chambers, it was observed that the use of a buffer fluid (Water,

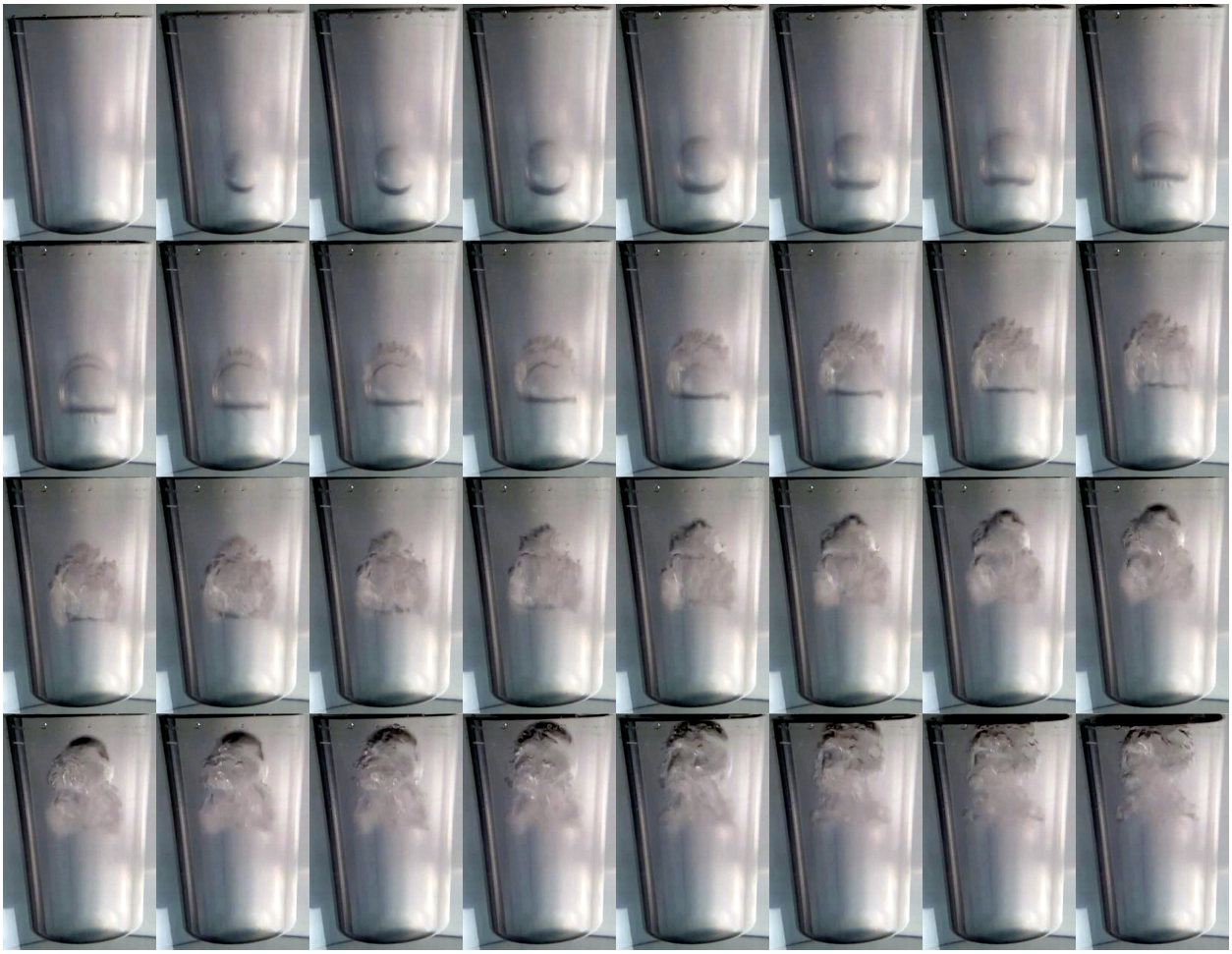

Figure 6.2: Bubble expansion in a Condensation Bubble Chamber. C_5F_{12} at 50 ˚C. Frame rate: 120 fps. Due to the low-pressure (approx. 6 PSIA), the bubble is already very large at the 2^{nd} frame. The bubble seems to reach its full size at the 5^{th} frame. The upward motion during the growth generates a low pressure zone underneath the bubble and fluid displacement flattens the underside of the bubble. The pressure equilibrium disrupts the surface of the bubble as the surface tension becomes insufficient for the bubble to keep a spherical shape.

glycol, LAB, etc.) increases detector stability [79] by limiting contact between the active fluid and the walls of the chamber. To keep the operating pressure as low as possible (to get a lower energy threshold), the choice of a buffer fluid with a low vapor pressure is favored. The choice of a fluid of higher viscosity can also help improve the active fluid-buffer interface stability during bubble nucleation.

CBCs present many advantages over traditional bubble chambers. First, the concept is mechanically simple, requiring no moving parts (no valves opening during runs, no bellows assembly) and

no active monitoring system (CCD cameras trigger) is required for operation. The detector is self controlled, requiring only two, off-the-shelf, circulation baths. Secondly, the active volume (bottom jar) can be increased virtually indefinitely, with no major modification to the detector design. Thirdly, the dead-time of this type of chamber is very small. Once the hot bubble is condensed at the top of the chamber, the pressure drops back automatically to the operating pressure and the chamber becomes active again, all in a matter of seconds. This increases the efficiency, which is beneficial for rare phenomenon observation. Lastly, CBCs can be produced and operated at low cost, which makes them ideal workbenches for testing and R&D.

6.1.1 Event characterization

As with PICO bubble chambers, the acoustic signature of bubbles can be recorded with piezoelectric sensors to characterize for the particle responsible for the nucleation. Pressure sensors are monitoring the inner pressure and a pseudo-3D reconstruction of events is done with CCD cameras to apply a fiducial cut.

In PICO bubble chambers, event cycles are characterized by controlled expansion and compression triggers, as explained in section 4.1. In a CBC, the pressure can't be controlled manually. The chamber is kept at its operating pressure, the vapor pressure of the active fluid at the temperature of the condenser. When a bubble is explosively produced, the pressure spontaneously rises to the equilibrium point, after which the growth of the bubble stops. If the chamber contains a buffer fluid, the bubble exiting the active zone will stop accreting liquid, stopping its growth earlier. The bubble rises up to the vapor region where it condenses in a matter of 15 to 20 seconds, lowering the pressure in the inner vessel gradually. When it reaches the operating pressure, the CBC is active again.

Figure 6.3 shows the pressure as a function of time of an active CBC. It is important to note that during the condensation period, in red in the figure, the nucleation threshold lowers continuously. If a particle were to deposit enough energy while the chamber is at a higher pressure, a bubble could still be produced although at much higher threshold. Even though the CBC is active during

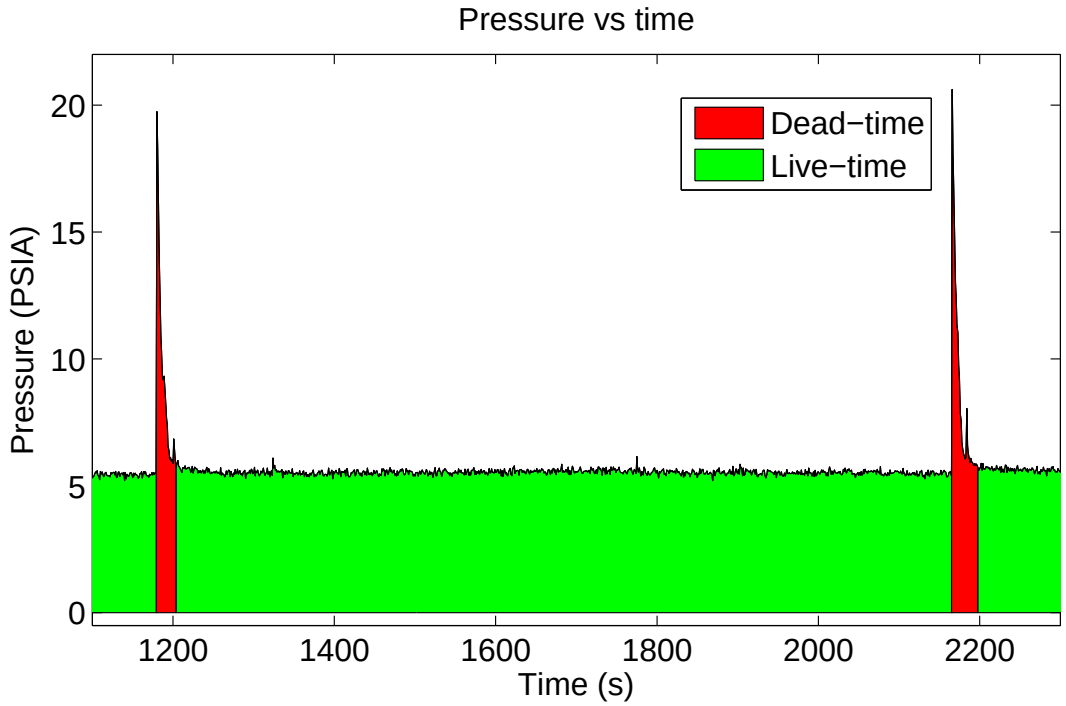

Figure 6.3: Event pressure pattern in CBCs. The red zones are considered as dead-time since the threshold is too high compared to the threshold at the equilibrium pressure. The green zones are live-time.

this period, the condensation period has to be considered a dead-time because of the uncertain threshold energy. The green zones are considered as live-time. The peak-pattern of CBCs allow for an easy event identification.

Chambers sometimes show repeated surface nucleation from hot spots, similar to the nucleation of carbon dioxide in carbonated drinks. In open systems, the overall pressure doesn't change. In CBCs however, this results in a global increase in pressure. Condensation and nucleation stay in equilibrium, rendering the chamber inoperable. Such a behavior can therefore be easily identified by the high pressure without a condensation phase as seen in Figure 6.4

6.2 PMMA CBC

This section describes a geyser prototype designed by Mathieu Laurin during his Ph.D. research [82]. This is the 6^{th} geyser designed at the Université de Montréal. This chamber was filled with C_5F_{12} so the Freon could be handled at room temperature, facilitating the filling. Linear

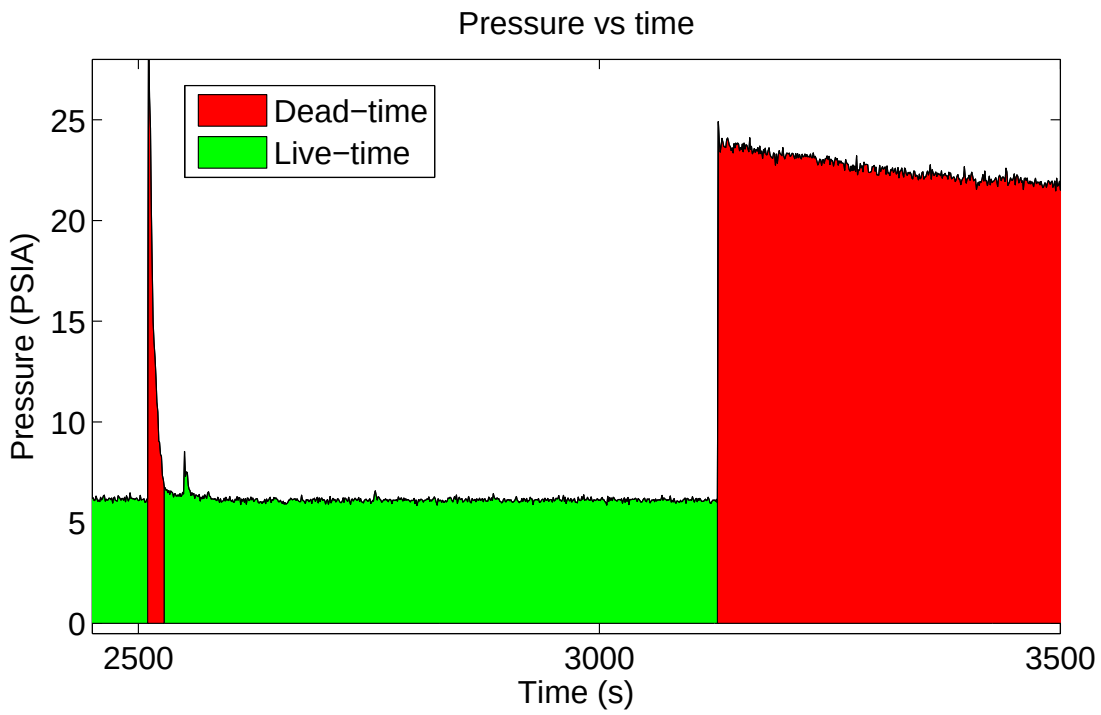

Figure 6.4: Boiling in CBCs.

alkylbenzene (LAB) was chosen as a buffer fluid to ensure that the Freon would be only in contact with the PMMA vessel. The choice of LAB was supported by the good behavior of the PICO-0.1 chamber with the same buffer fluid and its low vapor pressure, required for low pressure operation at higher temperature.

PMMA is an especially interesting material for the search for dark matter with bubble chambers. It is a radio-pure material and a neutron shielding due to its high concentration of hydrogen atoms. Chambers orders of magnitudes bigger could be built due to its ease of production and low production cost as demonstrated, for example, by the SNO, SNO+ and DEAP-3600 experiments at SNOLAB [83–85].

6.2.1 Detector design

Seen on Figure 6.5, the chamber is composed of a PMMA inner vessel (Figure 6.6) mounted on the stainless-steel main body by a metal flange. A rubber o-ring sits in a groove machined in the acrylic vessel to insure a good seal.

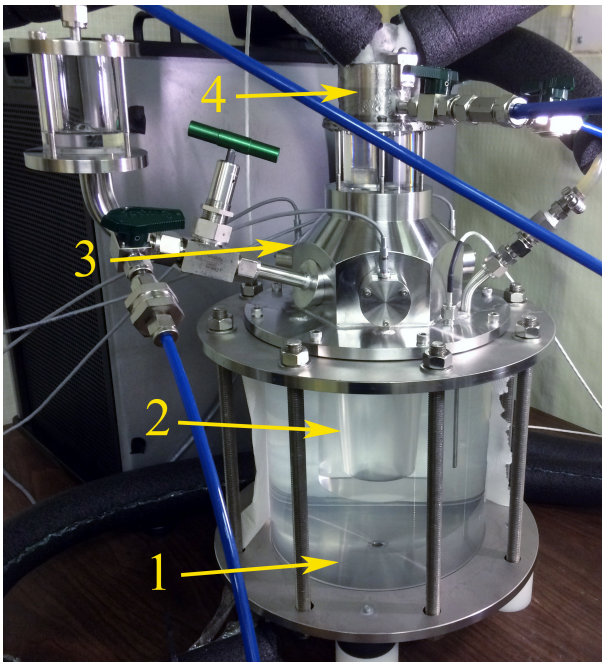

Figure 6.5: UdeM - Geyser 6. 1 - Heated thermal bath; 2 - PMMA vessel; 3 - Main stainless-steel chamber body; 4 - Stainless-steel condenser. A small hollow acrylic cylinder is located between those two parts to provide insulation between the cold condenser and the hot stainless-steel body, and to give visual access to the condenser.

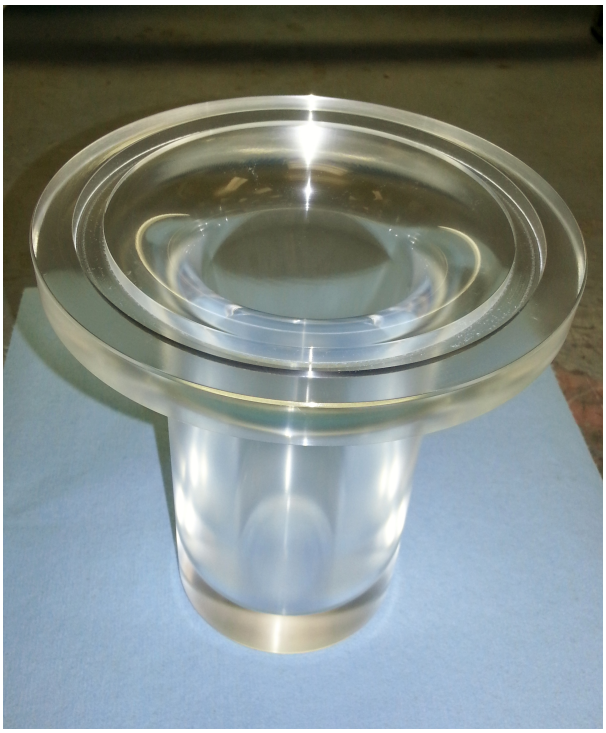

Figure 6.6: Geyser 6 - inner vessel. The vessel was custom-made at the Université de Montréal. The inside wall is machined at an angle to facilitate the rise of bubbles when they are produced near or at the wall.

The inside of the main body is hemispherical to minimize the presence of sharp edges. Three thin stainless-steel windows where piezo-electric sensors can be fixed are machined on the side faces. A round port also hosts the pressure sensor, which is in direct contact with the LAB buffer fluid.

When heated, both liquids (C_5F_{12} and LAB) dilate, increasing their volume significantly. Since it was noticed that bubbles have a smaller growth when the top vapor volume is smaller as the pressure in the chamber increases faster, an acrylic cylinder was installed under the condenser to facilitate fluid level adjustments. This part also serves as a thermal insulator.

The condenser is a hollowed out stainless-steel part where a refrigeration fluid circulates from a *PolyScience model PD15R-40* circulation bath. The part is shown in Figure 6.7. The underside of the condenser is conical. When the hot Freon vapor condenses on it, liquid droplets form on the

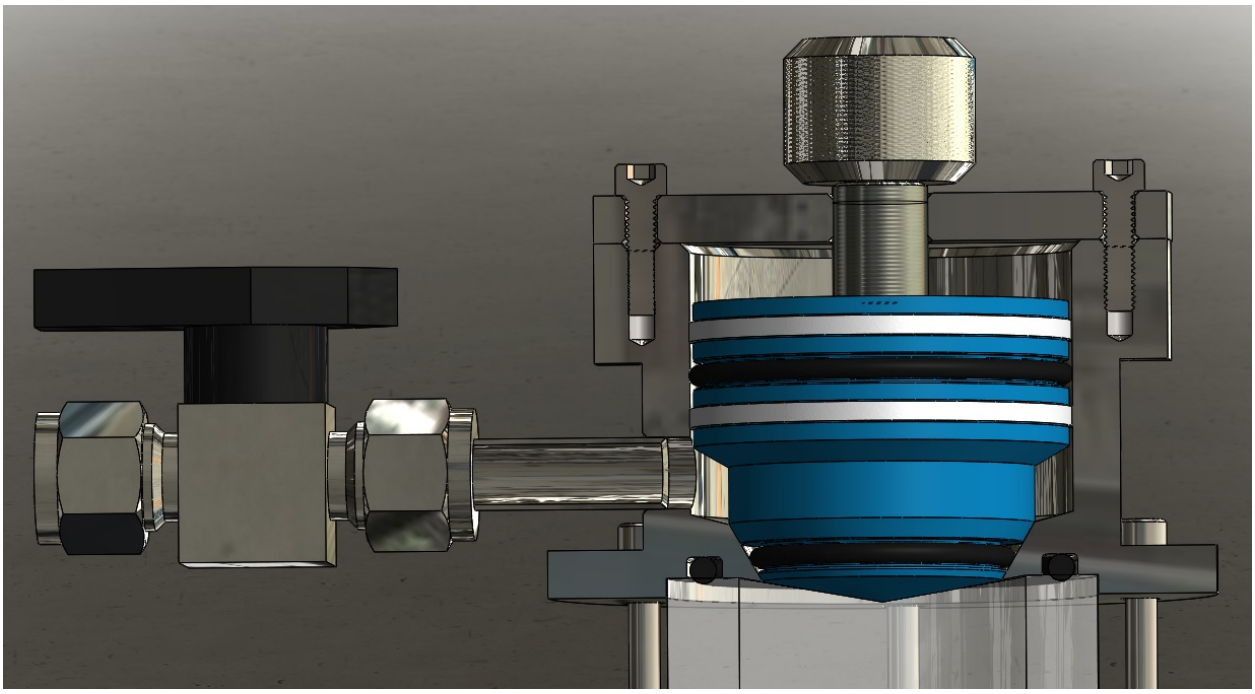

Figure 6.7: Geyser 6 - condenser. The condenser (highlighted in blue) is a hollow, stainless-steel part where the refrigeration fluid circulates. Two rubber o-rings are used as seals, while two Teflon rings serve as guides. A screw at the top can raise or lower the condenser, opening or isolating the chamber to the fill line.

tip by gravity in the center axis of the chamber. This insures that no Freon droplet sticks to any wall surface while descending, where they would nucleate after reheating.

The refrigeration fluid chosen for this CBC is the *Polycool PG -20*, a glycol based fluid from *PolyScience*. This fluid lowers the freezing point of water down to -20 ˚C, allowing for lower condensing temperatures [86]. Another circulation bath, a *PolyScience model PD15H200*, serves as the hot thermal bath of the chamber. Both circulation baths have external temperature probes that help to stabilize the temperature within ± 0.01 ˚C. The hot probe is placed at the top of the water tank, next to the water return, while the cold probe is located in the entry line of the refrigeration fluid. The baths are autonomous, but can be programmed into the DAQ for remote control.

The DAQ is powered by a *NIM* (Nuclear Instrumentation Module) crate connected to a National Instruments *NI PCI-6034E* acquisition card. A Windows XP computer runs a *LabView* program that records the pressure with an Omega PX103U pressure sensor, shown in Figure 6.8, at 1 sample/s. When the pressure rises over a preset threshold, the system records the pressure at 10^3

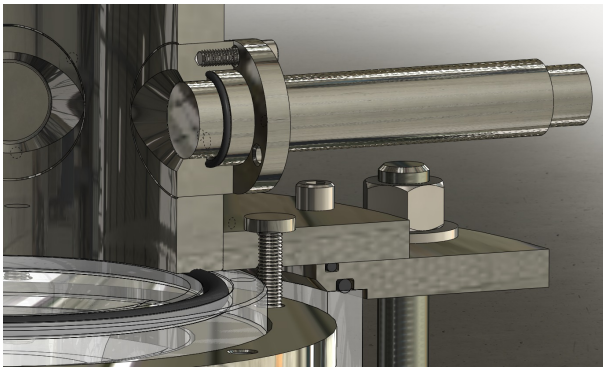

Figure 6.8: Geyser 6 - *Omega PX103U* pressure sensor.

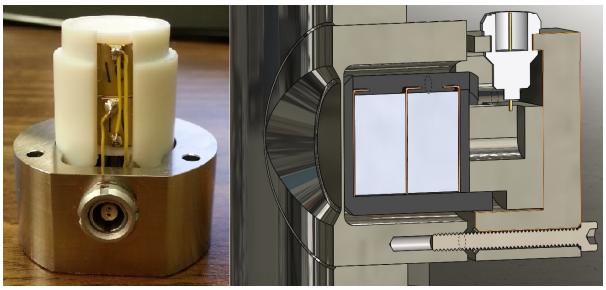

Figure 6.9: Geyser 6 - Piezo-electric sensor.

sample/s for 5 seconds, enough to record the whole bubble growth. A basic video system, composed of a *VX-3000* USB camera and the *VirtualDub* program allow for real-time, 30 fps recording. A more sophisticated system should be designed to reduce the data size by recording frames only when bubbles are formed, such as in PICO DAQs.

Finally, three piezo-electric sensors similar to PICASSO sensors are used, one shown in Figure 6.9. They are hooked-up to a PICASSO DAQ and record events independently from the pressure and camera systems. The acoustic signals were not included in this preliminary analysis.

6.2.2 Vessel Annealing

The acrylic vessel was made from a solid acrylic cylinder at the workshop of the Montreal *Groupe de Physique des Particules* (GPP). It was first machined on a lathe in a rough shape. The vessel was then blowtorched in an effort to smooth the acrylic surface.

The vessel was installed on the chamber, filled with C_5F_{12} and LAB and run at various temperatures, ranging from 40 ˚C to 54 ˚C for a couple of weeks. The appearance of crazing was noticed on the inside of the vessel. Shown in Figure 6.10, crazing is defined as the deformation of the material with a change in volume [87]. It is caused by stresses in polymers, where the material is held together by weak Van der Waals forces and strong covalent bonds. The stress applied can, over time, overcome the Van der Waals bonds while the covalent bonds continue to link the polymers. This results in the opening of gaps, called crazes, that aren't big enough to be felt on the surface

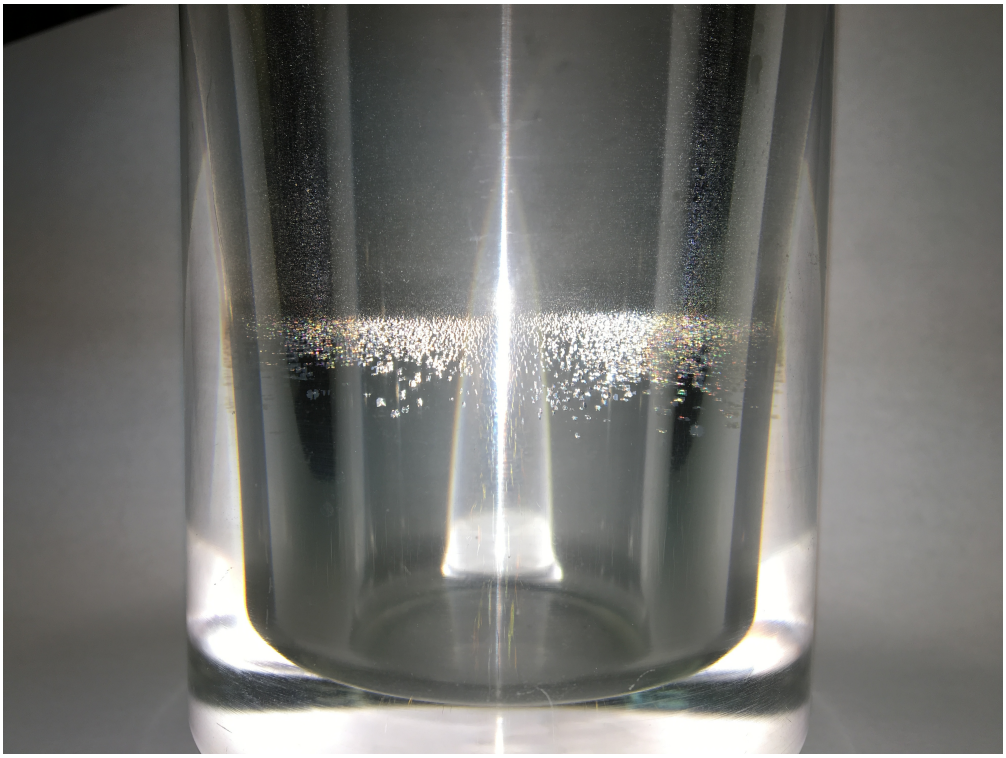

Figure 6.10: Crazing in the PMMA vessel. Vertical micro fissures appeared after a prolonged heating of the vessel. The fissures grew from the the inner surface outward. The crazing can be seen by light scattering, but can't be felt by touching.

of the material. Crazes can continue to grow if they are subjected to stress, leading to cracking or fatigue failure in the material. Even though the structural properties of the material aren't immediately affected by crazing (in some cases, polymers can even be strengthened by crazing), the presence of fissures in bubble chambers is known to lead to surface nucleation [68]. Therefore, this problem needed to be fixed.

In this CBC, the stress that induced the crazing was certainly created during the heating of the PMMA vessel in the thermal bath. A new vessel was fabricated and it was decided that this one would be annealed. Annealing consists in the gradual heating of a material up to temperatures nearing the melting point. This results in a rearranging of the polymers in the material, reenforcing the weaker bonds that are responsible for the crazing.

The vessel was first cleaned in an ultrasonic bath with *Radiacwash* radio-decontamination solution and ultra-pure water. It was then placed upside down, on an aluminum molding ring that

preserved the o-ring groove shape, in an annealing oven. The temperature was ramped up from room temperature to 80 ˚C over four hours. The vessel was kept at 80 ˚C for 24 hours, then the temperature was ramped down back to room temperature over four hours. This simple procedure apparently solved the problem since no crazing was observed with this annealed vessel.

6.2.3 Coating

At the Université de Montréal, different coating methods on the inner wall of inner vessels were tested with CBCs . These tests could also have been done with PICO type bubble chambers, but the low cost of CBCs, their ease of commissioning and operation makes them more suitable workbenches for this type of R&D. The motivation for this research was to explore the feasibility of using low cost, radio-pure materials, such as PMMA for coating.

Several commercial super-hydrophobic coatings were tested but then rejected due to either powdery deposits left after the application or uneven surface. However, one product appeared promising: the *Defender plastic series* coating from *Diamond-Fusion International*. According to the manufacturer's instruction, the coating was applied by vaporization over the surface, and then polished to a mirror shine with a lint-free, clean, dry lab wipe. The application process was repeated three times over the same surface. The chamber showed stable running down to a threshold energy of about 50 keV. At lower threshold, the Freon started boiling, rendering the detector nonoperational.

Tests where carried out with a 93 mCi ^{241}Am source. This α and γ-ray source appeared to produce neutrons via the process $\alpha(^{27}\mathrm{Al,n})^{30}\mathrm{P}$ reaction in the aluminum casing of the source. The neutrons produced have an energy spectrum ranging from 0 to 2 MeV, with a most probable energy of around 1 MeV [88]. Operating temperatures ranged from 42 ˚C to 56 ˚C, with a condenser temperature of 4 ˚C. Background data were also acquired.

Figure 6.11 shows the background-subtracted count rate of the chamber as a function of the threshold energy. The fit was done for 1 MeV neutrons and is thus not totally representative of reality as neutrons from the ^{241}Am source aren't mono-energetic. The background is subtracted

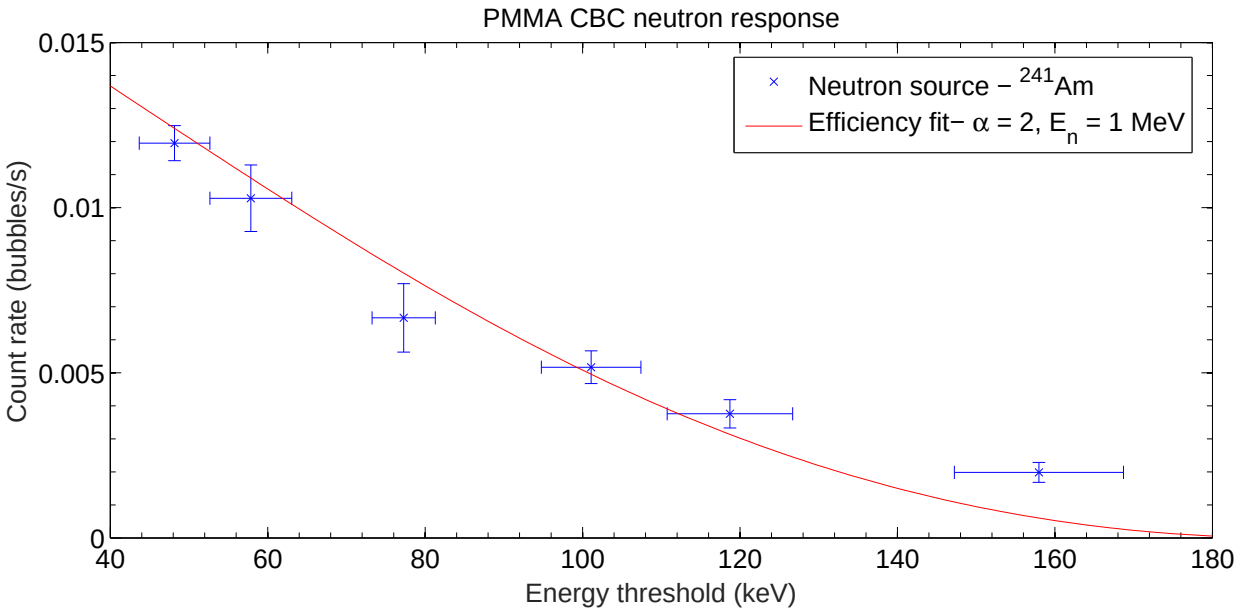

Figure 6.11: Geyser 6 - Results. The fit was performed from equations 3.5 and 3.6, with $\alpha = 2$ and an average neutron energy of 1 MeV.

but no cuts were applied. The data were fitted with equation 3.6, with $\alpha = 2$.

6.2.4 Outlook

These results demonstrate the feasibility of PMMA CBCs at higher threshold energies. More research should still be done to solve the wall nucleation problem at lower thresholds. Application of multiple layers of the coatings has shown promise and should be explored. Also, chemical vapor deposition of super-hydrophobic compounds should be explored. DEAP-3600, a dark matter direct detection experiment, deposited a wavelength shifter on their PMMA sphere with this technique [89]. This coating could be tested in the PMMA CBC. Other modifications could be made on the current geyser design. For example, a better DAQ, similar to the one of PICO-0.1, could improve the precision of the recorded data. Such a system could also unify the data acquisition, which would simplify data analysis.

CHAPTER 7

CONCLUSION

The questions relative to the nature of dark matter have yet to be answered, although its existence is now well established. Observations of galactic rotation curves, gravitational lensing, large scale structures of the Universe and anisotropies of the Cosmic Microwave Background all hint towards missing mass in the Universe.

The bubble chamber technology is continuously improved and is well suited for the direct detection of dark matter, as the recent world leading results of PICO-2L and PICO-60 prove [61, 62, 64]. The ability to easily change target fluids gives the PICO collaboration the ability to eventually provide a quick confirmation of a discovery from another experiment, but most importantly, the collaboration is well positioned to pioneer in the deployment of new target nuclei for dark matter search, including hydrogen and chlorine.

The increased knowledge acquired from calibration chambers about background interactions in bubble chambers will help to improve the sensitivity of PICO detectors. As part of the original work for this thesis, the neutron background measurement performed on PICO-0.1, alongside the high precision efficiency determination of the ^{3}He neutron counters will help to understand the neutron background in physics runs. γ-calibrations and the study of the effect of particulates in other test chambers are also giant steps towards the complete understanding of the low threshold bubble chamber technology. Finally, improved neutron shielding, active muon vetos and the clean environment of the SNOLAB underground facility are also helping to further manage background radiation along with increasingly precise Monte Carlo simulations to calculate the expected background contribution.

The PICO collaboration is putting forward new detector designs. In light of the particulate problem observed in both PICO-2L and PICO-60, a proposal for a right-side-up (RSU) chamber was made, named PICO-40L. Since particulates are thought to originate from the wear of materials

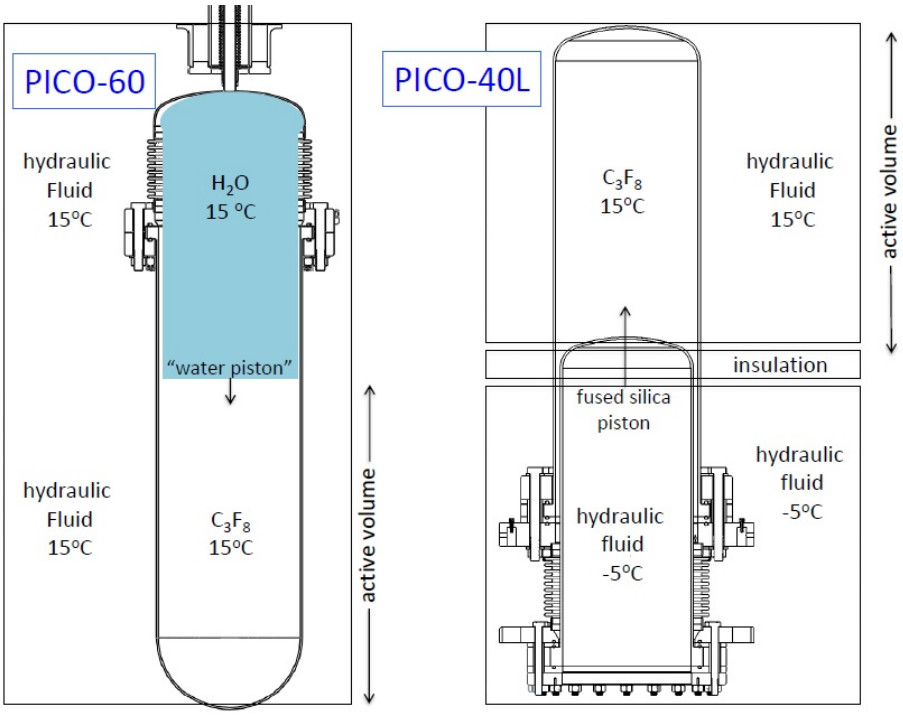

Figure 7.1: PICO-60 vs PICO-40L. The RSU chamber design should eliminate the particulate accumulation in the inner volume by allowing the filtration of the active fluid. This design also eliminates the need for a buffer fluid. The delimitation of the active zone is made by a sharp thermal gradient, keeping only the upper regions superheated.

of the detector itself and drop down in the inner vessel, particulates produced in a RSU chamber would drop out of the inner vessel, allowing for an easy filtration of the active fluid. This detector design comprises two nested fused silica parts: a PICO-60 sized inner vessel and an inner piston. The layout of the chamber is compared to the one of PICO-60 in Figure 7.1. An insulation ring slightly lower than the top of the piston delimits a sharp temperature gradient zone, keeping the upper part superheated while the lower part is cooled. RSU chamber installation at SNOLAB is planned for 2017.

The PICO collaboration is also working on a 30 ml LXe bubble chamber prototype (Figure 7.2). Superheated LXe can be operated in bubble chambers the same way Freon is, and nuclear interactions can produce scintillation. Photons emitted by scintillation are collected by a photomultiplier tube (PMT), in addition to the typical apparatus present on PICO bubble chambers (pressure transducer, piezo-electric sensors, cameras). The chamber is built in a similar way to PICO-40L.

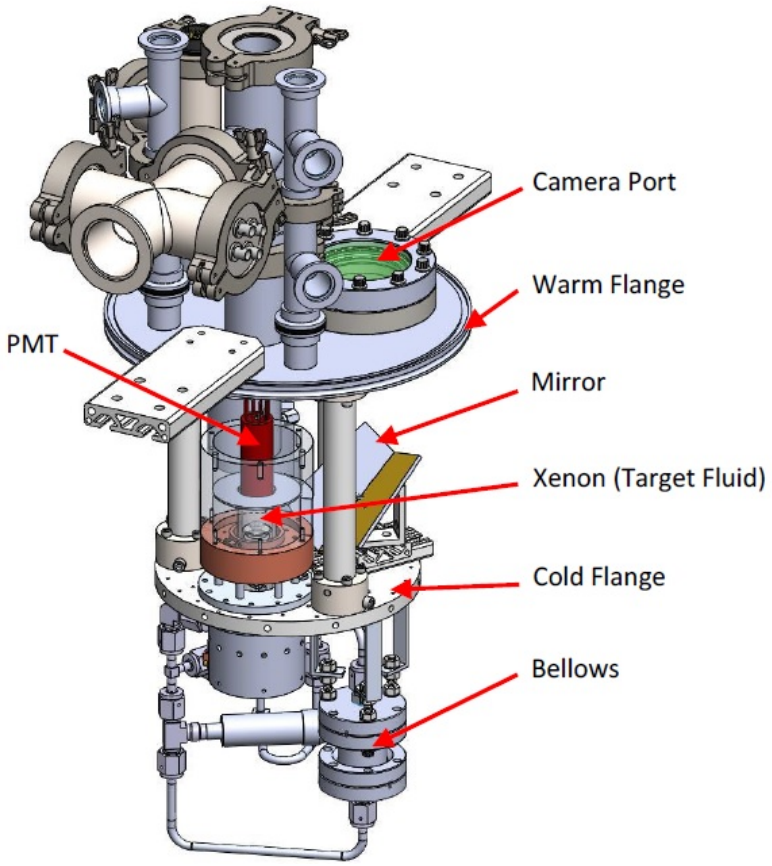

Figure 7.2: LXe scintillating bubble chamber. Scintillation light can be collected with a PMT.

Given the success of a prototype, a LXe bubble chamber of much larger size could be built, taking advantage of the self-shielding property of xenon to further reduce background. Such chambers could add scintillation analysis to the arsenal of the PICO experiment in the attempt to further increase background discrimination.

The long-term goal of the PICO collaboration is to build a ton-scale bubble chamber. The latest chamber proposed, PICO-500, would allow us to probe a large fraction of the cross-section and WIMP mass parameter space. Following a possible discovery, investigation with different nuclear targets could be undertaken with the same detector, including C_3F_8, CF_3I and $C_2H_2F_4$. Hydrogenated Freons would help probe lower WIMP masses while an iodine loaded fluid can be chosen to probe higher WIMP masses. In addition, a CF_3I physics run would significantly increase the sensitivity to SI interactions, with a projected cross-section exclusion over two orders of magnitude lower than run-I of PICO-60 as shown in Figure 7.3. As for SD interactions (Figure 7.4), C_3F_8

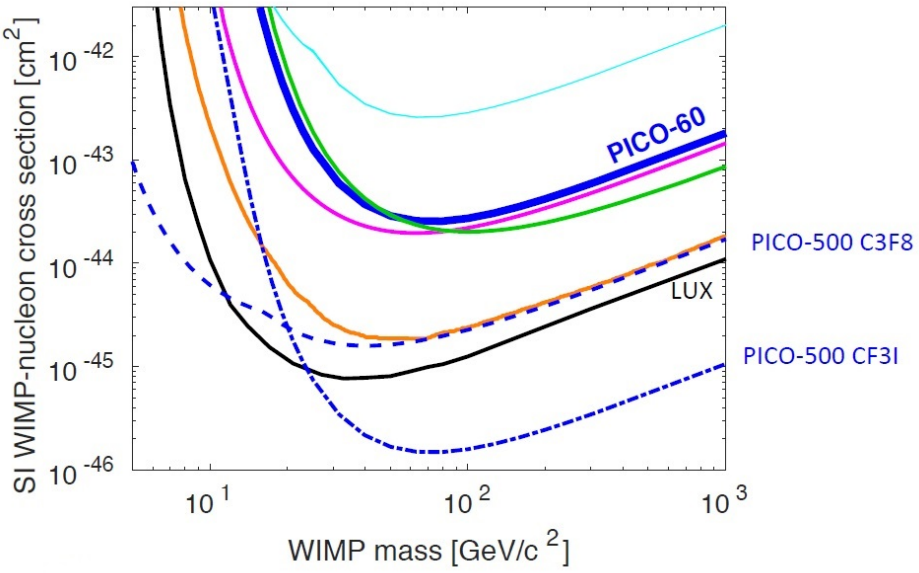

Figure 7.3: PICO-500 SI projection plot. Experimental exclusion curves are presented as solid curves. Projections are presented by dashed curves. Other limits shown are from COUPP (light blue), XENON100 (orange), LUX (black), CDMS-II (magenta), and Dark-Side-50 (green).

would allow to almost probe down to the edge of the solar neutrino floor, while $C_2H_2F_4$ operated at low threshold might allow us to probe the solar neutrino parameter-space for the first time. Finally, the development of coated PMMA vessels would be a significant achievement towards the build of ton-scale bubble chambers. Detectors could be up-scaled significantly at much lower cost while using stronger, radio-pure materials.

Future large scale detectors, such as the RSU PICO-40L design and the PICO-500 bubble chamber concept, will be facing new obstacles in the search for dark matter. As experiments become increasingly sensitive, the reach of the coherent neutrino background is soon going to become the dominant background in most direct detection experiments. Directional detectors might be, to date, the only technology capable of discriminating neutrino interactions from other elastic recoils [39]. Therefore, a combination of technological understanding and new analysis techniques will be required to push dark matter searches beyond this current limitation.

Given the majors advances achieved in recent years, it is needless to say that the future looks bright for dark matter research.

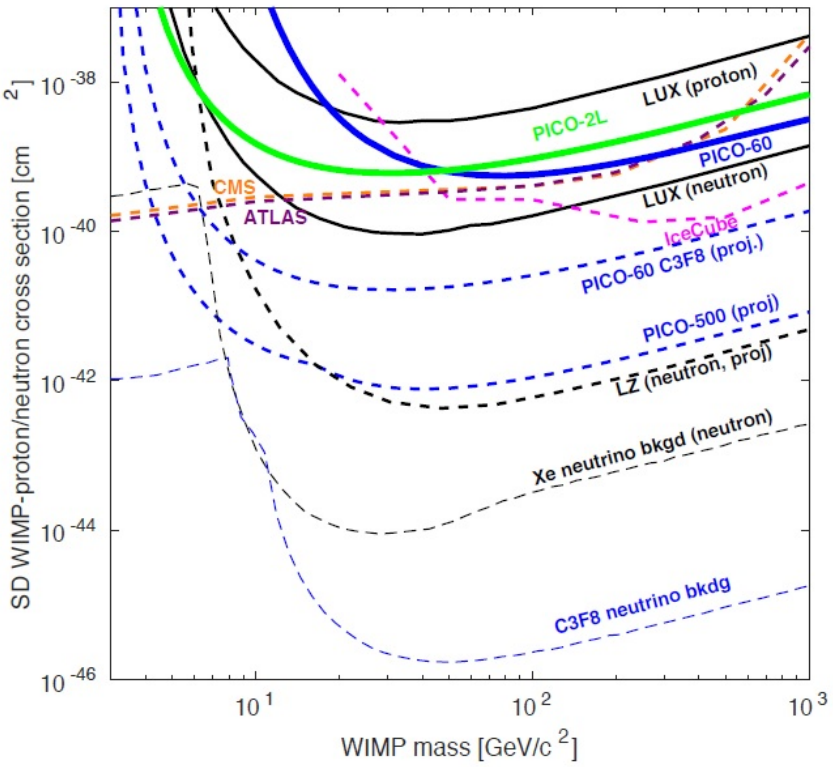

Figure 7.4: PICO-500 SD projection plot. Experimental exclusion curves are presented as solid curves. Projections are presented by bold dashed curves and neutrino backgrounds by light dashed curves.

BIBLIOGRAPHY

[1] E. Hubble, *A relation between distance and radial velocity among extra-galactic nebulae*, Proceedings of the National Academy of Sciences **15**, 168 (1929), http://www.pnas.org/content/15/3/168.

[2] S. Nerlich, Astronomy Without A Telescope - The Edge of Greatness, 2010, http://www.universetoday.com/81813/astronomy-without-a-telescope-the-edge-of-greatness/.

[3] D. D. Baumann, Cosmology - Lecture notes - Cambridge University, 2014, http://www.damtp.cam.ac.uk/user/db275/Cosmology/Chapter3.pdf.

[4] W. Seagrave, *History of the Universe* (Penny Press Ltd, 2012).

[5] J. B. Hartle, *Gravity: An Introduction to Einstein's General Relativity*, Pearson education ed. (Addison-Wesley, San Francisco, 2003).

[6] S. Weinberg, *Gravitation and cosmology: principles and applications of the general theory of relativity* (Wiley, 1972).

[7] K. A. Olive and others, *Review of Particle Physics*, Chin. Phys. **C38**, 090001 (2014).

[8] E. S. Agency, Planck cosmic recipe, http://www.esa.int/spaceinimages/Images/2013/03/Planck_cosmic_recipe.

[9] Dark Matter, http://cdms.phy.queensu.ca/Public_Docs/DM_Intro.html.

[10] F. Zwicky, *Die Rotverschiebung von extragalaktischen Nebeln*, Helv. Phys. Acta , 110 (1933).

[11] Astronomy Without A Telescope - Could Dark Matter Not Matter?, 2011, http://www.universetoday.com/91520/astronomy-without-a-telescope-could-dark-matter-not-matter/.

[12] V. C. Rubin and W. K. Ford, Jr., *Rotation of the Andromeda Nebula from a Spectroscopic Survey of Emission Regions*, apj **159**, 379 (1970).

[13] HubbleSite - NewsCenter - First ESA Faint Object Camera Science Images the Gravitational Lens G2237 + 0305 (09/13/1990) - Release Images, http://hubblesite.org/newscenter/archive/releases/1990/20/image/a/.

[14] F. Zwicky, *Nebulae as Gravitational Lenses*, Physical Review **51**, 290 (1937), http://link.aps.org/doi/10.1103/PhysRev.51.290.

[15] The Matter of the Bullet Cluster, http://apod.nasa.gov/apod/ap060824.html.

[16] Chandra - El Gordo, http://chandra.harvard.edu/photo/2014/elgordo/.

[17] M. Markevitch, A. H. Gonzalez, D. Clowe, A. Vikhlinin, W. Forman, C. Jones, S. Murray, and W. Tucker, *Direct Constraints on the Dark Matter Self-Interaction Cross Section from the Merging Galaxy Cluster 1E 0657–56*, The Astrophysical Journal **606**, 819 (2004), http://stacks.iop.org/0004-637X/606/i=2/a=819.

[18] M. Bradac, D. Clowe, A. H. Gonzalez, P. Marshall, W. Forman, C. Jones, M. Markevitch, S. Randall, T. Schrabback, and D. Zaritsky, *Strong and weak lensing united III: Measuring the mass distribution of the merging galaxy cluster 1E0657-56*, The Astrophysical Journal **652**, 937 (2006), http://arxiv.org/abs/astro-ph/0608408, arXiv: astro-ph/0608408.

[19] Nine Year Microwave Sky Image, http://map.gsfc.nasa.gov/media/121238/index.html.

[20] Polarisation of the Cosmic Microwave Background, http://www.esa.int/spaceinimages/Images/2015/02/Polarisation_of_the_Cosmic_Microwave_Background.

[21] A. A. Penzias and R. W. Wilson, *A Measurement of Excess Antenna Temperature at 4080 Mc/s.*, apj **142**, 419 (1965).

[22] M. A. Janssen and S. Gulkis, *Mapping the sky with the COBE differential microwave radiometers*, **359**, 391 (1992), http://adsabs.harvard.edu/abs/1992ASIC..359..391J.

[23] Seven Year Microwave Sky Image, https://map.gsfc.nasa.gov/media/101080/index.html.

[24] esa, Planck and the cosmic microwave background, http://www.esa.int/Our_Activities/Space_Science/Planck/Planck_and_the_cosmic_microwave_background.

[25] Cosmology, http://www.helsinki.fi/~hkurkisu/cosmology/Cosmo12.pdf.

[26] M. Milgrom, *A modification of the Newtonian dynamics as a possible alternative to the hidden mass hypothesis*, apj **270**, 365 (1983).

[27] M. Deliyergiyev, *Recent Progress in Search for Dark Sector Signatures*, Open Physics **14**, 281 (2016), http://www.degruyter.com/view/j/phys.2016.14.issue-1/phys-2016-0034/phys-2016-0034.xml.

[28] M. Srednicki, *Axions: Past, Present, and Future*, arXiv:hep-th/0210172 (2002), http://arxiv.org/abs/hep-th/0210172.

[29] P. Cushman *et al.*, *Snowmass CF1 Summary: WIMP Dark Matter Direct Detection*, arXiv:1310.8327 [astro-ph, physics:hep-ex, physics:physics] (2013), http://arxiv.org/abs/1310.8327.

[30] K. Garrett and G. Duda, *Dark Matter: A Primer*, Advances in Astronomy **2011**, 1 (2011), http://arxiv.org/abs/1006.2483, arXiv: 1006.2483.

[31] C. Alcock et al., *EROS and MACHO Combined Limits on Planetary-Mass Dark Matter in the Galactic Halo*, The Astrophysical Journal Letters **499**, L9 (1998), http://iopscience.iop.org/article/10.1086/311355/meta.

[32] M. Cannoni, *Exact theory of freeze out*, The European Physical Journal C **75** (2015), http://arxiv.org/abs/1407.4108, arXiv: 1407.4108.

[33] O. Buchmueller, C. Doglioni, and L.-T. Wang, *Search for dark matter at colliders*, Nature Physics **13**, 217 (2017), http://www.nature.com/nphys/journal/v13/n3/box/nphys4054_BX1.html.

[34] G. Aad *et al.*, *Observation of a new particle in the search for the Standard Model Higgs boson with the ATLAS detector at the LHC*, Physics Letters B **716**, 1 (2012), http://www.sciencedirect.com/science/article/pii/S037026931200857X.

[35] LHCb Collaboration *et al.*, *Observation of $J/\psi p$ Resonances Consistent with Pentaquark States in $\Lambda_b^0 \to J/\psi K^- p$ Decays*, Physical Review Letters **115**, 072001 (2015), https://link.aps.org/doi/10.1103/PhysRevLett.115.072001.

[36] J. Buckley *et al.*, *Cosmic Frontier Indirect Dark Matter Detection Working Group Summary*, arXiv:1310.7040 [astro-ph, physics:hep-ph] (2013), http://arxiv.org/abs/1310.7040.

[37] D. Bauer *et al.*, *Dark Matter in the Coming Decade: Complementary Paths to Discovery and Beyond*, Physics of the Dark Universe **7-8**, 16 (2015), http://arxiv.org/abs/1305.1605, arXiv: 1305.1605.

[38] D. R. Tovey, R. J. Gaitskell, P. Gondolo, Y. Ramachers, and L. Roszkowski, *A new model-independent method for extracting spin-dependent cross section limits from dark matter searches*, Physics Letters B **488**, 17 (2000), http://www.sciencedirect.com/science/article/pii/S0370269300008467.

[39] J. Billard, L. Strigari, and E. Figueroa-Feliciano, *Implication of neutrino backgrounds on the reach of next generation dark matter direct detection experiments*, Phys.Rev. **D89**, 023524 (2014).

[40] V. Barger, D. Marfatia, and K. Whisnant, *The Physics of Neutrinos* (Princeton University Press, 2012), Google-Books-ID: 879tdkeTXAcC.

[41] R. Bernabei *et al.*, *New results from DAMA/LIBRA*, The European Physical Journal C **67**, 39 (2010), http://arxiv.org/abs/1002.1028, arXiv: 1002.1028.

[42] DM-ICE, http://dm-ice.yale.edu/home.

[43] K. Fushimi *et al.*, *Search for cosmic dark matter by means of ultra high purity NaI(Tl) scintillator*, arXiv:1705.00110 [astro-ph, physics:physics] (2017), http://arxiv.org/abs/1705.00110.

[44] A. Gütlein, G. Angloher, C. Gotti, D. Hauff, M. Maino, S. S. Nagorny, L. Pagnanini, G. Pessina, F. Petricca, S. Pirro, F. Pröbst, F. Reindl, K. Schäffner, J. Schieck, and W. Seidel, *The COSINUS project: Development of new NaI-based cryogenic detectors for direct dark matter search*, Nuclear Instruments and Methods in Physics Research Section A: Accelerators, Spectrometers, Detectors and Associated Equipment **845**, 359 (2017), http://www.sciencedirect.com/science/article/pii/S0168900216305484.

[45] XMASS, http://www-sk.icrr.u-tokyo.ac.jp/xmass/index-e.html.

[46] XENON1t Dark Matter Search, http://www.xenon1t.org/.

[47] Plan for the Future | XMASS, http://www-sk.icrr.u-tokyo.ac.jp/xmass/about/future/index-e.html.

[48] LUX Dark Matter Collaboration, http://luxdarkmatter.org/.

[49] PandaX Dark Matter Experiment, https://pandax.physics.sjtu.edu.cn/.

[50] MiniCLEAN | SNOLAB, https://www.snolab.ca/science/experiments/miniclean.

[51] DEAP-3600 – Dark matter Experiment using Argon Pulse-shape discrimination, http://deap3600.ca/.

[52] Argon Dark Matter (ArDM) official web site, http://darkmatter.ethz.ch/.

[53] The DarkSide Homepage, http://darkside.lngs.infn.it/,http://darkside.lngs.infn.it/.

[54] Picasso experiment, http://www.picassoexperiment.ca/.

[55] PICO dark matter search experiment, http://www.picoexperiment.com/.

[56] D. A. Glaser and D. C. Rahm, *Characteristics of Bubble Chambers*, Physical Review **97**, 474 (1955), https://link.aps.org/doi/10.1103/PhysRev.97.474.

[57] P. Collaboration, *PICASSO, COUPP and PICO - search for dark matter with bubble chambers*, EPJ Web of Conferences (2015), https://www.osti.gov/scitech/servlets/purl/1214446.

[58] M.-C. Piro, *Doctoral Thesis: Fabrication et caractérisation de détecteurs à gouttelettes en surchauffe à bas bruit de fond au sein du projet PICASSO*, PhD thesis, Université de Montréal, 2008, https://papyrus.bib.umontreal.ca/xmlui/handle/1866/8020.

[59] F. Seitz, *On the Theory of the Bubble Chamber*, Physics of Fluids (1958-1988) **1**, 2 (1958), http://scitation.aip.org/content/aip/journal/pof1/1/1/10.1063/1.1724333.

[60] S. Archambault *et al.*, *New insights into particle detection with superheated liquids*, New Journal of Physics **13**, 043006 (2011), http://stacks.iop.org/1367-2630/13/i=4/a=043006.

[61] PICO Collaboration *et al.*, *Dark Matter Search Results from the PICO-2L C_3F_8 Bubble Chamber*, Physical Review Letters **114**, 231302 (2015), http://link.aps.org/doi/10.1103/PhysRevLett.114.231302.

[62] PICO Collaboration *et al.*, *Dark matter search results from the PICO-60 CF_3I bubble chamber*, Physical Review D **93**, 052014 (2016), http://link.aps.org/doi/10.1103/PhysRevD.93.052014.

[63] SNOLAB, https://www.snolab.ca/.

[64] PICO Collaboration *et al.*, *Improved dark matter search results from PICO-2L Run 2*, Physical Review D **93**, 061101 (2016), http://link.aps.org/doi/10.1103/PhysRevD.93.061101.

[65] C. Amole *et al.*, *Dark Matter Search Results from the PICO-60 C_3F_8 Bubble Chamber*, arXiv:1702.07666 [astro-ph, physics:hep-ex, physics:physics] (2017), http://arxiv.org/abs/1702.07666.

[66] N. Boukhira, I. Boussaroque, R. Gornea, M. Di Marco, L. Lessard, V. Pagé, J. Vinet, and V. Zacek, *Suitability of superheated droplet detectors for dark matter search*, Astroparticle Physics **14**, 227 (2000), http://www.sciencedirect.com/science/article/pii/S0927650500001237.

[67] L. Lessard, L.-A. Hamel, and V. Zacek, *Neutron response functions for superheated droplet detectors*, IEEE Transactions on Nuclear Science **46**, 1907 (1999).

[68] R. Cole, *Boiling nucleation*, Advances in Heat Transfer **10**, 85 (1974).

[69] High Voltage Engineering Europa B. V., Manual for Model 358 Duoplasmatron Ion Source, A-4-35-090-0002.

[70] J. H. Gibbons, R. L. Macklin, and H. W. Schmitt, *$^{51}V(p,n)^{51}Cr$ Reaction as a 5- to 120-kev*

Neutron Source, Phys. Rev. **100**, 167 (1955), http://link.aps.org/doi/10.1103/PhysRev.100.167.

[71] Brookhaven Instruments Corporation (BIC) - Model 1000c current integrator.

[72] A. Plante, *Master's thesis: Analyse et modélisation de la réponse des détecteurs du projet PICASSO pour la recherche de la matière sombre*, PhD thesis, Université de Montréal, 2015, https://papyrus.bib.umontreal.ca/xmlui/handle/1866/12472.

[73] V. Zacek, COUPP-doc-2064-v3: Understanding the response to 17 keV 35s recoils in C2clf5 (Part 2), https://coupp-docdb.fnal.gov/cgi-bin/private/ShowDocument?docid=2064.

[74] T. Bücherl, N. Kardjilov, C. L. v. Gostomski, E. Calzada, and A. M. ELGhobary, *A mobile neutron source based on the SbBe reaction*, Applied Radiation and Isotopes **61**, 659 (2004), http://www.sciencedirect.com/science/article/pii/S0969804304001940.

[75] NUCLEAR DATA SECTION, Live Chart of Nuclides, https://www-nds.iaea.org/relnsd/vcharthtml/VChartHTML.html.

[76] Princeton Gamma Tech, Detector User Manual - Gamma and X-ray Detectors, Part No. 2061-0100, Rev. 1, 2005.

[77] G. F. Knoll, *Radiation Detection and Measurement, Third Edition* (Wiley & Sons, University of Michigan, 2000).

[78] H. W. Reist, B. Hahn, *The geyser, a new detector for nuclear recoils*, Proceedings of the 5th International Conference on High-Energy Physics Nuclear Structure, pages 432-435 (1973).

[79] A. Pullia, *Searches for Dark Matter with Superheated Liquid Techniques*, Advances in High Energy Physics (2014), http://search.proquest.com/docview/1552469831/abstract/DEB5A0317F84267PQ/1.

[80] R. Bertoni, F. Chignoli, D. Chiesa, M. Clemenza, G. Lucchini, R. Mazza, P. Negri, A. Pullia, N. Redaelli, L. Zanotti, and D. Cundy, *A new technique for direct investigation of dark matter*, Nuclear Instruments and Methods in Physics Research Section A: Accelerators, Spectrometers, Detectors and Associated Equipment **744**, 61 (2014), http://www.sciencedirect.com/science/article/pii/S0168900214000461.

[81] M. Ardid, M. Bou-Cabo, I. Felis, and J. A. Martínez-Mora, *MOSCAB: direct dark matter search using the geyser technique*, Nuclear and Particle Physics Proceedings **273–275**, 2354 (2016), http://www.sciencedirect.com/science/article/pii/S2405601415008780.

[82] M. Laurin, *Recherche de la matière sombre à l'aide de détecteurs à liquides surchauffés dans le cadre de l'expérience PICO/Picasso*, PhD thesis, Université de Montréal, 2016.

[83] J. Boger *et al.*, *The Sudbury Neutrino Observatory*, Nuclear Instruments and Methods in Physics Research Section A: Accelerators, Spectrometers, Detectors and Associated Equipment **449**, 172 (2000), http://www.sciencedirect.com/science/article/pii/S0168900299014692.

[84] C. Kraus, *SNO with liquid scintillator: SNO+*, Progress in Particle and Nuclear Physics **57**, 150 (2006), https://www.sciencedirect.com/science/article/pii/S0146641005001481.

[85] M. Kuźniak *et al.*, *DEAP-3600 Dark Matter Search*, Nuclear and Particle Physics Proceedings **273–275**, 340 (2016), https://www.sciencedirect.com/science/article/pii/S2405601415005374.

[86] Polyscience - polycool PG -20 cooling liquid, https://www.polyscience.com/fluidaccessories/polycool-pg-20-1.

[87] R. A. C. Deblieck, D. J. M. van Beek, K. Remerie, and I. M. Ward, *Failure mechanisms in polyolefines: The role of crazing, shear yielding and the entanglement network*, Polymer **52**,

2979 (2011), http:
//www.sciencedirect.com/science/article/pii/S0032386111002631.

[88] E. F. E. F. . Shores, Los Alamos National Laboratory Report No. LA-UR-04-3600, 2004 (unpublished), http://www.osti.gov/scitech/biblio/977657.

[89] T. Bromwich, *TPB evaporations and sensitivity plots for the DEAP-3600 dark matter detector*, Master's these, University of Sussex, United-Kingdom, 2014, http://deap3600.ca/Contents/thesis/BromwichTalithaMSc.pdf.

[90] Vacuum Technology and Vacuum Pumps from the leader, https://www.pfeiffer-vacuum.com/en/.

Appendix I

PMMA CBC assembly and filling

As with all other chambers, CBCs are cleaned in a class 10000 cleanroom. All parts are washed in an ultrasonic bath with ultra-pure water and *Radiacwash* solutions for 30 minutes. Afterward, they are rinsed ultrasonically for 2x 15 minutes. The parts are then transferred to a class 1000 clean-room for drying. The chamber is assembled and put under vacuum to get rid of leftover water droplets and most of the radon from the air.

The chamber is then hooked-up to a *Pfeiffer*, model *HLT 560* leak tester to ensure that the chamber is airtight [90]. The leak-tester creates a vacuum in the chamber, and a very small quantity of gaseous helium is blown around every fittings and connections. A mass spectrometer in the leak tester ionizes the gas coming from the chamber and identifies traces of helium in the gas. Working slowly around the detector allows to localize and repair very small leaks, down to $5 \cdot 10^{-12}$ mbar l/s.

Once the chamber is leak-tight, it can be filled. Figure I.1 presents the filling set up. Filling is done in two steps. First, with the condenser raised, the buffer fluid (LAB) is transferred from a degassed filling bottle isolated by valves. A stainless-steel filter of 0.5 μm is located at the entry of the chamber to catch impurities. A small overpressure of nitrogen gas is created on the top of the LAB in the filling bottle while the chamber is kept under vacuum. LAB is transferred from the filling bottle to an intermediate reservoir where it can be degassed again if needed, and then it is transferred in the chamber. The intermediate reservoir must be kept half filled for future fluid level adjustments. The chamber is not entirely filled with buffer fluid to leave space for the C_5F_{12}.

Finally, the C_5F_{12} is filled from the top with the condenser cold and raised. A C_5F_{12} transfer bottle is hooked-up to the system and all the lines are kept under vacuum. The transfer bottle is heated in a water bath above the C_5F_{12} boiling temperature of 30 $^{\circ}$C. The valves to the chamber are opened and the Freon is condensed into the chamber. When the fill is complete, the valves are

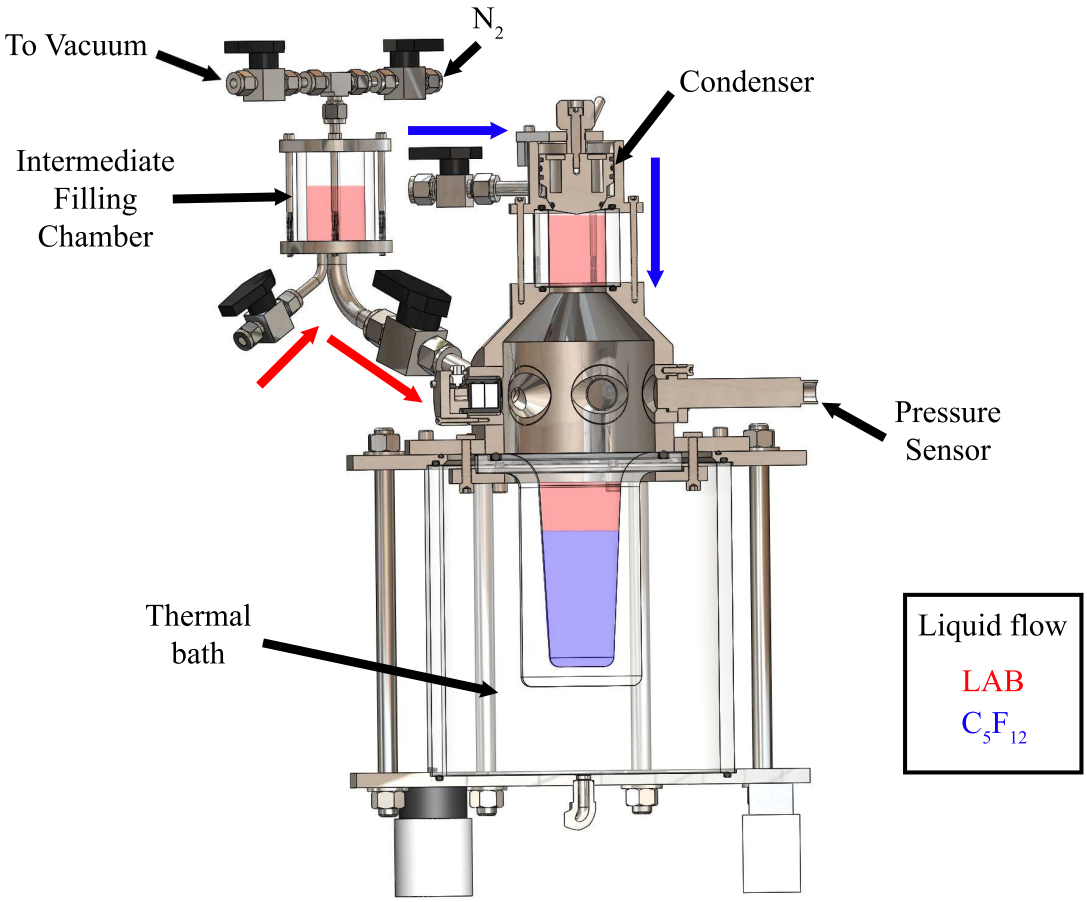

Figure I.1: Geyser 6 - Fill drawing. Colored arrows represent the flow of the liquids.

closed and the condenser is lowered, isolating the chamber. The amount of Freon transferred is calculated by weighing the transfer bottle before and after the transfer.

LAB can be added to or removed from the chamber using the intermediate filling chamber. Pressure from a nitrogen bottle can be added on top of the LAB and the flow direction can be reversed by using under pressure.

Appendix II

PICO-2L Paper - Run 1

Dark Matter Search Results from the PICO-2L C_3F_8 Bubble Chamber

C. Amole,[1] M. Ardid,[2] D. M. Asner,[3] D. Baxter,[4] E. Behnke,[5] P. Bhattacharjee,[6] H. Borsodi,[5] M. Bou-Cabo,[2] S. J. Brice,[7] D. Broemmelsiek,[7] K. Clark,[8] J. I. Collar,[9] P. S. Cooper,[7] M. Crisler,[7] C. E. Dahl,[4,7] S. Daley,[1] M. Das,[6] F. Debris,[10] N. Dhungana,[11] J. Farine,[11] I. Felis,[2] R. Filgas,[12] M. Fines-Neuschild,[10] F. Girard,[10] G. Giroux,[1] M. Hai,[9] J. Hall,[3] O. Harris,[5] C. M. Jackson,[10] M. Jin,[4] C. B. Krauss,[13] M. Lafrenière,[10] M. Laurin,[10] I. Lawson,[14,11] I. Levine,[5] W. H. Lippincott,[7] E. Mann,[5] J. P. Martin,[10] D. Maurya,[15] P. Mitra,[13] R. Neilson,[9,16] A. J. Noble,[1] A. Plante,[10] R. B. Podviianiuk,[11] S. Priya,[15] A. E. Robinson,[9] M. Ruschman,[7] O. Scallon,[11,10] S. Seth,[6] A. Sonnenschein,[7] N. Starinski,[10] I. Štekl,[12] E. Vázquez-Jáuregui,[17,14,11] J. Wells,[5] U. Wichoski,[11] V. Zacek,[10] and J. Zhang[4]

(PICO Collaboration)

[1]*Department of Physics, Queen's University, Kingston, Ontario K7L 3N6, Canada*
[2]*Universitat Politècnica de València, IGIC, 46730 Gandia, Spain*
[3]*Pacific Northwest National Laboratory, Richland, Washington 99354, USA*
[4]*Department of Physics and Astronomy, Northwestern University, Evanston, Illinois 60208, USA*
[5]*Department of Physics and Astronomy, Indiana University South Bend, South Bend, Indiana 46634, USA*
[6]*Saha Institute of Nuclear Physics, Astroparticle Physics and Cosmology Division, Kolkata, West Bengal 700064, India*
[7]*Fermi National Accelerator Laboratory, Batavia, Illinois 60510, USA*
[8]*Department of Physics, University of Toronto, Toronto, Ontario M5S 1A7, Canada*
[9]*Enrico Fermi Institute, KICP and Department of Physics, University of Chicago, Chicago, Illinois 60637, USA*
[10]*Département de Physique, Université de Montréal, Montréal, Québec H3C 3J7, Canada*
[11]*Department of Physics, Laurentian University, Sudbury, Ontario P3E 2C6, Canada*
[12]*Institute of Experimental and Applied Physics, Czech Technical University in Prague, Prague 12800, Czech Republic*
[13]*Department of Physics, University of Alberta, Edmonton, Alberta T6G 2G7, Canada*
[14]*SNOLAB, Lively, Ontario P3Y 1N2, Canada*
[15]*Bio-Inspired Materials and Devices Laboratory (BMDL), Center for Energy Harvesting Materials and Systems (CEHMS), Virginia Tech, Blacksburg, Virginia 24061, USA*
[16]*Department of Physics, Drexel University, Philadelphia, Pennsylvania 19104, USA*
[17]*Instituto de Física, Universidad Nacional Autónoma de México, México D. F. 01000, México*

(Received 2 March 2015; published 11 June 2015)

New data are reported from the operation of a 2 liter C_3F_8 bubble chamber in the SNOLAB underground laboratory, with a total exposure of 211.5 kg days at four different energy thresholds below 10 keV. These data show that C_3F_8 provides excellent electron-recoil and alpha rejection capabilities at very low thresholds. The chamber exhibits an electron-recoil sensitivity of $< 3.5 \times 10^{-10}$ and an alpha rejection factor of $> 98.2\%$. These data also include the first observation of a dependence of acoustic signal on alpha energy. Twelve single nuclear recoil event candidates were observed during the run. The candidate events exhibit timing characteristics that are not consistent with the hypothesis of a uniform time distribution, and no evidence for a dark matter signal is claimed. These data provide the most sensitive direct detection constraints on WIMP-proton spin-dependent scattering to date, with significant sensitivity at low WIMP masses for spin-independent WIMP-nucleon scattering.

DOI: 10.1103/PhysRevLett.114.231302 PACS numbers: 95.35.+d, 29.40.Gx, 29.40.Vj, 95.55.Vj

Understanding the nature of dark matter is one of the most important goals in modern particle physics [1,2]. A leading candidate to explain the dark matter is a relic density of cold, nonbaryonic weakly interacting massive particles or WIMPs, and direct detection dark matter experiments hope to observe the nuclei recoiling from the rare collisions of WIMPs with ordinary matter [3–6]. Historically, the interaction of dark matter with normal matter has been divided into two categories, spin dependent (SD) and spin independent (SI).

The superheated detector technology has been at the forefront of SD searches [7–10], using refrigerant targets including CF_3I, C_4F_{10} and C_2ClF_5, and two primary types of detectors: bubble chambers and droplet detectors. The PICO Collaboration (formed from the merger of PICASSO and COUPP) has now operated a 2.90 kg C_3F_8 bubble chamber from October 2013 to May 2014 in the SNOLAB underground laboratory in Canada, at 6010 m of water equivalent depth. Here, we report results from that run.

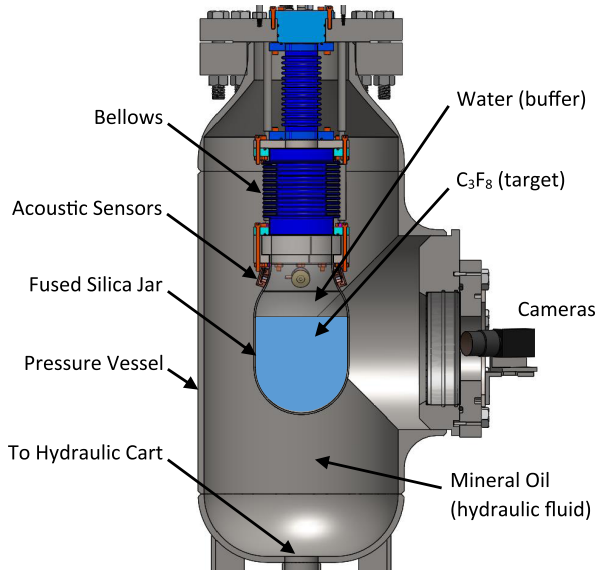

FIG. 1 (color online). A schematic of the PICO-2L bubble chamber.

The bubble chamber (called PICO-2L) deployed in this experiment was very similar to the 2 liter chambers described previously [7,8], primarily consisting of a fused-silica jar sealed to a flexible, stainless steel bellows, all immersed in a pressure vessel filled with hydraulic fluid. The jar was filled with 2.90 ± 0.01 kg of C_3F_8 (2.09 liters of fluid at a density of 1.39 kg/liter at 12 °C and 30 psia), as measured by a scale, with the uncertainty due to losses in the fill lines and electronic noise in the scale readout. To isolate it from contact with any stainless steel surfaces or seals, the C_3F_8 is topped with a water buffer layer. A schematic of the chamber is shown in Fig. 1.

Three lead zirconate (PZT) acoustic transducers epoxied to the exterior of the fused-silica jar recorded the acoustic emissions from bubble nucleations [11]. Previously, high levels of radioactivity in the transducers provided a measurable neutron rate [7]. For PICO-2L, we developed PZT sensors from source material with a factor 100 reduction in radioactivity. The acoustic signals were digitized with a sampling rate of 2.5 MHz. Two video graphics array resolution CCD cameras photographed the chamber at a rate of 100 frames per second.

The PICO-2L event cycle was similar to that described previously [7]. The chamber was operated at four pressure and temperature combinations, listed in Table I. The pressure and temperature determine the conditions for radiation-induced bubble nucleation, approximated by Seitz's "hot spike" model [12] in which the particle interaction must provide the energy necessary to produce a critically sized bubble. We follow the method described in [13] to calculate the Seitz threshold for bubble nucleation (E_T) for each run condition of PICO-2L and for the remainder of the Letter refer to each data set by the calculated threshold. We quote both experimental and theoretical uncertainties in E_T, the former from uncertainties in the pressure and temperature of the target fluid, and the latter from uncertainties in the surface tension for very small bubbles [13].

The chamber was exposed to an AmBe calibration source ten times during the run to monitor the detector response to nuclear recoils. All calibration data were hand scanned to check bubble multiplicities, and hand-scanned single bubble events were used to determine the data cleaning cut efficiencies.

The data analysis begins with an image reconstruction algorithm to identify bubbles and their locations in 3D space. An optical-based fiducial volume cut is derived from neutron calibration data such that 1% or fewer of wall or surface events, defined as events located on the glass jar or at the interface between the C_3F_8 and water buffer respectively, are reconstructed as bulk events, defined as bubbles that do not touch either the glass or water. The efficiency of the optical fiducial cut is determined to be 0.82 ± 0.01 by volume (all error bars on cut efficiencies are 1σ and represent total uncertainties).

In [7], the rate-of-pressure rise during an event was used as a highly efficient fiducial volume cut, as bubble growth is affected by proximity to the jar or the liquid interface. A similar analysis was implemented in PICO-2L with an efficiency of 0.92 ± 0.02, in agreement with [7]. The pressure-rise analysis could not be applied to all data as improvements to the PICO-2L data acquisition system and hydraulic cart reduced the time between trigger and compression, stopping bubble growth before the pressure could increase significantly. A trigger delay of 10–40 ms was imposed for most of the low threshold data to allow

TABLE I. Table describing the four operating conditions and their associated exposures. The experimental uncertainty on the threshold comes from uncertainties on the temperature (0.3 °C) and pressure (0.7 psi), while the theoretical uncertainty comes from the thermodynamic properties of C_3F_8 (primarily the surface tension).

T (°C)	P (psia)	Seitz threshold, E_T (keV)	Livetime (d)	WIMP exposure (kg day)	No. of candidate events
14.2	31.1	$3.2 \pm 0.2(\text{exp}) \pm 0.2(\text{th})$	32.2	74.8	9
12.2	31.1	$4.4 \pm 0.3(\text{exp}) \pm 0.3(\text{th})$	7.5	16.8	0
11.6	36.1	$6.1 \pm 0.3(\text{exp}) \pm 0.3(\text{th})$	39.7	82.2	3
11.6	41.1	$8.1 \pm 0.5(\text{exp}) \pm 0.4(\text{th})$	18.2	37.8	0

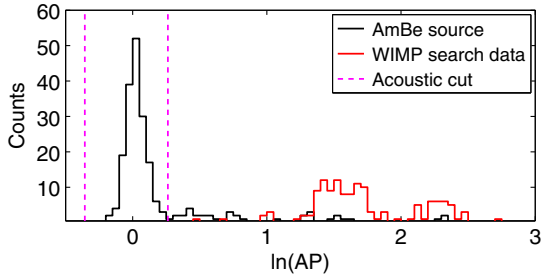

FIG. 2 (color online). AP distributions for neutron calibration data (black) and WIMP search data (red) at 4.4-keV threshold. Note that the x axis shows $\ln(AP)$. As discussed in the text, alphas from the ^{222}Rn decay chain can be identified by their time signature and populate the two peaks in the WIMP search data at high AP, with higher energy alphas from ^{214}Po producing larger acoustic signals.

more time for the bubble to evolve, enabling use of the pressure-rise cut. For the higher threshold data without the trigger delay, the optical fiducial cut is used.

The acoustic analysis follows the procedure described in [7] to define AP, a measurement of the acoustic power released in an event. Figure 2 shows the AP distributions for calibration and WIMP search data at a threshold of 4.4 keV. The AP distribution is normalized to have a value of unity at the nuclear recoil peak observed in the AmBe data, and an acoustic cut is applied to select these events. For the two low threshold data sets, we adopt the same acoustic cut as in [7,8], such that $0.7 < AP < 1.3$. Because of the decreased acoustic signal at higher operating pressure, the width of the calibration peak at 6.1-keV threshold is a factor of 1.5 larger than at low thresholds; the acceptance region for this data set is chosen such that the difference between the cut value and the mean divided by the resolution is the same as for low thresholds ($0.55 < AP < 1.45$). At 8.1-keV threshold, some neutron-induced events are too quiet to be registered acoustically, so all events with $AP < 2$ are counted as nuclear recoil events. The acceptance of these cuts for neutron-induced single bubble events was statistically indistinguishable for all data sets with a value of 0.91 ± 0.01.

A set of quality cuts is applied to all data to eliminate events with excessive acoustic noise, events where the cameras failed to capture the initiation of the bubble, and events in which the optical reconstruction algorithm failed to converge. The total efficiency of the data quality cuts is 0.961 ± 0.003. The total acceptance for neutron-induced, single nuclear recoils including fiducial, acoustic, and data quality cuts is 0.80 ± 0.02 for data with the trigger delay and the pressure rise based fiducial cut, decreasing to 0.72 ± 0.02 for the optical fiducial cut.

One of the main strengths of the superheated fluid detectors is their insensitivity to electronic recoils. The PICO-2L chamber was exposed to a 1 mCi ^{133}Ba source to confirm this behavior in C_3F_8. With no candidate events observed during the gamma exposure at 3.2 keV, the probability for a gamma interaction to nucleate a bubble was determined to be less than 3.5×10^{-10} at 90% C.L. by performing a GEANT4 [14] Monte Carlo simulation of the source and counting the total number of above-threshold interactions of any kind in the active target. Combining these results with a dedicated NaI measurement of the gamma flux at the location of the chamber in the absence of any sources [15], we expect electronic recoils to produce fewer than 0.05 events in the PICO-2L WIMP search data.

A second key method for background rejection in superheated detectors is the acoustic rejection of alpha decays [7,8,10,16]. PICO-2L observed a rate of high-AP events at 4.4-keV threshold immediately after the initial fill that decayed with a half-life consistent with that of ^{222}Rn to a steady state of about 4 events/day. None of the high acoustic power events leak into the nuclear recoil acceptance band in that data set, confirming that acoustic alpha rejection is present in the C_3F_8 target. The 4.4-keV data provide a statistics-limited, 90% lower limit on the alpha rejection in PICO-2L of 98.2%.

In addition to the acoustic discrimination, PICO-2L data show a dependence of AP on alpha energy that was not previously observed in CF_3I. At low threshold, two distinct peaks appear at high AP (see Fig. 2). The time structure of the high-AP peaks is consistent with that of the fast radon chain (^{222}Rn, ^{218}Po, and ^{214}Po decays having energies of 5.5, 6.0, and 7.7 MeV, respectively). The events in the louder peak come primarily from the third event in the chain, the high energy ^{214}Po decay. To our knowledge, this constitutes a first instance of particle energy spectroscopy using acoustic methods.

Background neutrons produced primarily by (α,n) and spontaneous fission from nearby ^{238}U and ^{232}Th can produce both single and multiple bubble events. We perform a detailed Monte Carlo simulation of the detector to model the neutron backgrounds, predicting 0.9 (1.6) single (multiple) bubble events in the entire data set, for an event rate of 0.004(0.006) cts/kg/day, with a total uncertainty of 50%. There were no multiple bubble events observed in the WIMP search data, providing a 90% C.L. upper limit of 0.008 cts/kg/day, consistent with the background model.

The sensitivity of the experiment to dark matter depends crucially on the efficiency with which nuclear recoils at a given energy produce bubbles. The classical Seitz model [12] indicates that nuclear recoils of energy greater than E_T will create bubbles with 100% efficiency, but past results show that the model does not accurately describe the efficiency for detecting low energy carbon and fluorine recoils in CF_3I [7,17]. This breakdown is attributed to the relatively large size of carbon and fluorine recoil tracks in CF_3I, as bubble nucleation only occurs if the energy deposition is contained within a critical bubble size. Iodine recoils in CF_3I have much shorter tracks and have

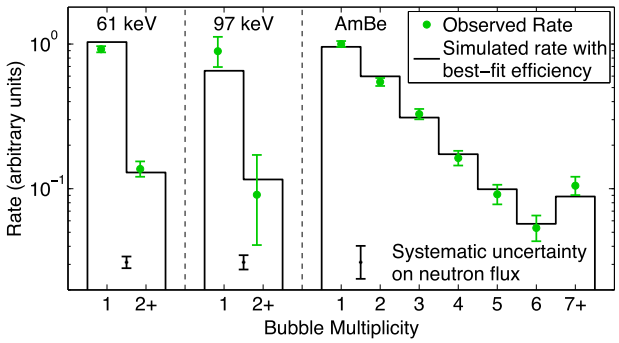

FIG. 3 (color online). The green points show the observed rates of single and multiple bubbles for the calibration sources at a thermodynamic threshold of 3.2 keV. Green error bars indicate statistical uncertainties, and the black error bars at the bottom show the systematic uncertainty on the neutron flux (a flat percent uncertainty that is common to all multiplicities in a given data set at the 10%, 12%, and 30% levels for 61-keV, 97-keV and AmBe data, respectively). The black histograms show the predicted rates from the simulation given the best-fit efficiency model derived from all calibration data.

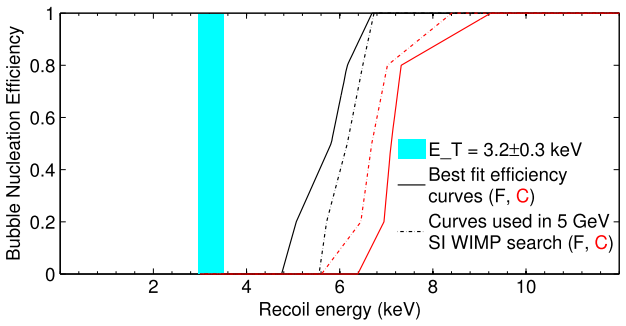

FIG. 4 (color online). The best-fit fluorine (black) and carbon (red) efficiency curves for 3.2-keV data are shown by the solid lines. The dashed lines show the curves used to determine sensitivity for a 5 GeV SI WIMP. The light blue band shows the calculated Seitz threshold with the experimental and theoretical uncertainties from Table I added in quadrature.

been shown to more closely match the Seitz model predictions [13]. Simulations of nuclear recoil track geometries using the SRIM package [18] as well as measurements in C_4F_{10} [19] indicate that fluorine recoils in C_3F_8 are also in the regime where the Seitz model is a close approximation for bubble nucleation.

To confirm this expectation, we performed neutron calibrations *in situ* in the PICO-2L chamber with an AmBe neutron source. We also deployed a ~30-ml C_3F_8 bubble chamber at the Tandem Van de Graaff facility at the University of Montreal, using well-defined resonances in the $^{51}V(p,n)^{51}Cr$ reaction to produce monoenergetic 61- and 97-keV neutrons. Each of the three neutron calibration experiments is simulated in MCNP [20] using updated differential cross sections for elastic scattering on fluorine [21].

A single calibration point, i.e., a bubble rate measured at a given thermodynamic threshold and produced by a single spectrum of nuclear recoil energies, can, in general, be fit by a family of possible nucleation efficiency curves. In this analysis, the fluorine and carbon efficiency curves at each threshold are fit by monotonically increasing, piecewise linear functions to allow for a variety of different efficiency shapes, with no reference to the Seitz theory except that bubble nucleation cannot occur for recoil energies below E_T (subject to the experimental uncertainties). In addition, the carbon efficiency is assumed to be less than or equal to the fluorine efficiency at a given recoil energy from track geometry considerations. Figure 3 shows the observed rates of single and multiple bubbles for the AmBe and test beam sources compared to the best-fit efficiency model at a thermodynamic threshold of 3.2 keV. The best-fit efficiency curves for fluorine and carbon at 3.2 keV are shown by the solid lines in Fig. 4.

We take a conservative approach when determining the sensitivity of PICO-2L to dark matter. For each WIMP mass and coupling, we select the pair of fluorine and carbon efficiency curves giving the worst sensitivity for that particular WIMP that is consistent with the calibrations at 1σ. As an example, the dashed lines in Fig. 4 show the actual efficiency curves used to determine the sensitivity of the experiment for a 5 GeV SI WIMP for the $E_T = 3.2$-keV data set. For this case, where most of the sensitivity to WIMPs comes from the lowest energy fluorine recoils, our conservative approach uses a weaker response to fluorine relative to the best-fit case (e.g., the turn-on is shifted to slightly higher energies). Because the total rate in the calibration data is unchanged, the fit compensates for the weaker fluorine response by assuming a larger contribution from carbon. The difference between the solid and dashed lines is small, attesting to how well the calibration data constrain the C_3F_8 response.

As shown in Table I, WIMP search data were taken at four different thresholds, with most data coming at thresholds of 3.2 and 6.1 keV. There are nine candidate events within the *AP* acceptance region at 3.2 keV and three candidate events at 6.1 keV, with no candidate events

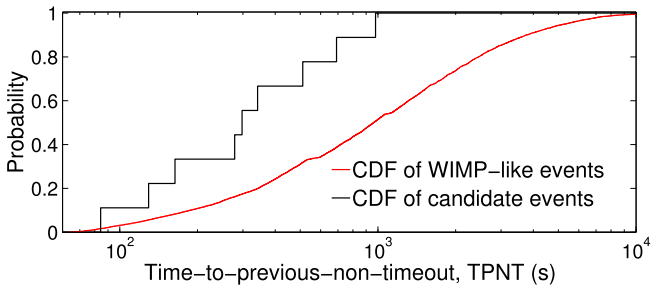

FIG. 5 (color online). The CDF of the TPNT for events with random timing (simulated WIMP-like events) and the 3.2-keV candidate events. The two distributions are not consistent with each other.

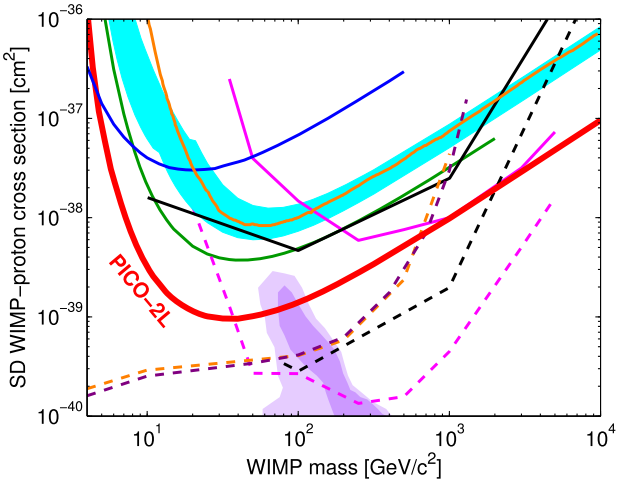

FIG. 6 (color online). The 90% C.L. limit on the SD WIMP-proton cross section from PICO-2L is plotted in red, along with limits from COUPP (light blue region), PICASSO (dark blue), SIMPLE (green), XENON100 (orange), IceCube (dashed and solid pink), SuperK (dashed and solid black), CMS (dashed orange), and ATLAS (dashed purple) [7,9,10,26–30]. For the IceCube and SuperK results, the dashed lines assume annihilation to W pairs while the solid lines assume annihilation to b quarks. Comparable limits assuming these and other annihilation channels are set by the ANTARES, Baikal, and Baksan neutrino telescopes [31–33]. The CMS and ATLAS limits assume an effective field theory, valid for a heavy mediator. The purple region represents parameter space of the constrained minimal supersymmetric model of [25].

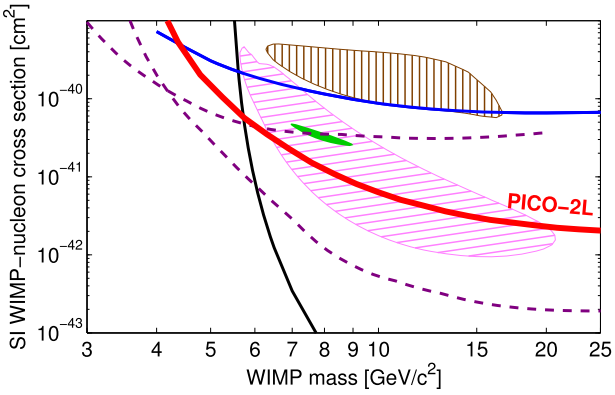

FIG. 7 (color online). The 90% C.L. limit on the SI WIMP-nucleon cross section from PICO-2L is plotted in red, along with limits from PICASSO (blue), LUX (black), CDMS-lite and SuperCDMS (dashed purple) [9,34–36]. Similar limits that are not shown for clarity are set by XENON10, XENON100, and CRESST-II [37–39]. Allowed regions from DAMA (hashed brown), CoGeNT (solid green), and CDMS-Si (hashed pink) are also shown [40–42].

observed at 4.4 and 8.1 keV. All 12 candidate events were hand scanned and found to be well reconstructed, bulk events.

In [7], WIMP-candidate events were observed exhibiting correlations with events in previous expansions, and the candidate events in PICO-2L exhibit similar correlations. To explore this anomaly further, simulated events with random timing are populated into the actual data to model the expected timing distribution of a potential WIMP signal. Figure 5 shows the cumulative distribution function (CDF) of the time to previous non-timeout (TPNT) for a randomly distributed sample, along with the TPNT for each candidate event at 3.2 keV. A Kolmogorov-Smirnov test comparing the two samples returns a p value of 0.04 that they are drawn from the same distribution. Given these results, the candidate events are not treated as evidence for a dark matter signal but instead as an unknown background. Studies are now underway to test hypotheses for the source of these events.

The correlation of the candidate events with previous bubbles can be used to set a stronger constraint on WIMP-nucleon scattering by applying a cut on TPNT. Since there is no valid basis for setting the cut value *a priori*, a method based closely on the optimum interval method [22] is used to provide a true upper limit with TPNT cuts for each WIMP mass optimized simultaneously over all four operating thresholds. The optimum cuts remove all 12 candidate events at each WIMP mass, while retaining 49%–63% of the efficiency weighted exposure, with the range due to changes in the relative weighting of the four threshold conditions for different WIMP masses. If the optimum cuts had simply been set *a posteriori*, without applying the tuning penalty inherent in the optimization method, the cross section limits would be a factor of 1.2–2.4 lower than reported here, with the bigger factor applying to higher WIMP masses.

The limit calculations assume the standard halo parametrization [23], with $\rho_D = 0.3$ GeV c^{-2} cm^{-3}, $v_{\rm esc} = 544$ km/s, $v_{\rm Earth} = 232$ km/s, $v_0 = 220$km/s, and the spin-dependent parameters from [24], and the resulting 90% C.L. limit plots for spin-independent WIMP-nucleon and spin-dependent WIMP-proton cross sections are presented in Figs. 7 and 6. Using the same parameters as in [23] would yield approximately 5%–20% stronger limits depending on the WIMP mass. The results shown here represent the most stringent constraint on SD WIMP-proton scattering from a direct detection experiment and the first time supersymmetric parameter space has been probed by direct detection in the SD-proton channel (e.g., the purple region, taken from [25]).

The PICO Collaboration would like to thank SNOLAB and its staff for providing an exceptional underground laboratory space and invaluable technical support. This material is based upon work supported by the U.S. Department of Energy, Office of Science, Office of High Energy Physics under award DE-SC-0012161. Fermi National Accelerator Laboratory is operated by Fermi Research Alliance, LLC under Contract

No. De-AC02-07CH11359. Part of the research described in this paper was conducted under the Ultra Sensitive Nuclear Measurements Initiative at Pacific Northwest National Laboratory, a multiprogram national laboratory operated by Battelle for the U.S. Department of Energy. We acknowledge the National Science Foundation for their support including Grants No. PHY-1242637, No. PHY-0919526, and No. PHY-1205987. We acknowledge the support of the National Sciences and Engineering Research Council of Canada (NSERC) and the Canada Foundation for Innovation (CFI). We also acknowledge support from the Kavli Institute for Cosmological Physics at the University of Chicago. We acknowledge the financial support of the Spanish Ministerio de Economía y Competitividad, Consolider MultiDark CSD2009-00064 Grant. We acknowledge support from the Department of Atomic Energy (DAE), Government of India, under the Center for AstroParticle Physics II project (CAPP-II) at Saha Insititute of Nuclear Physics (SINP), Kolkata. We acknowledge the Czech Ministry of Education, Youth and Sports, Grant No. LM2011027. We acknowledge technical assistance from Fermilab's Computing, Particle Physics, and Accelerator Divisions, and from A. Behnke at IUSB.

[1] S. Ritz *et al.*, http://www.usparticlephysics.org/p5/.
[2] P. Cushman *et al.*, arXiv:1310.8327.
[3] E. Komatsu *et al.*, Astrophys. J. Suppl. Ser. **180**, 330 (2009), and references therein.
[4] G. Jungman, M. Kamionkowski, and K. Griest, Phys. Rep. **267**, 195 (1996).
[5] G. Bertone, D. Hooper, and J. Silk, Phys. Rep. **405**, 279 (2005); J. L. Feng, Annu. Rev. Astron. Astrophys. **48**, 495 (2010).
[6] M. W. Goodman and E. Witten, Phys. Rev. D **31**, 3059 (1985).
[7] E. Behnke *et al.*, Phys. Rev. D **86**, 052001 (2012).
[8] E. Behnke *et al.*, Phys. Rev. Lett. **106**, 021303 (2011).
[9] S. Archambault *et al.*, Phys. Lett. B **711**, 153 (2012).
[10] M. Felizardo *et al.*, Phys. Rev. D **89**, 072013 (2014).
[11] D. A. Glaser and D. C. Rahm, Phys. Rev. **97**, 474 (1955).
[12] F. Seitz, Phys. Fluids **1**, 2 (1958).
[13] E. Behnke *et al.*, Phys. Rev. D **88**, 021101 (2013).
[14] S. Agostinelli *et al.*, Nucl. Instrum. Methods Phys. Res., Sect. A **506**, 250 (2003); J. Allison *et al.*, IEEE Trans. Nucl. Sci. **53**, 270 (2006).
[15] D. Fustin, Ph.D. thesis, University of Chicago, 2012; A. Robinson, COUPP Doc. 630: High Energy Gamma Flux and Photonuclear Rates in COUPP-4kg at SNOLAB, 2012 (unpublished).
[16] F. Aubin *et al.*, New J. Phys. **10**, 103017 (2008).
[17] A. Robinson, https://kicp-workshops.uchicago.edu/IDM2012/depot/talk-robinson-alan.pdf.
[18] J. F. Ziegler *et al.*, *SRIM: The Stopping and Range of Ions in Solids* (Pergamon Press, New York, 1985).
[19] S. Archambault *et al.*, New J. Phys. **13**, 043006 (2011).
[20] S. A. Pozzi, E. Padovani, and M. Marseguerra, Nucl. Instrum. Methods Phys. Res., Sect. A **513**, 550 (2003).
[21] A. E. Robinson, Phys. Rev. C **89**, 032801 (2014).
[22] S. Yellin, Phys. Rev. D **66**, 032005 (2002).
[23] J. D. Lewin and P. F. Smith, Astropart. Phys. **6**, 87 (1996).
[24] D. R. Tovey , R. J. Gaitskell, P. Gondolo, Y. Ramachers, and L. Roszkowski, Phys. Lett. B **488**, 17 (2000).
[25] L. Roszkowski, R. R. de Austri, and R. Trotta, J. High Energy Phys. 07 (2007) 075.
[26] E. Aprile *et al.*, Phys. Rev. Lett. **111**, 021301 (2013).
[27] M. G. Aartsen *et al.*, Phys. Rev. Lett. **110**, 131302 (2013).
[28] T. Tanaka *et al.*, Astrophys. J. **742**, 78 (2011).
[29] S. Chatrchyan *et al.*, Phys. Rev. Lett. **108**, 261803 (2012).
[30] ATLAS Collaboration, Eur. Phys. J. C 75 (2015).
[31] S. Adrián-Martínez *et al.*, J. Cosmol. Astropart. Phys. 11 (2013) 032.
[32] S. Demidov and O. Suvorova, J. Cosmol. Astropart. Phys. 06 (2010) 018.
[33] A. D. Avrorin *et al.*, Astropart. Phys. **62**, 12 (2015).
[34] D. S. Akerib *et al.*, Phys. Rev. Lett. **112**, 091303 (2014).
[35] R. Agnese *et al.*, Phys. Rev. Lett. **112**, 241302 (2014).
[36] R. Agnese *et al.*, Phys. Rev. Lett. **112**, 041302 (2014).
[37] J. Angle *et al.*, Phys. Rev. Lett. **107**, 051301 (2011).
[38] E. Aprile *et al.*, Phys. Rev. Lett. **109**, 181301 (2012).
[39] G. Angloher *et al.*, Eur. Phys. J. C **74**, 3184 (2014).
[40] R. Bernabei *et al.*, Eur. Phys. J. C **56**, 333 (2008).
[41] C. E. Aalseth *et al.*, Phys. Rev. D **88**, 012002 (2013).
[42] R. Agnese *et al.*, Phys. Rev. D **88**, 031104 (2013).

Appendix III

PICO-2L Paper - Run 2

RAPID COMMUNICATIONS

PHYSICAL REVIEW D **93,** 061101(R) (2016)

Improved dark matter search results from PICO-2L Run 2

C. Amole,[1,*] M. Ardid,[2] I. J. Arnquist,[3] D. M. Asner,[3] D. Baxter,[4] E. Behnke,[5] P. Bhattacharjee,[6] H. Borsodi,[5] M. Bou-Cabo,[2] S. J. Brice,[7] D. Broemmelsiek,[7] K. Clark,[8] J. I. Collar,[9] P. S. Cooper,[7] M. Crisler,[7] C. E. Dahl,[4,7] M. Das,[6] F. Debris,[10] S. Fallows,[11] J. Farine,[12] I. Felis,[2] R. Filgas,[13] M. Fines-Neuschild,[10] F. Girard,[12,10] G. Giroux,[1] J. Hall,[3] O. Harris,[5] E. W. Hoppe,[3] C. M. Jackson,[10] M. Jin,[4] C. B. Krauss,[11] M. Lafrenière,[10] M. Laurin,[10] I. Lawson,[12,14] A. Leblanc,[12] I. Levine,[5] W. H. Lippincott,[7] E. Mann,[5] J. P. Martin,[10] D. Maurya,[15] P. Mitra,[11] S. Olson,[1] R. Neilson,[16] A. J. Noble,[1] A. Plante,[10] R. B. Podviianiuk,[12] S. Priya,[15] A. E. Robinson,[7] M. Ruschman,[7] O. Scallon,[12,10] A. Sonnenschein,[7] N. Starinski,[10] I. Štekl,[13] E. Vázquez-Jáuregui,[17] J. Wells,[5] U. Wichoski,[12] V. Zacek,[10] and J. Zhang[4]

(PICO Collaboration)

[1]*Department of Physics, Queen's University, Kingston, K7L 3N6, Canada*
[2]*Departamento de Fisica Aplicada, Universitat Politècnica València, València 46022, Spain*
[3]*Pacific Northwest National Laboratory, Richland, Washington 99354, USA*
[4]*Department of Physics and Astronomy, Northwestern University, Evanston, Illinois 60208, USA*
[5]*Department of Physics, Indiana University South Bend, South Bend, Indiana 46634, USA*
[6]*Saha Institute of Nuclear Physics, AstroParticle Physics and Cosmology Division, Kolkata 700064, India*
[7]*Fermi National Accelerator Laboratory, Batavia, Illinois 60510, USA*
[8]*Department of Physics, University of Toronto, Toronto, Ontario M5S 1A7, Canada*
[9]*Enrico Fermi Institute, KICP and Department of Physics, University of Chicago, Chicago, Illinois 60637, USA*
[10]*Département de Physique, Université de Montréal, Montréal H3C 3J7, Canada*
[11]*Department of Physics, University of Alberta, Edmonton T6G 2E1, Canada*
[12]*Department of Physics, Laurentian University, Sudbury P3E 2C6, Canada*
[13]*Institute of Experimental and Applied Physics, Czech Technical University in Prague, Prague Cz-12800, Czech Republic*
[14]*SNOLAB, Lively, Ontario P3Y 1N2, Canada*
[15]*Bio-Inspired Materials and Devices Laboratory (BMDL), Center for Energy Harvesting Material and Systems (CEHMS), Virginia Tech, Blacksburg, Virginia 24061, USA*
[16]*Department of Physics, Drexel University, Philadelphia, Pennsylvania 19104, USA*
[17]*Instituto de Física, Universidad Nacional Autónoma de México, México D.F. 01000, México*

(Received 15 January 2016; published 21 March 2016)

New data are reported from a second run of the 2-liter PICO-2L C_3F_8 bubble chamber with a total exposure of 129 kg-days at a thermodynamic threshold energy of 3.3 keV. These data show that measures taken to control particulate contamination in the superheated fluid resulted in the absence of the anomalous background events observed in the first run of this bubble chamber. One single nuclear-recoil event was observed in the data, consistent both with the predicted background rate from neutrons and with the observed rate of unambiguous multiple-bubble neutron scattering events. The chamber exhibits the same excellent electron-recoil and alpha decay rejection as was previously reported. These data provide the most stringent direct detection constraints on weakly interacting massive particle (WIMP)-proton spin-dependent scattering to date for WIMP masses < 50 GeV/c^2.

DOI: 10.1103/PhysRevD.93.061101

I. INTRODUCTION

The evidence for nonbaryonic dark matter is well established [1,2] and understanding the nature of particle dark matter is currently one of the most important quests in the field of particle physics [3]. Weakly interacting massive particles (WIMPs) are a leading candidate for the cold dark matter in the Universe and provide solutions for outstanding issues in both cosmology and particle physics [4].

The sensitivity of a dark matter direct detection experiment depends on the WIMP mass and on the nature and strength of its coupling to atomic nuclei [5–7]. Since theory provides little guidance as to the WIMP mass or coupling, it is important to explore multiple nuclear targets sensitive to various WIMP-nucleon couplings, including spin-dependent WIMP-proton, spin-dependent WIMP-neutron and spin-independent interactions. The ^{19}F nucleus, because

*camole@owl.phy.queensu.ca

of its single unpaired proton and 100% isotopic abundance, provides a unique target to search for the spin-dependent WIMP-proton interactions. Experiments utilizing superheated fluorine-based liquids have consistently produced the strongest constraints on such interactions [8–13].

The PICO Collaboration recently reported the observation of anomalous background events in dark matter search data with the 2-liter PICO-2L C_3F_8 bubble chamber [8] deployed in the SNOLAB underground laboratory. The events were correlated in time with previous activity in the bubble chamber, and thus they were inconsistent with dark matter interactions and known backgrounds. Anomalous events with similar characteristics have also been reported in CF_3I bubble chambers [9,10]. While analysis cuts based on the event timing were able to recover the dark matter sensitivity in Run-1 [8], the presence of an unexplained background clearly indicated a limit to the technology and precluded scaling to a larger experiment.

PICO-2L Run-2 was initiated to explore the hypothesis that the anomalous background events observed in Ref. [8] were caused by particulate contamination in the bubble chamber fluid. Particulate contamination is not present on the bubble chamber components following ultrasonic cleaning, yet it is expected from both the silica and stainless steel components of the bubble chamber. Stainless steel particulate is not produced in significant quantity during the assembly of the bubble chamber, but is expected to appear over the course of the run due to metal fatigue from the flexing action of the bellows and from corrosion. Silica particulate contamination is expected to arise primarily from fracturing of the mating surface of the silica inner vessel flange due to the mechanical stresses associated with its seal to the metal bellows flange. Stress fracturing [14] can result in significant production of silica particulate during the assembly of the vessel and, once initiated, stress corrosion fatigue is expected to provide an ongoing source of new silica particulate contamination.

II. PARTICULATE MITIGATION

Measures taken to reduce the silica particulate contamination prior to Run-2 include the replacement of the quartz flange originally supplied on the fused silica inner vessel with a new flange fabricated from Corning 7980 Fused Silica [15]. In addition to being lower in radioactivity than quartz, the Corning material has fewer impurities, inclusions, and surface flaws and is therefore more likely to be resistant to stress fracturing [14,16] and to the production of silica particles. A second measure was to modify the assembly sequence and fixtures to facilitate a more thorough rinse of the assembled vessel to remove silica particles that might have been generated during the assembly of the seal. Following the final rinse, the inner vessel assembly was dried using filtered gas flow and elevated temperature and it was evacuated and leak-checked using a turbo vacuum pump [17], eliminating all exposure of the inner vessel to a scroll vacuum pump [18] that was identified as a potential source of contamination in Ref. [8].

No measures were taken to mitigate the production of stainless steel particulate from the bellows prior to Run-2. Possible measures that were considered included specialized coatings to suppress particulate emission, a plastic bellows liner to contain the stainless steel particles, and replacement of the stainless steel bellows with a bellows formed from an alternative material. To avoid the possibility that the introduction of new construction materials might complicate the comparison of Run-2 to Ref. [8], the measures to mitigate the stainless steel contamination were deferred. For the same reason, a system developed for recirculation and filtering of chamber fluids was not implemented in Run-2. Consequently, the initial condition of the Run-2 bubble chamber was as identical as possible to the initial condition of Ref. [8], except for the reduction of silica and possible scroll pump particulate contamination, allowing for a direct comparison free from systematic differences.

Additional measures were also taken to reduce the agitation of the chamber to encourage settling of particulate, and to avoid stirring up any particles that might have settled out on the bubble chamber surfaces or the fluid interface. These measures include a careful optimization of triggering, expansion, and compression parameters, increasing the compression time between bubble nucleation events, and raising the pressure of the chamber from 31.1 psia, as in Ref. [8], to 37.2 psia, reducing the volatility of bubble growth. The Run-2 temperature was correspondingly increased in order to maintain the same 3.3 keV thermodynamic energy threshold as Ref. [8].

III. OTHER MODIFICATIONS

Several technical improvements unrelated to background reduction were implemented to improve the performance of the bubble chamber for Run-2. The number of temperature sensors was doubled and additional cooling was added to the top flange of the pressure vessel and to the camera enclosures to improve temperature uniformity across the active volume. Modifications were made to add over-voltage protection to the lead zirconate acoustic transducers and their number was increased from three to six to address a reliability problem encountered in Ref. [8]. The VGA resolution cameras (491×656) used in Ref. [8] were replaced with higher-resolution (1280×1024) devices to improve the spatial resolution of bubble position reconstruction.

IV. OPERATIONS

The target mass of 2.91 ± 0.01 kg of C_3F_8 was kept in a superheated state at a temperature of 15.8 °C and a pressure of 37.2 psia. For these run conditions, the thermodynamic threshold energy is estimated using the Seitz "hot spike" model [19] and is calculated to be $3.3 \pm 0.2(\text{exp}) \pm 0.2(\text{th})$ keV, with the experimental uncertainty originating

from the uncertainty in temperature (0.3 °C) and pressure (0.7 psi) and the theoretical uncertainty attributed to the thermodynamic properties of C_3F_8. The Run-2 thermodynamic threshold is equivalent to the lowest threshold reported in Ref. [8] but at a higher temperature and pressure. The gross activity of the chamber in Run-2, measured by the number of expansions and the mean superheat time per expansion was comparable to Ref. [8].

A total of 66.3 live-days of WIMP search data was collected at the 3.3 keV thermodynamic threshold between June 12 and September 25, 2015. During this time, the detector was twice exposed to an AmBe calibration source to monitor the response to nuclear recoils from neutrons, and twice to a ^{133}Ba source to evaluate the response to gamma-induced electron recoils. Data collected within 24 hours after any technical interruption were not included in the WIMP search.

V. ANALYSIS

The data analysis presented here uses techniques similar to those described in Ref. [8]. All the neutron calibration data were scanned by eye to check the bubble multiplicities and the identified single-bubble events were used to evaluate the efficiency of the data analysis cuts.

A set of data quality cuts was applied to remove events with failed optical reconstruction (bubble position and/or multiplicity), excessive acoustic noise, or poor agreement in the evaluated time of the bubble nucleation from the six acoustic transducers. The combined efficiency of the data quality cuts was 0.85 ± 0.02. The acoustic analysis was performed using a procedure described in Ref. [10], and the same acoustic parameter (AP) cut range of $0.7 < \mathrm{AP} < 1.3$ as in Refs. [8,10,11] was adopted. The AP distributions for WIMP search and calibration data are shown in Fig. 1. The

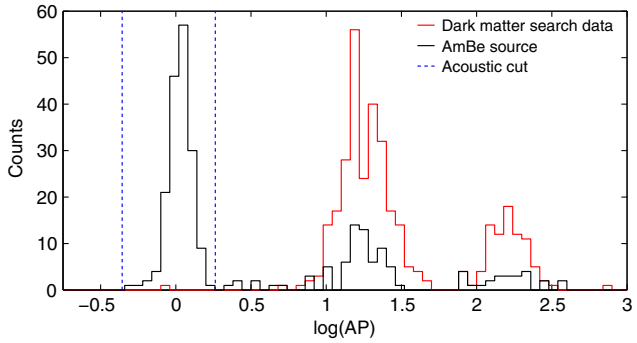

FIG. 1. AP distributions (in log scale) of the single-bubble events originating within the optical fiducial volume for neutron calibration data (black) and WIMP search data (red). The signal region in AP for single nuclear recoils is indicated between the dashed blue lines. In both the calibration and WIMP search data, the two peaks at higher AP are from ^{222}Rn chain alphas, with higher-energy alphas from ^{214}Po decay producing larger acoustic signals [8,9]. The observed rate of alpha decays is consistent between WIMP search and neutron calibration data.

AP cut has an acceptance of 0.94 ± 0.02 for neutron-induced single-bubble events and an alpha rejection of $> 98.8\%$ (90% C.L.). An optical-based fiducial volume cut was derived such that less than 1% of the events originating at the interfaces (between C_3F_8, water buffer and glass walls) were accepted to be in the fiducial bulk volume and had an efficiency of 0.84 ± 0.01.

The total acceptance for single-bubble nuclear-recoil events including data quality, AP, and fiducial cuts in this run was 0.67 ± 0.03, resulting in a total exposure after cuts of 129 kg-days. The position and acoustic resolution were significantly improved for Run-2, resulting in higher fiducial and AP cut efficiencies. However, the acceptance of the data quality cuts, and the total acceptance, was lower than in Ref. [8] due to water droplets on the inside wall of the inner vessel compromising the optical reconstruction of a fraction of the events, and additional transient acoustic noise.

To search for neutron-induced multiple-bubble events in the WIMP search data, all events for which more than one bubble is reconstructed in one or both of the camera images were manually scanned. The acceptance of this selection criterion was determined using the neutron calibration data to be 0.93 ± 0.01. This is substantially higher than the acceptance for single nuclear-recoil events since no acoustic or fiducial cuts are needed to identify multiple-bubble events.

VI. BACKGROUNDS

A constant rate (4 cts/day) of AP-tagged alpha decay events was observed, similar to Ref. [8]. Based on detailed Monte Carlo simulations, the background contribution from (α, n) and spontaneous fission neutrons was predicted to be 0.008(0.010) counts/kg/day for single(multiple)-bubble events, with a total uncertainty of 50%. This is higher than the estimate from Ref. [8], due to the addition to our simulation of (α, n) reactions on ^{14}N from radon-chain decays in air within the neutron shielding. The background model predicts 1.0(1.8) single(multiple)-bubble events from neutrons after all cuts. Fewer than 0.02 electron-recoil events were expected, based on a measurement of 4 candidate events during 12.2 live-days of exposure to a 1 mCi ^{133}Ba source coupled with a Monte Carlo simulation in GEANT4 [20] of the natural gamma flux at the location of the chamber [21,22]. The ^{133}Ba calibration result corresponds to a measured efficiency of $(2.2 \pm 1.2) \times 10^{-11}$ for electron recoils in C_3F_8 at a 3.3 keV thermodynamic threshold.

VII. RESULTS

A total of 1(3) single(multiple)-bubble nuclear-recoil events were observed in the 129 kg-day exposure. These data show the absence of the anomalous background events observed in the first run [8] of PICO-2L (Fig. 2). The

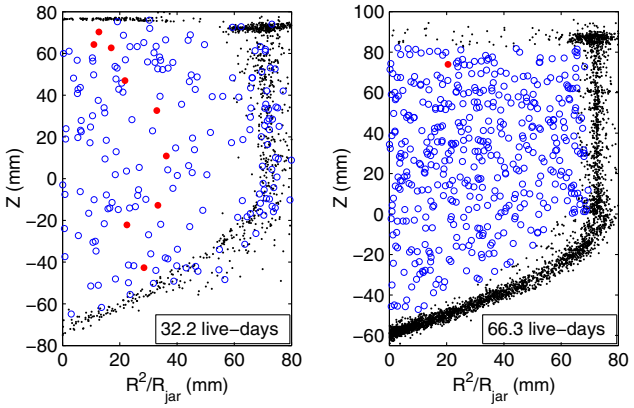

FIG. 2. Spatial distribution of bubble events in the 3.3 keV WIMP search data for Run-1 [8] (left, 32.2 live-days) and Run-2 (right, 66.3 live-days). Z is the reconstructed vertical position of the bubble, R is the distance from the center axis and R_{jar} is the nominal inner radius of the silica jar (72.5 mm). Red filled circles are WIMP-candidate events in the fiducial bulk volume, blue open circles are alpha-induced bulk events, and black dots are nonbulk events. The rate of pressure rise, measured by an AC-coupled transducer, was used for the fiducial volume cut in Ref. [8]. An identical transducer installed for Run-2 failed during commissioning, and the Run-2 fiducial volume cut is entirely based on the improved optical reconstruction.

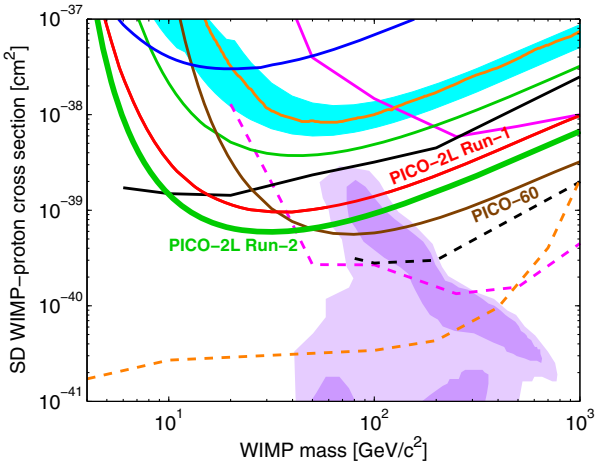

FIG. 3. The 90% C.L. limit on the SD WIMP-proton cross section from Run-2 (Run-1 [8]) of PICO-2L is plotted in green (red), along with limits from PICO-60 (brown), COUPP-4 (light blue region), PICASSO (dark blue), SIMPLE (thin green), XENON100 (orange), IceCube (dashed and solid pink), SuperK (dashed and solid black) and CMS (dashed orange) [9,10,12,13,25–29]. For the IceCube and SuperK results, the dashed lines assume annihilation to W pairs while the solid lines assume annihilation to b quarks. Comparable limits assuming these and other annihilation channels are set by the ANTARES, Baikal and Baksan neutrino telescopes [30–32]. The CMS limit is from a monojet search and assumes an effective field theory, valid only for a heavy mediator [33,34]. Comparable limits are set by ATLAS [35,36]. The purple region represents the parameter space of the constrained minimal supersymmetric standard model of Ref. [37].

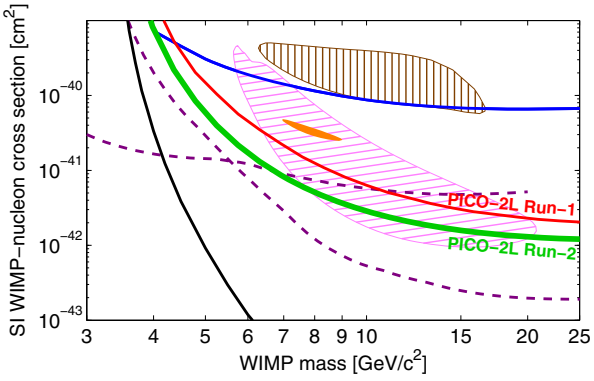

FIG. 4. The 90% C.L. limit on the SI WIMP-proton cross section from Run-2 (Run-1 [8]) of PICO-2L is plotted in green (red), along with limits from PICASSO (blue), LUX (black), CDMSlite and SuperCDMS (dashed purple) [12,38–40]. Similar limits that are not shown for clarity are set by XENON10, XENON100 and CRESST-II [41–43]. Allowed regions from DAMA (hashed brown), CoGeNT (solid orange), and CDMS-II Si (hashed pink) are also shown [44–46].

observed rate of both single- and multiple-bubble nuclear-recoil events is consistent with the expected background from neutrons. No neutron background subtraction is attempted, and the WIMP scattering cross-section upper limits reported here are simply calculated as the cross sections for which the probability of observing one or fewer signal events in the full 129 kg-day exposure is 10%.

The same conservative nucleation efficiency curves are used as in Ref. [8], with sensitivity to fluorine and carbon recoils above 5.5 keV. The standard halo parametrization [23] is adopted, with $\rho_D = 0.3$ GeV c^{-2} cm^{-3}, $v_{esc} = 544$ km/s, $v_{Earth} = 232$ km/s, $v_o = 220$ km/s, and the spin-dependent parameters are taken from Ref. [24]. Limits at the 90% C.L. for the spin-dependent WIMP-proton and spin-independent WIMP-nucleon elastic scattering cross sections are calculated as a function of WIMP mass and are shown in Figs. 3 and 4. These limits indicate an improved sensitivity to the dark matter signal compared to the previous PICO-2L run and are currently the world-leading constraints on spin-dependent WIMP-proton couplings for WIMP masses < 50 GeV/c^2. For WIMP masses higher than 50 GeV/c^2, only the constraints from PICO-60 [9] are stronger.

VIII. DISCUSSION

These data demonstrate the excellent performance of the PICO detector technology and provide strong evidence that particulate contamination suspended in the superheated fluid is the cause of the anomalous background events observed in the first run of this bubble chamber. Preliminary indications suggest that the radioactivity present in the particulate may be insufficient to account

for the events as originating with alpha decays, so the bubble-nucleation mechanism associated with the particulate contamination is still unknown. Nonetheless, the identification of particulate contamination as the origin of the anomalous background events observed in Ref. [8] provides the critical engineering guidance needed to develop a larger-scale background-free experiment.

ACKNOWLEDGMENTS

The PICO Collaboration thanks SNOLAB for their exceptional laboratory space and technical support. We also thank Fermi National Accelerator Laboratory (Contract No. DE-AC02-07CH11359) and Pacific Northwest National Laboratory for their support. This work is supported by the National Sciences and Engineering Research Council of Canada (NSERC), the Canada Foundation for Innovation (CFI), the National Science Foundation (NSF) under the Grants No. PHY-1242637, No. PHY-0919526, No. PHY-1205987, and No. PHY-1506377 and by the U.S. Department of Energy under Award No. DE-SC-0012161. We also acknowledge the support of Department of Atomic Energy (DAE), Government of India, under the Center of AstroParticle Physics II project (CAPP-II) at Saha Institute of Physics (SINP); the Czech Ministry of Education, Youth and Sports (Grant No. LM2011027); the Spanish Ministerio de Economia y Competitividad, Consolider MultiDark (Grant No. CSD2009-00064) and DGAPA-UNAM through grant PAPIIT No. IA100316.

[1] K. A. Olive *et al.* (Particle Data Group), Chin. Phys. C **38**, 090001 (2014).
[2] E. Komatsu *et al.*, Astrophys. J. Suppl. Ser. **180**, 330 (2009) and references therein.
[3] S. Ritz *et al.*, Particle physics projects prioritization panel report, 2014.
[4] G. Jungman, M. Kamionkowski, and K. Griest, Phys. Rep. **267**, 195 (1996).
[5] M. W. Goodman and E. Witten, Phys. Rev. D **31**, 3059 (1985).
[6] P. Cushman *et al.*, arXiv:1310.8327.
[7] G. Bertone, D. Hooper, and J. Silk, Phys. Rep. **405**, 279 (2005); J. L. Feng, Annu. Rev. Astron. Astrophys. **48**, 495 (2010).
[8] C. Amole *et al.*, Phys. Rev. Lett. **114**, 231302 (2015).
[9] C. Amole *et al.*, arXiv:1510.07754 [Phys. Rev. D (to be published)].
[10] E. Behnke *et al.*, Phys. Rev. D **86**, 052001 (2012).
[11] E. Behnke *et al.*, Phys. Rev. Lett. **106**, 021303 (2011).
[12] S. Archambault *et al.*, Phys. Lett. B **711**, 153 (2012).
[13] M. Felizardo *et al.*, Phys. Rev. D **89**, 072013 (2014).
[14] R. H. Doremus, in *Treatise on Materials Science and Technology, Vol. 22*, edited by R. H. Doremus and M. Tomozawa (Academic Press, New York, 1982), p. 169.
[15] Corning Incorporated, Specialty Materials Division.
[16] A. G. Evans, J. Mater. Sci. **9**, 1145 (1974).
[17] Pfeiffer Vacuum HiCube 80 Eco Turbo Pumping Station.
[18] Edwards nXDS6i scroll vacuum pump.
[19] F. Seitz, Phys. Fluids **1**, 2 (1958).
[20] S. Agostinelli *et al.*, Nucl. Instrum. Methods Phys. Res., Sect. A **506**, 250 (2003).
[21] D. Fustin, Ph.D thesis, University of Chicago, 2012.
[22] A. E. Robinson, Ph.D thesis, University of Chicago, 2015.
[23] J. D. Lewin and P. F. Smith, Astropart. Phys. **6**, 87 (1996).
[24] D. R. Tovey, R. J. Gaitskell, P. Gondolo, Y. Ramachers, and L. Roszkowski, Phys. Lett. B **488**, 17 (2000).
[25] E. Aprile *et al.*, Phys. Rev. Lett. **111**, 021301 (2013).
[26] M. G. Aartsen *et al.*, Phys. Rev. Lett. **110**, 131302 (2013).
[27] T. Tanaka *et al.*, Astrophys. J. **742**, 78 (2011).
[28] K. Choi *et al.*, Phys. Rev. Lett. **114**, 141301 (2015).
[29] V. Khachatryan *et al.* (CMS Collaboration), Eur. Phys. J. C **75**, 235 (2015).
[30] S. Adrián-Martínez *et al.*, J. Cosmol. Astropart. Phys. 11 (2013) 032.
[31] S. Demidov and O. Suvorova, J. Cosmol. Astropart. Phys. 06 (2010) 018.
[32] A. D. Avrorin *et al.*, Astropart. Phys. **62**, 12 (2015).
[33] G. Busoni, A. de Simone, E. Morgante, and A. Riotto, Phys. Lett. B **728**, 412 (2014).
[34] O. Buchmueller, M. J. Dolan, and C. McCabe, J. High Energy Phys. 01 (2014) 025.
[35] ATLAS Collaboration, Eur. Phys. J. C **75**, 299 (2015).
[36] ATLAS Collaboration, Eur. Phys. J. C **75**, 92 (2015).
[37] L. Roszkowski, R. R. de Austri, and R. Trotta, J. High Energy Phys. 07 (2007) 075.
[38] D. S. Akerib *et al.*, arXiv:1512.03506.
[39] R. Agnese *et al.*, Phys. Rev. Lett. **116**, 071301 (2016).
[40] R. Agnese *et al.*, Phys. Rev. Lett. **112**, 241302 (2014).
[41] J. Angle *et al.*, Phys. Rev. Lett. **107**, 051301 (2011).
[42] E. Aprile *et al.*, Phys. Rev. Lett. **109**, 181301 (2012).
[43] G. Angloher *et al.*, Eur. Phys. J. C **76**, 25 (2016).
[44] R. Bernabei *et al.*, Eur. Phys. J. C **56**, 333 (2008).
[45] C. E. Aalseth *et al.*, Phys. Rev. D **88**, 012002 (2013).
[46] R. Agnese *et al.*, Phys. Rev. D **88**, 031104 (2013).

Appendix IV

PICO-60 Paper - CF_3I

PHYSICAL REVIEW D **93,** 052014 (2016)

Dark matter search results from the PICO-60 CF_3I bubble chamber

C. Amole,[1] M. Ardid,[2] D. M. Asner,[3] D. Baxter,[4] E. Behnke,[5] P. Bhattacharjee,[6] H. Borsodi,[5] M. Bou-Cabo,[2] S. J. Brice,[7] D. Broemmelsiek,[7] K. Clark,[8] J. I. Collar,[9] P. S. Cooper,[7] M. Crisler,[7] C. E. Dahl,[4,7] S. Daley,[1] M. Das,[6] F. Debris,[10] N. Dhungana,[11] S. Fallows,[13] J. Farine,[11] I. Felis,[2] R. Filgas,[12] F. Girard,[11,10] G. Giroux,[1] A. Grandison,[5] M. Hai,[9] J. Hall,[3] O. Harris,[5,†] M. Jin,[4] C. B. Krauss,[13] M. Lafrenière,[10] M. Laurin,[10] I. Lawson,[14,11] I. Levine,[5] W. H. Lippincott,[7,*] E. Mann,[5] D. Maurya,[15] P. Mitra,[13] R. Neilson,[9,16] A. J. Noble,[1] A. Plante,[10] R. B. Podviianiuk,[11] S. Priya,[15] E. Ramberg,[7] A. E. Robinson,[9] R. Rucinski,[7] M. Ruschman,[7] O. Scallon,[11,10] S. Seth,[6] P. Simon,[7] A. Sonnenschein,[7] I. Štekl,[12] E. Vázquez-Jáuregui,[17,14,11] J. Wells,[5] U. Wichoski,[11] V. Zacek,[10] J. Zhang,[4] and I. A. Shkrob[18]

(PICO Collaboration)

[1]*Department of Physics, Queen's University, Kingston, Ontario K7L 3N6, Canada*
[2]*Universitat Politècnica de València, IGIC, 46730 Gandia, Spain*
[3]*Pacific Northwest National Laboratory, Richland, Washington 99354, USA*
[4]*Department of Physics and Astronomy, Northwestern University, Evanston, Illinois 60208, USA*
[5]*Department of Physics and Astronomy, Indiana University South Bend, South Bend, Indiana 46634, USA*
[6]*Saha Institute of Nuclear Physics, Astroparticle Physics and Cosmology Division, Kolkata 700064, India*
[7]*Fermi National Accelerator Laboratory, Batavia, Illinois 60510, USA*
[8]*Department of Physics, University of Toronto, Toronto, Ontario M5S 1A7, Canada*
[9]*Enrico Fermi Institute, KICP and Department of Physics, University of Chicago, Chicago, Illinois 60637, USA*
[10]*Département de Physique, Université de Montréal, Montréal Québec H3C 3J7, Canada*
[11]*Department of Physics, Laurentian University, Sudbury, Ontario P3E 2C6, Canada*
[12]*Institute of Experimental and Applied Physics, Czech Technical University in Prague, Prague 12800, Czech Republic*
[13]*Department of Physics, University of Alberta, Edmonton, T6G 2G7, Canada*
[14]*SNOLAB, Lively, Ontario P3Y 1N2, Canada*
[15]*Center for Energy Harvesting Materials and Systems (CEHMS), Virginia Tech, Blacksburg, Virginia 24061, USA*
[16]*Department of Physics, Drexel University, Philadelphia, Pennsylvania 19104, USA*
[17]*Instituto de Física, Universidad Nacional Autónoma de México, México D. F. 01000, México*
[18]*Chemistry Division, Argonne National Laboratory, Argonne, Illinois 60439, USA*

(Received 6 November 2015; published 28 March 2016)

New data are reported from the operation of the PICO-60 dark matter detector, a bubble chamber filled with 36.8 kg of CF_3I and located in the SNOLAB underground laboratory. PICO-60 is the largest bubble chamber to search for dark matter to date. With an analyzed exposure of 92.8 livedays, PICO-60 exhibits the same excellent background rejection observed in smaller bubble chambers. Alpha decays in PICO-60 exhibit frequency-dependent acoustic calorimetry, similar but not identical to that reported recently in a C_3F_8 bubble chamber. PICO-60 also observes a large population of unknown background events, exhibiting acoustic, spatial, and timing behaviors inconsistent with those expected from a dark matter signal. These behaviors allow for analysis cuts to remove all background events while retaining 48.2% of the exposure. Stringent limits on weakly interacting massive particles interacting via spin-dependent proton and spin-independent processes are set, and most interpretations of the DAMA/LIBRA modulation signal as dark matter interacting with iodine nuclei are ruled out.

DOI: 10.1103/PhysRevD.93.052014

I. INTRODUCTION

The nature of dark matter is one of the most fundamental questions facing particle physics and cosmology [1–3], and a leading explanation for dark matter is a relic density of weakly interacting massive particles (WIMPs) [4,5]. Direct detection dark matter experiments are sensitive to the nuclear recoils resulting from collisions between WIMPs and ordinary matter. The main challenge in the field has been to scale up detector target masses while eliminating or rejecting backgrounds to a potential dark matter signal [6].

The superheated detector technology provides a unique approach to direct detection, with excellent rejection of gamma and beta events, excellent alpha rejection using the acoustic emission of bubble formation, and the ability to

*hugh@fnal.gov
†harriso@iusb.edu

employ different targets [7–14]. Located in the SNOLAB underground laboratory [15] at an approximate depth of 6000 meters water equivalent, the PICO-60 bubble chamber is the largest bubble chamber to search for dark matter to date. We report results from the first run of PICO-60, with a dark matter exposure of 3415 kg days taken at SNOLAB between June 2013 and May 2014.

II. EXPERIMENTAL METHOD

The PICO-60 bubble chamber consists of a 30-cm-diameter by 1-m-long synthetic fused silica bell jar sealed to a flexible stainless-steel bellows and immersed in hydraulic fluid, all contained within a stainless-steel pressure vessel. The pressure vessel is 60 cm in diameter and 167 cm tall. The hydraulic fluid in PICO-60 is propylene glycol, and the pressure in the system is controlled by an external hydraulic cart via a 3.8-cm-inner-diameter hydraulic hose. The stainless-steel bellows balances the pressure between the hydraulic volume and the bubble chamber fluid. For this run, the chamber was filled with 36.8 ± 0.2 kg of CF_3I (18.4 l with density 2.05 kg/l at 22 °C and atmospheric pressure). A buffer layer of ultrapure water sits on top of the CF_3I to isolate the active fluid from contact with stainless-steel surfaces. A schematic of the detector is shown in Fig. 1.

Parts per million of free iodine molecules in CF_3I are known to absorb visible light. To prevent any discoloration, the buffer water contains 5 mmol/l of sodium sulfite, which reacts at the water/CF_3I interface with any iodine in the organic phase to form colorless iodide (I^-) that is then extracted into the aqueous phase. This reaction is known in chemistry as the iodine clock reaction, and it efficiently removes any traces of free iodine from the CF_3I. No discoloration of the fluids was observed during the run.

The pressure vessel is located in a 2.9-m-diameter by 3.7-m-tall water tank in the Ladder Labs area of SNOLAB [15]. The water tank provides shielding from external sources of radiation as well as temperature control. The water bath temperature is regulated by the combination of circulation through an external heater and a second heating wire located inside the tank for fine control. The water tank, pressure vessel, hydraulic fluid, and bubble chamber are all in thermal contact. The temperature is monitored by eight resistive temperature detectors (RTDs) in the water bath and four RTDs in the pressure vessel, bracketing the bubble chamber volume.

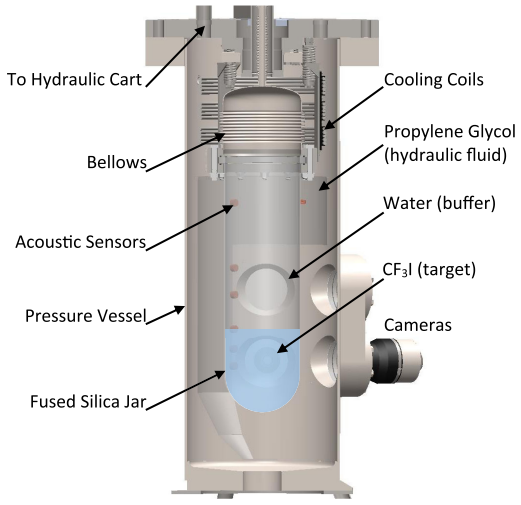

FIG. 1. A schematic of the PICO-60 bubble chamber.

Transducers monitoring the pressure are connected to the inner volume, the pressure vessel, and the hydraulic cart. An additional fast ac-coupled pressure transducer monitors the pressure rise in the chamber during bubble growth [16]. Gross pressure control is accomplished using a piston with a 1:4 area ratio connected to a pressure-regulated air reservoir. A stepper motor controlling a hydraulic pump provides fine pressure control.

Two 1088×1700 CMOS cameras are used to photograph the chamber at a stereo angle of 60° at a rate of 50 frames per second. A set of LEDs mounted next to the cameras flash at the same rate as the camera shutter, and a sheet of retroreflector mounted inside the pressure vessel behind the jar reflects the LED light back to the cameras, effectively backlighting the chamber. The stereo images from the cameras are used to identify bubbles and reconstruct their spatial coordinates within the chamber. Figure 2 shows images of a seven-bubble event produced during a neutron calibration run.

Thirteen piezoelectric acoustic transducers were synthesized from low radioactivity, lead-zirconate-titanate-based ceramics in an ultrahigh purity environment to prevent any contamination during mixing, calcination, and sintering. The transducers are epoxied to the exterior

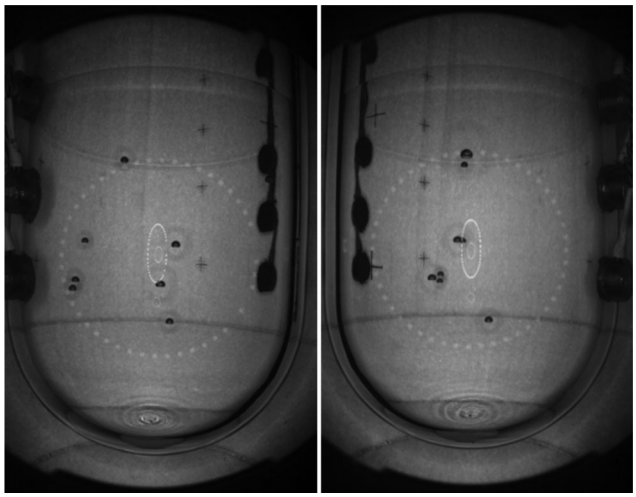

FIG. 2. Images of a multiple scattering neutron event from the two PICO-60 cameras. Reflection of the LED rings used for illumination are clearly visible on the front and back of the jar. The two vertical strings of acoustic sensors are visible running up the sides of the jar.

of the bell jar to record the acoustic emissions from bubble nucleations [14,17]. These sensors are mounted in vertical strings, and several sensors from each string are visible in the images in Fig. 2. Five of the sensors failed during the run, leaving eight working sensors for the duration of the experiment.

A PICO-60 cycle or expansion begins by relieving the pressure in the hydraulic cart (i.e., relieving the air behind the piston) to a target pressure of between 20 and 55 psia over 4–5 s, at which point the chamber is in the "expanded" state and the CF_3I is superheated. To allow for transient behaviors to subside, dark matter data begin accumulating only after the chamber is stable at the target pressure for 25 s. Differences in live images from one frame to the next provide the primary trigger, initiating compression. Optical and acoustic data surrounding the trigger time are logged, as well as the pressure and temperature record over the entire expansion. The compression is accomplished by reapplying compressed air to the piston, raising the hydraulic pressure to ~200 psia within 250 ms. Triggers are also generated by the hydraulic controller in response to pressure spikes, and by the data acquisition system if no trigger is received after a "timeout" time of between 500 and 2000 s. The timeout time was increased twice during the run to increase the live fraction. The system remains in the compressed state for 30 s after every cycle, with a longer compression of 300 s after every tenth cycle, to ensure that all evaporated gas condenses and thermal equilibrium is regained.

The chamber was filled with CF_3I on April 26, 2013, and the acquisition of physics data in the complete water shield began on June 13. Data taking was paused three times for maintenance or repair, with the detector running continuously after the last stoppage from January 21 to May 22. A total exposure of 155.1 livedays was collected over the course of the run. The live fraction increased from 80% at the beginning of the run to 93% by the end (partly due to increasing the timeout time). To explore bubble rates over a variety of different operating conditions, the chamber was run at nine discrete pressure set points: 23.5, 26.4, 28.5, 30.3, 33.4, 38.3, 43.2, 48.2 and 53.2 psia. Over 80% of the data were taken at $34.5 \pm 1.5\,°C$ (the temperature control early in the run was only good to about 1 °C, although we measure the temperature to within 0.1 °C for each cycle). The remaining data are split between two periods of higher ($37.5 \pm 0.5\,°C$) and lower ($31.5 \pm 1.5\,°C$) temperature running to explore bubble rates as a function of temperature, with around 6.6 days of <30 °C data taken during periods of cooling down to or warming back up from room temperature. The data include over 33 000 events from AmBe neutron calibration runs, spread throughout the data-taking period.

The acoustic signal is a strong function of operating pressure and only provides a clear signal below 35 psia; we therefore only use data taken at pressures less than or equal to 33.4 psia to search for dark matter. The 6.6 days of running below 30 °C are also removed, keeping 92.8 livedays in the final WIMP search data set.

III. BUBBLE NUCLEATION THRESHOLD AND EFFICIENCY

A. Calculating the energy required to form a bubble

The sensitivity of PICO-60 to dark matter interactions depends on the energy threshold and efficiency for bubble nucleation from recoiling nuclei, with the majority of spin-independent (SI) sensitivity coming from iodine and the spin-dependent (SD) sensitivity coming from a combination of fluorine and iodine. The pressure and temperature of the active fluid determine the conditions for radiation-induced bubble nucleation. The Seitz "hot spike" model [18] calculates the enthalpy necessary to produce a critically sized bubble and assumes that the full energy deposited by a particle interaction is used to form a bubble. The critically sized bubble is defined by Gibbs as a bubble in which the pressure differential across the surface is balanced by the surface tension [19]:

$$P_b - P_l = \frac{2\sigma}{r_c}, \tag{1}$$

where P_b is the pressure in the bubble, P_l is the pressure in the liquid, σ is the bubble surface tension, and r_c is the critical bubble radius. The heat input required to produce this bubble is given by

$$E_T = 4\pi r_c^2\left(\sigma - T\frac{\partial\sigma}{\partial T}\right) + \frac{4\pi}{3}r_c^3\rho_b(h_b - h_l) - \frac{4\pi}{3}r_c^3(P_b - P_l), \tag{2}$$

where T is the temperature, ρ_b is the bubble vapor density, h_b and h_l are the specific enthalpies of bubble vapor and superheated liquid, respectively, and the surface tension σ and temperature derivative are taken along the usual saturation curve. As an approximation, $h_b - h_l$ may be replaced by the heat of vaporization, and P_b and ρ_b by the saturated vapor pressure and density at temperature T. All thermodynamic values in this paper are taken from the REFPROP database maintained by the National Institute of Standards and Technology [20].

We refer to E_T in Eq. (2) as the Seitz threshold for bubble nucleation, and we use E_T calculated individually for each cycle to classify our data. Because of the temperature variations during the run, the pressure set points listed above do not correspond to fixed E_T, instead representing a continuum of Seitz thresholds between 7 and 20 keV. The temperature did not vary on the time scale of single chamber cycles, however, and we therefore count the accumulated livetime in a given expansion as taken at the calculated E_T for that expansion. Figure 3 shows the

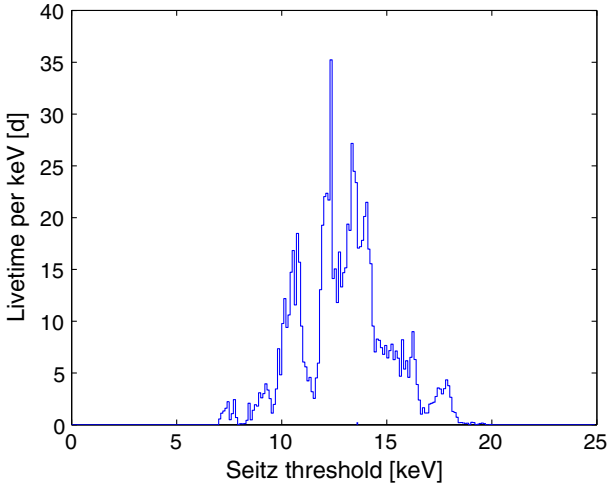

FIG. 3. Total livetime in the dark matter search data vs Seitz threshold. Because of the temperature variations and the many pressure set points, the data sample a continuum of Seitz thresholds between 7 and 20 keV. There are a total of 92.8 livedays in the dark matter search data.

total amount of exposure vs Seitz threshold, with a total of 92.8 livedays in the dark matter search data.

As we discuss in the next section, we do not rely on the Seitz model to determine the threshold and efficiency for bubble nucleation. However, the Seitz theory does set a well-defined energy scale for the problem of bubble nucleation, and most inefficiencies should scale with either the Seitz threshold or its nearly related quantity, the critical radius. As already mentioned, we use E_T calculated individually for each expansion to classify our data.

B. Determining the efficiency for bubble nucleation

In the classical Seitz model, a particle depositing energy greater than E_T will nucleate a bubble with 100% efficiency. Previous neutron calibration data using both broad spectrum AmBe sources and low energy, monoenergetic YBe sources have shown that the Seitz model is not an accurate picture of bubble nucleation in CF_3I, particularly for carbon and fluorine recoils [10,21,22]. A recent analysis of all available neutron data shows that carbon and fluorine recoils in CF_3I do not efficiently produce bubbles until their energies are significantly above the calculated Seitz threshold [23]. Simulations of carbon and fluorine tracks in CF_3I using the Stopping Range of Ions in Matter (SRIM) package [24] provide an explanation for the observed inefficiency—carbon and fluorine tracks are comparable in size to, and often larger than, the critical bubble size. Iodine recoils produce much shorter tracks, and bubble chamber data taken with a pion beam at the Fermilab Test Beam Facility show that the iodine response is much closer to the nominal Seitz model [25].

To determine the sensitivity of PICO-60 to dark matter, we perform a global fit to the YBe and AmBe neutron data collated in [23] and the pion beam data of [25] to simultaneously find the probability for bubble nucleation from iodine, fluorine, and carbon recoils as a function of recoil energy, $P_{\mathrm{I,F,C}}(E)$. The carbon and fluorine responses are constrained primarily by the neutron data, while the iodine response is constrained by the pion beam data of [25]. As in [14], the efficiency curves are fit by monotonically increasing, piecewise linear functions, with the constraints that no nucleation occurs below E_T and that $P_{\mathrm{I}}(E) \geq P_{\mathrm{F}}(E) \geq P_{\mathrm{C}}(E)$. The solid lines in Fig. 4 show the best fit iodine, fluorine, and carbon efficiency curves at 13.6 keV. Note that the onset of efficiency for fluorine and carbon recoils occurs at energies higher than twice the calculated Seitz threshold. The allowed shapes are well constrained by the data, particularly for iodine because of the quality of the data in [25]. To give a sense of the uncertainties, the worst-case efficiency curves for each element allowed by the global fit at 1σ are shifted to the

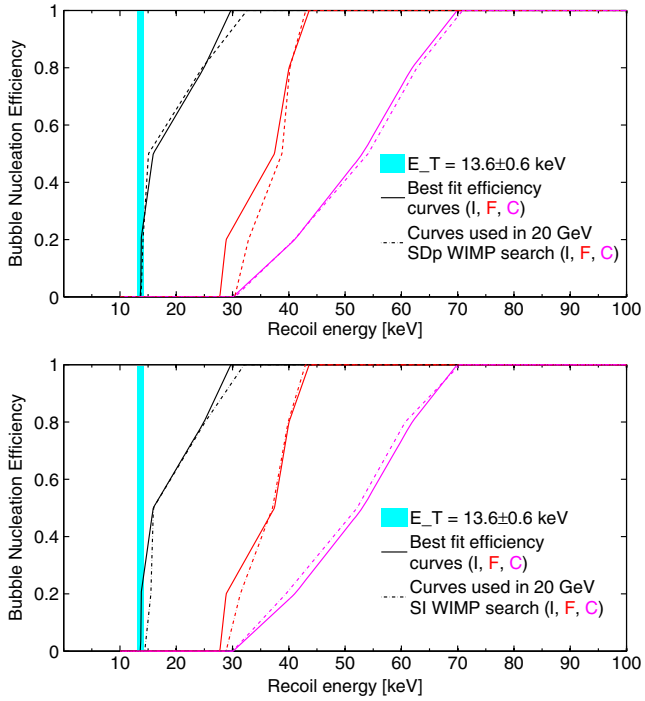

FIG. 4. The best fit iodine (black), fluorine (red), and carbon (magenta) efficiency curves for $E_T = 13.6$ keV data are shown by the solid lines, and the light blue band shows the calculated Seitz threshold with the experimental and theoretical uncertainties (the solid curves are the same in both the top and bottom panels). In the top panel, the dashed lines show the curves used to determine sensitivity for a 20 GeV SD WIMP, corresponding to the set of curves with the least sensitivity to 20 GeV SD WIMP scattering consistent with the calibration data at 1σ, while the dashed lines in the bottom panel show the curves used to determine sensitivity for a 20 GeV SI WIMP. The onset of nucleation for fluorine and carbon recoils occurs at energies greater than twice the Seitz threshold, while the response to iodine is much closer to the Seitz model.

right by about 10% on average relative to the solid curves of Fig. 4 (and only 5% for the onset of iodine efficiency). We note, however, that one cannot simultaneously achieve the worst-case shapes for all three elements and still be consistent with calibration data.

Because the pion beam data of [25] were taken at a single Seitz threshold of $E_T = 13.6$ keV, we can only perform the full global fit at that threshold. PICO-60 data were taken at a continuum of Seitz thresholds between 7 and 20 keV, however, with E_T calculated individually for each expansion based on the temperature and pressure for that expansion. We therefore must translate the derived efficiency curves at 13.6 keV to the other operating conditions of the experiment. Previous calibrations in superheated droplet detectors parameterized the efficiency response for recoils in C_4F_{10} as an explicit function of E/E_T [26], finding good agreement with neutron calibration data above 7 keV. As iodine recoils follow the Seitz model rather closely, scaling the curve shown in Fig. 4 using E/E_T is a natural way to translate the iodine response at 13.6 to the other operating conditions. One might be hesitant to apply the same scaling to carbon and fluorine recoils given their strong deviation from the nominal Seitz model. However, fits of the YBe and AmBe neutron calibration data of [23] between 7 and 40 keV for carbon and fluorine recoils are consistent with a single derived efficiency shape that also scales with E/E_T, and we therefore apply that scaling to translate the efficiency curves of Fig. 4 for all three recoil species on an expansion by expansion basis to determine our sensitivity to dark matter.

To determine dark matter sensitivities for a specific WIMP mass and coupling (SI or SD), we take the combination of efficiency curves allowed by the global fit at 1σ that provides the least sensitivity to that particular dark matter mass and coupling. While the various calibration data sets are dominated by recoils of a particular nucleus (e.g. iodine in the pion beam data of [25]), they do contain contributions from all three nuclei. In the global fit, the size of the contribution from each individual recoil is allowed to float to minimize sensitivity to a given dark matter candidate. As an example, the curves used to determine the sensitivity to a 20 GeV SD WIMP are shown as the dashed lines in the top panel of Fig. 4. Since the SD sensitivity mostly arises through fluorine interactions, our analysis assumes the weakest possible response for fluorine allowed by the data by maximizing the contributions from carbon and iodine. The bottom panel of Fig. 4 shows the curves used to determine sensitivity to a 20 GeV SI WIMP, where the iodine response is reduced in favor of increased carbon and fluorine responses.

As 75% of the livetime was accumulated at thresholds within 20% of 13.6 keV, deviations from the characteristic observed E/E_T scaling behavior have a small effect on the final result. To give an extreme example, if all data taken at $E_T < 13.6$ followed the same response function as that measured at 13.6 keV (i.e., assuming no improvement in sensitivity at the lower Seitz thresholds) and we scale by E/E_T for $E_T > 13.6$, the final results presented in Sec. VI for both SI and SD WIMP scattering would be 13% less sensitive for a 100 GeV WIMP mass and 10% less sensitive for WIMP masses greater than 200 GeV.

IV. BACKGROUND MODELING AND PREDICTION

Neutrons in the active volume can be produced by (α, n) reactions and fission neutrons from radioactivity in the detector components, by cosmogenic activation, and by photonuclear interactions. Before installation, all detector components in proximity to the active volume were screened for radioactivity, and the results from this screening are incorporated into a detailed Monte Carlo simulation of the detector. Neutron production rates and energy spectra for (α, n) reactions are evaluated with a modified version of the SOURCES-4C code [23,27], where the contributions to neutron backgrounds primarily come from alpha decays in the ^{238}U, ^{232}Th and ^{235}U decay chains. The rate and angular distribution of cosmogenic neutrons produced in the cavern rock are taken from [28] and normalized to the muon flux measured by the SNO experiment [29]. The neutrons are propagated through the detector using GEANT4 [30] (version 4.10.00p03) to the target fluid. The predicted number of neutron-induced single-bubble events during the WIMP search data is 1.0 ± 0.3. The simulation returns the same number of multiple-bubble events as single-bubble events, and the predicted number of neutron-induced multiple-bubble events is also 1.0 ± 0.3. The uncertainty on the prediction arises from a combination of screening uncertainties, (α, n) cross section uncertainties, and imperfect knowledge of the material composition of some components. The leading source of events is cosmogenic neutrons produced in the rock and punching through the water shield, accounting for about 1/3 of the neutron backgrounds. The remainder come primarily from a combination of (α, n) sources in acoustic sensor cabling, a set of thermocouples in the pressure vessel, and the retroreflector used for illumination.

We use the Monte Carlo simulations with input from screening of materials to predict the rate of gamma interactions in the detector from the ^{238}U, ^{232}Th and ^{235}U decay chains, as well as from ^{40}K decays. Previously we found the nucleation efficiency for gamma interactions to decrease exponentially with threshold, from 5×10^{-8} at 7 keV threshold to $<10^{-9}$ for thresholds above 11 keV [10], where the efficiency is defined as the fraction of above-threshold interactions of any kind that nucleate bubbles. This excellent gamma rejection was confirmed with *in situ* gamma calibrations and results in an expectation of fewer than 0.1 electronic recoil nucleation events during the entire physics run, dominated by the 1.2 livedays of exposure below 8.2 keV threshold.

High-energy gamma rays also indirectly produce background events via photonuclear (γ, X) reactions in the CF_3I and (γ, n) reactions in the surrounding water, silica, and steel. We use Monte Carlo simulations to predict the (γ, n) background rate from internal gamma emitters and from the flux of >3 MeV external gammas produced by neutron and alpha captures in the rock, previously measured at SNOLAB [31]. Based on these simulations and measurements, we expect fewer than 0.1 total photonuclear background events, with the largest contributions from $^{127}I(\gamma, n)^{126}I$ and $^{2}H(\gamma, n)^{1}H$ reactions, with gamma-energy thresholds of 9.14 and 2.23 MeV, respectively.

V. DATA ANALYSIS

The data analysis begins with an image reconstruction algorithm to identify clusters of pixels that change significantly from one frame to the next. The derived bubble pixel coordinates from the two cameras are converted into spatial coordinates with an accuracy of about a millimeter. An optical-based fiducial volume cut is defined on neutron calibration data to eliminate events occurring close to the glass jar ("wall events") and events near the water/CF_3I interface ("surface" events). These cuts are defined such that 1% or fewer of wall and surface events are reconstructed into the bulk region and are located 5 mm from the wall of the jar and 6 mm from the surface. The acceptance of the fiducial cut is 0.90 ± 0.01 by volume.

All data undergo a set of data quality cuts. The first cut removes events where the optical reconstruction is poor. In particular, as can be seen in Fig. 2, the acoustic sensors obscure small regions of the inner volume close to the jar wall; while the entire volume is visible to at least one camera, a well-reconstructed event requires that both cameras observe the bubble and agree on the number of bubbles observed. Roughly halfway through the run, one of the cameras began observing increased digital noise. While the images were still of high quality, the noisy camera had to be removed from the trigger, leading to the late observation of bubbles that formed in the areas partially hidden from the second camera. These late triggers are also cut. The acceptance of the optical reconstruction cut for neutron-induced single-bubble events in the bulk of the fluid is 0.995 ± 0.005, dropping to 0.95 ± 0.01 for data taken with the single-camera trigger.

Additional quality cuts are applied to all data to eliminate events with excessive acoustic noise and events where the acoustically reconstructed time of bubble formation was outside of the expected range. The acceptance of the above cuts is pressure dependent because the acoustic signal-to-noise ratio decreases at higher pressures. The total acceptance of the above data quality cuts is 0.94 ± 0.02 at 23.5 psia decreasing to 0.89 ± 0.02 at 33.4 psia.

An acoustic parameter (AP) is used to characterize the acoustic power of an event [9,10,14]. The acoustic signal is divided into frequency bands, and each band is corrected for the position of the bubble within the chamber. Multiple versions of AP can be constructed using different combinations of frequency bands, and these AP distributions are normalized and corrected for changes in temperature and pressure to have a value of unity at the nuclear recoil peak observed in the AmBe data. The acoustic power decreases exponentially as a function of expansion pressure, and the AmBe calibration peak could not be well resolved at expansion pressures of 38.3 psia and above. Therefore, we restrict our analysis to the lower pressure data, containing 92.8 of the total 155 livedays collected during the run.

Two acoustic parameters are used in the analysis: AP_{low} is calculated as the sum of the normalized frequency bands

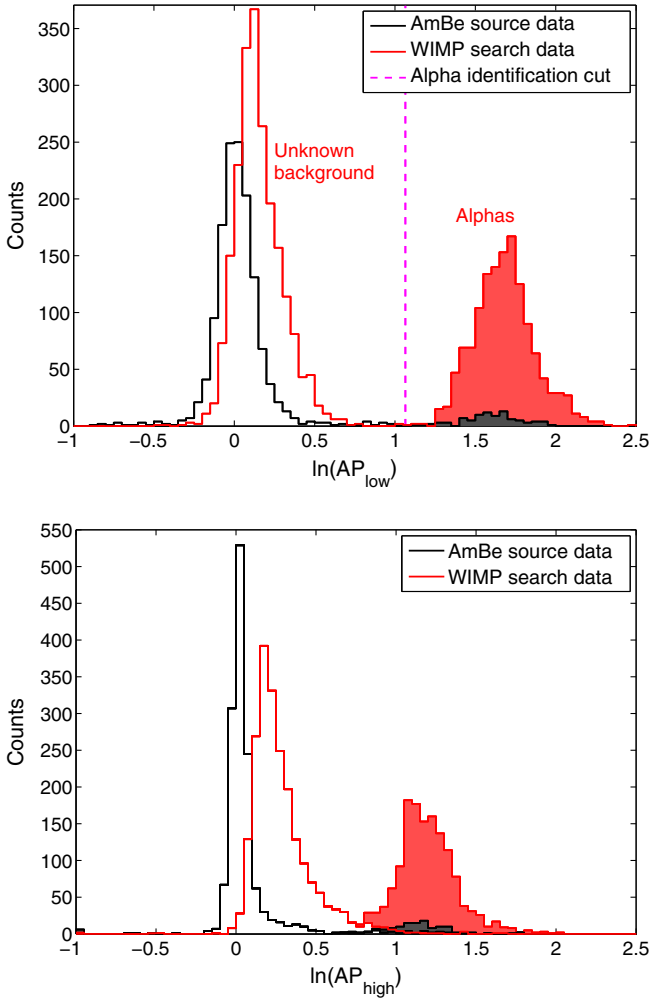

FIG. 5. AP distributions for neutron calibration (black) and WIMP search data (red) for all WIMP search data. The top figure shows AP_{low} for frequency bands between 7 and 63 kHz and the bottom figure shows AP_{high} for frequencies between 63 and 110 kHz. Events with $AP_{low} > 2.9$ are identified as alpha-decay events and shaded in both histograms. The rate of observed alpha decays is consistent between WIMP search data and calibration runs.

between 7 and 63 kHz, and similarly AP_{high} from frequencies between 63 and 110 kHz. The piezos located above the CF_3I/water interface are found to have a better acoustic response at frequencies above ~60 kHz, and as a result the signals from only four out of the eight working piezos are used in AP_{high}. All eight piezos are used in AP_{low}. Figure 5 shows both AP distributions for calibration and WIMP search data. There are two clear peaks in the WIMP search data of Fig. 5.

A. Alpha events and acoustic calorimetry

The AP has previously been found to discriminate alpha decays from nuclear recoils [9,10,14,32]. Alpha decays are responsible for the peak at higher values of AP seen in Fig. 5, with 1337 alphas observed in this data set. In the WIMP-search analysis, a cut on AP_{low} is used to identify alpha-decay events, defined as $AP_{low} > 2.9$. Recent results from a C_3F_8 chamber [14] included a dependence of detected acoustic power on alpha energy. A similar effect is reported here for CF_3I, albeit with some key differences.

The alpha decays in PICO bubble chambers predominantly originate from the prompt ^{222}Rn decay chain, shown in Fig. 6. The decays of ^{222}Rn and its daughters, ^{218}Po and ^{214}Po, produce alphas with energies 5.48, 6.0, and 7.68 MeV, respectively. Given the half-lives of the various decays in the chain, 90% of the first and second alpha decays are separated by less than 10 min, and 90% of the second and third alpha decays are separated by less than 130 min. Eighty-two triplets of consecutive alpha events consistent with this time structure are identified in the data set. Each triplet is required to be isolated in time with respect to other alpha events in order to increase the purity of the sample of events assigned to each decay. With this data set we find that the acoustic power and its frequency spectrum is dependent on alpha energy. AP_{low} and AP_{high} do not provide sufficient frequency resolution to capture

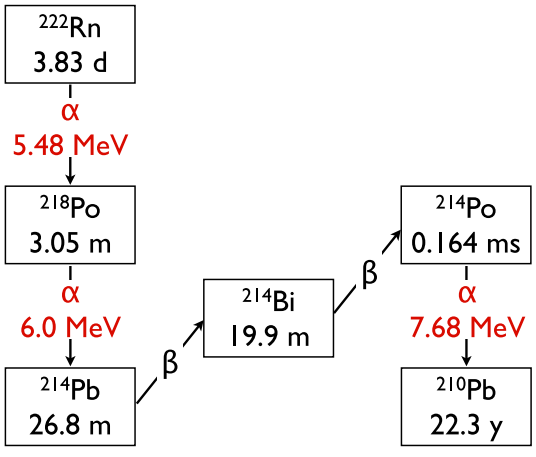

FIG. 6. The decays of ^{222}Rn and its daughters ^{218}Po and ^{214}Po produce alphas with energies 5.48, 6.0, and 7.68 MeV, respectively, with the half-lives shown.

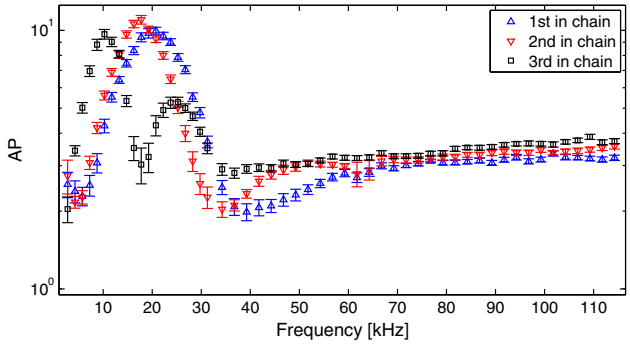

FIG. 7. The mean AP as a function of frequency bin for the first, second, and third decays of 82 triplets of consecutive alpha events whose timing is consistent with the fast radon decay chain. The data are normalized in each frequency bin to the neutron calibration data; i.e., the mean AP for neutron calibration data would appear flat at a value of 1.

this dependence, so the AP is calculated separately in bins of size 1–3 kHz between 2 and 115 kHz. Figure 7 shows the mean AP as a function of frequency bin for each of the three alpha decays (where AP is normalized to have a value of unity for neutron calibration data).

For frequencies above 40 kHz, the highest energy ^{214}Po decays produce 15% louder acoustic signals than ^{222}Rn. A reanalysis of data from CF_3I in a 2-liter chamber [10] finds the same result. A similar but much stronger effect was also observed in a 2-liter chamber filled with C_3F_8 [14], where the acoustic difference was more than a factor of 2, as shown in Fig. 8. Below 40 kHz the character of the relationship between alpha energy and acoustic energy is less straightforward. For example, near 20 kHz the lower energy ^{222}Rn and ^{218}Po decays produce larger acoustic responses (by more than a factor of 2) than the higher energy ^{214}Po decay. The same result is found for CF_3I in the small 2-liter chamber. In contrast, the C_3F_8 data from [14] shows no indication of similar behavior below 40 kHz in C_3F_8, remaining monotonic in alpha energy (see Fig. 8).

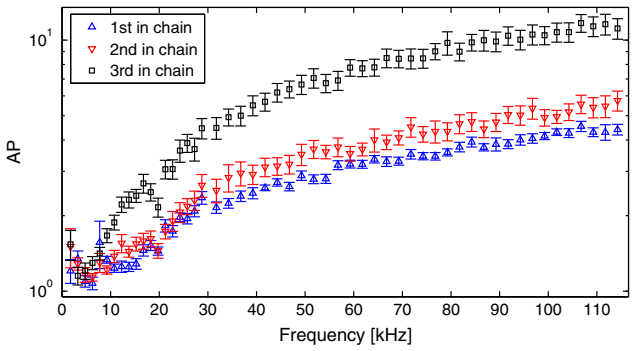

FIG. 8. The mean AP as a function of frequency bin in C_3F_8 [14] for the first, second, and third decays in 18 triplets of consecutive alpha events whose timing is consistent with the fast radon decay chain.

We have not observed any similar dependence of acoustic response on the energy of neutron-induced nuclear recoils. The AmBe calibration source produces nuclear recoils with an exponentially falling spectrum from keV to MeV energies, and the AP spectrum of these recoils is approximately normally distributed for all frequency ranges studied.

B. The low AP peak

The peak in Fig. 5 at lower values of AP contains 2111 events. Given an observed count of 1337 alpha events in the high AP peak and an upper limit on the failure of alpha rejection of 0.7% observed previously [10], we expect less than 10 events to be produced by a failure of acoustic rejection of alphas. As discussed in Sec. IV, we expect less than 1.2 events from neutron and gamma activity. Therefore, these events represent a background of unknown origin. The rate of these events decreases with increasing threshold, but they appear for all temperatures and pressures. Due to the large number of background events and the ability to cleanly distinguish them from alphas using AP_{low}, the characteristics of these events can be studied in detail. The events have several characteristics that differentiate them from a dark matter signal.

First, as can be seen in Fig. 5, the background produces bubbles that are on average louder than those produced from neutron calibration data, an effect that is more pronounced at higher frequencies.

The second feature that distinguishes the background events from a potential dark matter signal is time correlations, similar to those observed in previous bubble chambers [10,14]. Figure 9 shows the rate of these events as a function of "expansion time," the amount of time spent in the expanded state before bubble formation (note that we do not include data for expansion times less than 25 s, as discussed in Sec. II). Also shown are the alpha events (the high AP peak in Fig. 5). A WIMP signal would have no preference as to when in an expansion it appeared and would therefore appear flat. On the other hand, the background events exhibit very strong timing correlations, preferentially occurring at short expansion times. Although a small fraction of alpha decays do have timing correlations relevant on these scales (the ^{218}Po decays), the total alpha distribution is nearly flat in expansion time and can be viewed as a proxy for a dark matter signal.

The third feature of the background events is their nonuniformity in space, as seen in Fig. 10 showing the XYZ distribution of alpha events (left) and the low AP events (right). We expect a dark matter signal to be homogeneous in the detector, a distribution that would appear to be uniform in these units. Again, as a rough proxy for a dark matter signal, the alpha events do appear uniform in space, although we do observe correlations between events in a given decay chain, with daughter nuclei moving upward relative to the previous decay. Low AP events,

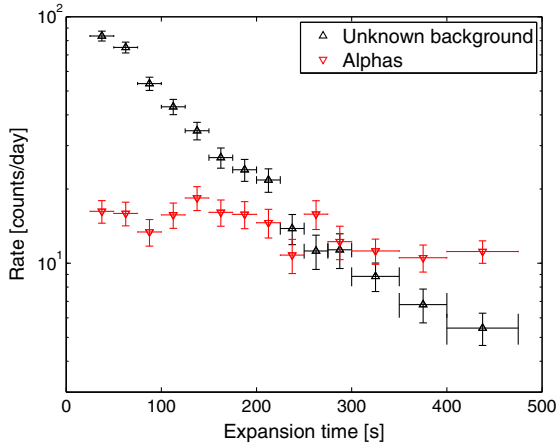

FIG. 9. Event rate of the nonalpha background events (black) and alpha events (red) as a function of the length of time the chamber was in an expanded state. The rate is calculated for intervals of expansion time indicated by the horizontal error bars; the rates measured in neighboring bins are uncorrelated. A dark matter signal would be flat; by contrast, the background events cluster at early expansion times. Although a fraction of alpha decays do have timing correlations relevant on these scales (the ^{218}Po decays), the total alpha distribution is dominated by the uncorrelated decays, nearly flat in expansion time, and can be viewed as a rough proxy for a dark matter signal. We include the alpha distribution here to show that systematic effects cannot account for the distribution of the background events.

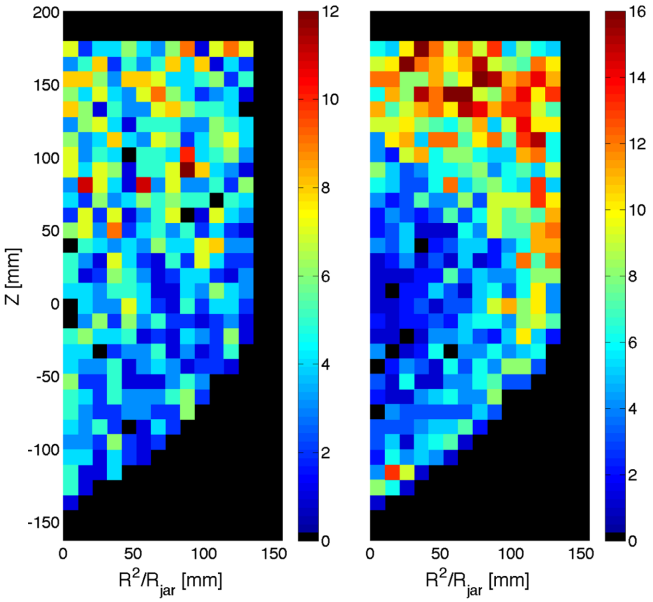

FIG. 10. Two-dimensional histogram of bubble location (R^2/R_{jar} vs Z). The left-hand plot shows all alpha events while the right-hand plot shows the background events. A dark matter signal would be isotropic in these units. As a proxy for a dark matter signal, the alphas are more uniformly distributed in the jar than the background events, which are concentrated along the walls and near the interface.

however, are nonuniform, clustering towards the jar walls and CF_3I surface.

The background events exhibit correlations between AP, position and expansion time; for example, events that occur at long expansion times tend to have higher AP values and be located at higher Z. The background event rate is also sensitive to rapid changes in the temperature of the active fluid.

Combinations of cuts on AP_{high}, expansion time, distance to the CF_3I surface, and distance to the jar wall can be used to efficiently remove background events while retaining a large fraction of the WIMP exposure. A cut optimization method, used previously in [14] and based closely on the optimum interval method [33], is used to provide an unbiased upper limit on the rate of dark matter interactions in the detector. This method provides a statistical framework for optimizing a set of free cut parameters on the dark matter search data to derive the most stringent upper limit. It allows for background rejection without an explicit model for the background and is appropriate in cases where the cut variables provide discrimination against poorly known backgrounds, as is the case for PICO-60. The method is described in detail in the Appendix.

After performing the cut optimization, the final cuts on the four discriminating variables are as follows:

(i) $0.7 < AP_{high} < 1.020$,
(ii) expansion time > 45.7 s,
(iii) distance to the surface, Zsurf > 67.8 mm ($Z < 118.2$ mm), and
(iv) distance to jar wall, Dwall > 5.4 mm ($R^2/R_{jar} < 133.4$ mm in the cylindrical part of the jar).

C. Final cut acceptance

The final cut optimization depends on understanding the signal acceptance. The acceptances of the fiducial volume and expansion time cuts are easily derived (as a WIMP signal would populate those variables uniformly), but the AP_{high} cut acceptance has a larger uncertainty. The AP acceptance uncertainty depends on the quality of the calibration data, especially as the acoustic conditions vary with time and expansion pressure. In previous analyses, the acoustic cut was set far from the median of the AP distribution [10,14], but this analysis requires an acoustic cut set close to the median, rendering the result more susceptible to drifts in the normalization. The largest systematic comes from time variations of 3% in the median of AP_{high}, leading to an uncertainty on the cut acceptance of 12%. This variation is observed in both the calibration data and in the two peaks in the WIMP search data (alphas and background events).

There are two other leading sources of error. The first is uncertainty on the position corrections used to calculate AP_{high}, as the neutron source does not produce a spatially uniform distribution of events. The second is background contamination in the calibration data. These effects add about 7% to the uncertainty of the acceptance. Changes in acceptance as a function of pressure set point (due to changing signal to noise) were found to be subdominant. Because the final cut is close to the median of the AP_{high} distribution in this analysis, it is not very sensitive to the width. We combine all uncertainties in quadrature to obtain a final uncertainty of 14%. The acceptance for the final AP_{high} cut is 0.63 ± 0.09. We perform several cross checks by resampling the calibration data taken at different times, at different temperatures and pressure set points, and with different neutron source locations (producing a different spatial distribution), and the results are consistent to within the evaluated uncertainties. The uncertainty on the cut acceptance is included as a nuisance parameter in calculating the 90% C.L. limits as described in the Appendix.

VI. WIMP SEARCH RESULTS

The optimized cuts remove all events from the WIMP search data while retaining 48.2% of the exposure remaining after the data cleaning cuts described at the beginning of Sec. V. The final WIMP search exposure with all cuts is 1335 kg days. To illustrate the power of the discriminating variables and the absence of any surviving events, Fig. 11 shows a two-dimensional histogram of AP_{high} and expansion time after applying the optimum fiducial cuts, divided into bins of equal exposure to dark matter (i.e., a dark matter signal would appear uniform). All the background events populate the low expansion time and high AP_{high} region of the histogram. The optimum cuts on AP_{high} and expansion time are represented by the red rectangle, with zero events passing.

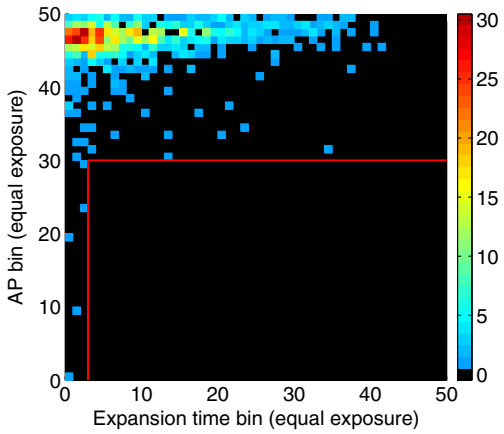

FIG. 11. A two-dimensional histogram of AP_{high} and expansion time after applying the optimum fiducial cuts, divided into bins of equal exposure to dark matter (i.e., a dark matter signal would appear uniform in the histogram). All the background events populate the left and top of the histogram. The optimum cuts are represented by the red rectangle.

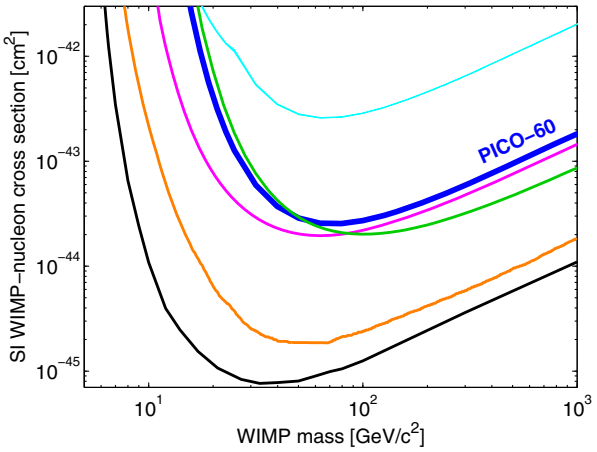

FIG. 12. The 90% C.L. limit on the SI WIMP-nucleon cross section from PICO-60 is plotted in blue, along with limits from COUPP (light blue), LUX (black), XENON100 (orange), DarkSide-50 (green), and the reanalysis of CDMS-II (magenta) [10,41–44].

In the total exposure, we expect 1.0 ± 0.3 single- and 1.0 ± 0.3 multiple-bubble events from background neutrons. Including the acceptance of the final cuts, the expectation for single-bubble events drops to 0.5 ± 0.2, consistent with the zero single-bubble events remaining after all cuts. We observe one multiple-bubble event (five bubbles) in the WIMP search data, also consistent with the prediction.

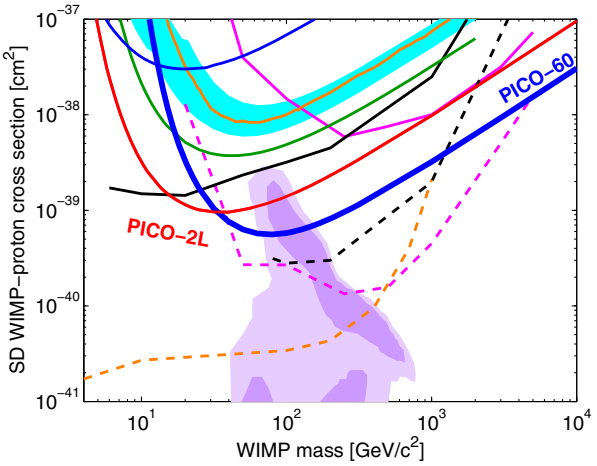

FIG. 13. The 90% C.L. limit on the SD WIMP-proton cross section from PICO-60 is plotted in blue, along with limits from PICO-2L (red), COUPP (light blue region), PICASSO (dark blue), SIMPLE (green), XENON100 (orange), IceCube (dashed and solid pink), SuperK (dashed and solid black) and CMS (dashed orange) [10,12,13,45–49]. For the IceCube and SuperK results, the dashed lines assume annihilation to W pairs while the solid lines assume annihilation to b quarks. Comparable limits assuming these and other annihilation channels are set by the ANTARES, Baikal and Baksan neutrino telescopes [50–52]. The CMS limit is from a monojet search and assumes an effective field theory, valid only for a heavy mediator [53,54]. Comparable limits are set by ATLAS [55,56]. The purple region represents parameter space of the CMSSM model of [57].

We use the optimized cuts to set limits on dark matter interactions with CF_3I, assuming the bubble nucleation efficiencies for C, F, and I described in Sec. III. The optimization procedure imposes a factor of 1.8 statistical penalty (i.e., trials factor) on the final sensitivity of the experiment. The limit calculations follow the formalism laid out in [34], using the modified Maxwell-Boltzmann halo model with a smooth velocity cutoff at the Galactic escape velocity described in [35] and the following halo parameters: $\rho_D = 0.3$ GeV c^{-2} cm^{-3}, $v_{\rm esc} = 544$ km/s, $v_0 = 220$ km/s, and $v_{\rm Earth} = 30$ km/s. We use the effective field theory treatment and nuclear form factors described in [36–39] to determine sensitivity to both spin-dependent and spin-independent dark matter interactions. For the SI case, we use the M response of Table 1 in [36], and for SD interactions, we use the sum of the Σ' and Σ'' terms from the same table. To implement these interactions and form factors, we use the publicly available DMDD code package [39,40]. The resulting 90% C.L. limit plots for spin-independent WIMP-nucleon and spin-dependent WIMP-proton cross sections are presented in Figs. 12 and 13. We note that adopting the best fit efficiency curves described in Sec. III B instead of the 1σ conservative cases would result in a factor of 5 (2.5) improvement in the limit for SI (SD) WIMPs at 10 GeV, with a 10% improvement above 40 GeV for both types of interactions.

VII. DISCUSSION

Despite the presence of a population of unknown origin in the data set, the combination of the discriminating variables results in a large total exposure with zero dark matter candidates. The SD-proton reach of bubble chambers remains unmatched in the field of direct detection, significantly constraining CMSSM model parameter space.

The leading hypothesis for the source of the background events is particulate contamination. One mechanism by which particulates can create bubbles is if an alpha decay from an atom embedded in a small dust particle resulted in a partial alpha track into the fluid with the daughter nucleus remaining in the particle, and such a track could provide the acoustic signature observed in the background events [26]. The timing and spatial distributions suggest convection currents as a potential source of particle movement, and particulate spike runs in a test chamber have shown that particulates do collect on the interfaces. Additionally, assays of the fluids taken after the run discovered many particulates with composition matching the wetted surfaces of the inner volume, as well as elevated levels of thorium in the chamber. A future run of PICO-60 with C_3F_8 will include upgrades to allow for improved cleaning of the glass and metal surfaces before filling and active filtration of the fluids.

Because of its atomic mass, spin content, and large magnetic moment, iodine is sensitive to a unique selection of potential dark matter interactions [36]. For over a decade, the DAMA/LIBRA experiment has observed a modulation signal in NaI crystals attributed to interactions with dark matter [58], but this signal has not been confirmed by other direct detection experiments. One can potentially reconcile the DAMA result with other null results by postulating that NaI is sensitive to a specific type of interaction of dark matter with iodine nuclei that other nuclear targets would not be sensitive to, for example via the magnetic moment or in inelastic dark matter models [59,60].

The DAMA/LIBRA Collaboration has reported a modulation amplitude of 0.0112 ± 0.0012 counts/kg/keV/day between 2 and 6 keV [58]. Most dark matter halo models require any observed modulation amplitude to be a fraction of the total dark matter signal, leading to a larger total rate of dark matter interactions. However, the smallest possible dark matter cross section compatible with the DAMA/LIBRA observation is obtained by assuming that the modulation signal encompasses the entire dark matter rate. The KIMS Collaboration has published an upper limit on dark matter interactions with iodine (in CsI crystals) of 0.0098 counts/kg/keV/day [61], leaving some room for an iodine interpretation for DAMA/LIBRA given the statistical and systematic uncertainties of the two experiments. Given the use of CF_3I as the target material and its size, the PICO-60 data presented here provide a stronger test of the hypothesis that DAMA/LIBRA is observing dark matter scattering from iodine nuclei.

We take the spectrum of the DAMA/LIBRA modulation between 2 and 6 keV and assume that all scatters come from iodine, correcting for the mass fraction of iodine in NaI. We then apply the quenching factor for iodine used by DAMA (0.09) to convert the observed energy in DAMA/LIBRA to an iodine-equivalent recoil energy of 22–67 keV. The modulation spectrum is convolved with the PICO-60 iodine recoil nucleation efficiency model and WIMP search exposure, taking into account the calendar time of the PICO-60 run. If DAMA/LIBRA were seeing dark matter interactions with iodine, we calculate that PICO-60 would have observed 49 events after applying the optimum cuts. The effective 90% C.L. upper limit on the number of observed events in PICO-60 after applying those cuts is 4.4 events (see the Appendix for details), more than a factor of 10 below the expectation. Because the DAMA/LIBRA modulation extends up to several tens of keV iodine-equivalent recoil energy, these results are quite robust to different models of the iodine nucleation efficiency consistent with the data in [25]. Recent measurements of quenching factors in NaI suggest that iodine has a smaller quenching factor than assumed by DAMA/LIBRA [22,62,63], which would only strengthen the limits presented here. We conclude that the signal in DAMA/LIBRA cannot be iodine recoils induced by dark matter interactions.

One caveat to this conclusion is the possibility of channeling effects, which can result in quenching factors for iodine recoils closer to 1 and have been suggested as a possible mechanism at play in DAMA/LIBRA [64]. Although theoretical work finds an upper limit on the possible channeling fraction of iodine recoils to be 10^{-4} at 2 keV and 10^{-3} at 6 keV [65] and recent calibrations of NaI quenching factors see no evidence for channeling [62,63], these calculations and measurements are subject to uncertainties, as pointed out in [66]. PICO-60 does not provide a test of the DAMA/LIBRA signal if that signal is produced by channeled iodine ions of less than 7 keV.

ACKNOWLEDGMENTS

The PICO Collaboration would like to thank SNOLAB and its staff for providing an exceptional underground laboratory space and invaluable technical support. We acknowledge technical assistance from Fermilab's Computing, Particle Physics, and Accelerator Divisions and from A. Behnke at IUSB. We thank V. Gluscevic and S. McDermott for useful conversations and their assistance with the DMDD code package. This material is based upon work supported by the U.S. Department of Energy, Office of Science, Office of High Energy Physics under Award No. DE-SC-0012161. Fermi National Accelerator Laboratory is operated by Fermi Research Alliance, LLC under Contract No. De-AC02-07CH11359. Part of the research described in this paper was conducted under the Ultra Sensitive Nuclear Measurements Initiative at Pacific Northwest National Laboratory, a multiprogram national laboratory operated by Battelle for the U.S. Department of Energy. We acknowledge the National Science Foundation for their support including Grants No. PHY-1242637, No. PHY-0919526, and No. PHY-1205987. We acknowledge the support of the National Sciences and Engineering Research Council of Canada (NSERC) and the Canada Foundation for Innovation (CFI). We thank the Kavli Institute for Cosmological Physics at the University of Chicago. We were also supported by the Spanish Ministerio de Economía y Competitividad, Consolider MultiDark CSD2009-00064 Grant. We thank the Department of Atomic Energy (DAE), Government of India, under the project CAPP-II at SINP, Kolkata. We acknowledge the Czech Ministry of Education, Youth and Sports, Grant No. LM2011027.

APPENDIX: CUT OPTIMIZATION METHOD

The optimization method used in this analysis provides a statistical framework for optimizing a set of free cut parameters on the dark matter search data to derive the most stringent upper limit, and it allows for background rejection without an explicit model for the background.

The method is similar to that outlined in [33], where the cut parameters to be optimized over were the two end points of an interval in a single variable. In [14] the method was generalized to be applicable to an arbitrary set of cuts and applied to threshold-dependent one-sided cuts on the time since the previous bubble event. Here we apply the generalized method to a set of four one-sided cuts on the parameters AP_{high}, expansion time, distance to the CF_3I surface (Zsurf), and distance to the jar wall (Dwall).

The principal idea of the method is to compare the data to a large number of simulated random data sets with various assumed WIMP-induced expected signal event rates and no background. By comparing the optimum cuts for the experimental and simulated data sets, we find the expected signal rate where the optimized cuts for 90% of simulated experiments with that expected signal rate have the same or worse sensitivity as the experimental data. The assumption of no background in the simulated data sets is conservative, since the inclusion of background events in the model can only reduce the number of events attributed to WIMP interactions, resulting in a more stringent upper limit on the WIMP-induced rate.

The cut optimization method assumes that all events in the data set constitute a potential dark matter signal. However, the distributions shown in Figs. 5, 9, and 10 are clearly inconsistent with such an assumption. Therefore, before the optimization method is applied, we restrict the data set to one whose distributions in each of the four discriminating variables are 3σ consistent with a dark matter hypothesis under a Kolmogorov-Smirnov (KS) test. The cuts on each of the variables are applied sequentially, and the ordering is chosen based on which of the remaining variables' distributions is the least consistent with dark matter.

To illustrate how this is applied, we begin with the full data set. We perform a KS test of the AP_{high} between the calibration data and the low AP peak of Fig. 5, as well as KS tests between the observed expansion time and Zsurf distributions and simulated dark matter signals. While all three KS tests return p values of less than 10^{-60} that the two samples under test are drawn from the same distribution, the largest KS-test statistic (corresponding to the smallest correspondence between the distributions under test) is found for AP_{high}. We therefore impose an upper limit cut on the value of AP_{high} and slowly lower that cut value until the KS test between the calibration data and the background events returns a p value > 0.003. This occurs for $AP_{high} < 1.022$, with 32 events remaining.

With the $AP_{high} < 1.022$ cut in place, we perform new KS tests of the expansion time and Zsurf distributions between the simulated dark matter signals and the remaining background, finding a p value for expansion time of $\sim 10^{-9}$ and the p value for the Zsurf distribution of $\sim 10^{-7}$. We follow the same procedure, increasing the one-sided cut on expansion time until once again the KS test returns a p value > 0.003. We repeat the process one more time on Zsurf. No cut is made on Dwall beyond the nominal fiducial cut, as the Dwall distribution is consistent with dark matter at the 3σ level. The corresponding cuts defining the restricted data set are shown in Table I. These cuts remove all but 16 events while keeping 63.8% of the total exposure.

TABLE I. Nominal, restricted and optimum cut values along with their acceptances (relative to the nominal case) and the number of background events passing the cuts. Variable definitions and the derivation of the restricted and optimum cut values is described in the text.

Cuts	Nominal	Restricted	Optimum
AP_{high}	···	<1.022	<1.020
Expansion time [s]	>25	>40.8	>45.7
Zsurf [mm]	>6	>9.0	>67.8
Dwall [mm]	>5	>5	>5.4
Acceptance	100%	63.8%	48.2%
Events passing	2111	16	0

At this stage, for a given expected signal rate, all possible sets of cut parameters are tested on the restricted data set to find the optimum cuts, defined as the cuts that maximize the probability of observing more events passing the cuts than actually do pass the cuts. That is, the cut parameters are found that provide the highest confidence level for excluding the assumed expected signal rate as too high. The probability and confidence levels are functions of the expected signal rate, as are, in principle, the optimum cuts, although we find the same optimum cuts over the full range of expected signal rate explored. The maximum confidence level is referred to as C_{max}. The quantity C_{max} is also calculated for each simulated data set with the expected signal rate applicable to that data set. The 90th percentile value of C_{max} over the set of simulations for a given expected signal rate is referred to as $\bar{C}_{max}$. The 90% upper limit on the expected signal rate is the smallest rate for which C_{max} of the data is greater than $\bar{C}_{max}$.

To determine C_{max} it is first necessary to evaluate the function $C_n(x,\mu)$, defined to be the probability, for a given expected signal rate without background, that all sets of cuts with $\leq n$ events passing have their expected number of events $< x$. Here μ is the expected number of signal events in the data set before cuts. For a large number of simulated data sets with μ expected events, $C_n(x,\mu)$ is the fraction of those data sets where all sets of cuts leaving n or fewer events have fractional acceptance less than x/μ. Uncertainty in the cut acceptance is incorporated as a nuisance parameter by allowing the expected number of events in each simulation to vary normally from μ with the width given by the percentage uncertainty.

For each data set (experimental or simulated), C_{max} is the maximum over all sets of cut parameters of $C_n(x,\mu)$—evaluated by finding the largest acceptance cuts allowing only n events to pass for each value of n, looking up the value of $C_n(x,\mu)$ applicable to those cuts, and then taking

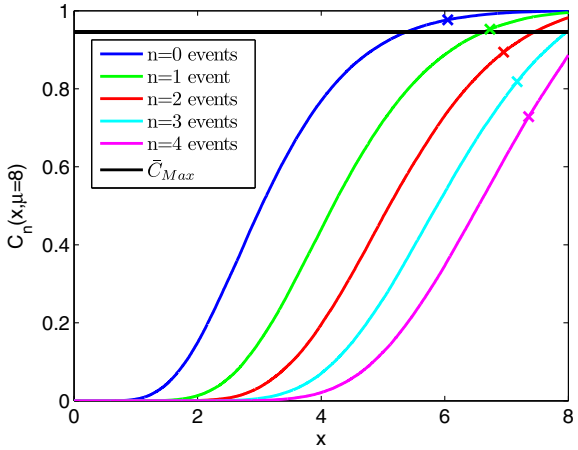

FIG. 14. $C_n(x,\mu)$ for $n = 0$, 1, 2, 3, 4 for simulations with $\mu = 8$. For each n, the maximum value of x for the restricted data set is indicated by an "x." Over all n, the maximum of $C_n(x,\mu)$ for the restricted data set is 0.978 for $n = 0$. For $\mu = 8$, $\bar{C}_{\max} = 0.946$, indicated by the horizontal black line. For both $n = 0$ and $n = 1$ the maximum of $C_n(x,\mu)$ exceeds $\bar{C}_{\max}$, thus excluding $\mu = 8$ as too large at greater than the 90% C.L.

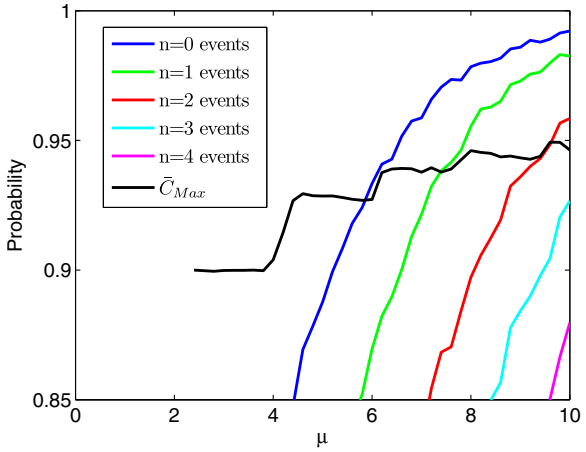

FIG. 15. Maximum of $C_n(x,\mu)$ for the restricted data set for $n = 0$, 1, 2, 3, 4, compared to $\bar{C}_{\max}$. Over the range of μ shown $C_{\max}$ is always taken from the $n = 0$ curve. All WIMP couplings corresponding to $\mu \geq 5.4$, where $C_{\max} > \bar{C}_{\max}$, are excluded at the 90% C.L.

the maximum over all n. Figure 14 shows an example distribution for $\mu = 8$. $C_{\max}$ for the experimental data is then compared to $\bar{C}_{\max}$, the 90th percentile value of $C_{\max}$ over the set of simulations. Any μ for which $C_{\max}$ of the data is larger than $\bar{C}_{\max}$ is excluded as too large at the 90% C.L.; thus, the most stringent upper limit on μ is set by scanning to find the smallest value of μ that is excluded, which we find to be $\mu = 5.8$ as shown in Fig. 15.

The final optimum cut values are shown in Table I. The optimum cuts remove all events while still keeping 48.2% of the total exposure. If the optimum cuts had simply been set *a posteriori*, without applying the tuning penalty inherent in the optimization method, the final sensitivity of the experiment would be a factor of 1.8 lower than reported here. To put it another way, the 90% C.L. upper limit of 5.8 events in the exposure of PICO-60 with restricted cuts applied is equivalent to 4.4 events with optimum cuts applied, where the 90% Poisson upper limit would have been 2.3 events for an exposure with zero observed counts (2.4 events after accounting for uncertainty in the cut acceptance).

[1] S. Ritz *et al.*, Particle Physics Projects Prioritization Panel Report, 2014.
[2] P. Cushman *et al.*, arXiv:1310.8327.
[3] E. Komatsu *et al.*, Astrophys. J. Suppl. Ser. **180**, 330 (2009), and references therein.
[4] G. Jungman, M. Kamionkowski, and K. Griest, Phys. Rep. **267**, 195 (1996).
[5] G. Bertone, D. Hooper, and J. Silk, Phys. Rep. **405**, 279 (2005); J. L. Feng, Annu. Rev. Astron. Astrophys. **48**, 495 (2010).
[6] M. W. Goodman and E. Witten, Phys. Rev. D **31**, 3059 (1985).
[7] W. J. Bolte *et al.*, Nucl. Instrum. Methods Phys. Res., Sect. A **577**, 569 (2007).
[8] E. Behnke *et al.*, Science **319**, 933 (2008).
[9] E. Behnke, J. Behnke, S. J. Brice, D. Broemmelsiek, J. I. Collar, P. S. Cooper, M. Crisler, C. E. Dahl, D. Fustin, J. Hall, J. H. Hinnefeld, M. Hu, I. Levine, E. Ramberg, T. Shepherd, A. J. Sonnenschein, and M. Szydagis, Phys. Rev. Lett. **106**, 021303 (2011).
[10] E. Behnke *et al.*, Phys. Rev. D **86**, 052001 (2012).
[11] S. Archambault *et al.*, Phys. Lett. B **682**, 185 (2009).
[12] S. Archambault *et al.*, Phys. Lett. B **711**, 153 (2012).
[13] M. Felizardo *et al.*, Phys. Rev. D **89**, 072013 (2014).
[14] C. Amole *et al.*, Phys. Rev. Lett. **114**, 231302 (2015).
[15] F. Duncan, A. J. Noble, and D. Sinclair, Annu. Rev. Nucl. Part. Sci. **60**, 163 (2010).
[16] DYTRAN 2005V, DYTRAN Instruments, Inc.
[17] D. A. Glaser and D. C. Rahm, Phys. Rev. **97**, 474 (1955).
[18] F. Seitz, Phys. Fluids **1**, 2 (1958).
[19] J. W. Gibbs, *The Scientific Papers of J. Willard Gibbs* (Ox Bow Press, Woodbridge, CT, 1993).
[20] E. W. Lemmon, M. L. Huber, and M. O. McLinden, NIST Standard Reference Database 23: Reference Fluid Thermodynamic and Transport Properties-REFPROP, Version 9.0,

National Institute of Standards and Technology, Standard Reference Data Program, Gaithersburg, 2010.
[21] A. Robinson, Identification of Dark Matter 2012, https://kicp-workshops.uchicago.edu/IDM2012/depot/talk-robinson-alan.pdf.
[22] J. I. Collar, Phys. Rev. Lett. **110**, 211101 (2013).
[23] A. Robinson, Ph.D. thesis, University of Chicago, 2015.
[24] J. F. Zeigler *et al.*, http://www.srim.org.
[25] E. Behnke *et al.*, Phys. Rev. D **88**, 021101 (2013).
[26] S. Archambault *et al.*, New J. Phys. **13**, 043006 (2011).
[27] W. B. Wilson *et al.*, Radiation Protection Dosimetry **115**, 117 (2005).
[28] D-M. Mei and A. Hime, Phys. Rev. D **73**, 053004 (2006).
[29] B. Aharmim *et al.*, Phys. Rev. D **80**, 012001 (2009).
[30] S. Agostinelli *et al.*, Nucl. Instrum. Methods Phys. Res., Sect. A **506**, 250 (2003); J. Allison *et al.*, IEEE Trans. Nucl. Sci. **53**, 270 (2006).
[31] D. Fustin, Ph.D. thesis, University of Chicago, 2012; A. Robinson, COUPP Document 630: High Energy Gamma Flux and Photonuclear Rates in COUPP-4 kg at SNOLAB, 2012 (unpublished).
[32] F. Aubin *et al.*, New J. Phys. **10**, 103017 (2008).
[33] S. Yellin, Phys. Rev. D **66**, 032005 (2002).
[34] J. D. Lewin and P. F. Smith, Astropart. Phys. **6**, 87 (1996).
[35] A. L. Fitzpatrick and K. M. Zurek, Phys. Rev. D **82**, 075004 (2010).
[36] A. L. Fitzpatrick, W. C. Haxton, E. Katz, N. Lubbers, and Y. Xu, J. Cosmol. Astropart. Phys. 02 (2013) 004.
[37] N. Anand, A. L. Fitzpatrick, and W. C. Haxton, Phys. Rev. C **89**, 065501 (2014).
[38] M. I. Gresham and K. M. Zurek, Phys. Rev. D **89**, 123521 (2014).
[39] V. Gluscevic, M. I. Gresham, S. D. McDermott, A. H. G. Peter, and K. M. Zurek, J. Cosmol. Astropart. Phys. 12 (2015) 057.
[40] V. Gluscevic and S. D. McDermott, 2015, DMDD, Astrophysics Source Code Library, record ascl:1506.002.
[41] D. S. Akerib *et al.*, Phys. Rev. Lett. **112**, 091303 (2014).
[42] E. Aprile *et al.*, Phys. Rev. Lett. **109**, 181301 (2012).
[43] P. Agnes *et al.*, arXiv:1510.00702v1.
[44] R. Agnese *et al.*, Phys. Rev. D **92**, 072003 (2015).
[45] E. Aprile *et al.*, Phys. Rev. Lett. **111**, 021301 (2013).
[46] M. G. Aartsen *et al.*, Phys. Rev. Lett. **110**, 131302 (2013).
[47] T. Tanaka *et al.*, Astrophys. J. **742**, 78 (2011).
[48] K. Choi *et al.*, Phys. Rev. Lett. **114**, 141301 (2015).
[49] CMS Collaboration, Eur. Phys. J. C **75**, 235 (2015).
[50] S. Adrián-Martínez *et al.*, J. Cosmol. Astropart. Phys. 11 (2013) 032.
[51] S. Demidov and O. Suvorova, J. Cosmol. Astropart. Phys. 06 (2010) 018.
[52] A. D. Avrorin *et al.*, Astropart. Phys. **62**, 12 (2015).
[53] G. Busoni, A. de Simone, E. Morgante, and A. Riotto, Phys. Lett. B **728**, 412 (2014).
[54] O. Buchmueller, M. J. Dolan, and C. McCabe, J. High Energy Phys. 01 (2014) 025.
[55] ATLAS Collaboration, Eur. Phys. J. C **75**, 299 (2015).
[56] ATLAS Collaboration, Eur. Phys. J. C **75**, 92 (2015).
[57] L. Roszkowski, R. R. de Austri, and R. Trotta, J. High Energy Phys. 07 (2007) 075.
[58] R. Bernabei *et al.*, Eur. Phys. J. C **73**, 2648 (2013).
[59] S. Chang, N. Weiner, and I. Yavin, Phys. Rev. D **82**, 125011 (2010).
[60] G. Barello, S. Chang, and C. A. Newby, Phys. Rev. D **90**, 094027 (2014).
[61] S. C. Kim *et al.*, Phys. Rev. Lett. **108**, 181301 (2012).
[62] J. I. Collar, Phys. Rev. C **88**, 035806 (2013).
[63] J. Xu *et al.*, Phys. Rev. D **92**, 015807 (2015).
[64] R. Bernabei *et al.*, Eur. Phys. J. C **53**, 205 (2008).
[65] N. Bozorgnia, G. B. Gelmini, and P. Gondolo, J. Cosmol. Astropart. Phys. 11 (2010) 019.
[66] R. Bernabei *et al.*, Int. J. Mod. Phys. A **28**, 1330022 (2013).

Appendix V

PICO-60 Paper - C_3F_8

Dark Matter Search Results from the PICO-60 C_3F_8 Bubble Chamber

C. Amole,[1] M. Ardid,[2] I. J. Arnquist,[3] D. M. Asner,[3] D. Baxter,[4,5,*] E. Behnke,[6] P. Bhattacharjee,[7] H. Borsodi,[6] M. Bou-Cabo,[2] P. Campion,[8] G. Cao,[1] C. J. Chen,[4] U. Chowdhury,[1] K. Clark,[9,10] J. I. Collar,[11] P. S. Cooper,[5] M. Crisler,[5] G. Crowder,[1] C. E. Dahl,[4,5] M. Das,[7] S. Fallows,[12] J. Farine,[9] I. Felis,[2] R. Filgas,[13] F. Girard,[9,14] G. Giroux,[1,†] J. Hall,[3] O. Harris,[6,15] E. W. Hoppe,[3] M. Jin,[4] C. B. Krauss,[12] M. Laurin,[14] I. Lawson,[9,10] A. Leblanc,[9] I. Levine,[6] W. H. Lippincott,[5] F. Mamedov,[13] D. Maurya,[16] P. Mitra,[12] T. Nania,[6] R. Neilson,[8] A. J. Noble,[1] S. Olson,[1] A. Ortega,[11] A. Plante,[14] R. Podviyanuk,[9] S. Priya,[16] A. E. Robinson,[5] A. Roeder,[6] O. Scallon,[9] S. Seth,[7] A. Sonnenschein,[5] N. Starinski,[14] I. Štekl,[13] F. Tardif,[14] E. Vázquez-Jáuregui,[17,9] J. Wells,[6] U. Wichoski,[9] Y. Yan,[16] V. Zacek,[14] and J. Zhang[4]

(PICO Collaboration)

[1] *Department of Physics, Queen's University, Kingston, K7L 3N6, Canada*
[2] *Departament de Física Aplicada, IGIC - Univesitat Politècnica de València, Gandia 46730 Spain*
[3] *Pacific Northwest National Laboratory, Richland, Washington 99354, USA*
[4] *Department of Physics, Northwestern University, Evanston, Illinois 60208, USA*
[5] *Fermi National Accelerator Laboratory, Batavia, Illinois 60510, USA*
[6] *Department of Physics, Indiana University South Bend, South Bend, Indiana 46634, USA*
[7] *Astroparticle Physics and Cosmology Division, Saha Institute of Nuclear Physics, Kolkata, India*
[8] *Department of Physics, Drexel University, Philadelphia, Pennsylvania 19104, USA*
[9] *Department of Physics, Laurentian University, Sudbury, P3E 2C6, Canada*
[10] *SNOLAB, Lively, Ontario, P3Y 1N2, Canada*
[11] *Enrico Fermi Institute, KICP and Department of Physics, University of Chicago, Chicago, Illinois 60637, USA*
[12] *Department of Physics, University of Alberta, Edmonton, T6G 2E1, Canada*
[13] *Institute of Experimental and Applied Physics, Czech Technical University in Prague, Prague, Cz-12800, Czech Republic*
[14] *Département de Physique, Université de Montréal, Montréal, H3C 3J7, Canada*
[15] *Northeastern Illinois University, Chicago, Illinois 60625, USA*
[16] *Bio-Inspired Materials and Devices Laboratory (BMDL), Center for Energy Harvesting Material and Systems (CEHMS), Virginia Tech, Blacksburg, Virginia 24061, USA*
[17] *Instituto de Física, Universidad Nacional Autónoma de México, México D. F. 01000, México*

(Dated: February 27, 2017)

New results are reported from the operation of the PICO-60 dark matter detector, a bubble chamber filled with 52 kg of C_3F_8 located in the SNOLAB underground laboratory. As in previous PICO bubble chambers, PICO-60 C_3F_8 exhibits excellent electron recoil and alpha decay rejection, and the observed multiple-scattering neutron rate indicates a single-scatter neutron background of less than 1 event per month. A blind analysis of an efficiency-corrected 1167-kg-day exposure at a 3.3-keV thermodynamic threshold reveals no single-scattering nuclear recoil candidates, consistent with the predicted background. These results set the most stringent direct-detection constraint to date on the WIMP-proton spin-dependent cross section at 3.4×10^{-41} cm^2 for a 30-GeV c^{-2} WIMP, more than one order of magnitude improvement from previous PICO results.

PACS numbers: 29.40.-n, 95.35.+d, 95.30.Cq, FERMILAB-PUB-17-058-AE-PPD

The evidence for nonbaryonic dark matter in the galactic halo is compelling [1, 2]. Many classes of theory, including supersymmetric extensions to the Standard Model (SUSY), provide promising dark matter candidates in the form of non-relativistic, weakly interacting, massive particles (WIMPs) [3]. The search for WIMPs is challenging due to the predicted small WIMP-nucleon scattering cross section and nuclear recoil energies in the range of 1 to 100 keV. Low thresholds, large exposures, and background suppression are therefore critical to obtain sufficient sensitivity. As the nature of the WIMP-nucleon interaction is unknown, explorations in both the spin-dependent (SD) and spin-independent (SI) couplings are essential [4–6].

The PICO collaboration searches for WIMPs using superheated bubble chambers operated in thermodynamic conditions at which they are virtually insensitive to gamma or beta radiation. Further background suppression is achieved through the measurement of the bubble's acoustic emission, allowing for discrimination between signals from alpha decays and those from nuclear recoils [7]. The PICO bubble chambers, filled with fluorine-rich liquids, have consistently provided the strongest constraints to spin-dependent WIMP-proton interactions [8–14]. Our largest bubble chamber to date, PICO-60, was recently filled with a 52.2 ± 0.5 kg C_3F_8 target, and op-

erated at SNOLAB in Sudbury, Ontario, Canada. Here we report results from the first run of PICO-60 with C_3F_8, with an efficiency-corrected dark matter exposure of 1167 kg-days, taken between November 2016 and January 2017.

The PICO Collaboration previously reported the observation of anomalous background events in dark matter search data with the 2-liter PICO-2L C_3F_8 [8] and the 18-liter PICO-60 CF_3I [10] bubble chambers. Improvements in fluid handling and bubble chamber operation eliminated this anomalous background in a second run of the PICO-2L detector [9]. A leading hypothesis for the cause of these background events is bubble nucleation due to surface tension effects introduced by the contamination of the active target with particulate matter and water droplets [15]. The PICO-60 detector was recommissioned following a rigorous cleaning procedure targeting particulate contamination. Every component was cleaned to MIL-STD-1246 Level 50 standard [16] prior to assembly, and samples of the water buffer were taken using an *in situ* filtration system during commissioning to monitor particulate injection. A final measurement after C_3F_8 distillation confirmed that the total assembly met MIL-STD-1246 Level 100, after which the inner volume was closed.

The PICO-60 apparatus was described in Ref. [10], and here we restrict ourselves to describing subsequent improvements and changes. A new seal design was deployed between the silica jar and the stainless steel bellows to minimize particulate generation, replacing the gold wire seal described in Ref. [10] with a PTFE gasket. The C_3F_8 target does not require the addition of chemicals to remove free ions, unlike CF_3I. While the same water tank is used, a new chiller system holds the temperature in the water tank uniform to approximately 0.1°C. The target volume was more than doubled, requiring a corresponding increase from two to four cameras (in two vertical columns). Eight piezoelectric acoustic transducers identical to those used in Ref. [9] were attached, evenly-spaced around the outside of the silica jar, using a spring loaded HDPE ring. Five sensors failed during commissioning, leaving three operable sensors for the duration of the experiment.

The chamber expansion cycle was similar to that employed in the previous run [10]. First, the chamber is expanded to a predetermined pressure, superheating the C_3F_8 active liquid. Following a trigger, the hydraulic system initiates a fast compression, raising the pressure above 150 psia in roughly 100 ms. The primary trigger uses the change in entropy between two consecutive camera images [17] to detect the appearance of a gas bubble in the chamber. A trigger is also sent if a rise in pressure is detected or when the chamber has been expanded for 2000 s. The chamber begins a new expansion after the chamber has been compressed for 100 s. A long compression of 600 s is imposed on every tenth compression or

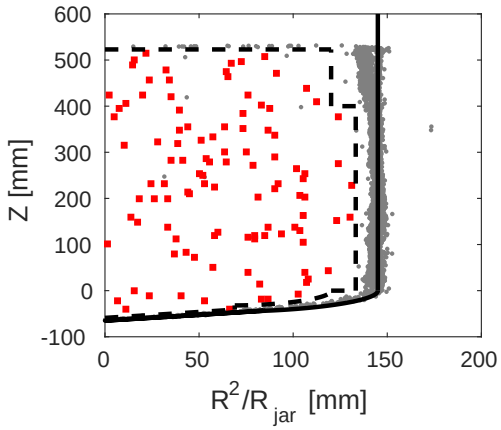

FIG. 1. Spatial distribution of bubble events in the WIMP search data. Z is the reconstructed vertical position of the bubble, and R^2/R_{jar} is the distance from the center axis squared, normalized by the nominal jar radius (145 mm). The fiducial cut is represented by the dashed line. Red squares are the 106 events in the fiducial bulk volume passing all cuts and grey dots are all other single-bubble events.

after a pressure-rise trigger. In the WIMP search dataset, the chamber was expanded for 34.3 of the 44.6 days that the detector was operational.

The WIMP search dataset was taken at 30.2 ± 0.3 psi and 13.9 ± 0.1°C, corresponding to a thermodynamic threshold of 3.29 ± 0.09 keV, the calculation of which is detailed in Ref. [10]. There is an additional 0.2 keV uncertainty in the threshold due to the thermodynamic properties of C_3F_8 [18]. *In situ* nuclear and electronic recoil calibrations were performed by exposing the chamber to AmBe and ^{252}Cf neutron sources and a ^{133}Ba gamma source both before and after the WIMP search run. Pre-physics background data were taken during commissioning to measure the alpha backgrounds due to ^{222}Rn chain decays. For the WIMP search run, we performed a blind analysis by masking the acoustic information that allows the discrimination between alpha decays and nuclear recoils. This information was processed only after cuts and efficiencies for single bulk nuclear recoil candidates were set, using source calibrations and pre-physics background data.

For the WIMP search dataset, periods of unstable operation are removed, these being defined as times within one hour of radioactive source transport near the detector or in a 24-hour window following any significant interruption to operation. The first 25 s of every expansion is discarded to remove transient effects. Of the 34.3 days the detector was expanded, 30.0 live-days (87.4%) are considered in the WIMP search.

Bubble images are identified using the same entropy algorithm as used for the optical trigger. The pixel coordinates are then reconstructed into spatial coordinates using ray propagation in a simulated optical geometry.

Dataset	Efficiency (%)	Fiducial Mass (kg)	Exposure (kg-days)	No. of events
Singles	85.1 ± 1.8	45.7 ± 0.5	1167 ± 28	0
Multiples	99.4 ± 0.1	52.2 ± 0.5	1555 ± 15	3

TABLE I. Summary of the final number of events and exposure determination for singles and multiples in the 30.0 live-day WIMP search dataset of PICO-60 C_3F_8 at 3.3 keV thermodynamic threshold.

The fiducial volume is determined by setting cut values on isolated wall and surface event distributions in the source calibration and pre-physics background datasets, as shown in Fig. 1. These cuts remove events on or near the surface or within 6 mm of the nominal wall location. For regions of the detector where the optics are worse, such as the transition to the lower hemisphere, the outer 13 mm are removed. The fiducial cuts accept a mass of 45.7 ± 0.5 kg, or 87.7% of the total C_3F_8 mass.

The first step in the WIMP candidate selection removes events that are written improperly on disk, events that were not triggered by the cameras, and events for which the pressure was more than 1 psi from the target pressure. The signal acceptance for these cuts is greater than 99.9%. Only events that are optically reconstructed as a single bubble are selected as WIMP candidates. This cut removes neutron-induced multiple bubble events and events for which the optical reconstruction failed. The acceptance of this cut is 98.0 ± 0.5%. In addition to the optical reconstruction fiducial cut, fiducial-bulk candidates are selected based on a rate-of-pressure-rise measurement, which is found to accept all optically reconstructed fiducial single bubbles in the source calibration data.

The acoustic analysis is similar to the procedure described in [11] to calculate the Acoustic Parameter (AP), a measurement of the bubble's nucleation acoustic energy. As AP is used to discriminate alpha particles from nuclear recoils, events with high pre-trigger acoustic noise or an incorrectly reconstructed signal start time are removed from the WIMP candidates selection. The efficiency for these cuts is 99.6 ± 0.2%. For this analysis, based on the pre-physics background and calibration data, AP is found to optimally discriminate alpha particles from nuclear recoils using the signals of two out of the three working acoustic transducers in the 55 kHz to 120 kHz frequency range. The AP distribution for nuclear recoil events is normalized to 1 based on AmBe and ^{252}Cf nuclear recoil calibration data.

An additional metric, NN score, is constructed from the piezo traces using a neural network [19] trained to distinguish pure alpha events (NN score = 1) from pure nuclear or electron recoil events (NN score = 0). The two-layer feedforward network takes as an input the bubble's 3D position, and the noise-subtracted acoustic energy of each of three working acoustic transducers in 8 frequency bands ranging from 1 kHz to 300 kHz. The network is

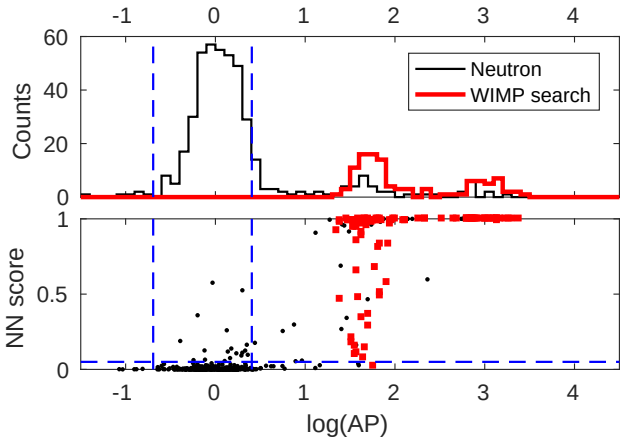

FIG. 2. Top: AP distributions for AmBe and ^{252}Cf neutron calibration data (black) and WIMP search data (red) at 3.3 keV threshold. Alphas from the ^{222}Rn decay chain can be identified by their time signature and populate the two peaks in the WIMP search data at high AP. Higher energy alphas from ^{214}Po are producing larger acoustic signals. Bottom: AP and NN score for the same dataset. The cuts for the nuclear recoil candidates, defined before WIMP search acoustic data unmasking, are displayed with dashed lines.

trained and validated with source calibration data and the pre-physics background data. A nuclear recoil candidate is defined as having an AP between 0.5 to 1.5 and a NN score less than 0.05. These combined acoustic cuts are determined to have an acceptance of 88.5 ± 1.6% based on neutron calibration fiducial-bulk singles.

In the WIMP search data, before unmasking the AP and NN score, all events passing cuts are identified and manually scanned. Any events with mismatched pixel coordinates are discarded. The same procedure is found to keep 98.7 ± 0.7% of fiducial-bulk singles in the neutron calibration data. The final efficiencies and exposure are summarized in Table I. A total of 106 single bulk bubbles, shown in Fig. 1, are found in the blinded WIMP search data.

Neutrons produced by (α,n) and spontaneous fission from ^{238}U and ^{232}Th characteristically scatter multiple times in the detector, resulting in multiple-bubble events 75% of the time for a chamber of this size. The multiple-bubble events are an unambiguous signature and provide a measurement of the neutron background. To isolate multiple-bubble events in the WIMP search data, we do

not apply acoustic or fiducial cuts, resulting in the larger exposure shown in Table I. Instead, given $99.5 \pm 0.1\%$ efficiency to reconstruct at least one bubble in the bulk for a multiple-bubble event, every passing event is scanned for multiplicity. This scan reveals 3 multiple-bubble events in the WIMP search dataset. Based on a detailed Monte Carlo simulation, the background from neutrons is predicted to be 0.25 ± 0.09 (0.96 ± 0.34) single(multiple)-bubble events. PICO-60 was exposed to a 1 mCi ^{133}Ba source both before and after the WIMP search data, which, compared against a Geant4 [20] Monte Carlo simulation, gives a measured nucleation efficiency for electron recoil events above 3.3 keV of $(1.80 \pm 0.38)\times10^{-10}$. Combining this with a Monte Carlo simulation of the external gamma flux from [15, 21], we predict 0.026 ± 0.007 events due to electron recoils in the WIMP search exposure. The background from coherent scattering of ^{8}B solar neutrinos is calculated to be 0.055 ± 0.007 events.

The unmasking of the acoustic data, performed after completion of the WIMP search run, reveals that none of the 106 single bulk bubbles are consistent with the nuclear recoil hypothesis defined by AP and the NN score, as shown in Fig. 2.

We use the same procedure and calibration data described in Ref. [8] to evaluate nucleation efficiency curves for fluorine and carbon recoils. We adopt the standard halo parametrization [22], with ρ_D=0.3 GeV c^{-2} cm^{-3}, $v_{\rm esc}$ = 544 km/s, $v_{\rm Earth}$ = 232 km/s, and v_o = 220 km/s. We use the effective field theory treatment and nuclear form factors described in Refs. [23–26] to determine sensitivity to both spin-dependent and spin-independent dark matter interactions. For the SI case, we use the M response of Table 1 in Ref. [23], and for SD interactions, we use the sum of the Σ' and Σ'' terms from the same table. To implement these interactions and form factors, we use the publicly available dmdd code package [26, 27]. The calculated limits at the 90% C.L. for the spin-dependent WIMP-proton and spin-independent WIMP-nucleon elastic scattering cross-sections, with no background subtraction, as a function of WIMP mass, are shown in Fig. 3 and 4. These limits are currently the world-leading constraints in the WIMP-proton spin-dependent sector and indicate an improved sensitivity to the dark matter signal of a factor of 17, compared to previously reported PICO results.

Constraints on the effective spin-dependent WIMP-neutron and WIMP-proton couplings a_n and a_p are calculated according to the method proposed in Ref. [28]. The expectation values for the proton and neutron spins for the ^{19}F nucleus are taken from Ref. [23]. The allowed region in the $a_n - a_p$ plane is shown for a 50 GeV c^{-2} WIMP in Fig. 5. We find that PICO-60 C_3F_8 improves the constraints on a_n and a_p, in complementarity with other dark matter search experiments that are more sensitive to the WIMP-neutron coupling.

The LHC has significant sensitivity to dark matter,

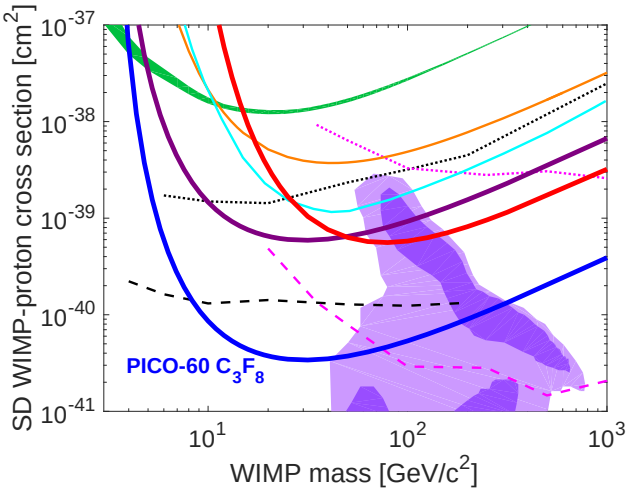

FIG. 3. The 90% C.L. limit on the SD WIMP-proton cross section from PICO-60 C_3F_8 plotted in blue, along with limits from PICO-60 CF_3I (red) [10], PICO-2L (purple) [9], PICASSO (green) [14], SIMPLE (orange) [33], PandaX-II (cyan) [34], IceCube (dashed and dotted pink) [35], and SuperK (dashed and dotted black) [36, 37]. The indirect limits from IceCube and SuperK assume annihilation to τ leptons (dashed) and b quarks (dotted). The purple region represents parameter space of the constrained minimal supersymmetric model of [38]. Additional limits, not shown for clarity, are set by LUX [39] and XENON100 [40] (comparable to PandaX-II) and by ANTARES [41, 42] (comparable to IceCube).

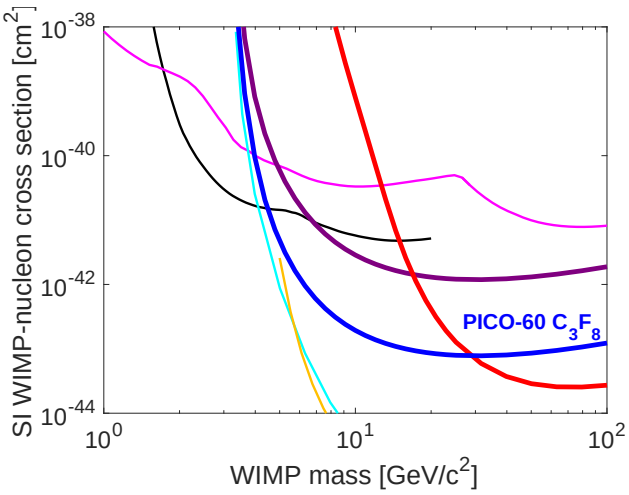

FIG. 4. The 90% C.L. limit on the SI WIMP-nucleon cross-section from PICO-60 C_3F_8 plotted in blue, along with limits from PICO-60 CF_3I (red) [10], PICO-2L (purple) [9], LUX (yellow) [43], PandaX-II (cyan) [44], CRESST-II (magenta) [45], and CDMS-lite (black) [46]. While we choose to highlight this result, LUX sets the strongest limits on WIMP masses greater than 6 GeV/c^2. Additional limits, not shown for clarity, are set by PICASSO [14], XENON100 [40], DarkSide-50 [47], SuperCDMS [48], CDMS-II [49], and Edelweiss-III [50].

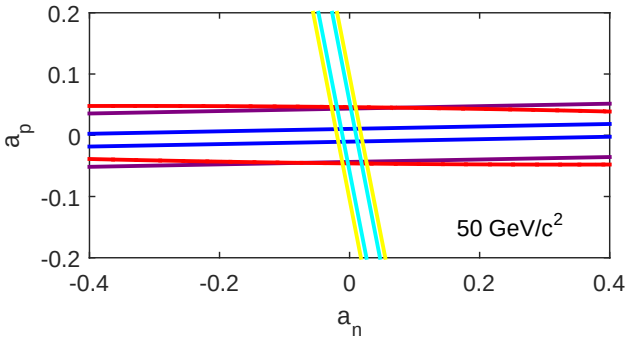

FIG. 5. PICO-60 constraints (blue) on the effective spin-dependent WIMP-proton and WIMP-neutron couplings, a_p and a_n, for a 50 GeV/c^2 WIMP mass. Also shown are results from PANDAX-II (cyan) [34], LUX (yellow) [39], PICO-2L (purple) [9], and PICO-60 C_3FI (red) [10].

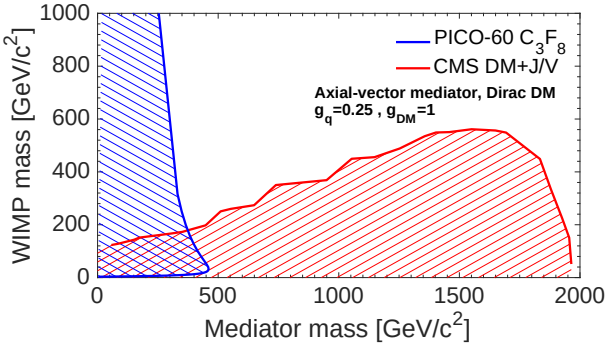

FIG. 6. Exclusion limits at 95% C.L. in the $m_{\rm DM} - m_{\rm med}$ plane. PICO-60 constraints (blue) are compared against collider constraints from CMS (red) [32] for an axial-vector mediator using the monojet and mono-V channels.

but to interpret LHC searches, one must assume a specific model to generate the signal that is then looked for in the data. This can make it difficult to compare LHC results with direct detection experiments, as the latter tend to be more general. The LHC Dark Matter Working Group (LHCDMWG) has made recommendations on a set of simplified models to be used in LHC searches and the best way to present such results [29–31]. For a given simplified model involving a mediator exchanged via the s-channel, there are four free parameters: the dark matter mass $m_{\rm DM}$, the mediator mass $m_{\rm med}$, the universal mediator coupling to quarks g_q, and the mediator coupling to dark matter $g_{\rm DM}$. The LHCDMWG recommends that results of simplified model searches be presented by plotting confidence level limits as a function of the two mass parameters $m_{\rm DM}$ and $m_{\rm med}$ for a fixed set of couplings g_q and $g_{\rm DM}$. Here, we follow the example set by the LHCDMWG to make a direct comparison of the sensitivity of PICO to that of CMS [32] by applying our results to the specific case of a simplified dark matter model involving an axial-vector s-channel mediator. Following Eq. 4.7-4.10 of Ref. [31], we find an expression for the spin-dependent cross section as a function of those free parameters, and we invert this expression to find $m_{\rm med}$ as a function of cross section. For this comparison, we assume $g_q = 0.25$ and $g_{\rm DM} = 1$. With this simple translation, we can plot our limits on the same $m_{\rm DM} - m_{\rm med}$ plane, and the results are shown in Fig. 6.

The PICO collaboration wishes to thank SNOLAB and its staff for support through underground space, logistical and technical services. SNOLAB operations are supported by the Canada Foundation for Innovation and the Province of Ontario Ministry of Research and Innovation, with underground access provided by Vale at the Creighton mine site. We are grateful to Kristian Hahn and Stanislava Sevova of Northwestern University and Björn Penning of the University of Bristol for their assistance and useful discussion. We wish to acknowledge the support of the National Sciences and Engineering Research Council of Canada (NSERC) and the Canada Foundation for Innovation (CFI) for funding. We acknowledge the support from National Science Foundation (NSF) (Grant 0919526, 1506337, 1242637 and 1205987). We acknowledge that this work is supported by the U.S. Department of Energy (DOE) Office of Science, Office of High Energy Physics (under award DE-SC-0012161), by the DOE Office of Science Graduate Student Research (SCGSR) award, by DGAPA-UNAM through grant PAPIIT No. IA100316 and CONACyT (Mexico) through grant No. 252167, by the Department of Atomic Energy (DAE), the Government of India, under the Center of AstroParticle Physics II project (CAPP-II) at SAHA Institute of nuclear Physics (SINP), the Czech Ministry of Education, Youth and Sports (Grant LM2015072) and the the Spanish Ministerio de Economía y Competitividad, Consolider MultiDark (Grant CSD2009-00064). This work is partially supported by the Kavli Institute for Cosmological Physics at the University of Chicago through NSF grant 1125897, and an endowment from the Kavli Foundation and its founder Fred Kavli. We also wish to acknowledge the support from Fermi National Accelerator Laboratory under Contract No. De-AC02-07CH11359, and Pacific Northwest National Laboratory, which is operated by Battelle for the U.S. Department of Energy under Contract No. DE-AC05-76RL01830.

* danielbaxter2013@u.northwestern.edu
† ggiroux@owl.phy.queensu.ca

[1] K.A. Olive *et al.* (Particle Data Group), Chinese Phys. C**38**, 090001 (2014).
[2] E. Komatsu *et al.*, Astroph. J. Suppl. **180**, 330 (2009) and refs. therein.
[3] G. Jungman, M. Kamionkowski, and K. Griest, Phys.

Rep. **267**, 195 (1996).
[4] M. W. Goodman and E. Witten, Phys. Rev. D **31**, 3059 (1985).
[5] P. Cushman *et al.*, Snowmass CF1 Summary: WIMP Dark Matter Direct Detection, arXiv:1310.8327 [hep-ex] (2013).
[6] G. Bertone, D. Hooper, and J. Silk, Phys. Rep. **405**, 279, (2005); J.L. Feng, Ann. Rev. Astr. Astroph., **48**, 496 (2010).
[7] F. Aubin *et al.*, New J. Phys. **10**, 103017 (2008).
[8] C. Amole *et al.*, Phys. Rev. **114**, 231302 (2015).
[9] C. Amole *et al.*, Phys. Rev. D **93**, 061101 (2016).
[10] C. Amole *et al.*, Phys. Rev. D **93**, 052014, (2016).
[11] E. Behnke *et al.*, Phys. Rev. D **86**, 052001 (2012).
[12] E. Behnke *et al.*, Phys. Rev. Lett. **106**, 021303 (2011).
[13] S. Archambault *et al.*, Phys. Lett. B **711**, 153 (2012).
[14] E. Behnke *et al.*, arXiv:1611.01499 [hep-ex] (2016).
[15] A.E. Robinson, Ph.D. thesis, University of Chicago (2015).
[16] MIL-STD-1246C, Product Cleanliness Levels and Contamination Control Program, US Department of Defense (1994).
[17] K. Klaasen, Galileo Technical Report JPL D-5880, 1625-210 (1993).
[18] E. W. Lemmon, M. L. Huber, and M. O. McLinden, NIST Standard Reference Database 23: Reference Fluid Thermodynamic and Transport Properties-REFPROP, Version 9.0, National Institute of Standards and Technology, Standard Reference Data Program, Gaithersburg (2010).
[19] MATLAB: Neural Network Toolbox, The MathWorks, Inc., Natick, Massachusetts, United States.
[20] S. Agostinelli *et al*, Nucl. Instr. Meth. A **506** 250-303 (2003); J. Allison *et al*, IEEE Trans. Nucl. Sci. **53** No. 1, 270-278 (2006).
[21] D. Fustin, Ph.D thesis, University of Chicago (2012).
[22] J.D. Lewin and P.F. Smith, Astrop. Phys. **6**, 87 (1996).
[23] A. L. Fitzpatrick *et al.*, J. Cosmol. Astropart. Phys. 02 (2013) 004.
[24] N. Anand, A. L. Fitzpatrick, W. C. Haxton, Phys. Rev. C **89**, 065501 (2014).
[25] M. I. Gresham and K. M. Zurek, Phys. Rev. D **89**, 123521 (2014).
[26] V. Gluscevic, M. I. Gresham, S. D. McDermott, A. H. G. Peter, and K. M. Zurek, J. Cosmol. Astropart. Phys. 12 (2015) 057.
[27] V. Gluscevic and S. D. McDermott, 2015, dmdd, Astrophysics Source Code Library, record ascl:1506.002.
[28] D.R. Tovey *et al.*, Phys. Lett. B **488**, 17 (2000).
[29] O. Buchmueller, M.J. Dolan, S.A. Malik *et al.*, J. High Energy Phys. **2015**, 037 (2015).
[30] D. Abercrombie *et al.* arXiv:1507.00966 [hep-ex] (2015).
[31] A. Boveia *et al.* Report Number CERN-LPCC-2016-001. arXiv:1603.04156 [hep-ex] (2016).
[32] CMS Collaboration, Report Number CMS-PAS-EXO-16-037 (2016).
[33] M. Felizardo *et al.*, Phys. Rev. D **86**, 072013 (2014).
[34] Changbo Fu *et al.* (PANDAX-II Collaboration), Phys. Rev. Lett. **118**, 071301 (2017).
[35] M.G. Aartsen *et al.* (IceCube Collaboration), arXiv:1612.05949 [astro-ph.HE] (2017).
[36] T. Tanaka *et al.*, Astroph. J. **742**, 78 (2011).
[37] K. Choi *et al.*, Phys. Rev. Lett. **114**, 141301 (2015).
[38] L. Roszkowski, R. R. de Austri, and R. Trotta, J. High Energy Phys. **2007**, 075 (2007).
[39] D. S. Akerib *et al.*, Phys. Rev. Lett. **116**, 161302 (2016).
[40] E. Aprile *et al.*, Phys. Rev. D **94**, 122001 (2016).
[41] S. Adrián-Martínez *et al.*, Phys. Lett. B **759**, 69 (2016).
[42] S. Adrián-Martínez *et al.*, J. Cosmol. Astropart. Phys. 05 (2016) 016.
[43] D. S. Akerib *et al.*, Phys. Rev. Lett. **118**, 021303 (2017).
[44] A. Tan *et al.*, Phys. Rev. Lett. **117**, 121303 (2016).
[45] G. Angloher *et al.*, Eur. Phys. J. C **76**: 25 (2016).
[46] R. Agnese *et al.*, Phys. Rev. Lett. **116**, 071301 (2016).
[47] P. Agnes *et al.*, Phys. Rev. D **93**, 081101 (2016).
[48] R. Agnese *et al.*, Phys. Rev. Lett. **112**, 241302 (2014).
[49] R. Agnese *et al.*, Phys. Rev. D **92**, 072003 (2015).
[50] L. Hehn *et al.*, Eur. Phys. J. C **76**: 548 (2016).